biomass coreh$_2$o premier

→ REPORT FOR MISSION SELECTION

An Earth Explorer to observe forest biomass

biomass coreh$_2$o premier

→ REPORT FOR MISSION SELECTION

An Earth Explorer to observe forest biomass

This report is based on contributions from following members of the Biomass Mission Advisory Group (MAG):

Shaun Quegan – MAG Chairman (University of Sheffield, GB)
Thuy Le Toan – MAG Chairman (Centre for the Study of the Biosphere from Space, FR)
Jérôme Chave (Evolution and Biological Diversity Laboratory, FR)
Jørgen Dall (Technical University of Denmark, DK)
Kostas Papathanassiou (DLR, DE)
Fabio Rocca (Politecnico di Milano, IT)
Lars Ulander (Swedish Defence Research Agency, SE)
Mathew Williams (University of Edinburgh, GB)

They were supported by two observers:

Sassan Saatchi (JPL, US)
Hank Shugart (University of Virginia, US)

The scientific content of the report was compiled by Klaus Scipal (Scientific Coordinator) with additional contributions, in particular, from Philippe Ciais (LSCE, FR), Pascale Dubois-Fernandez (ONERA, FR), Tim Hill (University of Edinburgh, GB), Philippe Peylin (LSCE, FR), Casey Ryan (University of Edinburgh, GB), Ludovic Villard (CESBIO, FR) and from ESA, Malcolm Davidson, Georg Fischer and Nicolas Floury.

The technical content of the report was compiled by Marco Arcioni (Technical Coordinator) with contributions from Edoardo Benzi, Christophe Caspar, Elena Daganzo-Eusebio, Franco Fois, Raffaella Franco, Antonio Gabriele, Chung-Chi Lin, Luca Massotti and Andrea Perrera (all from ESA), based on inputs derived from the industrial Phase-A system and technical activities.

Cover image: ESA/AOES Medialab

Contents

→ EXECUTIVE SUMMARY

Executive Summary

The Earth Explorer Biomass mission will provide the scientific community with the first accurate maps of tropical, temperate and boreal forest biomass, including height and disturbance patterns. This information is urgently needed to improve our understanding of the global carbon cycle and to reduce uncertainties in the calculations of carbon stocks and fluxes associated with the terrestrial biosphere.

Biomass addresses one of the most fundamental questions in our understanding of the land component in the Earth system, namely the status and the dynamics of forests, as represented by the distribution of biomass and how it is changing. Gaining accurate and frequent information on forest properties at scales that allow changes to be observed will mean that the scientific community is equipped to address a range of critical issues with far-reaching benefits for science and society. Moreover, Biomass will greatly improve our knowledge of the size and distribution of the terrestrial carbon pool, and provide much-improved estimates of terrestrial carbon fluxes. In addition, the mission responds to the pressing need for biomass observations in support of global treaties such as the United Nations Framework Convention on Climate Change initiative for the Reduction of Emissions due to Deforestation and Forest Degradation. These mission objectives respond directly to the specific scientific challenges in ESA's Living Planet Programme.

The emission of carbon dioxide to the atmosphere by human activity has been recognised as the major driver in climate change. Terrestrial ecosystems play an important role, both in the release of carbon through land use and deforestation and in the sequestration of carbon through vegetation growth processes. There is strong evidence that the terrestrial biosphere has acted as a net carbon sink over the last 30 years, removing from the atmosphere approximately one third of the carbon dioxide emitted from the combustion of fossil fuel. Nevertheless, terrestrial ecosystems are the largest source of uncertainty in the global carbon budget. Uncertainties lie in the spatial distribution of carbon stocks and carbon exchange, and in the estimates of carbon emissions resulting from human activity and natural processes. A central parameter in the terrestrial carbon budget is forest biomass, which is a proxy for carbon. Despite its crucial role in the terrestrial carbon budget, forest biomass in most parts of the world is poorly quantified owing to the difficulties in taking measurements from the ground and the lack in consistency when aggregating measurements across scales.

Biomass will be implemented as a P-band Synthetic Aperture Radar (SAR) mission. It will exploit the unique sensitivity of P-band SAR together with advanced retrieval methods to measure forest biomass, height and disturbance across the entire biomass range every six months. The resolution and accuracy of the Biomass products will be compatible with the needs of international reporting on carbon stocks and terrestrial carbon models. In addition, Biomass will provide the first opportunity to explore Earth's surface using the P-band wavelength. The data are also expected to be used for monitoring glacier and ice sheet velocities, mapping subsurface geology in deserts and mapping the topography of forest floors. Additional products and applications are likely to emerge and be evaluated during the life of the mission.

The Biomass space segment comprises a single satellite in a near-polar, Sun-synchronous orbit at an altitude of 637–666 km, depending on the different mission phases. The orbit is designed to enable repeat pass interferometric acquisitions throughout the mission's life and to minimise the impact of disturbances from the ionosphere.

The configuration of the satellite is strongly constrained by the accommodation of the very large reflector antenna (~12 m diameter) inside the

launcher. This large antenna must be folded for launch and deployed in orbit to form a stable aperture.

The Biomass P-band (435 MHz, ~69 cm wavelength) SAR has full polarimetric and multipass interferometric capabilities. The signal bandwidth is 6 MHz, a small value dictated by the frequency spectrum allocation. The SAR will operate in a stripmap mode with a swath illuminated by a single antenna beam, which is an imaging configuration similar to that of the ERS-1/2 SAR. Global coverage is obtained by the interleaved stripmap operations between two or three complementary swaths.

The satellite has a launch mass of ~1200 kg, versus a launcher nominal capability of 1364 kg, and a power generation capability of ~1.5 kW at end of life. The instantaneous instrument data rate of 110–120 Mbit/s requires, for the different communication architecture under consideration, an onboard mass memory of ~1000 Gbit and a data downlink capacity in the range of 310–520 Mbit/s.

The baseline launcher is Vega. Compatibility of the satellite with backup launchers such as Soyuz and Antares has also been ensured. The mission is designed to exploit acquisitions made at dawn/dusk, i.e. 06:00/18:00 local time (at the equator).

The SAR data are delivered to the Kiruna ground station in Sweden via an X-band downlink. Auxiliary data, which are required to quantify the characteristics of the propagation path of the radar signal, are used in the end-to-end system calibration and processing of the SAR data.

The Biomass mission will last five years and comprises a short tomographic phase (~55 days) followed by the nominal operational phase with an orbit repeat period of up to 25 days. The tomographic phase will be performed just after the commissioning phase, which will be carried out with the satellite flying in the nominal orbit or in the tomographic orbit depending on the final design. Upon completion of the tomographic phase, the satellite will be transferred into the nominal orbit until the end of the mission. Finally, a deorbiting phase (satellite disposal) will take place. This does not require any provision of fuel thanks to the mission's low orbit.

The ground segment uses the generic Earth Explorer ground segment infrastructure. This comprises the Flight Operations Segment and the Payload Data Ground Segment.

During Phase-A, supporting scientific studies and campaigns were initiated to answer all critical scientific issues that had been identified for the mission, including those set out by the Earth Science Advisory Committee at the mission down-selection following Phase-0.

New campaign data greatly aided the understanding of the physics underlying the sensitivity of P-band SAR to forest properties in different biomes and contributed to the development of novel retrieval algorithms. Retrieval methods have been applied successfully to campaign data, and, in particular, were demonstrated under the conditions of hilly heterogeneous dense tropical forest in French Guiana and boreal forest in Sweden. Performance assessment of these algorithms showed that the required accuracy can be achieved.

The main sources of uncertainty influencing the retrieval performance have been identified. Efforts to address these issues are continuing and will benefit from further work on the full use of ascending and descending measurements, exploiting multiple acquisitions, and a better understanding of the error structure in the height and biomass measurements to optimise their combined use. Major progress was also made in understanding and mitigating the impact of the ionosphere on the measurements. The dawn/dusk orbit selected for Biomass means that scintillations have negligible effect on biomass inversion performance in the observed regions. Distortion of data caused by Faraday rotation can be corrected to accuracies that render it negligible with regard to biomass inversion.

In terms of the technical maturity of the mission concept, the maturity of the satellite platform is different than for the SAR payload. No critical elements have been identified for the development of the platform. At payload level, limited development risks are associated with specific elements of the P-band SAR, specifically in the feed system, the power amplifier and the instrument calibration aspects. In all cases, dedicated activities are being conducted to mitigate these risks.

At mission level, the operation of Space Objects Tracking Radar (SOTR) systems restricts the imaging opportunities for Biomass because of the potential impact on the SOTR performance from the Biomass SAR signal. It is noted that, according to the relevant ITU-R Recommendation, the operational limitation is due to the SOTR vulnerability with respect to the Biomass transmission – a very different situation to radio frequency interference from sources on the ground that impairs the operations of, for instance, Earth-observing radiometers. These SOTR stations are under the authority of the US Department of Defense (DoD). The impact of not operating Biomass when in sight of an SOTR, as requested by DoD, will be a reduction of the observed forested areas, which affects the mission's primary objectives. However, this limitation is considered to be acceptable because the most critical forest regions, such as the tropical forest belt, the boreal forest of Siberia and the temperate forests of China, would still be covered.

Assuming the expected successful outcome of ongoing pre-developments, the maturity of critical technologies will reach the required level prior to the start of the implementation phases. The worst-case operational restriction that could arise following the request of the US DoD would not significantly affect the primary objectives of the mission. The development schedule is compatible with a launch in 2019.

→ INTRODUCTION

1. Introduction

The changing Earth system poses significant scientific challenges and opportunities for Earth observations from the vantage point of space. As part of its Earth Observation Envelope Programme, the European Space Agency's (ESA's) series of Earth Explorer missions offers new observational capabilities to explore and understand different aspects of the Earth system.

These missions are developed in response to priorities identified by the scientific community. They address and fulfil ESA's Living Planet Programme strategic objectives (SP-1304, 2006) and comprise a critical component of the global Earth observing system.

The fundamental principle of defining, developing and operating Earth Explorer missions in close cooperation with the scientific community provides an efficient tool to address pressing Earth-science questions as effectively as possible. Coupled with an ability to develop and embark novel sensing technologies, this gives the possibility to substantially advance the frontier of our scientific knowledge of the Earth system and the human impact on natural processes.

Since the science and research elements of the Living Planet Programme were established in the mid-1990s, this user-driven strategy has resulted in the selection of six Earth Explorer missions for implementation. Together, they cover a broad range of scientific topics. Importantly, the complementarity between the selected missions also offers new opportunities for exploiting mission synergies, thereby establishing a stimulus for the development of new applications of Earth observation data.

Earth Explorer missions are split into two categories: Core and Opportunity. Core Earth Explorers are larger missions addressing complex issues of scientific interest and which require substantial elements of new technology. By contrast, Opportunity missions are smaller and have more focused scientific goals that are normally achieved by novel uses of existing lower-risk technologies. Through a process of peer review and selection, both types are implemented in separate cycles to ensure a steady flow of missions to address key Earth-science questions.

The first cycle for Core missions resulted in the Gravity field and steady-state Ocean Circulation Explorer, GOCE, which was launched in March 2009, and the Atmospheric Dynamics Mission ADM-Aeolus, scheduled for launch in 2014. The second cycle, initiated in 2000, resulted in the Earth Clouds Aerosols and Radiation Explorer, EarthCARE, due for launch in 2015. The first cycle for Opportunity missions resulted in the ice mission CryoSat, which was rebuilt and launched in April 2010 following a launch failure in 2005, and the Soil Moisture and Ocean Salinity, SMOS, mission, also launched in 2009. The second cycle resulted in the magnetic field mission, Swarm, which is scheduled to be launched in 2012.

A third cycle of Earth Explorer Core missions was initiated by a Call for Ideas released in 2005. In May 2006, six of the candidate missions were selected for Assessment Study following a peer review of 24 proposed mission ideas. Upon completion of Pre-Feasibility Study (Phase-0), a User Consultation Meeting was held in January 2009 in Lisbon, Portugal, at which the six candidates were presented to the scientific community together with their accompanying Reports for Assessment (SP-1313, 2008).

In February 2009, three out of the six candidate missions were selected for Feasibility Study (Phase-A): Biomass, Cold Regions Hydrology high-resolution Observatory (CoReH$_2$O) and Process Exploration through Measurement of infrared and millimetre-wave Emitted Radiation (PREMIER).

— Biomass aims to observe forest biomass for a better understanding of the carbon cycle.

— CoReH$_2$O aims to observe snow and ice for a better understanding of the water cycle.

— PREMIER aims to observe atmospheric composition for a better understanding of chemistry–climate interactions.

The Report for Mission Selection for each candidate captures the status of the respective mission concept at the end of Phase-A activities. The three reports are provided to the Earth observation research community prior to the User Consultation Meeting to be held in 2013 and subsequent selection of a single Earth Explorer 7 mission.

The three reports follow a common structure comprising this introductory first chapter and eight subsequent chapters as follows:

— Chapter 2 – identifies the background and scientific issues to be addressed by the mission, considering the contribution of past and present activities in the field. It provides the justification for the mission, set within the post-2018 time frame, and includes a review of the current scientific understanding of the issue in question while identifying the potential 'delta' that the mission could provide.

— Chapter 3 – drawing on arguments presented in Chapter 1 and Chapter 2, this chapter summarises the specific research objectives of the mission.

— Chapter 4 – outlines the mission requirements, including required geophysical data products and observational parameters, the need for observations from space and aspects of timeliness and timing of the mission.

— Chapter 5 – provides an overview of the system elements, including the space and ground segments; and of the operations, calibration and data processing up to Level-1b.

— Chapter 6 – describes the advances in scientific algorithms and processing, validation and assimilation techniques which may be required to meet the data product requirements.

— Chapter 7 – makes a comparison of expected versus required performance and ability to fulfil the research/observational objectives based upon the documented system concept.

— Chapter 8 – documents the maturity of the scientific user community in respect to planned use of the anticipated scientific products, the global context in terms of complementary missions as well as the operational or applications potential of the data products.

— Chapter 9 – outlines a programme of implementation. It also addresses scientific and technical maturity, the development status of key technologies, risks, logistics and schedules.

This Report for Selection covers the Biomass mission.

→ BACKGROUND AND SCIENTIFIC JUSTIFICATION

2. Background and Scientific Justification

2.1 Introduction

The most important environmental challenge in the early 21st century is to improve our understanding of global change and how it will affect the Earth system and the feedbacks within the system. This is important so that societies can predict, mitigate and adapt to any likely impacts.

The carbon cycle is fundamental to the functioning of Earth, involving many intermeshed processes through which carbon is exchanged between the atmosphere, land and ocean. Quantifying this global cycle is essential to understanding many of the dramatic changes taking place in the Earth system. In particular, the disturbance to the carbon cycle from the burning of fossil fuel and land-use change is the most significant driver of global change (IPCC, 2007).

Terrestrial processes play a crucial role in the carbon cycle through carbon uptake and respiration associated with vegetation growth and emissions from disturbance caused by both natural processes, such as wildfires, and land-use change through human activity. There is strong evidence that over the last 50 years the terrestrial biosphere has acted as a net carbon sink, removing from the atmosphere approximately one third of the CO_2 emitted by fossil fuel combustion (Canadell et al., 2007). However, the status, dynamics and evolution of the terrestrial biosphere are the least understood and most uncertain elements in the carbon cycle.

This uncertainty spans a wide range of temporal scales: the interannual variability of atmospheric CO_2 is controlled mainly by the terrestrial biosphere, while the IPCC has identified coupling between the terrestrial carbon cycle and climate as one of the major areas of uncertainty in climate change over decadal to century time-scales. Spatially, there are major uncertainties in the distribution of carbon stocks and carbon exchange, in the estimates of carbon emissions due to forest disturbances, and in the uptake of carbon through forest growth.

A fundamental parameter characterising the spatial distribution of carbon in the biosphere is biomass, which is the amount of living organic matter in a given space, usually measured as mass or mass per unit area. Half of all biomass is carbon (*IPCC Good Practice Guide,* 2003). Biomass therefore represents a basic accounting unit for carbon. Forests comprise ~80% of terrestrial above-ground biomass (Houghton, 2005).

Because of its importance for climate, biomass is identified by the United Nations Framework Convention on Climate Change (UNFCCC) as an Essential Climate Variable (ECV) needed to reduce uncertainties in our knowledge of the climate system (Global Climate Observing System (GCOS), 2003; 2004; 2010). In addition, sequestration of carbon in forest biomass is a critical mechanism for mitigating climate change, as recognised under the Kyoto Protocol (whose first commitment period ends in 2012), other than reducing emissions.

While global observation programmes for most of the terrestrial ECVs are advanced or evolving, there is currently no such effort for biomass (Houghton et al., 2009).

Arising from the UNFCCC, the United Nations initiative for Reducing Emissions through Deforestation and Forest Degradation (REDD+) is a set of steps designed to use market and financial incentives to reduce the emissions of greenhouse gases from deforestation and forest degradation (UN-REDD Programme, 2008). The objective of REDD+ is to promote sustainable management of forests, maintain their carbon stores, reduce emissions of CO_2 from forest loss, and thereby mitigate climate change. It is also recognised that REDD+ can deliver substantial environmental and social benefits. This

Basic facts

– Large scale values of biomass are usually described in metric gigatonnes of carbon (GtC)

– Small scale values are usually quoted in terms of metric tonnes per hectare (t ha^{-1}), where 1 ha=10^4 m^2, though the carbon modelling community often works in gC m^{-2}

– About 5% of incident solar radiation is fixed in biomass by plants

– Terrestrial biomass holds 363–650 GtC

– Terrestrial ecosystems contain about 99% of the world's biomass

– Forests hold 70–90% of Earth's above-ground biomass, with the majority of forest biomass located in the Tropics

– About 50% of forest biomass is carbon

is because of the importance of forests in biodiversity conservation, water quality, prevention of erosion, local climate, flood control and so on, and because of the contribution REDD+ can make to alleviate poverty. Essential to the successful implementation of REDD+ are reliable Monitoring, Reporting and Verification (MRV) systems to support the carbon accounting on which it is based. This involves mapping the carbon content of forests and estimating the changes in carbon due to disturbance and forest growth. Obtaining spatially explicit and consistent knowledge on biomass is therefore a basic requirement for understanding and managing the processes involved in the carbon cycle, while supporting REDD+ and other international policies for climate change mitigation and adaptation.

The importance of improved quantitative knowledge about the terrestrial carbon cycle is stressed in *The Changing Earth* (ESA, SP-1304, 2006). This publication draws attention to the need for better estimates of biomass stocks, fluxes and processes to quantify terrestrial carbon exchange. The measurement of biomass structure, status and dynamics is specifically recognised as an observational priority. Furthermore, SP-1304 recognises that data have to be effectively linked to models in order to understand the connections and interactions within and between different components of the Earth system, and to improve the predictive power of models. The Biomass mission concept has been developed to be entirely consistent with these principles, as this document demonstrates. Biomass will make significant contributions to several other areas identified in SP-1304, notably the water cycle, ecosystem characteristics and disturbances, land-use change, biodiversity and the exploitation of natural resources such as wood for fuel.

Biomass will provide maps of forest biomass stocks at a spatial resolution in the order of 4 ha, twice a year over the life of the five-year mission. These maps will greatly improve on existing forest inventories, such as national Global Forest Resource Assessments (GFRAs) produced by the UN Food and Agriculture Organization (FAO, 2010), and give vastly improved information for managing Earth's forest resources.

Biomass will also provide spatially-resolved maps of biomass change, which can be linked to disturbance, degradation, land-use change, forest growth and spread. In addition, the full resolution of the instrument of around 0.25 ha will be used to detect deforestation; linking this to the coarser-resolution maps of biomass will allow associated carbon loss to be estimated at scales commensurate with the processes of land-use change.

2.2 The Global Carbon Cycle

Fundamental to understanding the global carbon cycle is accurate knowledge of how much carbon is stored in the atmosphere, ocean and terrestrial biosphere, i.e. the carbon stocks or pools, and the rate of flow between the different pools, usually referred to as fluxes. Fluxes are often subdivided into sources (emissions to the atmosphere) and sinks (uptake from the atmosphere). The net flux for a given component of the cycle is the difference between its source and sink strengths.

Figure 2.1 shows our current knowledge on the size of the atmospheric, ocean and terrestrial biosphere pools of carbon and the net fluxes between them for the 2000s. The pools and fluxes are derived from IPCC (2007) and more recent studies (Le Quere et al., 2009; Friedlingstein et al., 2010). They clearly highlight the key role of the terrestrial biosphere in the carbon cycle.

The net flux to the atmosphere is the sum of the sources and sinks, but is measured independently and is well-constrained, with an uncertainty of about 3% of the mean value. The estimate of net ocean-atmosphere flux is derived from models, but the same value is derived for the 1990s using the O_2:N_2 ratio (IPCC, 2007). It has well-defined error bars and an uncertainty of roughly 20%
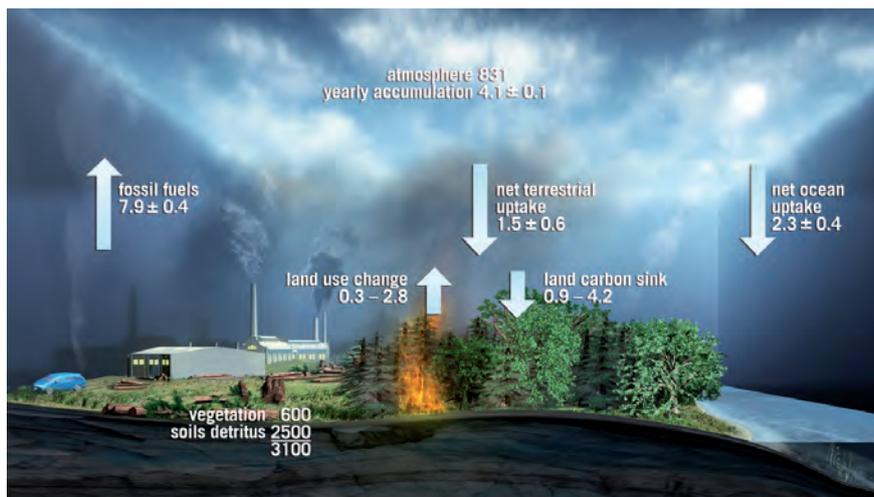
Figure 2.1. The global carbon cycle for 2000–09 showing estimated sizes in GtC of the atmospheric, ocean and terrestrial carbon pools, and the net annual fluxes between them in GtC yr^{-1}. Estimates are from the Global Carbon Project (*www.globalcarbonproject.org/carbonbudget*). A small carbon runoff term from land to ocean has been omitted from the figure. (ESA/AOES Medialab)

of the mean value. Emissions from the burning of fossil fuel are also well-known, with uncertainties approximately 6% of the mean value.

The net terrestrial land-atmosphere flux is not measured directly, but is inferred by subtracting the fossil fuel and net ocean-atmosphere fluxes from the observed atmospheric increase. This inevitably causes the net land-atmosphere flux to have the largest uncertainty amongst all the net fluxes. The land surface is found to be a net carbon sink, with uncertainty of the same order as its magnitude.

The land sink is actually made up of a source owing to land-use change (mainly tropical deforestation) and a larger, poorly understood sink, both of which have large uncertainties. These uncertainties are coupled, since the sum of the two fluxes must provide the net flux. Changes in either can have very significant consequences for the whole carbon balance.

2.2.1 The Terrestrial Carbon Pool

The terrestrial biospheric carbon pool in its entirety, biomass and soil organic matter, is roughly four times larger than that of the atmosphere (~3100 GtC vs. 831 GtC). The carbon in vegetation, mainly in forest biomass, is roughly equivalent to that of the atmosphere. Most recent estimates indicate that >70% of the world's biomass is located in tropical forests (Pan et al., 2011). The uncertainty in total biomass is, however, very large, with recent estimates ranging from 363 GtC (Pan et al., 2011) to 650 GtC (FAO, 2010). Consistent and accurate global forest biomass estimates would greatly reduce these uncertainties.

The uncertainty in the total stocks of biomass carbon in the major terrestrial pools (e.g. stem wood) reflects even greater uncertainty in its spatial distribution at regional to national scales (Subsection 2.3.1) and local scales. Natural forests, which dominate the Tropics where most biomass is located, are often multi-aged and bio-diverse, with varied growth forms and life histories, leading to a significant spatial variability in biomass.

This variability is determined by stochastic processes of mortality and disturbance, making sampling difficult and giving rise to significant variation in estimates of mean biomass. As an example, analysis of data from Japan Aerospace Exploration Agency's (JAXA's) Advanced Land Observing Satellite (ALOS) Phase Array L-band Synthetic Aperture Radar (PALSAR) over an area in central Mozambique shows that, even in areas far from human activity, there is considerable natural disturbance in forests, but at small scales. In areas affected by human activity, disturbance is spatially clumped and exhibits much larger sizes (Fig. 2.2).

Figure 2.2. Histograms of deforestation event size distributions for two regions in the Sofala Province of Mozambique with contrasting land use, based on analysis of ALOS PALSAR data (Ryan et al., 2012). LCC indicates land-cover change.
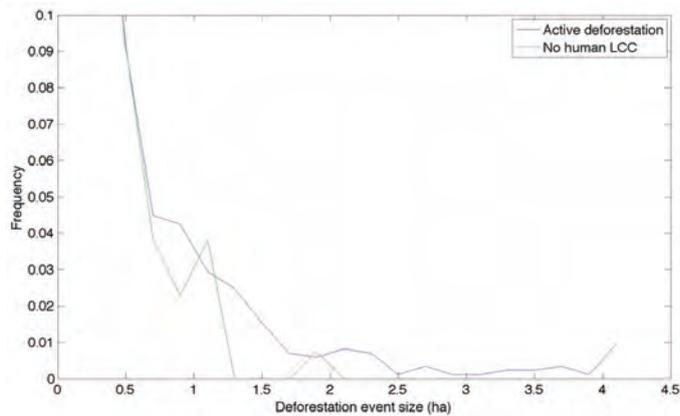
2.2.2 Terrestrial Carbon Fluxes

There are very large uncertainties in our knowledge of the carbon fluxes between land and atmosphere. This is in sharp contrast with the other components of the carbon cycle (Fig. 2.1). The land flux has two components, a source term mainly due to deforestation and forest degradation in the Tropics, and a poorly understood sink term. The source term only can be estimated from current observations, and reported estimates have an average value of 1.1 GtC yr^{-1} for the 2000s (see Table 2.1, which also contains estimates for the 1980s and 1990s). The uncertainty in this value is indicated as a range, which arises from uncertainties both in the area deforested and in the biomass in the disturbed regions (DeFries et al., 2002; Houghton et al., 2009).

Taking the extremes of the range means that land-use change contributed 4–26% to the total anthropogenic flux to the atmosphere in the 2000s. To balance the carbon budget, the land must have absorbed around 2.5 GtC yr^{-1} in the 2000s if the mean value for the land emissions is adopted (Fig. 2.3).

This land sink is calculated as the difference between the net land sink (which is inferred) and the estimated emissions from land-use change, and is known as the residual land sink. Errors in estimating emissions translate directly into errors in estimating the residual land sink. There is an uncertainty of roughly 70% (low) to 150% (high) of the mean value, and the location and the processes underlying it are the source of hot debate.

Nonetheless, the residual land sink is clearly important in controlling climate warming. Adding a land-use change flux of 1.1 GtC yr^{-1} to fossil fuel emissions implies a total anthropogenic flux of 9 GtC yr^{-1} to the atmosphere in the 2000s. Of this, 43% has remained, contributing to the ever-increasing level of CO_2 in the atmosphere, while 27.5% was absorbed by the oceans. Hence, the land absorbed around 29.5% of the total carbon emissions, but with very large uncertainties as described above.

Terrestrial carbon uptake is also highly variable around these average values, ranging from almost zero in some years to more than the entire total fossil fuel input in others, and shows some correlation with the El Niño–La Niña climate oscillation (Sarmiento & Gruber, 2002); the reasons for this variability are poorly understood (Le Quere et al., 2009). A key question, therefore, is how much of this missing sink is due to carbon being fixed in forest biomass?

It is a remarkable fact that the accelerating growth in emissions has been accompanied by increasing take-up of atmospheric CO_2 by the land and oceans (Table 2.1). This is insufficient to stop the increasing rise of CO_2 in the atmosphere, but it does slow it down. However, recent evidence suggests that the effectiveness of the terrestrial control on atmospheric buildup of CO_2 may have decreased by 0.25±0.21% yr^{-1} since Keeling began his systematic measurements of atmospheric CO_2 in 1958 (Canadell et al., 2007; Le Quere et al., 2009).

	1980–89	1990–99	2000–09
Atmospheric increase	3.3±0.1	3.2 ±0.1	4.1±0.1
Emissions (fossil fuel and cement)	5.4±0.3	6.4±0.4	7.9±0.4
Net ocean to atmosphere flux	−1.8±0.8	−2.2±0.4	−2.3±0.5
Net land to atmosphere flux	−0.3±0.9	−1.0±0.6	−1.5±0.6
The net land flux is partitioned as:			
Land-use change flux	1.4(0.4 to 2.3)	1.6(0.5 to 2.7)	1.1(0.3 to 2.8)
Residual terrestrial sink	−1.7(−3.4 to 0.2)	−2.6(−4.3 to −0.9)	−2.5(−4.2 to −0.9)

Table 2.1. The global carbon budget in GtC yr^{-1}, with land fluxes indicated in blue. The errors represent ±1 standard deviation estimates and not interannual variability, which is larger. Positive fluxes are emissions to the atmosphere, negative fluxes are losses from the atmosphere. The uncertainties in the source and sink terms making up the net land to atmosphere flux are large and indicated only as ranges. (IPCC, 2007; Le Quere et al., 2009; Friedlingstein et al., 2010)

If this decrease continues, as models predict (some even predicting that the land will become a carbon source in the latter part of the 21st century (Cox et al., 2000; Friedlingstein et al., 2006)), the buildup of atmospheric CO_2 will accelerate and speed up climate warming. Increased emissions from deforestation would further exacerbate this rise, while an increase in land takeup would mitigate it. Hence, knowledge about these land processes is crucial, both to understand their contribution and for efforts to manage the carbon cycle to mitigate climate change.

In addition to the global estimates of net land carbon fluxes reported above, coarse spatial detail at sub-continental scale has been added by use of 'atmospheric inversion'. This technique exploits the differences between CO_2 concentrations measured from *in situ* stations around the world, together with atmospheric transport models, to infer sources and sinks at scales of several degrees of latitude and longitude (Gurney et al., 2002; Jacobson et al., 2007; Rödenbeck et al., 2003; Baker et al., 2006; Stephens et al., 2007; Gurney & Eckels, 2011).

Table 2.2 collates a set of recent results from this approach, aggregated into broad latitudinal bands. The estimated total net land fluxes range from −2.3 GtC yr^{-1} to −1.1 GtC yr^{-1}, and the variation in the fluxes estimated by latitude is even larger. Northern latitudes are consistently found to be a carbon sink, though of widely varying magnitude, but even the sign of the tropical flux is unknown. Hence, atmospheric inversion results provide only weak constraints on the land carbon cycle, and only at sub-continental scales.
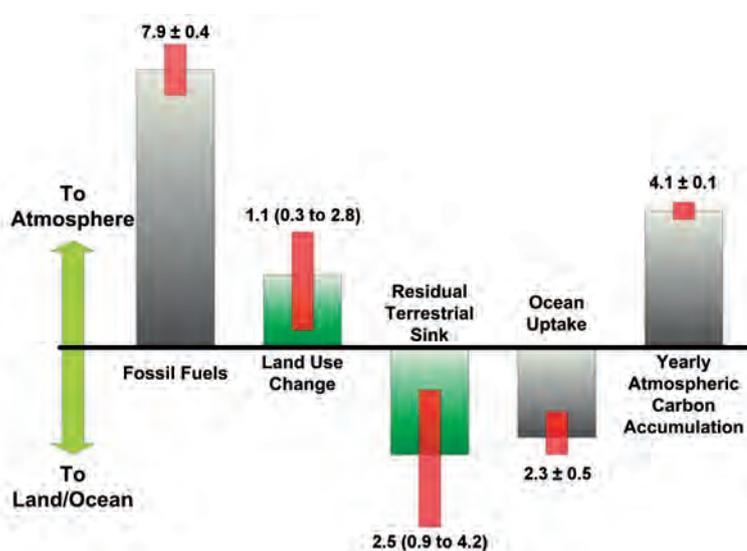
Figure 2.3. Global carbon flux budget for the 2000s, partitioned into emissions to the atmosphere from the burning of fossil fuels and land-use change and uptake from the land and ocean. Fluxes related to land are in green. The yearly accumulation of carbon (net flux) to the atmosphere is given in the far-right bar; this is the sum of all the component fluxes, but is measured independently. The uncertainties in each of the flux estimates are indicated by red error bars. The large uncertainties in the terrestrial fluxes relative to other flux sources are reflected in the significantly larger error bars. (ESA)

	Gurney et al., 2002	Jacobson et al., 2007	Rödenbeck et al., 2003	Baker et al., 2006	Stephens et al., 2007	Transcom 1996–2008
Southern hemisphere (<20°S)	−0.2±1.1(0.2)	−2.4±2.0	0.0±0.2	−1.2	0.1±1.1	−0.3±0.4
Tropics (20°S to 20°N)	1.1±1.3(1.5)	4.2 ±2.7	−1.0±0.4	1.6	0.7±1.4	1.1±0.8
Northern hemisphere (>20°N)	−2.3±0.6(0.7)	−2.9 ±1.0	−0.7±0.2	−2.7	−2.2±0.6	−2.0±0.5
Total net flux	−1.4	−1.1	−1.8	−2.3	−1.4	−1.1±0.9

Table 2.2. Estimates of net land surface CO_2 fluxes for 1992–1996 (first five columns) and 1996–2008 (Transcom) in broad latitudinal bands calculated in a range of studies. Compiled values are taken from Emanuel Gloor (private communication) for 1992–1996 values and derived from Transcom data in 14 different inversion studies (*http://transcom.lsce.ipsl.fr*) for the final column. Positive values indicate a carbon source to the atmosphere. Units are GtC y^{-1}.

In summary, the uncertainties in current estimates of the global carbon budget are dominated by uncertainties about the size and location of the terrestrial sources and sinks. The main land source is thought to be deforestation in the Tropics, but there is an uncertainty of around 20% in the total net annual anthropogenic CO_2 flux to the atmosphere. A land sink is needed to close the global carbon budget, but its nature, size and location are highly uncertain. Estimates of land emissions and land uptake would be significantly improved if reliable estimates of global biomass and changes were available.

2.3 The Need for Improved Observations of Forest Biomass

The previous section summarised our knowledge of the global carbon cycle and highlighted the large uncertainties in the terrestrial elements of the cycle. The key role of forest biomass as the main repository of vegetation carbon and the importance of biomass in carbon emissions and uptake fluxes was stressed. In this section, we document the need for improved observations of forest biomass, spatial distribution and change with time, which will contribute in four distinct ways to a new understanding:

— improved knowledge of the terrestrial carbon pools by direct inference of carbon stocks from forest biomass and through improved vegetation modelling.

— improved estimates of carbon emissions from land-use change and forest degradation.

— improved estimates of land carbon uptake from forest growth.

— improved vegetation modelling and long-term climate predictions through data assimilation, model calibration and verification of vegetation models.

2.3.1 Improved Knowledge of Terrestrial Carbon Pools

2.3.1.1 International reporting on biomass

Maps of biomass stocks are the basis for calculating emissions based on land-use change. In addition, biomass maps are of enormous value in themselves: they tell us about the world's forest resources. This is crucial because of the role of forests for renewable raw materials and energy, mitigating climate change, maintaining biological diversity, protecting land and water resources,

improving air quality and providing food; they also have enormous value for recreation and spiritual well-being.

The importance of knowing about forests and the very wide range of ecosystem services they provide underlies the production of the GFRAs by the UN FAO every 5–10 years since 1946.

These are the main sources of information on worldwide forest biomass stocks and provide, *inter alia*, forest area and average values of biomass at country level. Country statistics are based on data from national forest inventories, which, in turn, are based on sample plots and direct measurement of tree characteristics, such as growing stock at ground level. However, these assessments suffer from data gaps, sampling biases, inconsistent methods, a lack of spatial information, and unrepresentative samples (Grainger, 2008). This problem is particularly acute in the Tropics, where forest reporting has weak institutional support in many countries.

Ultimately, these limitations mean that GFRA data cannot identify forest carbon sinks or sources at the requisite scales or accuracy for constraining the global carbon cycle. Similarly, these data cannot support the implementation of a carbon trading scheme through REDD+ protocols.

2.3.1.2 Improved mapping of biomass

Forest biomass cannot be measured directly on any but the smallest scales (typically much less than 1 ha). This is because it involves the complete harvest of the trees and very laborious measurements to determine the mass of wood in stems, roots and branches. For stand scales (ha), inventory approaches can be used, based on trunk diameter measurements on all stems within a study area. These can be converted to biomass using allometric equations derived from a small number of destructive harvests of trees (Chave et al., 2005). This is labour-intensive, and includes uncertainties related to sparse data on below-ground biomass stocks and larger stems. Major efforts have been expended on developing such allometries in temperate plantation forests, because of the needs of commercial forestry, but particularly in tropical forests the destructive harvest data required to develop allometric models are much rarer. For larger scales (sq km), direct sampling of biomass is impossible.

Extrapolation over larger areas can be undertaken using: (1) classification into different land covers, which are then assigned a mean biomass density based on literature data (Achard et al., 2002; DeFries et al., 2002); or (2) calibration of remotely-sensed data against local biomass data to generate regional maps (Saatchi et al., 2007a; Baccini et al., 2008). However, different mapping efforts yield inconsistent results (Goetz et al., 2009).

Both methods have proven problematic, particularly in tropical forests. The plot data required for parameterisation and validation are scarce in these areas, despite recent efforts (Malhi et al., 2002; Lewis et al., 2009; Ryan et al., 2012). For method (1) there are problems in assigning regions to the appropriate class, even at the coarsest classification of forest vs. non-forest, which is a major cause of variability even among comparable approaches (Houghton, 2005). In addition, the use of default biome biomass estimates ignores the variability in biomass within biomes (Keith et al., 2009).

There is no current source of global gridded biomass data, except at very coarse-spatial resolutions, and at present there is no remote-sensing instrument capable of measuring forest biomass with adequate accuracy globally.

Optical data cannot be used directly, although vegetation or greenness indices derived from optical data have been related statistically to Leaf Area Index (LAI). Only weak relationships exist between LAI and biomass; these are neither robust nor meaningful above a low value of LAI. SAR C-band backscatter data are of limited value for global biomass mapping as they saturate at very low biomass values (e.g. less than 30 t ha^{-1}). However, very long time series

of ESA's Environmental Satellite (Envisat) Advanced Synthetic Aperture Radar (ASAR) Wide Swath Mode and Global Monitoring Mode data have been used to map biomass in boreal forests at 1 km resolution with a relative error of approximately 50% (Santoro et al., 2010). At L-band, ALOS PALSAR (2006–2011) has provided the first systematic global forest observations from space (Rosenqvist et al., 2007), and has been used to produce regional biomass maps below the L-band saturation level of ~100 t ha^{-1} (Mitchard et al., 2011; Saatchi et al., 2011). PALSAR winter coherence has also proved very effective in mapping boreal forest biomass (Thiel et al., 2009). However, L-band data have limited value for estimating carbon stocks in moist tropical forests.

Nonetheless, the urgent need for biomass maps has motivated efforts using multiple data sources, including remote-sensing instruments designed for other applications (e.g. Saatchi et al., 2011). Several regional biomass maps have been produced, most notably for the Amazon (Houghton et al., 2003). A comparison between such Amazon maps shows differences in total biomass from 39–93 GtC and very different spatial distributions. Indeed, a comparison of seven Amazon biomass maps by Houghton et al. (2001) found that the level of agreement was only slightly better than would be expected by chance. Most of these maps extrapolate information gathered at a limited number of forest plots, mainly in undisturbed regions; for example, the map of the 3.4 million sq km of Brazilian Amazonia by Malhi et al. (2006) is derived from just 227 plots in old growth forest. This extrapolation is in some cases aided by models (e.g. Olson et al., 1983) and/or ancillary information from remote sensing (DeFries et al., 2002; Potter et al., 1999).

Airborne waveform lidar has also proved effective for local area biomass mapping (e.g. Zhao et al., 2009), but there is no spaceborne lidar optimised for vegetation. However, data from NASA's Ice, Cloud and Land Elevation Satellite (ICESat) Geoscience Laser Altimeter System (GLAS) have been used to give estimates of vegetation canopy height and biomass along transects (Lefsky et al., 2005) and fused with other data sources for biomass mapping (Mitchard et al., 2012; Saatchi et al., 2011). ICESat-1 failed in 2009 and a replacement, ICESat-2, is scheduled for launch in 2016, but is again optimised for ice sheet, cloud and aerosol applications (*http://icesat.gsfc.nasa.gov*).

2.3.1.3 Summary

Knowledge about forest biomass levels and distribution is fundamentally important in assessing the size of the land carbon pool, managing Earth's resources and for current methods of estimating emissions from land-use change. However, present methods for assessing the magnitude and spatial distribution of the terrestrial biomass pool are inadequate. Information from international reporting on forest growing stock is not spatially explicit and contains unknown errors and bias. Explicit biomass maps exist in some parts of the world, but these only cover small areas or are at coarse resolution, contain unknown spatially-varying biases and, in regions most critical for the carbon balance (the Tropics), are too uncertain to support accurate calculations of carbon fluxes. Existing or planned satellite missions have limited capability to measure forest biomass.

A dedicated satellite mission providing global, consistent maps of forest biomass at scales consistent with changes resulting from deforestation would greatly improve our knowledge about the current magnitude of biomass stocks, their geographical distribution and fluxes associated with forest disturbance and growth.

2.3.2 Improved Estimation of Terrestrial Carbon Fluxes

The terrestrial carbon flux between the biosphere and atmosphere varies greatly from year to year (Canadell et al., 2007) and is linked to both natural

Biomass increment (TgC yr^{-1})	1990–1999	2000–2007
Boreal	117	120
Temperate	345	454
Tropical intact	1167	870
Tropical regrowth	1361	1497
All Tropics	2529	2367
Global	2991	2941

Table 2.3. Biomass increments for 1990–1999 and 2000–2007 by latitude zone and globally (values taken from Pan et al., 2011). Tropical intact forests are primary forests that have no history of deforestation. Tropical regrowth indicates forests recovering from recent deforestation.

and human-induced disturbance in forests, and climate-driven changes in the processes controlling biomass accumulation such as photosynthetic metabolism, which can have rapid effects on these fluxes. Both processes are linked to biomass. Of global forest biomass increment, >80% occurs within the Tropics (Table 2.3), because this region has the largest forest biomass stocks, and the greatest levels of disturbance and deforestation. Identifying changes in tropical biomass stocks is therefore a key priority. Because of the existence of dead organic matter pools generated from forest disturbance (stem mortality), and the differing fates and lifespans of dead organic matter (burned, converted to charcoal, stored in timber, left to decay naturally, accumulation into soil) there is a complex and temporally decoupled link between terrestrial carbon fluxes and changes in biomass.

2.3.2.1 Improved estimates of terrestrial carbon emissions

A major uncertainty in the current global carbon budget arises from estimation of deforestation. Over the last 50 years, this has been concentrated in the Tropics (FAO 2010), with ~13 million ha/yr of forest being lost between 1990–2005. This has occurred through a variety of processes, varying within and between countries. The growth of populations in tropical countries has led to an increasing demand for timber, fuel, charcoal and food. Natural forest has been cleared for agriculture and caused deforestation as new agricultural land is brought into production. Monitoring has been poor in many countries owing to lack of regulation, confused land ownership, weak or corrupt governments, poorly resourced land management, and the lack of infrastructure capable of exploiting available data sources, such as satellite data.

Accurate information on both forest area and biomass are fundamental in current methods of quantifying fluxes linked to forest changes. Most current estimates of carbon emissions, C_{em} from deforestation such as those recommended in the UNFCCC *Good Practice Guide* (IPCC, 2003) are based on the following expression:

$$C_{em} = \sum_{i=1}^{m} \Delta A_i \cdot B_i \cdot E_i \qquad (2.1)$$

where ΔA_i is the change in area of forest type i, which has mean biomass B_i (in carbon units) and a burning or removal efficiency, E_i, that quantifies the fraction of biomass carbon emitted to the atmosphere.

Calculating the subsequent behaviour of carbon fluxes requires accounting for associated temporal changes in other components of the ecosystem (e.g. dead biomass, soil organic carbon, etc.), removal of wood products and possible regrowth.

On the basis of idealised curves representing the historical changes, Houghton (2003) developed a book-keeping approach that allows the temporal trajectory of the carbon balance to be calculated at regional scales, given estimates of the rate of disturbance. A similar approach has been adopted by other authors (e.g. DeFries et al., 2002). On this basis, Houghton (2005)

Figure 2.4. Annual emissions of carbon from land-use change in the Tropics 1850–2000, according to published estimates of tropical deforestation and average biomass (Houghton, 2005). The blue curves use the same deforestation rate but different forest biomass estimates. The difference between these curves is due to uncertainty in forest biomass. The curves in red reflect additional uncertainties owing to different estimates of deforestation rate. (ESA)
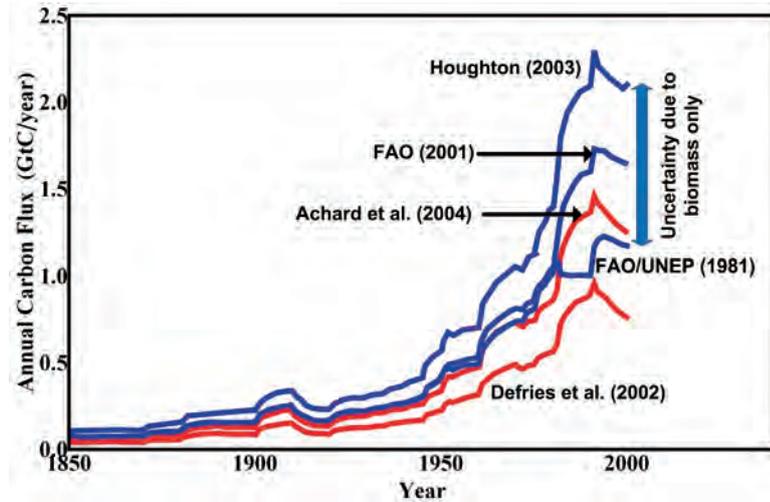
calculated the annual carbon emissions due to land-use change in the Tropics using three different values of mean deforestation rate: those reported by FAO (2001), Achard et al. (2004) and DeFries et al. (2002). Three different mean biomass values were also used, taken from Houghton (2003), which was also used by DeFries et al. (2002); FAO, (2001) and FAO/UNEP (1981). The combined effect of differences in mean biomass and mean deforestation rate leads to the large differences in estimated carbon emissions shown in Fig. 2.4. Uncertainty in the biomass term alone generates an uncertainty of 1 GtC yr^{-1}.

Measurements of deforestation emphasise replacement of forest by a landscape devoid of trees. It is increasingly recognised that this misses a critical component of the carbon cycle arising from forest degradation (removal of biomass for fuel, selective logging, increased fire frequency near settlements, etc.). This can cause significant biomass loss and associated fluxes to the atmosphere (Nepstad et al., 1999). For example, a recent study suggests that degradation fluxes may be similar in magnitude to deforestation fluxes in tropical woodlands (Ryan et al., 2012). However, degradation is very hard to monitor with any current space technology (Gibbs et al., 2007; Asner et al., 2010).

Estimates of global carbon emissions from degradation are therefore sparse, and vary between 5–132% of the emissions from deforestation (Houghton et al., 2009). This lack of any reliable estimates of losses of biomass and associated fluxes due to forest degradation means that they have not been included in recent analyses of global land-use change fluxes (IPCC, 2007) and this contributes to the high uncertainty in such analyses.

The effectiveness of biomass estimates for understanding how degradation affects carbon dynamics was illustrated in Ryan et al. (2012). For selected areas of open low-biomass woodlands in Mozambique where L-band HV backscatter does not saturate, ALOS PALSAR time series data could be used to generate biomass histograms. Within protected areas of the Gorongosa National Park, the distribution of biomass remained static and is indicative of the natural patterns of disturbance and recovery. In contrast, inhabited areas outside the park showed a clear shift towards lower biomass values due to degradation. This indicates that use of a longer wavelength and a systematic forest observation strategy would provide fundamental knowledge about the landscape scale effects of forest degradation, which in turn would give great insight into key ecosystem indicators, such as rate and intensity of disturbance.

— The largest uncertainty in estimating emissions from land-use change is the change in above-ground biomass when tropical forests are converted to other land uses.

— Carbon source and sink estimates generated by carbon models all suffer from the lack of spatially specific estimates of biomass density. There are unknown biases resulting from the use of mean (and unreliable) national biomass estimates, rather than local values where forest disturbance occurs. This yields at least half the uncertainty in carbon emission estimates.

— Forest degradation is not taken into account.

— Measuring biomass at a scale comparable to disturbances (1–4 ha) is important for accurate emission calculations, but no current system is capable of achieving this globally.

2.3.2.2 Improved estimates of terrestrial carbon uptake

While forest disturbance is a large carbon source, the land surface nonetheless acts as a significant net sink of magnitude 1–4 GtC yr^{-1}, as inferred from the difference between emissions (fossil-fuel burning and land-use change), and changes in the atmospheric and ocean carbon pools (IPCC, 2007). This sink has never been directly measured or located, and its magnitude has large uncertainties. Two processes are likely to be involved in this sink: biomass accumulation and metabolic changes resulting from changing environmental conditions.

For a landscape in steady state, sources and sinks of carbon resulting from disturbance and recovery should be in balance. However, changes in management and environmental conditions can disturb this, e.g. the abandonment of fields in northeastern USA in the early 20th century had long-term impacts on carbon stocks as forest re-established (Houghton & Hackler, 2000). Alterations in disturbance patterns, particularly fire, may also influence carbon sinks by adjusting forest structure. These decadal responses, while well documented at research sites, are poorly quantified at regional scales (Houghton et al., 2009), inhibiting identification of any mid-latitude sink. Inventory studies suggest that China's forest carbon sink increased by 34% in 1990–1999 and 2000–2007, with the biomass sink almost doubling owing to intensive afforestation (Pan et al., 2011).

The ability to quantify regrowth will depend on the mean annual increment in a given forest, its age and its spatial pattern of disturbance or management history. In the Tropics, average biomass increments can exceed 5.6 t ha^{-1} yr^{-1} and reach 12 t ha^{-1} yr^{-1} in forest plantations (Achard et al., 2002). Temperate forests are often managed and show a wide range of growth rates, but values exceeding 4 t ha^{-1} yr^{-1} seem to be general, with many temperate forests showing much higher growth rates (Keeling & Phillips, 2007). Boreal forests grow much more slowly, and assessing the size of their increment requires measurements taken over several years. Over the five years of the Biomass mission it seems likely that regrowth, afforestation and reforestation will be measurable over a large part of the world's forests.

2.3.2.3 Summary

Present methods of estimating emissions due to land-use change involve the product of very uncertain estimates of deforested area and even more uncertain estimates of the mean biomass of this area. Even if the mean biomass were well-known, this procedure would be biased if the deforested areas were consistently of high or low biomass relative to the mean. Existing approaches also omit biomass loss through forest degradation. The direct measurements of biomass loss to be provided by the Biomass mission convey two major advantages: (1) separate estimates of deforested area and biomass are not needed, and land-use change arises as a subsidiary output; (2) the

actual biomass loss in the disturbed area is used, not a mean regional value. Furthermore, Biomass will provide access to very poorly known emissions from forest degradation in the Tropics. Biomass will also reduce the large uncertainties in how much of the residual carbon sink arises from forest growth by measuring biomass increment over several years. In addition, this will greatly improve estimates of carbon flux due to post-disturbance forest regrowth in models of carbon balance.

2.3.3 Using Biomass to Improve Process Model Calculations

Process models of the carbon cycle are required to represent important processes that affect carbon fluxes, such as interannual and longer term variations in climate, spatial variation in soil properties or the effects of enhanced atmospheric CO_2 on plant growth. At the heart of all such models are two basic equations, whose simplest forms are:

Mass balance equation: $\quad \Delta C = \Delta B_A + \Delta B_B + \Delta L + \Delta S$ $\qquad$ (2.2)

Process equation: $\qquad \Delta C = GPP - R_P - R_H - D$ $\qquad$ (2.3)

where Δ indicates a change and the other symbols are defined as:

C $\quad$ carbon sequestered by vegetation and soil; negative values imply loss to the atmosphere
B $\quad$ biomass (A: above and B: below ground)
L $\quad$ litter
S $\quad$ soil carbon
GPP $\quad$ Gross Primary Production (photosynthesis)
R $\quad$ respiration (P: plant and H: heterotrophic)
D $\quad$ carbon loss by disturbance (mainly fire)

These equations can be applied globally or locally, but in the latter case lateral flows of carbon (e.g. carbon runoff in rivers or transport after harvest) may need to be accounted for. Above-ground biomass is not only an explicit term in Eq. 2.2, but is linked to rates of GPP and is strongly related to below-ground biomass and litter production, and through litter to changes in soil carbon. It also has a direct impact on Eq. 2.3 through the disturbance term. Within these equations, the dynamics of the above-ground biomass pool depend on two poorly known parameters, the fraction of net primary production allocated to stem growth, a_w, and the turnover rate of wood, t_w, which is linked to lifespan:

Wood biomass equation:

$$\Delta B_A = a_w \cdot (GPP - R_P) - t_w \cdot B_A \qquad (2.4)$$

Losses from the wood pool are transferred to the litter and/or soil pools.

The processes by which carbon is exchanged between the ecosystem and the atmosphere are identified in Eq. 2.3, and process models are used to couple Eq. 2.2 with Eq. 2.3. There is a range of such models, which vary in the details of their structure and process representations. The simplest box models, such as the Data Assimilation Land Ecosystem Carbon Model (DALEC) (Williams et al., 2005), focus on Eq. 2.2–2.4, and resolve mass balance and fluxes alone. More detailed models, such as the Organizing Carbon and Hydrology In Dynamic Ecosystems model (ORCHIDEE) (Krinner et al., 2005), include vegetation dynamics (competition among plant types) and more detailed processes, for example those linking carbon fluxes to hydrological status. Recent developments aim to include forest structure, disturbance and management, but the approaches remain simplistic and largely untested

due to scarcity of data, particularly on biomass pattern and change. Because biomass is so deeply embedded in these core equations, improved knowledge about its distribution and changes over time can be exploited to improve model calculations, as we now illustrate.

2.3.3.1 Assimilating biomass into models

Models of the terrestrial carbon cycle are fundamentally important in climate calculations since they are components of the Land Surface Models embedded in Global Circulation Models and Earth System Models (ESMs). Improvements in carbon models by exploiting biomass, therefore, have direct impacts on climate models and ESMs. The need for such improvements is brought strikingly home by Friedlingstein et al., (2006), where comparison of 11 ESMs coupled to the land carbon cycle showed vastly different estimates of the rate of climate warming due to feedbacks between the terrestrial carbon cycle and climate. These feedbacks were recognised by the IPCC (2007) as a major source of uncertainty in climate predictions.

Models rely on sound process representation, for example of the processes driving wood accumulation and loss. However, analysis of multiple model simulations of the response of Amazon biomass to climate change has shown that different mechanisms are involved in each model (e.g. sensitivity to temperature, soil moisture and humidity), and whether any model is correct is unclear (Galbraith et al., 2010). Global inter-comparisons show significant differences in modelled sensitivity of plant production to changing climate and atmospheric CO_2 concentrations, and sensitivity of soil respiration to climate (IPCC, 2007).

If biomass information is available, it provides novel constraints on model parameterisation that can reduce this uncertainty. Data assimilation methods based on measurements of net CO_2 fluxes contain limited information on carbon transfers among ecosystem pools (e.g. from biomass to litter and soils) (Fox et al., 2009). However, studies that include biomass in the assimilation can reduce uncertainty in prediction of carbon fluxes by up to 50% (Richardson et al., 2010).

ESMs have largely ignored the role of natural and human disturbance in forests. This is partly because global models have used biogeochemical state variables, and few of them include the age structure of forests. In recognition of this, there has been recent emphasis on introducing age structures (e.g. Fisher et al., 2010) and disturbance. A problem for these models is the lack of biomass data for calibration and testing. Below we illustrate how such data could be used, and the difference it makes to carbon flux calculations.

A simple modification to Eq. 2.4 includes a spatially stochastic disturbance process depending on the probability of disturbance (P) and the fraction of biomass lost (F), corresponding to intensity of disturbance:

Wood biomass equation with disturbance:

$$\Delta B_A = a_w \cdot (GPP - R_P) - t_w B_A - P \cdot F \cdot B_A \qquad (2.5)$$

This causes varying trajectories of forest growth and biomass. While the steady state outcome of Eq. 2.4 is a homogeneous landscape with constant biomass, Eq. 2.5 yields a more realistic dynamic equilibrium, with forest patches recovering from disturbance and variation in biomass across the landscape.

Information on intensity of disturbance is very important for determining carbon sinks and sources, and for improving model representation of fluxes. To illustrate this, the DALEC model (Williams et al., 2011) was used to determine the sensitivity of carbon fluxes to disturbance intensity. A large ensemble of model runs systematically varied the probability (P) of disturbance in Eq. 2.5 while keeping the magnitude of biomass loss, M, constant, where $M = PF$ and F

Figure 2.5. Variations in estimated disturbance flux (colour bar, tC ha^{-1} yr^{-1}) based on combinations of the fraction of biomass lost in disturbance (F) and the annual probability of a patch being disturbed (P). Simulations were run for 10 years with an initial state which replicated the mean state of Miombo woodland in Mozambique with biomass mean carbon stocks of 33 t ha^{-1}. The lines plot three biomass loss magnitudes, $M = 0.01$, 0.05 and 0.1, where $M = PF$ (see Williams et al., 2011 for details). (T. Hill)
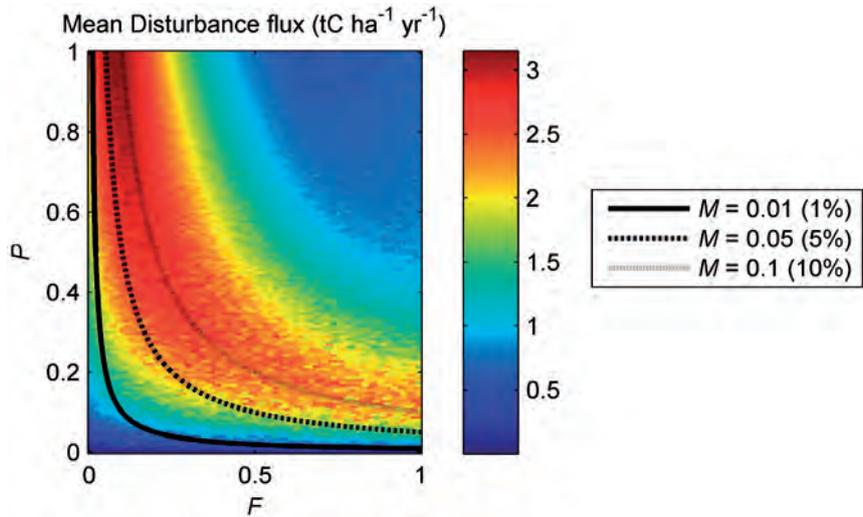
is the intensity of disturbance (i.e. the quantity of biomass lost in a disturbance event).

After 10 years of disturbance, the results in Fig. 2.5 show that intensity of disturbance is important, otherwise the contour plot would be symmetrical about the 1:1 line. The disturbance flux and net carbon balance (not shown) both depend on the interaction between intensity and probability of disturbance. For the same overall magnitude of biomass loss, different types of disturbance (e.g. frequent but low intensity or infrequent but high intensity) result in significantly different fluxes, owing to changes in forest structure. Using DALEC modelling of carbon mass balance, it has been shown that biomass maps with resolutions comparable to the scale of disturbance can constrain estimates of both the disturbance intensity and frequency (Williams et al., 2011).

The role of management in forest carbon balance has also largely been ignored, but has major impacts in, for example, Europe, North America and China. To remedy this, a new version of the ORCHIDEE global carbon-vegetation model has been developed that includes forest management and forest age structure (ORCHIDEE-FM) (Bellassen et al., 2010). Under even-aged management, a given biomass corresponds to a unique age, but in ORCHIDEE-FM, the ages of forest stands for a given biomass obey a Gaussian distribution (Bellassen et al., 2010). This changes the net ecosystem production, i.e. Net Ecosystem Production (NEP). Comparing the simulated NEPs, when all forest stands are assumed to be 40–50 years old (Fig. 2.6a) with NEP based on an age-map reconstructed from biomass data (Fig. 2.6b), we clearly see lower levels of NEP in regions like central and northeastern France, where forests are notably older. At continental scales, by using data on age derived from biomass, ORCHIDEE-FM gives an average simulated NEP
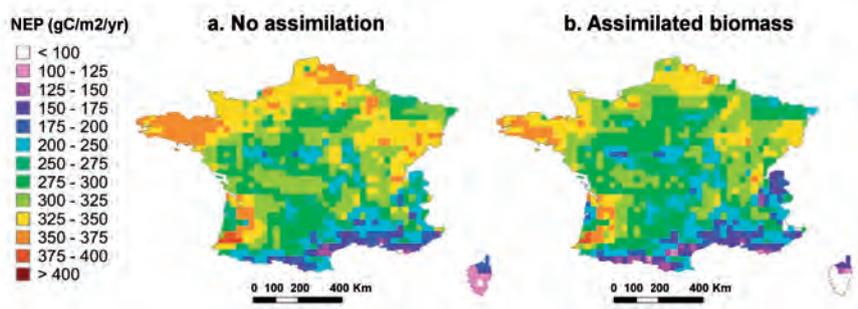
Figure 2.6. NEP simulated by ORCHIDEE-FM without (a) and with (b) input age maps constructed from biomass data. (V. Bellassen)

of 175±52 gC m^{-2} yr^{-1} (Bellassen et al., 2011). Without biomass information the estimate is significantly lower (around 35 gC m^{-2} yr^{-1}).

The above has emphasised that global monitoring of biomass and its changes will greatly improve the representations of disturbance and management in ESMs. In addition, calculations without correct initialisation of biomass can include large biases and high uncertainty. Typically, ESMs use a spin-up procedure, during which the model is run for a long period until the large of carbon (e.g. wood biomass) have reached steady state. The model is then perturbed with different climates to examine the forest's response. The inadequacy of this approach is illustrated in Delbart et al. (2010), where above-ground woody biomass and above-ground woody Net Primary Production (NPP) at 220 sites across the Amazon were compared with ORCHIDEE simulations. Large discrepancies were found between the simulations and measurements, and linked to underestimation of NPP and overestimation of the loss of woody biomass by mortality. These could be reduced by introducing a mortality rate that is related to productivity. Here biomass data at sites were fundamental in identifying and diagnosing model errors; Biomass would extend this knowledge globally.

A further value of the Biomass mission to models would be in the benchmarking of ESMs for the IPCC *Fifth Assessment Report* (Randerson et al., 2009). This includes comparison with tropical biomass data, and preliminary results show that models overestimate Amazon biomass by a factor of two. However, this comparison is seriously weakened by the unreliability of biomass estimates for the Amazon and the highly simplified representation of disturbance in the models, as noted above. The opportunity to test models against regularly updated biomass maps with confidence intervals would deliver a step change in progress.

2.3.3.2 Summary

Carbon models and ESMs suffer from a lack of process detail on biomass dynamics and disturbance, related to a lack of global datasets to constrain their calculations of these processes. This contributes to the wide discrepancies between predictions produced by different models. A consistent, up-to-date, global, gridded biomass dataset is needed to test such models, particularly their predictions of the slow processes of carbon uptake in forest ecosystems, and interactions with natural and human disturbance that lead to spatially variable age and biomass structure. Such data are also needed to support assimilation of data into process models, and constrain predictions of the future carbon balance.

2.3.4 Managing REDD+

The UN initiative for REDD+ is designed to value forest resources and encourage their sustainable management (UN-REDD Programme, 2008). Developed countries, the largest polluters, will pay developing countries, mostly in the Tropics, to maintain their carbon stores in forests. This would reduce CO_2 emissions from forest loss, and help mitigate climate change. Co-benefits result by sustaining the many ecosystem services provided by forests, and the economic, environmental and social goods for countries and communities that depend on these. It is predicted that financial flows from developed to developing countries under REDD+ could reach $30 billion a year. This would provide a huge incentive for developing countries to protect and better manage their forest resources. For this process to succeed an independent, global mechanism to evaluate how well the goals are achieved is needed. Such an evaluation can only be realised through a global biomass monitoring system.

Small-scale efforts to reduce deforestation and forest degradation in tropical countries have had some success (Gibbs et al., 2007; Grace et al.,

2010). However, these projects are hard to upscale due to a lack of regional, spatially-detailed data, and are associated with possible leakage. This occurs when deforestation in the project area is shifted to nearby locations outside the project, yielding no reduction. Without effective and global monitoring of biomass change using remote sensing, the success of REDD+ schemes at scales from local to national and continental cannot be judged effectively.

Current estimates of carbon fluxes due to land-use change and deforestation are based on the IPCC *Good Practice Guidance for Land Use, Land-Use Change and Forestry*, hereafter referred to as the GPG (Penman, 2006). The GPG manual presents a set of equations for calculating national level biomass loss based on national, regional and continental data sources e.g. (FAO, 1993; 2001; 2006; Penman, 2006; FAO, 2010; Wilkie, 2010). Within the GPG, a hierarchy, known as 'Tiers', of estimates is defined. Progressing to higher Tiers results in more complex but potentially more accurate estimates of biomass change.

An assessment of biomass change using the GPG hierarchy provides insight into the needs and challenges for REDD+ (Williams et al., 2011). It used an area in central Mozambique with extensive *in situ* data, and estimated biomass losses over 2007–10. The Tier 1 approaches used default coefficients from the GPG to estimate carbon stock change in biomass (ΔC) from land-use conversions

$$\Delta C = A \cdot L \cdot B \tag{2.6}$$

where L is the annual rate of land conversion and B is the biomass representative of the land cover. For an area covering 6700 sq km, and using values from the available literature at the national/continental scale (Tier 1), uncertainties in L and B led to an enormous spread of estimates of biomass loss, from 74–604 t yr^{-1}. Using *in situ* estimates of B (Tier 2) reduced this to 60–180 t yr^{-1}. In order to make the estimates spatially explicit, biomass change (rather than land-use change) was estimated from ALOS PALSAR data calibrated against field plots (Ryan et al., 2012). The estimated biomass loss (including degradation) was 580±775 t yr^{-1} (95% confidence interval). These higher values arise from inclusion of degradation, which was not estimated in the results based on average biomass values. The very large uncertainty for Tier 3 reflects the limitations of ALOS PALSAR for measuring biomass, even in this region of moderate biomass levels. Biomass would be expected to reduce the uncertainties by at least an order of magnitude across the full range of biomass levels met in tropical forests.

2.3.5 Additional Benefits of Forest Biomass Information for Climate and Management of Earth's Resources

Accurate forest biomass measurements will greatly improve land carbon models and the Earth system models in which they are fundamental components. They will also bring basic information for quantifying and managing ecosystem services and resources for human well-being. These wider connections are discussed briefly below.

2.3.5.1 Biomass, the water cycle and climate

Earth's vegetation cover acts as an important moderator of biogeochemical cycles and has a profound influence on energy, momentum, trace gas and water transport between the atmosphere and the soil (Teuling et al., 2010). Vegetation actively and directly controls evaporation through leaf processes, and vegetation canopies intercept radiation and rain and remove subsurface water, affecting the lateral distribution of water in soils and modifying the transport of nutrients and sediments. Changes in biomass are fundamentally important to the water cycle because they affect evapotranspiration (globally,

the volume of transpired water is nearly equal to the total river runoff). This strongly affects freshwater supply in river runoff (Gedney et al., 2006). Changes in the water cycle also impact the production of biomass as water available for growth may vary. At a basic level, carbon and water are inextricably linked in biophysical processes, and knowledge about one can be used to constrain the other (Beer et al., 2010). Exploitation of Biomass measurements will therefore greatly improve water cycle calculations.

Use of Biomass data to improve carbon and water cycle calculations will lead directly to improved climate and ESMs (Bonan, 2008). Particularly strong connections exist between vegetation structure and climate through vegetation controls on surface roughness, albedo and surface energy balance. Removal of forest cover not only affects global climate by altering the carbon cycle, but also through direct effects on energy partitioning. However, current climate models show very varied sensitivities to imposed land-cover change (Pitman et al., 2009), reflecting considerable uncertainties in the coupled processes. The importance of biomass for climate led to it being identified as an ECV (GCOS, 2003; 2006; 2010). However, the original view taken by GCOS of biomass as a control on climate has subsequently been widened because of its growing use for generating bio-energy (Sessa & Dolman, 2008).

2.3.5.2 Biomass, forest structure and biodiversity

Forests are home to 90% of terrestrial species, and tropical primary forests are irreplaceable for sustaining biodiversity (Gibson et al., 2011). Disturbance strongly affects ecosystem biodiversity (Barlow et al., 2007), so that habitat loss and ecosystem fragmentation are recognised as basic factors in worldwide loss of biodiversity (Pimm & Raven, 2000). Field studies have shown how large-scale and rapid change in the dynamics and biomass of tropical forests lead to forest fragmentation and increase the vulnerability of plants and animals to fires (Malhi & Phillips, 2004). Bunker et al. (2005) also showed that above-ground biomass was strongly related to biodiversity. Regional to global information on how human activity affects biodiversity requires accurate determination of forest structure and forest degradation, especially in areas of fragmented forest cover. This is also fundamental for ecological conservation. Current sensors are inadequate to provide such information, but the provision of regular, consistent, high-resolution mapping of biomass and its changes would be a major step forward in meeting this information gap.

2.3.5.3 Biomass and human use of ecosystems

Above-ground biomass stocks are a key factor in the economic and biofuel potential of land surfaces. Humans appropriate ~31 Pg of biomass each year, i.e., 24% of potential NPP (Haberl et al., 2007). This estimate, is based on national statistics provided through FAO, so has considerable uncertainty. However, the magnitude demonstrates the importance of biomass to the global economy.

Biomass is also a major energy source in subsistence economies, contributing around 9–13% of the global supply of energy (i.e. $35–55 \times 10^{18}$ J yr^{-1}; Haberl & Erb, 2006). Reducing these large uncertainties in the use of forests as energy sources requires frequently updated information on biomass stocks and their change over time, to be combined with other data on human populations and socio-economic indicators.

2.3.6 The Priority for Tropical Biomass Measurements

The preceding sections have argued the need for a global biomass product to address an array of science questions. However, the text also highlights that the Tropics are particularly important to many of these issues. The greatest

biomass stocks are located in tropical forests, but these stock estimates have high uncertainties, because generally tropical biomass stock data from national reporting is of low quality. Annual biomass increment in forests is concentrated in the Tropics. Deforestation and forest degradation are also concentrated in the tropical regions. The most biodiverse of global biomes is tropical moist forest. REDD+ activity is focused on tropical countries. Human reliance on forests for energy supplies is concentrated in tropical countries. Thus, while temperate and boreal forests play a role, the most significant impact of a global biomass product will be in constraining tropical forest states and dynamics.

2.4 Secondary Scientific Objectives

Several potential secondary mission objectives arise from the opportunity to explore Earth for the first time with a P-band SAR system. The Biomass Secondary Objectives Assessment Study (Paillou et al., 2011) identified a variety of secondary applications and assessed whether their requirements could be accommodated within the mission specifications. In particular, the three objectives outlined in this section are expected to benefit significantly from the long P-band wavelength, while at the same time being feasible and compatible with Biomass.

2.4.1 Mapping Subsurface Geology

Geological maps are crucial for mineral and groundwater exploration, and remote sensing is an important tool in establishing such maps. Space-based optical sensors, such as the Landsat Thematic Mapper and Spot HRV, are often used to classify groups of surface minerals. However, in arid regions, such as North Africa, the geology is mostly hidden under a thin layer of dry, sandy sediments. For example, the eastern part of the Sahara including Chad, northern Sudan, western Egypt and Libya, has a yearly rainfall of less than 1 mm, and is characterised by large flat areas buried under a few metres of sand. The bedrock, which is made up of sandstone, limestone and volcanic rocks, can provide valuable geological and hydrological information, but cannot be mapped by optical remote sensing instruments.

In contrast, low-frequency SAR is able to penetrate dry sediments and map the subsurface down to several metres, because of low absorption and little volume scattering. For example, L-band SAR has proven capable of penetrating a few metres of dry, homogeneous material such as sand (Elachi et al., 1984; Farr et al., 1986). If the sand surface is smooth, the subsurface of interest will not be masked, and the measured backscatter will provide an image of the subsurface roughness and slope. This can then be turned into information that is useful for exploration and geophysical prospecting. Numerous examples of this capability are available from L-band data. The Shuttle Imaging Radar-A revealed unknown palaeo-drainage channels hidden under sediments in the Bir Safsaf region in southern Egypt (McCauley et al., 1982). The Japanese Earth Resource Satellite provided complete coverage with L-band data of the eastern Sahara, and the L-band PALSAR has covered the entire Sahara and Arabia at HH and HV polarisation, identifying a 1200-km palaeo-drainage network that connected the Mediterranean coast with the Kufrah Basin in eastern Libya in the Miocene (Paillou et al., 2009). This explains why large aquifers can be exploited in the Kufrah region.

The capabilities demonstrated with L-band SAR are striking, but will be significantly enhanced at P-band because penetration depth is proportional to wavelength when absorption dominates over volume scattering. Aircraft campaigns have illustrated the capacity of P-band SAR to penetrate at least 4 m of dry sediment (Farr, 2001; Paillou & Dreuillet, 2002). The enhanced capabilities at P-band will also be important in groundwater exploration,

where geological maps are commonly used to identify where to carry out detailed field exploration, such as drilling.

Access to freshwater resources is already a major concern: in Saharan and sub-Saharan Africa, most people do not have access to safe water supplies, and the situation is expected to get worse in the future. In 2025, more than two billion people could suffer from lack of fresh water, possibly leading to famine, political instability and even war. This issue has been formally recognised by ESA through its Tiger Initiative, which aims is to 'assist African countries in overcoming problems faced in the collection, analysis and use of water related geo-information by exploiting the advantages of Earth observation technology'. P-band data from Biomass will offer a powerful tool in support of this initiative.

2.4.2 Measuring Terrain Topography under Dense Vegetation

Digital Terrain Models (DTMs) represent the elevation of the ground in the absence of vegetation, buildings and so on. These 'bare-earth' images are crucial in a range of applications, including ecology, forest management, water resource management, mineral exploitation, national security and scientific research. However, currently available large-scale products are more accurately described as Digital Elevation Models (DEMs) because in forested areas they differ significantly from a true DTM.

Two such DEMs have been produced by space-based SAR interferometric missions dedicated to topographic mapping: the Shuttle Radar Topography Mission (SRTM), which used a C-band radar (Rosen et al., 2000; Werner et al., 2001; Rabus et al. 2003) and DLR's TerraSAR-X-Add-on for Digital Elevation Measurements (TanDEM-X) mission, which uses X-band (Moreira et al., 2004; Krieger et al., 2007). Both DEMs use comparatively short wavelengths (6 cm for SRTM and 3 cm for TanDEM-X), hence suffer biases with respect to the bare earth in dense forest.

Airborne lidar technologies can provide DTMs for such areas, but apart from the profiling ICESat GLAS sensor, no space-based Earth observation lidars have been launched, and there is little current prospect of producing an accurate, global, consistent DTM from this technology. At P-band, vegetation causes less attenuation, therefore Biomass can fill this major gap in our knowledge of global topography. In addition, the scattering centre of the tree-ground double-bounce signal occurs at ground level and can be isolated using polarimetry. Tomographic measurements (see Subsection 4.2.3 and Fig. 4.6) show that this is possible, even for very dense tropical forest. In addition, a long wavelength provides higher coherence, since: (i) the ratio between scatterer displacement and the wavelength is smaller, leading to smaller phase perturbations; (ii) the backscatter predominantly comes from large, more stable scatterers, such as large branches and tree trunks.

Over its lifetime, Biomass will produce a DTM of the terrain topography under dense vegetation, thus removing the biases in DEMs using shorter wavelengths, such as the SRTM DEM. Biomass will also be able to exploit this new DTM for slope corrections associated with the primary objectives, allowing initial products generated with current DEMs to be reprocessed, thus refining the biomass products.

2.4.3 Measuring Glacier and Ice Sheet Velocities

Large and unexpected changes of the Greenland and Antarctic ice sheets have been observed over the last decade. Along the entire grounded margins of the ice sheets, laser altimetry data show dynamic thinning (Pritchard et al., 2009), and SAR data show a significant acceleration of glacier velocities both in Greenland (Rignot & Kanagaratnam, 2006) and in Antarctica (Rignot et al., 2008). These observations have made it clear that ice sheets have response

times ranging from millennia to years and even seasons. With the prospect of increased global warming, additional thinning and retreat of outlet glaciers is expected.

Ice sheets and glaciers store almost 70% of Earth's fresh water (Allison et al., 2009). The mass loss of ice sheets currently contributes to a sea-level rise of 1.8 mm/yr. According to the IPCC, this will increase, and the total sea-level rise estimated for 2090–99 relative to 1980–99 is between 0.18 m and 0.59 m (IPCC, 2007). These estimates have tended to increase since the IPCC Fourth Assessment Report in 2007, where they were computed from physical climate models. New semi-empirical approaches based on past temperature and sea-level data suggest a rise in 2090–99 of 0.3–2.15 m (Grinsted et al., 2009; Rahmstorf, 2010).

Antarctica is particularly important in terms of sea-level rise. If the entire Antarctic ice sheet melted, the average sea level would rise 61.1 m, while a complete melt of the Greenland ice sheets would cause a sea-level rise of 7.2 m (IPCC, 2007). Furthermore, an ice loss in Antarctica will mainly affect sea level in the northern hemisphere, while an ice loss in Greenland has maximum effect in the less populated southern hemisphere. This is a consequence of the self-gravitation and isostatic/elastic adjustments of Earth (Milne et al., 2003).

The mass balance of an ice sheet or a glacier catchment is the difference between its input (snow accumulation) and output (iceberg calving, basal melting and surface runoff). Calving represents 90% of the total mass loss in Antarctica, and 40–60% in Greenland. A negative mass balance translates directly into a rise in sea level. The mass balance of ice sheets can be estimated by subtracting the ice discharge and melting losses from the snow accumulation (Rignot & Thomas, 2002; Ahlstrøm et al., 2008). The discharge (e.g. across the grounding line) is computed from the ice-thickness profile and the ice-velocity field. For constant snow accumulation, melting and ice thickness, mass balance change is proportional to an ice velocity change.

The velocity field of glaciers and ice sheets can be measured using two classes of SAR techniques: Differential SAR Interferometry (DInSAR) (Massonnet et al., 1993) and offset tracking (Gray et al., 1998; Michel & Rignot, 1999). These techniques measure the ice displacement between two observations, and require some coherence between the observations. DInSAR offers better velocity precision and finer spatial resolution, but requires higher coherence and cannot be applied to fast-moving glaciers unless the temporal baseline is very small.

Shuttle Imaging Radar (SIR-C) data have shown that the temporal coherence of snow and ice surfaces is higher at L-band than at C-band (Rignot, 2008). Likewise, L-band PALSAR data provide better ice motion results than C-band data (Rignot, 2008), and offset tracking works well at L-band in areas where it fails at C-band (Boncori et al., 2010).

The benefits of the longer wavelengths are thought to result from deeper penetration (Rignot, 2008) and less sensitivity to surface melt and snowfall. P-band is therefore likely to offer three advantages:

— Measurement of seasonal variations of ice velocities. Higher radar frequencies only have sufficient coherence in the melt season.

— Increased coverage. At higher frequencies, temporal decorrelation causes many datasets to be rejected.

— Increased velocity precision, where (and if) the reduced temporal decorrelation allows offset tracking to be replaced by DInSAR. DInSAR will still not be applicable to fast glaciers, though the larger P-band wavelength contributes to an increased velocity range.

Set against this are some disadvantages:

— The impact of the ionosphere at high latitudes may prevent application of Biomass for ice velocity measurements. The ionospheric delay must be corrected for and although novel recent algorithms appear promising, it is currently not known if the residual delay is prohibitive. This is particularly critical for the DInSAR technique as it measures displacements on a wavelength scale.

— The spatial resolution will be coarser, as Biomass will have a smaller bandwidth.

— Low backscatter in the central part of the ice sheets may cause excessive decorrelation.

→ RESEARCH OBJECTIVES

3. Research Objectives

3.1 Primary Objectives

The Biomass mission addresses one of the most fundamental questions in our understanding of the land component of the Earth system – the status and the dynamics of Earth's forests, as represented by the distribution of forest biomass and its changes. Gaining accurate, frequent and global information on these forest properties at scales comparable with forest changes will allow us to address a range of critical issues with far-reaching scientific and societal consequences.

3.1.1 Reducing Uncertainties in Land-use Change Carbon Flux

Land-use change emissions, mainly due to tropical deforestation and degradation, represent about 10–20% of atmospheric carbon loading. This term has the largest uncertainty of any measured term in the global carbon balance, and by far the largest relative uncertainty. By not only measuring the areas of deforestation and forest degradation, but also the biomass lost during disturbances, the Biomass mission will drastically reduce the uncertainty in land-use change fluxes.

The land uptake of carbon is calculated as the residual in the carbon balance after the other terms are estimated. Hence, errors in estimates of land-use emissions directly affect the uncertainty of this term, and it has the largest uncertainty of any term in the global carbon balance. This profoundly affects the identification of the mechanisms involved in the land-carbon sink. Biomass will not only greatly sharpen our knowledge of the size of the terrestrial sink, but over the five years of the mission it will allow us to identify and directly measure the growth of many tropical and temperate forests, especially young forests and plantations.

3.1.2 Providing Scientific Support for International Treaties and Agreements

All current methods to estimate carbon emissions from land-use change and/or forest degradation rely on estimates of biomass stock and how it changes under different types of land modification, be it loss or renewal of forest. Current methods to provide such estimates have very large biases and typically involve extrapolation of very limited and localised information to very large areas. Biomass data will remove bias and enable spatially explicit estimates of biomass and its change, putting existing methods on a much firmer footing.

3.1.3 Landscape Carbon Dynamics and Prediction

Predicting the fate of carbon in a landscape is crucially dependent on knowing its current state. Biomass measurements will provide baseline stock maps and enable inferences on past disturbances, ongoing degradation, and forest recovery at critical scales. Biomass will, therefore, shed light on both ecological processes and human impacts on forest structure. This information will provide the basis for studying the effects of climate change, shifting patterns of disturbance, and effects of increased exploitation of forest resources. By covering the full spectrum of forest types, Biomass will provide novel information on this critical resource including the critically exploited tropical dry forests, boreal forests, and the vast tropical moist forests.

3.1.4 Initialising and Testing the Land Element of Earth System Models

An essential component of fully-coupled ESMs is the interaction between the land and climate, with land feedbacks predicted to contribute up to an extra 1°C to climate warming in the 21st century, but with very large uncertainties (Friedlingstein et al., 2006). However, the increasing emphasis on decadal and regional climate forecasting places much more constraints on model initialisation and representation of spatial variability and dynamics. Also, the need to make political decisions based on such models means that they must be much more stringently tested. Current comparisons show that different models give radically different predictions of the current distribution of biomass, but at present we have little evidence to assess which is closest to the truth. Measurements from Biomass will be central to these issues of model evaluation.

3.1.5 Forest Resources and Ecosystem Services

Measuring forest change is of major importance in quantifying the pressures on forests owing to the growing human population and the demand for forest-derived ecosystem services. This information is fundamental in predicting the resilience of societies for which forests are a basic resource, for example, for fuel. More generally, management of forest resources is one of the most significant challenges facing society, in particular in tropical developing countries, because of the long-term consequences for the environment, climate, water quality, provision of ecosystem services and access to REDD+ and forest project development funds.

3.1.6 Biodiversity and Conservation

The erosion of biodiversity is of fundamental international concern and is strongly related to changes of habitat because of land-use change, especially in tropical forests. Changes in habitat are a function of changes in forest structure, which is more correlated with changes in biomass than with forest cover, through forest degradation and deforestation. Climate may also alter biodiversity, and through its contribution to climate mitigation measures, Biomass will contribute significantly to implementing policies for biological conservation.

3.2   Secondary Objectives

Several secondary applications have been identified in the ESA *Biomass Secondary Objectives Assessment Study* (Paillou et al., 2011). Three of these are considered ready for implementation, based on results from airborne P-band SAR data, extrapolations from higher frequencies and theory.

Other potential applications are still being explored, or their requirements conflict with the primary mission objectives, but the Biomass mission could provide useful data for other applications (Paillou et al., 2011). Examples include near-surface properties of ice sheets and glaciers, inundation under dense vegetation, ionospheric mapping, sea-ice mapping, soil salinity, ocean winds, soil moisture, permafrost monitoring and ice sounding. The value of Biomass to these applications is likely to become clear once data become available. Thus, unforeseen products and applications may emerge and be evaluated during the life of the mission.

3.2.1 Subsurface Geology

Freshwater resources are scarce in arid regions such as North Africa, and are becoming an increasingly important economic, social and environmental issue. Water prospecting is typically based on geological maps and may involve satellite imagery acquired at optical frequencies. However, in arid regions, most geological features are buried under a thin layer of dry, sandy sediments. With L-band SAR, subsurface geology hidden down to 1.5 m of dry sediment can be mapped (McCauley et al., 1982; Elachi et al., 1984), and large palaeo-drainage channels have been discovered (Paillou et al., 2009), which can be linked to aquifers. Biomass will allow a much better mapping of such palaeo-hydrological features, because the penetration depth at P-band is about three times larger than at L-band, while the masking effect of surface and volume scattering is reduced.

3.2.2 Terrain Topography under Dense Vegetation

DTMs are crucial for many applications, such as hydrology, geology and construction. Global-scale topographic maps can be generated with SAR interferometry, e.g. from SRTM C-band data (Rosen et al., 2000) or from TanDEM-X X-band data (Krieger et al., 2007), but these topographic maps are inaccurate over vegetation because the vegetation causes a positive elevation bias with respect to the terrain. Unlike SRTM and TanDEM-X, Biomass will offer bare-earth terrain maps and eliminate this bias. It will achieve this by taking advantage of the larger P-band penetration depth and using polarimetry to enhance the ground return.

3.2.3 Glacier and Ice Sheet Velocities

Glaciers and ice sheets currently contribute about 1.8 mm/yr to sea-level rise and this will increase significantly (IPCC, 2007b; Rahmstorf, 2010). Ice velocities, sufficiently resolved in space and time, are required to constrain, improve and test ice mass-balance models. Since many glaciers exhibit large interannual and seasonal variations, a significant velocity bias results if ice velocities cannot be measured in the melt season. Due to deeper penetration, surface changes cause less temporal decorrelation at P-band than at higher frequencies. Biomass will therefore provide better observations of seasonal variation of ice velocities. In addition, it will be able to measure the velocity of ice sheets and most glaciers with higher precision and finer spatial resolution.

→ OBSERVATIONAL REQUIREMENTS

4. Observational Requirements

4.1 Introduction

Chapter 2 set out the urgent need for improved measurements of forest biomass, its spatial distribution and change with time. It also emphasised the limitations of current sources of information, including existing or planned satellite missions. This chapter outlines the basic measurements to be made by the Biomass mission to fill this information gap and to meet the science objectives summarised in Chapter 3.

Section 4.2 outlines the observational approach and provides a general framework for transforming Level-1 radar data into geophysical products. In Section 4.3, the geophysical product requirements to meet the mission objectives are detailed and the Biomass geophysical products are identified. In Section 4.4, the geophysical product requirements are translated into Level-1 SAR data requirements which form the basis for defining the Biomass system in Chapter 5.

4.2 Observational Approach

Addressing the primary science objectives set out in Chapter 3 requires repeated measurements of biomass at temporal and spatial scales that are compatible with the needs of national inventories and carbon flux calculations. The only economically viable way of providing this information is by remote sensing. Two forms of measurement are required: (1) remotely-sensed estimates of forest characteristics related to biomass and (2) *in situ* measurements of forest biomass for calibration and validation.

The remote sensing component of Biomass is envisaged as a P-band polarimetric SAR mission with controlled inter-orbit distances (baselines) between successive revisits to the same site. At each acquisition, the radar will measure the scattering matrix, from which the backscattering coefficients (equivalent to radar intensity) will be derived in each of the different linear polarisation combinations, i.e. HH, VV, HV & VH (where H and V stand for horizontal and vertical transmitted and received), and the inter-channel complex correlation. For interferometric image pairs, the system will provide the complex interferometric correlation (coherence) between the images at each linear polarisation. Polarimetric interferometric SAR (PolInSAR) coherence and Polarimetric SAR (PolSAR) backscatter observations provide independent, complementary information that can be combined to give robust, consistent and accurate retrieval of biomass.

Biomass marks a major step forward compared to existing and planned satellite missions because of the unique capabilities of P-band SAR:

— P-band backscatter has the highest sensitivity to biomass compared to all other frequencies that can be exploited from space.

— P-band displays high temporal coherence over repeat passes separated by several weeks, even in dense forest, allowing the use of PolInSAR to retrieve forest height and, for the first time, retrieval of forest vertical structure from space during the experimental tomographic phase.

— P-band is highly sensitive to disturbances and temporal change of biomass.

By exploiting these capabilities through a dedicated strategy, Biomass will build up a unique archive of information about the world's forests and their dynamics.

Note that below-ground biomass cannot be measured by Biomass (or any other remote sensing instrument), but can be inferred from above-ground biomass using conversion factors (Cairn et al., 1997, Mokany et al., 2006). Therefore, throughout this report, 'biomass' denotes 'above-ground biomass'.

The *Biomass Report for Assessment* (ESA, 2008) described the development of relationships between P-band SAR measurements and forest parameters, and our understanding of these relationships in terms of physical processes. Underpinning this analysis was the availability of a large amount of P-band campaign data gathered by the NASA Airborne Synthetic Aperture Radar (AIRSAR) system in the 1990s and the DLR Experimental Airborne SAR System (ESAR) in the early 2000s from a variety of temperate, boreal and tropical forests under a wide range of environmental conditions.

However, more recent ESA airborne campaigns and ground-based experiments, together with new techniques, such as tomography, have brought fundamental new understanding of the radar scattering mechanisms in boreal and tropical forests. These new data have been vital in refining the observational approach underlying the Biomass mission, and in developing biomass and height retrieval methods that are adapted to the conditions encountered in these major forest biomes.

Five major ESA airborne campaigns have been carried out (three in boreal and two in tropical ecosystems) using ESAR and Système Expérimental de Télédétection Hyperfréquence Imageur (SETHI, Onera, France) P-band SARs, and a P-band ground-based tropical experiment is still continuing. Brief descriptions of the objectives and locations of these campaigns are given in Table 4.1.

Table 4.1. Main campaign data used in developing and testing the Biomass retrieval algorithms.

Campaign	Objectives	Test sites	Time	Forest conditions
INDREX-2 (Hajnsek et al., 2008)	Forest height retrieval in tropical forest and measurement of repeat-pass temporal decorrelation	Sungai-Wai & Mawas Borneo, Indonesia	Nov 2004	Tropical rain forest. Sungai-Wai: lowland with biomass up to 600 t ha^{-1}. Mawas: peat swamp with biomass up to 200 t ha^{-1}
TropiSAR (Dubois-Fernandez et al., 2012)	Biomass estimation in tropical forest, multiday decorrelation	Paracou & Nouragues French Guiana	Aug 2009	Tropical rain forest with biomass up to 500 t ha^{-1}, lowland and hilly terrain
Tropiscat (Albinet et al., 2012)	Ground-based high temporal resolution measurements to determine long-term temporal decorrelation	Paracou, French Guiana	Oct. 2011– Oct. 2012	Tropical rain forest with biomass up to 500 t ha^{-1}
BioSAR-1 (Hajnsek et al., 2008)	Biomass estimation in hemi-boreal forest and measurement of multimonth temporal decorrelation	Remningstorp, southern Sweden	Mar–May 2007	Hemi-boreal forest, low topography with biomass up to 300 t ha^{-1}
BioSAR-2 (Hajnsek et al., 2009)	Topographic influence on biomass estimation in hilly boreal forests	Krycklan, northern Sweden	Oct 2008	Boreal forest, hilly, with biomass up to 300 t ha^{-1}
BioSAR-3 (Ulander et al., 2011a)	Forest change and multiyear coherence relative to BioSAR-1	Remningstorp, southern Sweden	Sep 2010	Hemi-boreal forest, low topography with biomass up to 400 t ha^{-1} (includes additional high biomass stands compared to 2007 campaign)

These six campaigns comprise the most accurate and complete set of P-band SAR (PolSAR, PolInSAR and tomographic SAR) and associated *in situ* data currently available over boreal and tropical forests.

Each was designed to answer critical questions about P-band behaviour in forest biomes and, with the exception of INDREX-2 and BioSAR-1, all were conducted in response to recommendations from ESA's Earth Science Advisory Committee associated with the selection of Biomass for Phase-A. Temperate forests were the subject of many earlier studies, as reported in the next section, and recovery of biomass and forest height from airborne P-band data with high accuracy has been well-demonstrated. Hence, the emphasis of these studies was on boreal and tropical forests, which comprise 75% of the world's forest cover. They present particularly demanding conditions for biomass recovery, and were the most poorly documented in terms of P-band SAR data.

4.2.1 Forest Biomass Retrieval Using P-band SAR Intensity

Earlier campaigns investigated the value of P-band intensity data for estimating biomass (Le Toan et al., 1992; Dobson et al., 1992; Beaudoin et al., 1994; Rignot et al., 1994; Imhoff, 1995; Rignot et al., 1995; Kasischke et al., 1997; Ranson et al., 1997; Ferrazzoli et al., 1997; Hoekman and Quinones, 2000; Lucas et al., 2006; Saatchi et al., 2007b). The demonstration that P-band could provide a powerful tool for measuring forest biomass played a major part in the decision by the International Telecommunication Union to allocate a 6 MHz bandwidth at P-band for remote sensing (ITU, 2004).

Initial work focused on studying the relationship between biomass and SAR intensity at HV, VV and HV polarisations. Although experiments were performed over different forests, there was an emphasis on managed temperate forests with even-aged mono-species (mainly coniferous) stands (Le Toan et al., 1992; Dobson et al., 1992; Beaudoin et al., 1994; Kasischke et al., 1997; Ranson et al., 1997).

HV and HH were found to be strongly correlated to biomass, while the correlation between biomass and VV was often weak. HV was identified as the best polarisation for biomass inversion because it is less affected by temporal change and topography, and exhibits the largest dynamic range between low and high biomass forests. The relative simplicity of many temperate forest systems allowed accurate biomass inversion methods to be developed (Le Toan et al., 2011), as exemplified in Fig. 4.1. This biomass map shows a section of the Landes pine plantation forest in France, which has flat and homogenous stands with biomass in the range 0–200 t ha^{-1}. The map was derived by inverting P-band HV backscatter alone, and has a root mean square error of about 10 t ha^{-1} when compared with reference plots.

The interpretation of these experimental data was largely based on forest scattering models (Ulaby et al., 1990; Karam et al., 1992; Hsu et al., 1994; Lang et al., 1994; Fung, 1994; Saatchi & McDonnald, 1997; Ferrazzoli et al., 1997; Picard et al., 2004). The radar wavelength was found to determine the dominant scatterers: leaves and needles are the main contributors at X-band (λ = 2.5–3.75 cm), branches at L-band (λ = 15–30 cm), and big branches and trunks at P-band (λ = 30–100 cm). Models also showed that double-bounce scattering dominated at HH and volume scattering at HV, while VV resulted from both mechanisms. However, most of these model studies were carried out under conditions applicable to temperate forests, and for biomass not exceeding 200 t ha^{-1}.

More recently, much progress in our understanding has come about through airborne campaigns in boreal (BioSAR 1–3) and tropical forest (TropiSAR), which permitted P-band polarimetry, PolInSAR and SAR tomography. Boreal forests are host to a limited number of species (mainly coniferous), and exhibit relatively open canopies with biomass up about 300 t ha^{-1}. In areas with low topography, strong relationships are found between forest backscatter at HV
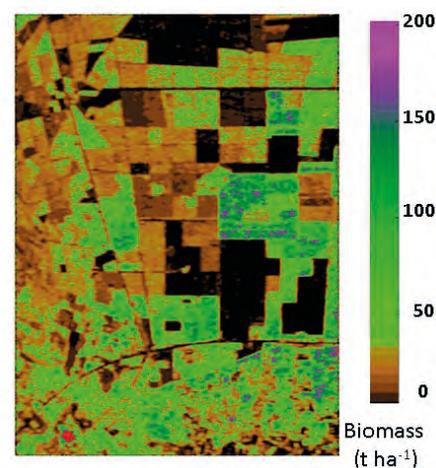
Figure 4.1. Biomass map produced by inverting P-band HV data over the Landes forest, southern France. The dataset comes from the AIRSAR campaign in carried out in 1989 (Le Toan, 1992), and the inversion is based on a general relation between biomass and HV, established using a range of datasets. (Le Toan et al., 2011)

and HH for biomass up to 300 t ha^{-1}, whereas VV is uncorrelated with biomass (Sandberg et al., 2011). As a result, the HH and HV returns are well correlated, but neither HH nor HV shows any significant correlation with VV. Because of the double-bounce mechanism, soil moisture variation affects the backscatter in all three linear polarisations. In addition, topography affects the double-bounce mechanism, leading to considerable variability in the backscatter. However, it has been shown that biomass can still be consistently retrieved using multiple polarisations together with coarse-resolution ground slope data (Ulander et al., 2011b; Soja et al., submitted).

In contrast, tropical forests are characterised by a large number of species and a dense canopy. Biomass values can reach 500 t ha^{-1} or greater in 1 ha plots. For dense forest over terrain with slopes, volume scattering and branch-ground double-bounce scattering are present in all three polarisations. As a result, the HH, VV and HV polarisations measured during the TropiSAR campaign were all highly correlated and displayed very similar relationships with biomass. Of great importance is that backscatter was very stable over time: at plot scale, the temporal variation during the 22 days of the campaign was less than 0.5 dB in all polarisations.

Figure 4.2 shows HV backscatter against *in situ* biomass in a log-log plot for recent ESA airborne campaigns in Sweden and French Guiana, together with AIRSAR data gathered in 2004 from Costa Rica, to extend the range of biomass in tropical forest. The figure shows near-linear relationships for each site with similar gradients (sensitivity of backscatter to biomass). Analysis over many varied datasets reveals that this sensitivity is remarkably stable (Le Toan et al., 2011, shown in natural, not log, units). Although the tropical sites exhibit a very similar relationship between backscatter and biomass, the offset between the tropical and boreal sites is a sign of differences between forest structures. It is important to note that the boreal data in Fig. 4.2 are from a forest site with low topography and that the plotted data correspond to a single date; considerable variability arises from topography and environmental change such as soil moisture variation. Successful methods to counter this variation and retrieve biomass in the boreal zone are described in Chapter 6. For dense tropical forests, environmental conditions tend to be more stable, and the major disturbing effect needing correction is topography.
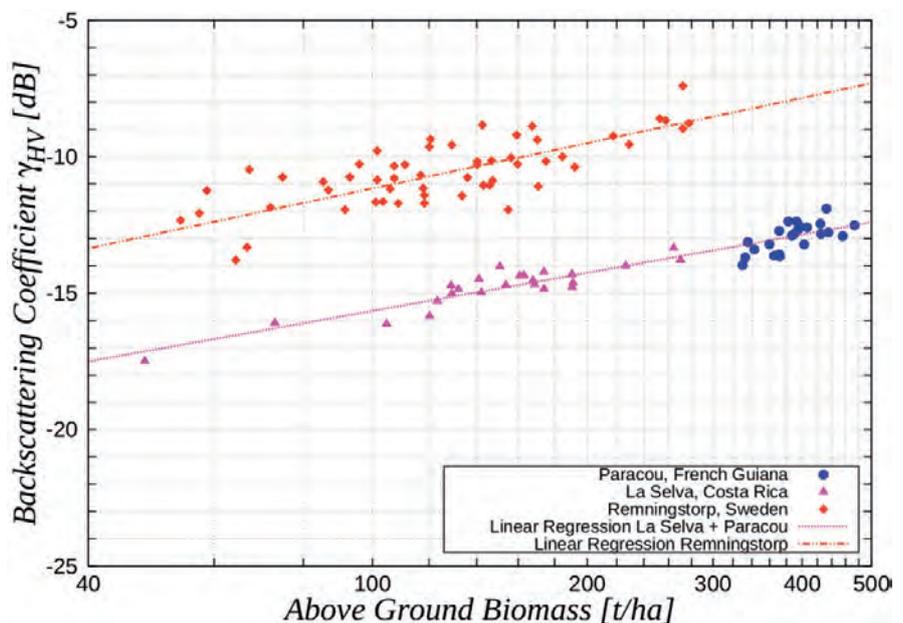
Figure 4.2. P-band backscatter at HV polarisation over tropical forests and boreal forests as a function of biomass. Data over Paracou forest, French Guiana, were acquired by the SETHI SAR system in 2011 (Dubois-Fernandez et al., 2012), the data over La Selva forest, Costa Rica, in 2004 by the AIRSAR system (Antonarakis et al., 2011) and Remningstorp, Sweden, by the ESAR system in 2007. (see Sandberg et al., 2011) (Le Toan)

4.2.2 Forest Height Retrieval Using Polarimetric Interferometry

Over the last decade, PolInSAR has been established as a powerful technique that allows the investigation of the three dimensional structure of forest scattering based on the coherent combination of SAR interferograms at different polarisations (Cloude & Papathanassiou 1998, Papathanassiou & Cloude 2001). The main PolInSAR observable is the interferometric coherence, which is the modulus of the complex correlation coefficient between two interferometric images of a given scene acquired with slightly different geometries. The images can be acquired in a dual- or quad-polarimetric mode, either simultaneously (single-pass) or at different times (repeat-pass): only the latter is available for Biomass. After correction of decorrelation induced by the system and the acquisition geometry, the coherence can be expressed as (Bamler & Hartl 1998; Zebker & Villasenor 1992):

$$\gamma = \gamma_T \cdot \gamma_{SNR} \cdot \gamma_{Vol} \tag{4.1}$$

Here the volume coherence γ_{Vol} is the contribution that contains information on vertical forest structure, while γ_T and γ_{SNR} are nuisance terms describing the loss of coherence due to temporal change and system noise. Accordingly, PolInSAR inversion techniques use γ_{Vol} measurements at different polarisations and/or spatial baselines to reconstruct vertical forest structure parameters, such as forest height (Papathanassiou & Cloude, 2001).

In recent years, PolInSAR has matured and developed, and forest height has become a well understood product. Numerous experiments, carried out over a variety of temperate, boreal and tropical test sites, have demonstrated the ability of PolInSAR to estimate forest height and other key forest parameters with high accuracy over natural and plantation forests under different stand and terrain conditions (Papathanassiou & Cloude, 2001; Praaks et al., 2007; Lee at al., 2008; Garestier et al., 2008; 2010; Kugler et al., 2007; Hajnsek et al., 2008, Garestier et al., 2010a).

Figure 4.3 shows a forest height map of the Mawas region, Indonesia, derived from P-band PolInSAR data acquired during the INDREX-2 campaign in 2004. In the forested area, height ranges are 15–27 m. The trails from by logging activities 10–15 years earlier are clearly visible, as well as the higher degree of disturbance close to the trails (Hajnsek et al., 2009). Lidar height data are available along a transect over this site, and the scatterplot in Fig. 4.2 indicates the close agreement between the lidar and radar estimates of height. The left part of Fig. 4.3 shows a forest height map derived from PolInSAR over the Remningstorp site, and the corresponding lidar map (produced by a scanning lidar) is on the right. The maps clearly correspond in the high and low areas, indicating the ability of PolInSAR to track forest height and the associated biomass dynamics.

However, it is important to realise that the estimation of forest parameters from PolInSAR requires the decorrelation due to temporal change and noise to be small; i.e. both γ_T and γ_{SNR} must not depart too far from 1 (see Eq. 4.1). Noise decorrelation is introduced into the received signal by system noise and primarily affects scatterers with low backscatter; at P-band, it is normally of secondary importance over forests. Temporal decorrelation is caused by weather and environmental changes occurring between the acquisitions, and depends on the temporal stability of the scatterers and the time interval between the two acquisitions. Since it cannot be controlled or compensated, it is the most critical performance parameter in a repeat-pass implementation of PolInSAR. The Biomass sensor is designed to maximise γ_{SNR} and γ_T, so providing γ_{Vol} estimates that optimise inversion performance. Both aspects are discussed in more detail in Chapters 6 and 7.

Figure 4.3. Left: forest height map of the Mawas region, Indonesia, derived from P-band PolInSAR data acquired during the INDREX-2 campaign in 2004 (Right: plot of PolInSAR height against lidar height along a transect. (DLR)
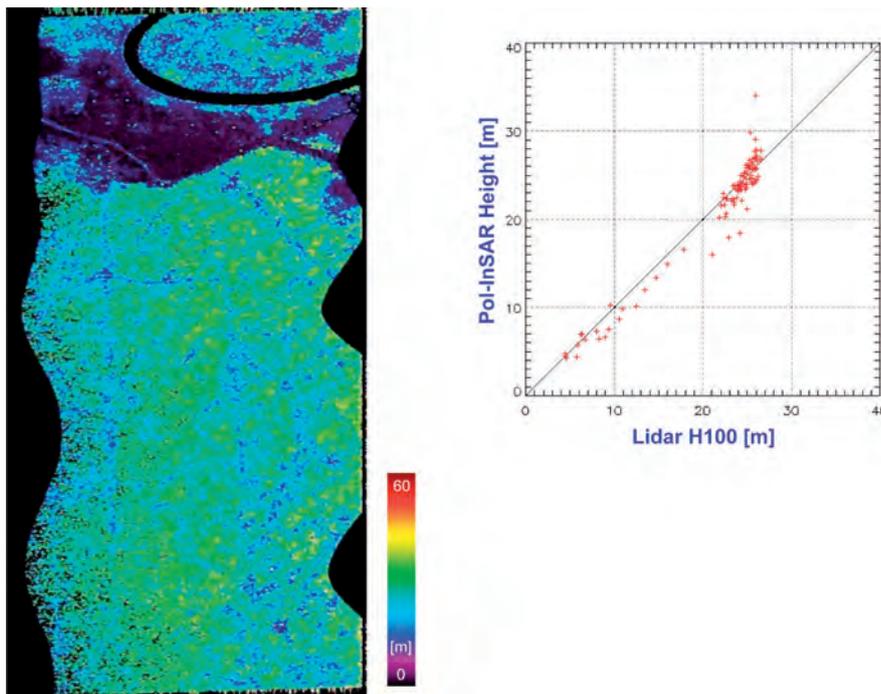
Figure 4.4. Left: forest height map for part of the Remningstorp test site, Sweden, derived from P-band PolInSAR measurements. Right: lidar forest-height map. (DLR)
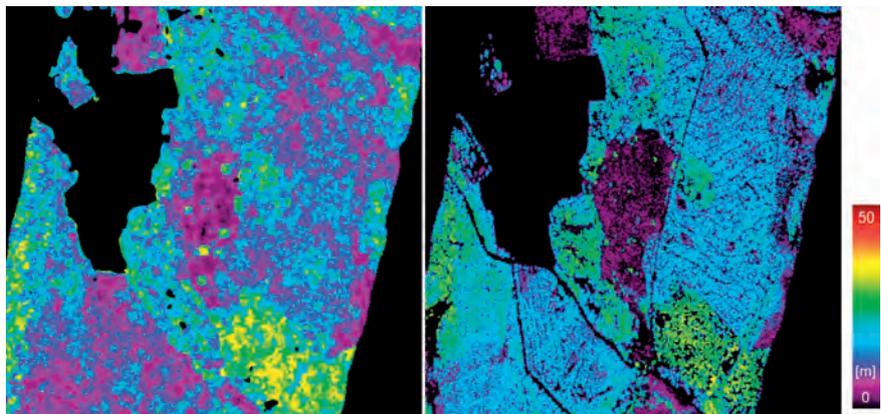
Figure 4.5. Left: acquisition geometry for a multibaseline SAR system. Right: slant-range/cross-range extension of the tomographic resolution cell. (POLIMI)
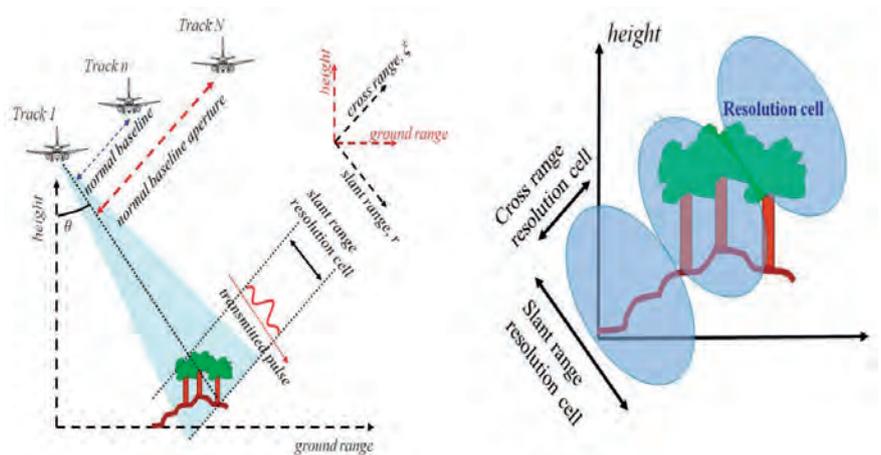
4.2.3 SAR Tomography

In the initial phase of the mission, an important reference dataset will be acquired using SAR tomography. In recent years, SAR tomography has emerged as an important tool for investigating forested areas by virtue of its capability to resolve the vertical structure of the target based on multibaseline observations (Cloude, 2007; Tebaldini, 2010; Tebaldini & Rocca, 2012). In technical terms, it is the extension of conventional two-dimensional SAR imaging principles to three dimensions (Reigber & Moreira, 2000).

The concept behind SAR tomography is relatively simple. Consider a multibaseline SAR system, where a scene is imaged from different viewpoints, as depicted in Fig. 4.5.

Such a system offers the possibility of gathering backscattered echoes not only in the azimuth direction, but also in the cross-range direction, defined by the axis orthogonal to the line of sight and the orbital track. Accordingly, the echoes can be focused in the slant range-azimuth plane and in the whole 3D space. It follows that, if the carrier frequency is low enough to guarantee penetration of the scattering volume, the vertical profile of the scatterers can be retrieved. The tomographic phase of Biomass foresees multiple repeat passes to build up the vertical structure of the forest scatterers. It requires slightly different incidence angles and a 1–4 day revisit cycle to maximise target coherence (the amplitude of the complex correlation coefficient). The vertical resolution improves with the total angle span covered, while the baseline spacing dictates the interferometric height of ambiguity. This must be larger than twice the forest height to avoid data superposition. To separate 3–4 layers in forests of 50 m high, 5–6 passes are needed.

Figure 4.6 shows two tomograms, one from a boreal forest in northern Sweden investigated during BioSAR-2, and one from a tropical forest in French Guiana investigated during TropiSAR. The colour scale in each panel indicates the relative backscattered power associated with each bin in the slant range-height plane. The total backscattered power at each range bin (i.e. along each column) is normalised to 1, so as to highlight the vertical distribution of the backscattered power. Both panels are relative to the HV polarisation. Comparison between the two panels shows that the vertical distribution of the backscattered power in the tropical forest is distributed at canopy level and ground level, indicating volume scattering and double-bounce scattering. In boreal forest, most of the backscattered power is associated with ground level,
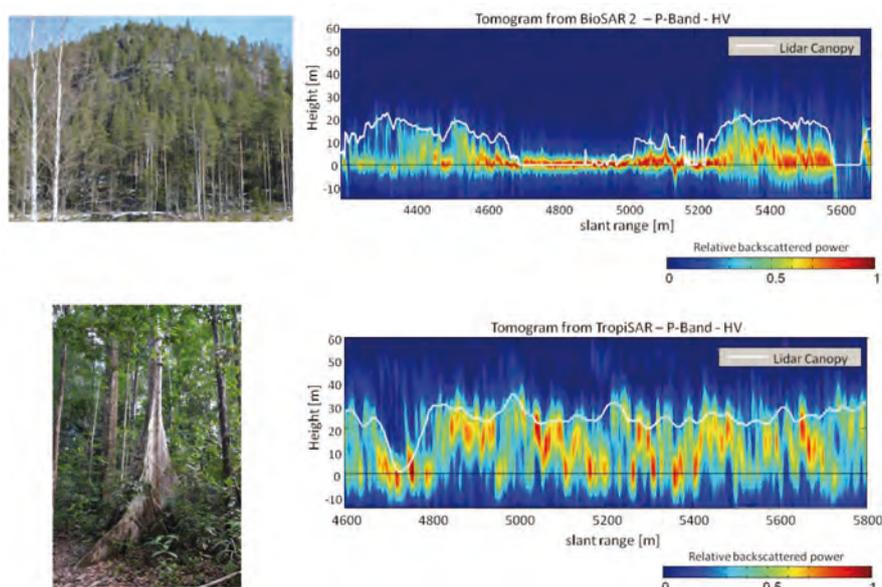
Figure 4.6. Top: tomographic transects of boreal forest from BioSAR 2008 data (Tebaldini & Rocca, 2012). Bottom: tropical forest from TropiSAR data (Tebaldini et al., 2011). The colour code shows the vertical distribution of the normalised power along a transect. The green lines show forest height derived from lidar data. (POLIMI)

indicating strong double-bounce returns from trunk-ground or canopy-ground interactions.

The orbit requirements for tomography are such that global coverage would take around 3.5 years, which competes with the science requirement for six-monthly global coverage; hence it cannot be used as the primary mission mode. The tomographic phase will, therefore, be restricted to around 50 days early in the mission, during which it will provide coverage of around 10–15% of the global forest area. The orbit configuration in this phase will be selected to cover regions representing the world's major forest types and biomes, so that the tomographic data can be used as a reference during the remainder of the mission.

4.2.4 Change Maps Derived from Biomass Images

An important use of Biomass will be to monitor biomass changes related to growth and different forms of disturbance. Change maps derived from differences between individual biomass maps have the advantage that any systematic bias, e.g. from structure and topography, is removed. Against this, the variances of the zero-mean errors in the measurements will be additive. Therefore, biomass-change measurements will have poorer precision than individual measurements. Experimental results, indeed, show that the sensitivity to changes is high. Figure 4.7 (right) shows a map of biomass change between 2007 and 2010 derived from P-band HV data (Ulander et al., 2011a). The scaling is in logarithmic units, as shown in the colour bar, and subtle changes are emphasised by clipping the values at –1. Red indicates clear-cuts, green indicates growth in young forest, and orange indicates forest affected by thinning, which typically removes 20–30% of the biomass. The map on the left is for the same period and is compiled from small-footprint helicopter lidar, *in situ* forest measurements and aerial photography. The lower figures show the two original lidar height images; the areas of regrowth and clear cutting are evident. Thinning activities can also be seen, particularly the winding network of roads used for removing trees. The remarkable agreement between the two biomass-change maps indicates that Biomass will be able to measure changes with high sensitivity; it is very important to note that this includes areas of regrowth.

4.3   Geophysical Product Requirements

4.3.1 Coverage

Chapter 2 outlined the need for a global biomass product to address an array of science questions. However, the text also highlighted a particular tropical focus to many of these issues. Thus, while covering the global forested areas, including tropical, temperate and boreal forests is desirable, covering tropical-forested areas is critical for a successful mission.

Information on the location and extent of global forests can be derived from global land-cover maps, such as the Global Land Cover 2000 Project (GLC2000) dataset produced by the European Commission Joint Research Centre at a resolution of 1 km, or the more recent GlobCover derived from Medium Resolution Imaging Spectrometer (MERIS) data, which has a resolution of 300 m. To derive a basic coverage requirement we consolidate the GLC2000 map into fewer, more general, classes. Figure 4.8 shows forested areas in green (GLC2000 classes 1–10). The major forest regions (e.g. Amazonia) to be covered by the mission are enclosed within the boxes in the figure.

The regions related to secondary mission objectives (arid zones in yellow and ice sheets in grey) are also identified in Fig. 4.8 and provide a baseline coverage requirement. Antarctica is not included in the figure, but it should be

Lidar-based change map

SAR change map (from HV-pol)

Lidar 2007

Lidar 2010
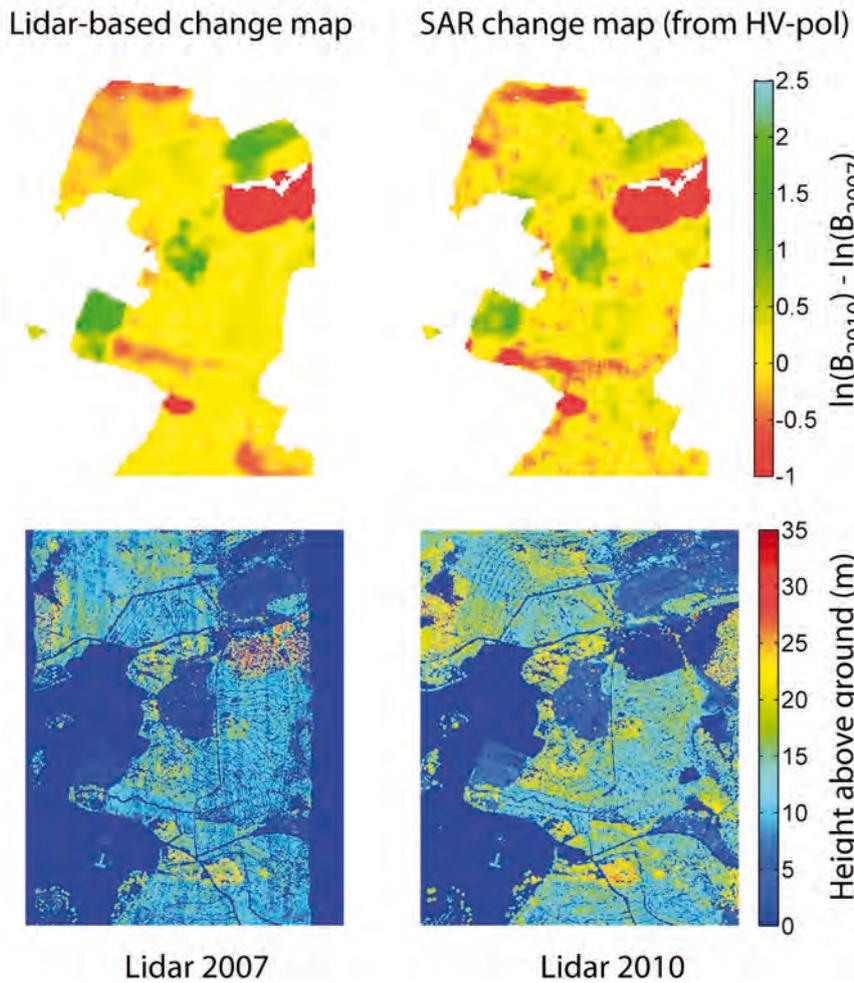
Figure 4.7. Top right: map of biomass change between 2007 and 2010, derived from P-band HV backscatter data from the BioSAR-1 and BioSAR-3 campaigns, averaged to 50 m spatial resolution. The B denotes biomass (t ha^{-1}) and the colour scale is based on natural log (values below −1 are clipped to show subtle biomass changes and not only the clear-cuts). Top left: map of biomass change over the same period derived from lidar, *in situ* data and aerial photography. Bottom row: lidar-height maps. Clear-cuts, regrowth and thinning can be observed, as well as an overall growth of the forest between 2007 and 2010. The images cover an area measuring 1.2×1.3 km. (Chalmers University)

Figure 4.8. Simplified map derived from the GLC2000 land-cover map. Green indicates forest, yellow shows arid zones and grey corresponds to ice. (ESA)
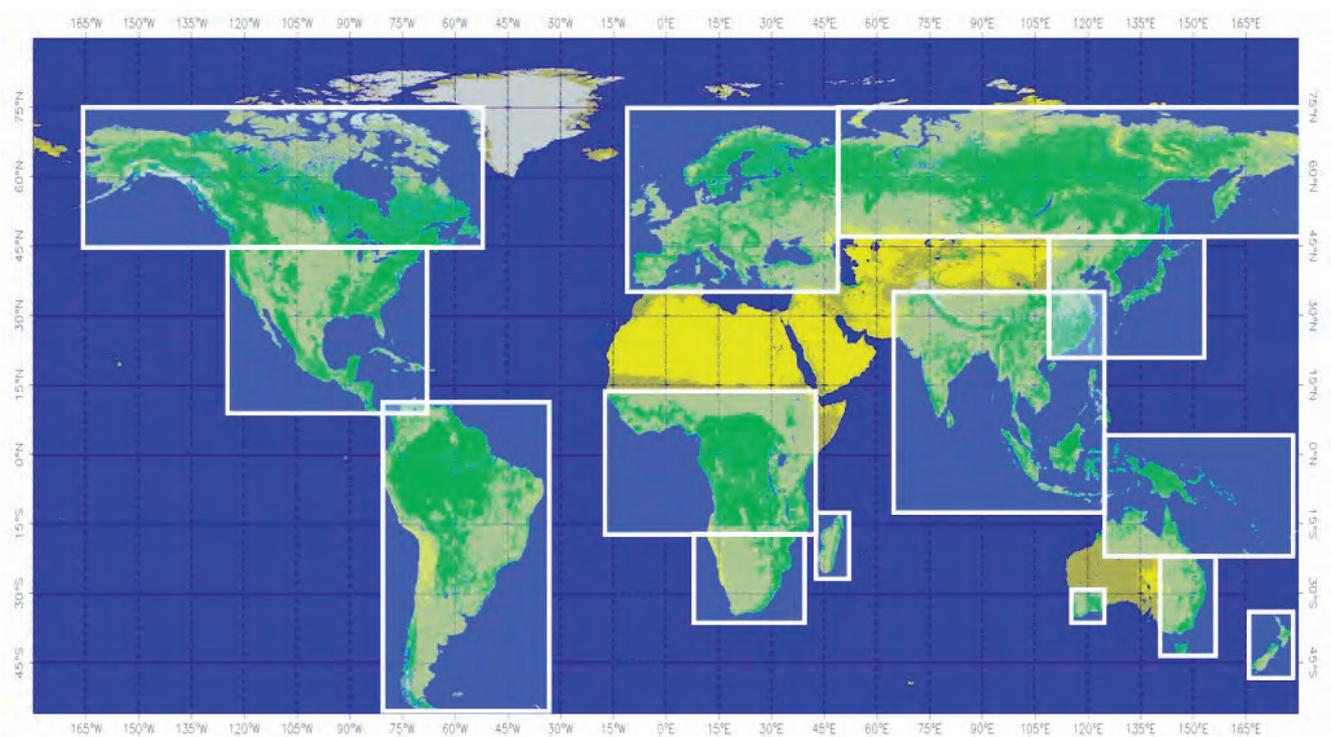
mapped as far south as possible, though the central part of the continent is of least interest. In addition, it is desirable to obtain global coverage at least once during the lifetime of Biomass. This would provide the basis for development of P-band applications that have not yet been identified.

4.3.2 Spatial Resolution

The spatial resolution of the Level-2 products has to be consistent with the scales of the factors underlying the variability in biomass. The different rates of change expected for different processes suggest a dual approach for defining spatial resolution, one for deforestation and one for degradation/accumulation (Houghton et al., 2009).

To detect disturbances from human exploitation, fine spatial resolution should be used, in order to give greater accuracy in area affected (Zheng et al., 2008). Following the discussion in Chapter 2, a resolution around 0.25 ha is required to detect deforestation. Secondly, for areas with potential degradation or biomass accumulation, spatial resolution can be forfeited to gain greater accuracy over pixels that are large enough to capture a representative biomass. In natural forests, most of the biomass is stored in a relatively small fraction of large stems; for instance, 5% of the stems can hold more than 50% of the biomass in tropical forests. Small sample areas would tend to give overestimates or underestimates of biomass, depending on whether they include a large tree or not. The appropriate measurement (pixel) size should capture large trees in proportion to their abundance, indicating a resolution of ~4 ha. However even coarser resolutions up to 1 sq km can provide far superior information than current global estimates (Hall et al., 2011).

Note that the above discussion is in terms of pixel area (ha), which is more important than the side-length when discussing biomass. However, in the document it is sometimes convenient to talk in terms of linear dimensions, and '50 m resolution' is used to refer to 0.25 ha and '200 m resolution' to refer to 4 ha, etc.

4.3.3 Temporal Sampling

Forest biomass does not increase very rapidly and is not a driver in terms of temporal sampling requirements. The fastest forest regrowth rates occur in the Tropics, where they are in the order of 5–12 t ha^{-1} yr^{-1} for forests regenerating naturally and for plantations. To observe these changes at least two observations over a five-year period is a minimum requirement (Houghton et al., 2009). Intervals of less than a year are normally too short to measure changes due to natural regrowth accurately.

The objective of quantifying the role of disturbance in year-to-year variations in relation to rate of increase in atmospheric CO_2 is a more important driver determining the temporal sampling. Mapping disturbances on a biannual basis covering major forest biomes at 0.25 and 4 ha resolution will make it possible to distinguish whether variation in disturbance (e.g. due to fire), degradation or metabolism (photosynthesis and respiration) is responsible for variations in the atmospheric CO_2.

Subsurface geology and DEM generation do not require repeated maps. One map during the mission is sufficient to meet the objectives. For ice flow, yearly maps are needed to monitor changes. To investigate seasonal variations, at least one winter/summer coverage during the mission's life is desirable.

4.3.4 Uncertainty

To reduce the large uncertainty in the global net flux of carbon from land-use change requires biomass to be measured with accuracy better than 10 t ha^{-1} for biomass <50 t ha^{-1} and better than 20% for biomass values above this, at

a scale of 4 ha. (Note that here and in following sections accuracy is usually defined in terms of relative error, i.e. coefficient of variation, defined as standard deviation divided by the mean.)

Current uncertainty estimates in the global net flux of carbon from land-use change are in the range of ±33% (Canadell et al., 2007) to ±70% (Denman et al., 2007). By contrast the next most uncertain term in the global carbon balance is the net uptake of carbon by oceans, with an uncertainty of ±18% (Fig. 2.3). Achieving a comparable uncertainty would constitute a major step forward in our ability to constrain and understand the global net flux of carbon (Houghton et al., 2009). Given the large uncertainties in current biomass estimates reported in Section 2.2, global measurements with even larger uncertainties would still be immensely valuable, as long as they are unbiased, so that error cancellation would be effective (Williams et al., 2011).

This threshold also matches our current ability to measure biomass stocks on the ground. Analysis of ground observations showed that the accuracy of forest biomass measurements based on a single plot of 0.25 ha is 21% in tropical forest at the Paracou research station (Blanc et al., 2009) and 33% in a seasonal moist tropical forest on Barro Colorado Island, Panama. These results suggest that a globally available biomass product with an accuracy of 20% is comparable in accuracy to ground-based observations (though at coarser resolution), and marks a major improvement in our current information on biomass.

The requirements on the accuracy of height measurements from Biomass need different treatment. Foresters do not normally exploit height when developing allometric relations to estimate biomass; they instead rely on quantities that are much easier to measure *in situ*, such as the tree diameter at breast height. The ability of Biomass to provide an independent estimate of height adds a new quantity for foresters to use in estimating biomass, and provides a significant opportunity to develop new allometric relations and to test and validate them against *in situ* biomass measurements derived by more traditional methods.

Hence, the Biomass mission itself will provide the strongest means of determining accuracy requirements for height. As discussed in Chapter 6, height will be used to predict biomass using available height-biomass allometric equations. Results from the BioSAR and TropiSAR campaign experiments suggest that an accuracy of 20% is adequate to derive a robust biomass estimate.

4.3.5 Timing of the Mission

There is no specific timing requirement for the mission, since it does not depend on any other mission nor is there any crucial environmental constraint, although ionospheric effects (Faraday rotation (FR) and scintillation) would be reduced if the mission straddled sunspot minimum (predicted around 2020–22). However, the proposed orbit ensures that the primary mission objectives would not be significantly affected, even during sunspot maximum. This is because: (i) Faraday rotation is measurable and correctable using the polarimetric SAR observations, for any level of ionospheric electron density; (ii) satellite beacon data gathered since the 1970s (i.e., covering the last three solar cycles) show that scintillation effects will be negligible if Biomass is put into a dawn/dusk orbit, except over the northernmost boreal forests in the North American sector. However, for high-latitude ice applications, ionospheric effects are likely to cause significant disturbance under all conditions, though these will be worse during sunspot maximum. Recently developed methods also indicate that even the effects of high-latitude scintillations may be correctable (Quegan et al., 2012).

4.3.6 Latency

The mission objectives impose no strong data latency requirement and no need for near-realtime access to the products. Data access is expected to take place offline though subscription to the mission archive. As a guideline, a data latency of one month is considered sufficient.

4.3.7 Mission Duration

A mission of five years would be adequate to satisfy the need for information (Houghton, 2009). However, a longer mission is preferable in that it would enable more accurate observations of rates of change, particularly in forests with smaller regrowth rates.

4.3.8 Summary of Level-2 Products

An important objective of Biomass is to map disturbances and sudden forest change. These quantities can be derived from biomass products by simple subtraction; an example is shown in Fig. 4.7. However, as for optical satellite products (Hansen et al., 2008; Mesquita et al., 2008), the accuracy of these change maps is likely to be improved by using methods aimed more directly at measuring rapid change from the radar signal itself, rather than as a difference of two separate biomass maps. Methods to do this have not been specifically addressed during Biomass studies, but should form part of pre-launch development if Biomass is selected.

4.4 Level-1 Data Requirements

The previous section detailed the geophysical product requirements. Here these are translated into requirements for the SAR observables to ensure that the uncertainty of the retrieved geophysical products is within the specified range. The total uncertainty of the retrieved biomass is a combination of uncertainties introduced by speckle, uncompensated bias and drift in the radar instrument, residual errors after system calibration and ionospheric correction, intrinsic uncertainties in our knowledge of forest systems (e.g. the relation between forest height and biomass), and environmental effects that disturb the relation between biomass and the radar measurements. The last of these may include effects for which the signal can be compensated (e.g. soil moisture,

Table 4.2. Summary of main Level-2 products

Level-2 Product	Definition	Information Requirements
Forest biomass	Above-ground biomass (dry weight of woody matter + leaves) expressed in t ha^{-1}.	- 200 m resolution - accuracy of 20%, or 10 t ha^{-1} for biomass ‹50 t ha^{-1} - 1 biomass map every 6 months - global coverage of forested areas
Forest height	Upper canopy height defined according to the H100 standard used in forestry	- 200 m resolution - accuracy required is biome-dependent, but shall be ~20% for trees higher than 10 m - 1 height map every 6 months - global coverage of forested areas
Deforestation detection	Map product showing areas of forest clearing	- 50 m resolution - 90% classification accuracy - 1 map every 6 months - global coverage of forested areas

topography) or which may be unknown and require a design that reduces them to acceptable levels (e.g. temporal decorrelation, ionospheric scintillation). To address these various factors the setting of Level-1 data requirements was based on analysis of campaign data (Table 4.1) and the use of simulation tools.

4.4.1 Selection of Frequency

The increasing sensitivity of SAR backscatter to forest biomass as frequency decreases has been documented in many publications (see Le Toan et al., 2011 for refs.). In addition, for a single-satellite SAR mission, the ability to retrieve forest height depends on high temporal coherence between acquisitions, which can only be maintained at P-band.

The selection of the P-band frequency is therefore essential if Biomass is to meet its primary goal, which is to map forest biomass across the entire range of forest types.

Temporal decorrelation is related primarily to the temporal stability of the location and dielectric properties of the scatterers within a SAR resolution cell. POLinSAR height inversion is affected because temporal decorrelation is superimposed on the volume decorrelation contribution, which carries the information about the vertical forest structure, in particular forest height. P-band is highly resistant to temporal decorrelation for four main reasons:

— The long wavelength allows deeper penetration into the vegetation layer, ensuring interaction with the ground beneath the canopy (necessary for PolInSAR) even for dense forests.

— At this wavelength the major interactions in the canopy are with the larger tree structures which carry most of the biomass.

— Both the ground and large tree structures are more stable scatterers than smaller tree elements, such as branches, leading to higher temporal coherence at P-band than at shorter wavelengths.

— The decorrelation caused by motion of the scatterers is lower for longer wavelengths, so P-band not only scatters from more stable structures but is less sensitive to their motion.

This has been validated by recent experimental results derived from airborne campaigns. The TropiSAR airborne experiment reported median coherence values exceeding 0.85 for temporal baselines of 22 days over a dense tropical forest (Fig. 4.9) (Dubois-Fernandez et al., 2012). Similarly, temporal coherence over a boreal forest site obtained in the frame of the BioSAR-1 airborne experiment remained high at P-band (γ_T = 0.9) but dropped significantly at L-band (γ_T = 0.65) for a temporal baseline of 30 days (Hajnsek et al., 2008). Figure 4.10 highlights the ensuing large height error at L-band and much smaller effect at P-band.

The global frequency allocation enabling P-band spaceborne radar missions was established at the World Radiocommunications Conference in 2003 and fixed as the frequency range 432–438 MHz (Article 5 in the International Telecommunication Union (ITU) radio regulations, 2004), corresponding to a centre frequency of 435 MHz with a bandwidth of 6 MHz. One of the main reasons for the frequency allocation request was to permit Earth observation at P-band.

4.4.2 Polarisation

As noted in Section 4.2, different polarisations respond to different properties of the forest canopy/soil system and thus can be used to acquire different

Figure 4.9. Observed P-band coherence for tropical forest in French Guiana at HH (red), HV (green) and VV (blue) polarisations for different temporal baselines. The mode is indicated by a square and the bars show the range of coherence over which the histogram exceeds half its modal value, i.e., from γ_1 to γ_2 as indicated by the inset. (Onera)
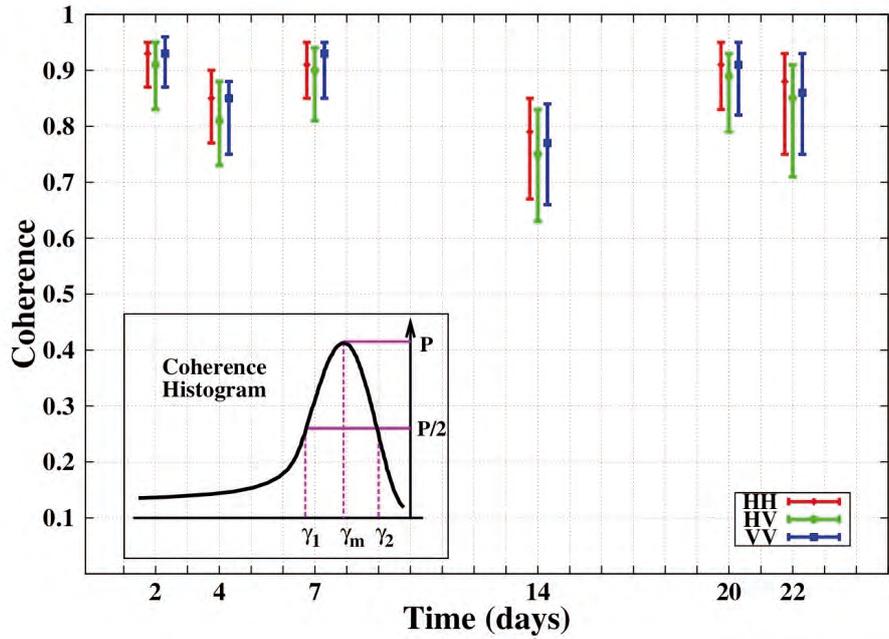
types of information. Both direct biomass retrieval and forest height retrieval requires use of all the terms in the polarimetric covariance matrix (other than the co-polarised/cross-polarised covariances, which should be zero under homogeneous forest conditions), including the relative phases of the polarisation channels, i.e., fully-polarimetric data. Products related to secondary mission objectives, such as mapping of terrain elevation under dense vegetation and ice properties over land, also require fully-polarimetric data. As well as these needs for science, a crucial reason for acquiring polarimetric data is that algorithms to correct for FR induced by the ionosphere need such data, as described in Subsection 6.2.1. In addition, the availability of several polarimetric channels can be used to improve the radiometric accuracy of Level-1 products through multichannel filtering techniques (Quegan & Yu, 2001). This will play an important part in delivering radiometrically accurate products at the required spatial resolution. For all these reasons, Biomass must operate in a fully-polarimetric mode.
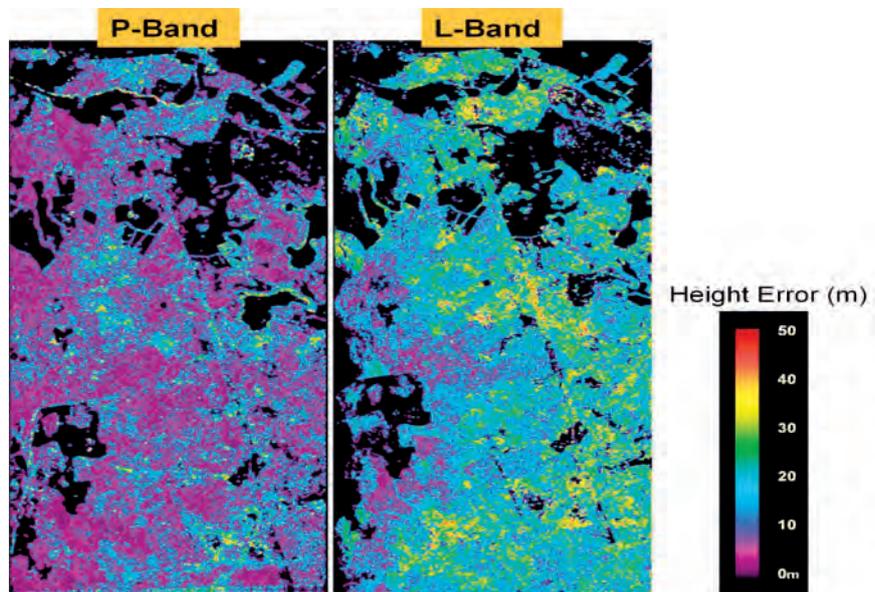
Figure 4.10. PolInSAR forest height retrieval errors at P- and L-band using images acquired 30 days apart. The L-band errors (right) are significantly higher than those at P-band (left) due to higher temporal decorrelation. The airborne radar data were acquired from the Remningstorp test site in Sweden during the BioSAR-1 airborne campaign. (Hajnsek et al., 2008)

4.4.3 Incidence Angle

Both analysis of airborne radar datasets and theory demonstrate that use of steeper incidence angles tends to reduce the dynamic range between bare surfaces and mature forest and to increase biomass retrieval errors based on backscatter. The polarimetric information used for height retrieval from PolInSAR is also reduced with steeper incidence angles, leading to larger errors. Hence, larger incidence angles are desirable, but system considerations place strong constraints on possible incidence ranges and favour steeper incidence angles. Studies based on airborne data have shown that incidence angles above 25° are acceptable for forest biomass retrieval (Dubois-Fernandez et al., 2004), and it is expected that slightly lower incidence angles (by 1–2°) will not harm the retrieval performance. The threshold requirement for the incidence angle of the Biomass mission is therefore set to be greater than 23°, and the goal to be greater than 25°.

4.4.4 Revisit Requirements

As outlined in Section 4.2, biomass maps are required twice a year. However, the main driver defining the revisit period is the need to minimise the impact of temporal decorrelation on the forest height product. As demonstrated theoretically and using airborne SAR data, temporal decorrelation causes PolInSAR forest height measurements to be overestimated and increases their dispersion. While the dispersion can be reduced by averaging at the expense of spatial resolution, this will not remove the bias.

Figure 4.13 shows theoretical estimates of the height bias as a function of temporal decorrelation for different levels of forest height. The key features to note are: (i) for a given level of temporal decorrelation, bias decreases as forest height increases; and (ii) for a given height, bias increases as temporal decorrelation increases.

To meet the requirement of ~20% accuracy in forest height, temporal decorrelation levels have to be less than 0.15. In Subsection 4.4.1, it was demonstrated that this can be achieved over revisit times of 20–25 days. This also makes extra passes available that can be used in PolSAR retrieval, improving the radiometry and reducing uncertainty.

With regard to the secondary objectives, the maximum ice velocity gradient that can be measured with DInSAR (Massonnet et al., 1993) is inversely proportional to the revisit time (Kwok, 1996). A Biomass revisit time of 25 days would imply a maximum measurable glacier velocity on the order of 100 m yr^{-1}. For faster glaciers, the offset tracking technique (Gray et al., 1998) must be applied. This can cope with lower coherence and does not involve phase unwrapping, but is also less accurate, around 50 m yr^{-1} for a 25-day revisit, or 5–10 m yr^{-1} for a six-month revisit (if temporal decorrelation permits). Another constraint imposed by the revisit time is that a DEM is required to separate velocity from topography in case of a drifting orbit, for which the revisit time and the spatial baseline are proportional. (Paillou et al., 2011)

4.4.5 Error Sources Arising from the Biomass Radar System

This section deals only with the impact of speckle and system errors on the uncertainty of the retrieved biomass information. Their effect on the final biomass product can best be estimated using end-to-end simulation tools, which generate an 'ideal' scene that is perturbed by the various noise sources inherent to SAR systems. The perturbed scene is then used to invert biomass and compare to the ideal scene. Such simulators typically employ a Monte Carlo approach to predict the geophysical retrieval performance as a function of the wide range of uncertainties. The simulator used here uses the model proposed in Saatchi et al. (2007b) to relate backscatter to forest biomass, and
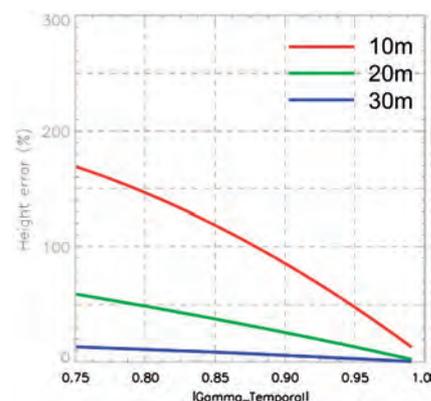
Figure 4.11. Theoretical estimates of the height bias as a function of temporal decorrelation for different levels of forest height. (DLR)

Figure 4.12. Relative error of retrieved biomass against biomass for different numbers of looks under a simplified inversion scheme using only the HV channel. (ESA)
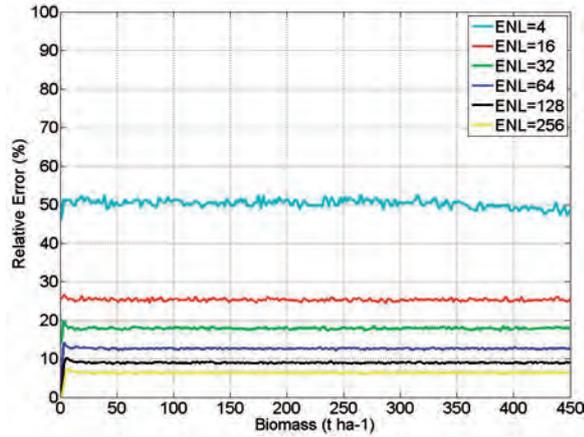
Figure 4.13. Classification error as a function of contrast between disturbed/ undisturbed forest classes. The individual curves and their labels correspond to different number of looks applied to the input radar data. (ESA)
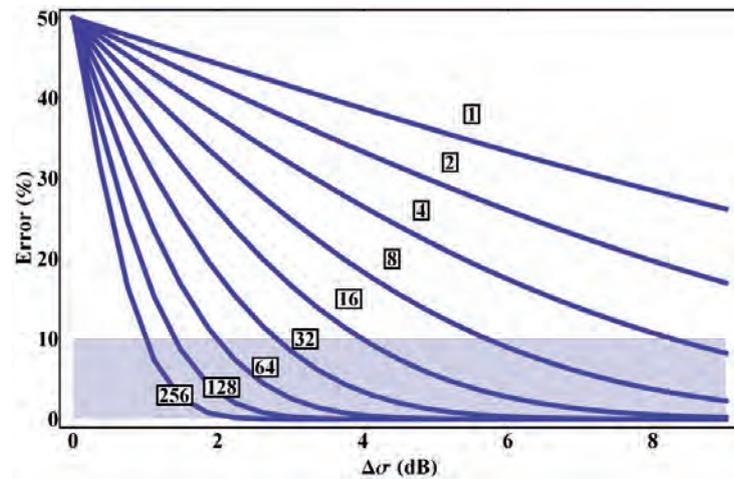
we limit the simulation of the inversion to HV backscatter observations. This is a simplified version of the full algorithm outlined in Chapter 6 and the performance of which is evaluated in Chapter 7. Nevertheless, for the initial definition of requirements, this approach provides robust requirements with sufficient confidence.

4.4.5.1 Resolution and number of looks

In Section 4.3 we defined the resolution required to meet the mission objectives. In technical terms, the resolution of a SAR system is limited by the bandwidth and the antenna length. The 6 MHz bandwidth available to Biomass limits the (across-track) resolution to 59 m at an incidence angle of 25°. The azimuth (along-track) resolution is only limited by the antenna length, and is expected to be 12.5 m. In SAR terminology this resolution is referred to as 'single-look' resolution. Although single-look data have high resolution they are impractical to work with, as they are characterised by a strong noise-like quality called speckle. This arises from interference between the different scatterers within a single SAR resolution cell (Oliver & Quegan, 1998). To reduce this uncertainty, radar intensity images are typically incoherently averaged. The number of independent samples in the average is known as the equivalent number of looks (ENL). For Biomass averaging four looks in azimuth will give rise to pixels with an area of ~0.25 ha.

Figure 4.12 shows the impact of different ENLs (4–256 looks) on the relative error for a biomass range of 0–450 t ha^{-1} and an inversion exploiting HV information only. Bearing in mind the contribution of other sources of

uncertainty, achieving the required biomass accuracy of 20% was found to need 64 looks. This accuracy is needed at the scale of 200 m (see Subsection 4.2.2) which is equivalent to requiring an ENL of four at 50 m resolution. In practice, this is a conservative requirement since extra polarisations would be used in the inversion and multichannel filtering would be used to increase the ENL of the individual channels. Following Quegan and Yu (2001), such filtering would lead to an increase in ENL by about a factor of five for a time series of six polarimetric images, depending on the degree of correlation between the polarimetric channels and between images gathered at different times (i.e., if the Biomass data in each of the input images were 4-look, the ENL would be increased to 20, with almost no loss of spatial resolution).

An ENL of 4 at 50 m resolution is also compliant with the requirement for the forest disturbance product. This will classify the input radar images into two classes (disturbed and undisturbed), and has an accuracy requirement of 90%. Typically, such products are generated using multitemporal change detection algorithms. For a single channel, the requirement in terms of ENL and radar contrast to classify with 90% accuracy is readily calculated from expressions in Rignot & van Zyl (1993), as shown in Fig. 4.13. For an ENL of 4, it is possible to map disturbances causing changes in radar intensity of more than 8 dB with 90% accuracy (Fig. 4.13). Since the contrast between completely deforested areas and mature forest is of the order 10–12 dB at P-band, the accuracy requirement is easily achieved. Performance would be even better when fully-polarimetric data are used (Conradsen et al., 2003).

4.4.5.2 Radiometric bias and stability

The radiometric accuracy is made up of two components:

— The absolute radiometric bias, defined as the bias in the measured radar cross-section of a calibration target over the mission lifetime. Correction for this bias (absolute calibration) is unlikely to be critical, as it can be compensated for in the retrieval algorithm (see Section 6.1). It becomes relevant principally when comparing data from the Biomass instrument with other P-band instruments, such as airborne sensors or a P-band follow-on mission. A threshold of 1 dB is considered to be adequate, since such constant offsets can be dealt with by cross-calibration.

— The radiometric stability, defined as the standard deviation of the measurements of the radar cross-section of an unsaturated invariant target, taken at different times. This is critical for Biomass as PolSAR retrieval relies on the stability of the relationship between backscatter and forest biomass. Figure 4.14 shows the impact of a system with a radiometric stability of either 0.5 dB or 0.16 dB on the accuracy of biomass for an inversion exploiting HV information only. It can be seen that for a radiometric stability of 0.16 dB the error budget is dominated by speckle (based on an ENL of 64) and the radiometric uncertainty contributes little to the total uncertainty. At 0.5 dB the contribution becomes significant and the total error budget is close to the 20% error threshold imposed by the scientific objectives. Hence Biomass should support a radiometric stability of better than 0.5 dB in order to meet the observation requirements.

4.4.5.3 Instrument noise

The Noise Equivalent σ^0 (NESN) represents the backscattering coefficient that is equivalent to the background noise in the SAR image. It is caused by thermal noise together with digital converter and A/D quantisation noise. The main impact on the mission will be on the retrieval of lower biomass values and

the secondary objective of mapping subsurface geomorphology in arid zones. The HV channel is worst affected because it has lower backscatter than the co-polar channels. For low-biomass areas, the HV backscattering coefficient is typically around –25 dB, and NESN must be below this value to allow biomass retrieval in young or sparse forest. Keeping NESN below –27 dB will provide a Signal-to-Noise ratio (SNR = σ^0/NESN) in excess of 2 dB across the full range of backscatter encountered in forest stands, which is sufficient for adequate retrieval performance. This is confirmed by end-to-end simulation results, which show that a NESN of better than –27 dB is sufficient to meet the mission objectives (see Fig. 4.15).

The NESN also affects interferometric measurements, reducing the coherence by a factor:

$$\gamma_{SNR} = \frac{1}{1 + SNR^{-1}} \tag{4.2}$$

For mature forested areas, where interferometric measurements are most needed, $\sigma^0 \approx$ –12 dB; hence, if NESN = –27 dB, SNR = 15 dB, and γ_{SNR} = 0.97, which is acceptable.

One of the secondary objectives, subsurface geology, requires a NESN between –30 dB and –40 dB, but in this case the NESN can be improved by coherent averaging of several images (Paillou et al., 2011).

4.4.5.4 Range and azimuth ambiguities

Range and azimuth ambiguities are important design parameters as they influence technical choices, such as the antenna dimensions. Range and azimuth ambiguities are typically specified by the total ambiguity ratio (TAR), which is given by the ratio of powers from distributed targets in the ambiguous and unambiguous zones. The unambiguous zone is defined in the across-track direction by the nominal swath width and in the along-track direction by the total processed Doppler bandwidth. The ambiguous zone is outside this area. TAR depends on system and operating parameters as well as the scattering characteristics of the scene, hence quantitative guidelines on acceptable values of TAR are difficult to establish from user requirements. Nonetheless, a broad consensus based on experience with SAR missions at other frequencies is that TARs less than –20 dB do not strongly affect applications over natural surfaces.

For interferometry, range and azimuth ambiguities in the individual images combine incoherently, reducing the coherence. If the range and azimuth ambiguities are considered as additional additive noise terms, the coherence is reduced by the factor:
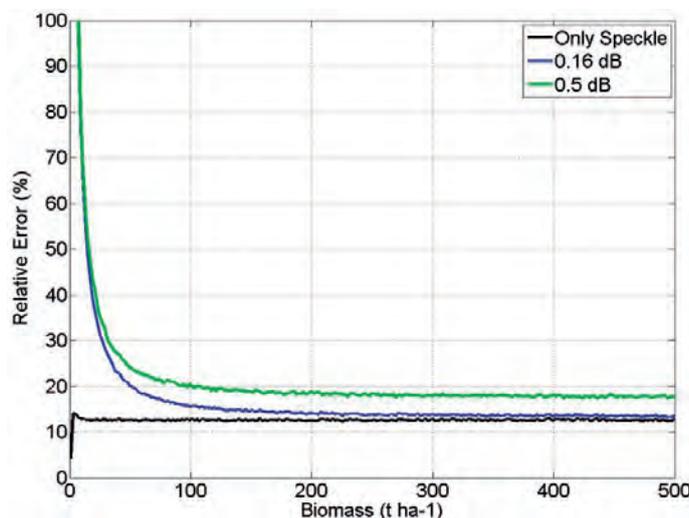
Figure 4.14. Relative error of retrieved biomass against biomass for radiometric stability of 0.5 and 0.16 dB under a simplified inversion scheme using only the HV channel and for an ENL of 64. (ESA)
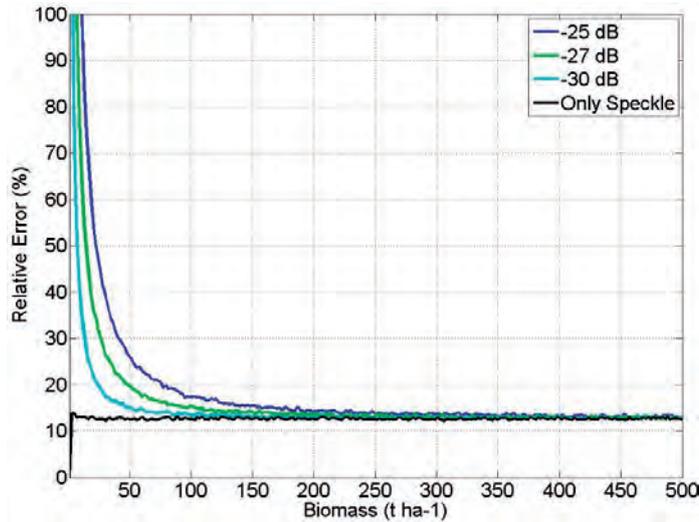
Figure 4.15. Impact of different levels of NESN on the relative error of biomass retrieval against biomass under a simplified inversion scheme using only the HV channel and 64-look data. (ESA)

$$\gamma_{AMB} = \frac{1}{1 + RASR} \frac{1}{1 + AASR} \tag{4.3}$$

where RASR and AASR are the range and azimuth ambiguity-to-signal ratios. If these are both of order –20 dB, then γ_{AMB} = 0.98.

4.4.5.5 Summary of radar system error sources

Figure 4.16 shows the total error budget associated with the dominant error sources of a radar system, namely speckle, instrument noise and radiometric stability. The analysis represents a worst case scenario in which the uncertainty terms are set to the threshold requirement: the ENL is set to 64, instrument noise to –27 dB, and radiometric stability to 0.5 dB. With these settings, the Biomass system will meet the required accuracy. It is important to note that additional uncertainty sources have to be considered in the system evaluation and as outlined in the introduction to Subsection 4.4.5. As will be highlighted in Chapter 6, these include effects for which the signal can be compensated (e.g. soil moisture, topography). However, combination of different polarisations and the exploitation of multitemporal data will significantly reduce the speckle contribution, as discussed in Subsection 4.4.5.1. This is of major importance, since in the simplified scheme from which Fig. 4.16 was derived, speckle contributes over half the relative error.
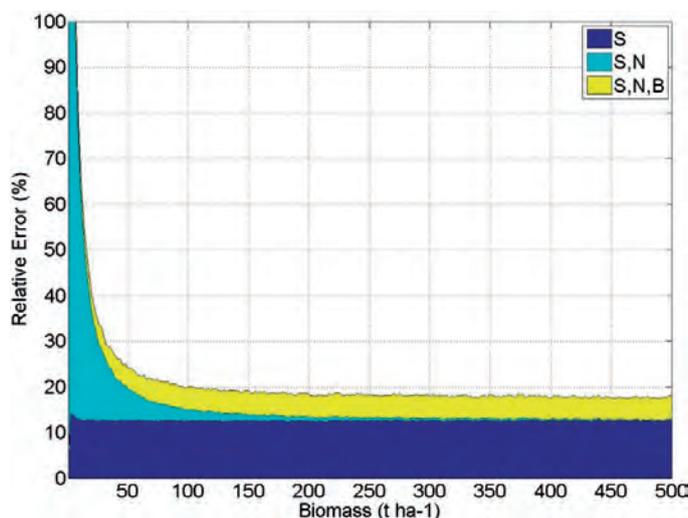
Figure 4.16. Impact of radar system error sources on the relative error of biomass retrieval against biomass under a simplified inversion scheme only using the HV channel. Error sources considered are Speckle (S) at 64-looks, instrument noise (N) at –27 dB and radiometric stability (B) of 0.5 dB. (ESA)

4.4.6 Geolocation Requirements

The requirement on geolocation accuracy is driven by the need to ensure that forest plots used for parameterisation and validation of the inversion scheme are accurately located within the scene. Forest plot networks (particularly in the Tropics) aim to sample at scales that are coarse enough to average out large local fluctuations in biomass due to large stems, thus reducing the variance of the *in situ* biomass estimates to acceptable levels. A stronger constraint is that plots need to be large enough to reduce the intrinsic uncertainty from speckle to acceptable levels, and indicates a minimum size of 4 ha, so that a geolocation accuracy of better than 25 m is sufficient.

4.4.7 Orbit/Mission Phases

The Biomass mission is envisaged as having two phases, which determine the orbit requirements:

— The nominal main mission phase will make repeated interferometric polarimetric observations to address both the major mission objectives and the secondary objectives.

— During a single tomographic phase of around 50 days or 3% of the total mission duration, tomographic measurements will be acquired with 10–12 spatial baselines and a revisit time of 1–4 days.

4.4.7.1 Nominal phase

A key driver in the orbit selection is the time sampling requirements needed for repeat-pass interferometry. Forest height inversion using PolInSAR requires the repeat interval to be short enough to maintain high temporal coherence between SAR acquisitions. Airborne experiments indicate that a time interval from 25–45 days is acceptable.

A second important driver in orbit selection is the ionosphere. The state of the ionosphere varies with position, time of day, day of the year, the solar cycle and magnetic conditions. Strong scintillations due to ionospheric irregularities occur throughout the auroral zones (especially within the electron precipitation boundary), and the post-sunset equatorial zone (local time later than approximately 19:30). The local time of the orbital node at the equator must be chosen to avoid this post-sunset scintillation hotspot. Although orbits closer to the dayside encounter increased mean ionospheric election densities because of the greater solar illumination, this creates little problem, since there are well-established methods to correct for the associated FR. Hence, a suitable orbit, which is also favourable from a satellite system perspective, would have a local time of the descending/ascending node around 06:00. Ionospheric simulations indicate that data acquired on both the ascending and descending tracks will then be usable.

A third requirement in the choice of orbit comes from the accuracy requirements of PolInSAR height inversion. In a single-baseline scenario, large baselines between acquisitions are advantageous as they help to compensate for errors introduced by temporal and other decorrelation sources. However, the maximum baseline is limited by the 6 MHz system bandwidth available at P-band because of range spectral decorrelation. The critical (horizontal) baseline Bc between successive acquisitions is given by:

$$B_c = \frac{\lambda}{2Rr_g \cos^2\theta} \tag{4.4}$$

where λ represents the wavelength, R the orbit height, r_g the ground range resolution and Θ the incidence angle. A baseline of about 40–60% of B_c provides an optimal compromise between the accuracy of forest height retrieval and range spectral decorrelation. The orbit control should be sufficient to avoid spectral decorrelation, requiring orbit maintenance within 10% of the critical baseline. The same orbit control requirements apply for the tomographic phase.

4.4.7.2 Tomographic phase

The tomographic phase orbit repeat cycle will be 1–4 days. The baseline between two successive orbit cycles will be $B_c/3$ at the equator, where B_c is given by Eq. 4.4. Assuming a vegetation layer 50–60 m high, the necessary number of passages for tomographic imaging is about 5–6 per site. More passages can be exploited to enhance system robustness against ionospheric disturbances.

→ SYSTEM CONCEPT

5.   System Concept

5.1   Introduction

This chapter provides the technical description of the Biomass mission, as derived from the preparatory activities in Phase-A, for implementation as an Earth Explorer in the frame of ESA's Living Planet Programme. It shows how candidate implementation concepts can respond to the scientific mission requirements defined in the previous chapters. The system description is based mainly on the results of the work performed during parallel Phase-A system studies by two industrial consortia (EADS Astrium Ltd., 2011 and Thales Alenia Space Italy, 2011). Two implementation concepts (A and B) are described, which provide options capable of meeting the mission requirements.

After an overview of the mission architecture and the proposed orbit (Sections 5.2 and 5.3), the space segment is described in detail (Section 5.4) followed by the launcher, ground segment and operations concepts (Sections 5.5, 5.6 and 5.7). The overall mission performance is summarised in Chapter 7.

5.2   Mission Architecture Overview

The main architectural elements of the Biomass mission are shown in Fig. 5.1. The space segment comprises a single spacecraft carrying a P-band SAR, operating in a near-polar, Sun-synchronous quasi-circular frozen orbit at an altitude of 637–666 km, depending on the different mission phases. The orbit is designed to enable repeat pass interferometric acquisitions throughout the mission's life and to minimise the impact of ionospheric disturbances.

The baseline Vega launcher will inject the satellite into its target orbit. Compatibility of the satellite with backup launchers such as Soyuz and Taurus II has also been ensured. The mission is designed to exploit acquisitions made at dawn/dusk, i.e. 06:00/18:00 local time (at the equator), to minimise the adverse influence of the ionosphere on the radar signal. The SAR data are delivered to the Kiruna ground station via an X-band downlink. Auxiliary data, which are required to quantify the characteristics of the propagation path of the radar signal, are used in the end-to-end system calibration and processing
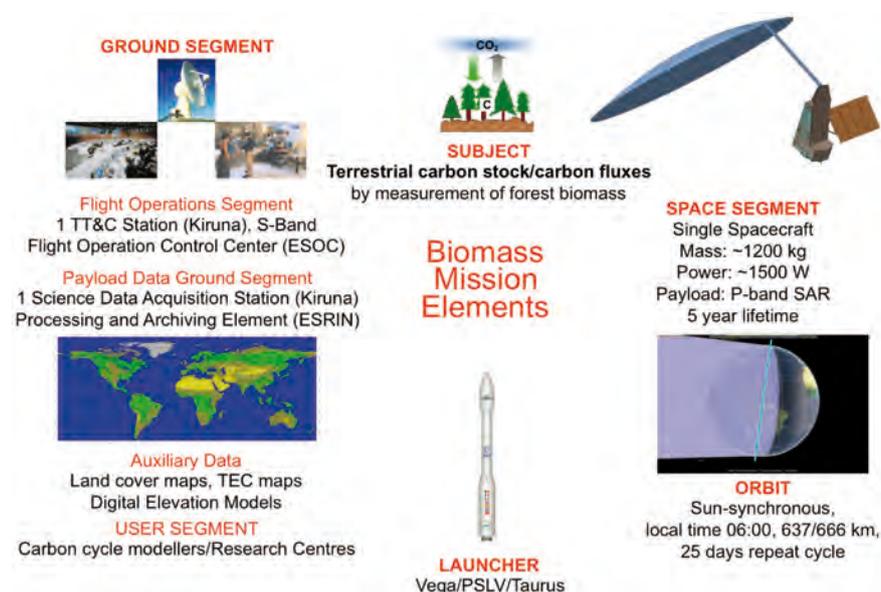
Figure 5.1. Biomass mission architecture.

Figure 5.2. Biomass mission phases for
Concept B.
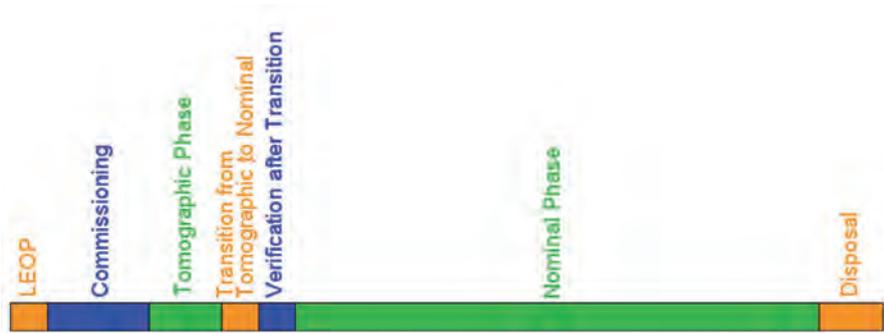
of the SAR data. The Biomass mission will last five years and comprise a short tomographic phase (~55 days) followed by the nominal operational phase, characterised by an orbit repeat period of 25 days.

The tomographic phase will be performed just after the end of commissioning phase, which will be carried out with the satellite flying in the nominal orbit or in the tomographic orbit, for Concept A or B respectively. Upon completion of the tomographic phase, the satellite will be transferred to the nominal orbit until the end of the mission when a deorbiting phase (satellite disposal) will take place, without requiring any fuel provision thanks to the low orbit.

Figure 5.2 shows the different mission phases for Concept B. The ground segment uses the generic Earth Explorer ground segment infrastructure and comprises:

— The Flight Operation Segment (FOS), which includes the Telemetry, Tracking and Command (TT&C) Ground Station and the Flight Operations Control Centre, and;

— The Payload Data Ground Segment (PDGS), which includes the Science Data Acquisition Station, the Processing and Archiving Element and the Mission Planning and Monitoring Element.

5.3   Mission Analysis and Orbit Selection

The Biomass mission will include two different phases: nominal and tomographic. The orbit Repeat Cycle (RC) for the nominal phase must be less than 45 days (threshold) with a goal of 25 days, whereas for the tomographic phase the RC will be 1–4 days. The choice of an RC goal of 25 days is driven by the need to minimise the temporal decorrelation in the acquisitions between successive cycles for the interferometric product generation. The tomographic phase is aimed at retrieving information on forest structure by exploiting tomographic acquisitions with a revisit time shorter than five days.

5.3.1 Single-baseline Interferometry

Sun-synchronous dawn/dusk orbits have been chosen for both mission phases, as summarised in Table 5.1. In order to minimise the ionospheric impact on data quality, the preferred local time for SAR acquisitions is 06:00, either at the ascending or descending node crossing. Orbit altitudes higher than 600 km have been selected, since at such altitudes the need for orbit maintenance manoeuvres is strongly reduced. The tomographic phase orbit is chosen at an altitude to minimise the fuel needed for the transition from the nominal orbit.

The orbit requirements can be subdivided into interferometric baseline requirements and orbit maintenance requirements. The interferometric baseline requirements are expressed in terms of a baseline B at the equator

	Concept A		Concept B	
	Nominal phase	Tomographic phase	Nominal phase	Tomographic phase
Orbits per day	14+17/25	14+2/3	14+19/25	14+3/4
Orbit altitude [km]	661.8	666.0	636.3	637.5
Local time	06:00 Ascending Node		06:00 Descending Node	
Critical Baseline, B_c [km]	4.867	4.860	4.762	4.785
Baseline, B [km]	2.920	1.620	2.857	1.595

Table 5.1. Candidate orbit characteristics for Concepts A and B.
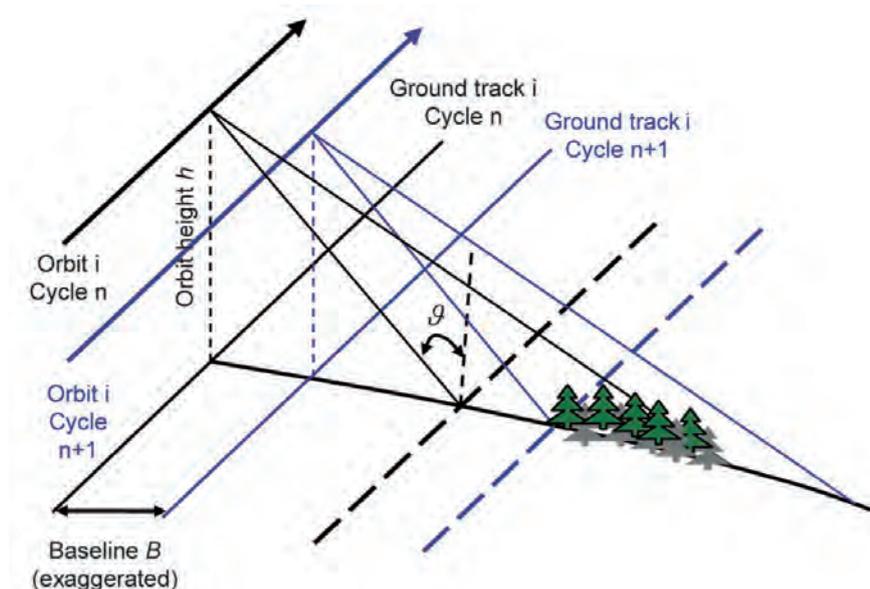
Figure 5.3. Observation geometry with interferometric baseline.

to be maintained between any orbit of cycle n and the corresponding orbit of cycle $n + 1$, as illustrated in Fig. 5.3. The baseline requirement is different for the nominal and the tomographic phases and is a function of the critical baseline B_c at the equator. In the nominal phase, the threshold requirement is for B to be less than 60% of B_c, with a goal of 40%. In the tomographic phase it is required that $B = B_c /3$.

The strategy for meeting the interferometric baseline requirement is based on the selection of an orbit with a 'controlled drift'. The amount of drift between successive orbital cycles is chosen to match the interferometric baseline requirement. In practice, the baseline is achieved by flying the satellite in an orbit where the altitude is a few metres higher or lower than that of the exact repeating orbit. Because of this small drift, the resulting orbit will have a quasi-repeat cycle of 25 days.

Figure 5.4 shows the repeat cycle vs. altitude. The green area refers to the tomographic phase, where two possible orbits with repeat cycle of three and four days are marked with dark-green circles. In order to reduce the fuel consumed for orbit changes, the difference in orbital altitude between the two phases of the mission must be very small (order of few km). The blue area in Fig. 5.4 refers to the nominal phase and the blue circles highlight the two orbits selected with a RC of 25 days. Table 5.1 lists the main orbit parameters. Figure 5.5 shows the geodetic altitude variation vs. latitude for the selected orbits, which has an impact on the payload and system design. The inclination is about ~97.9° for both concepts.

Figure 5.4. Repeat cycle vs. altitude. The circles represent the selected orbits.
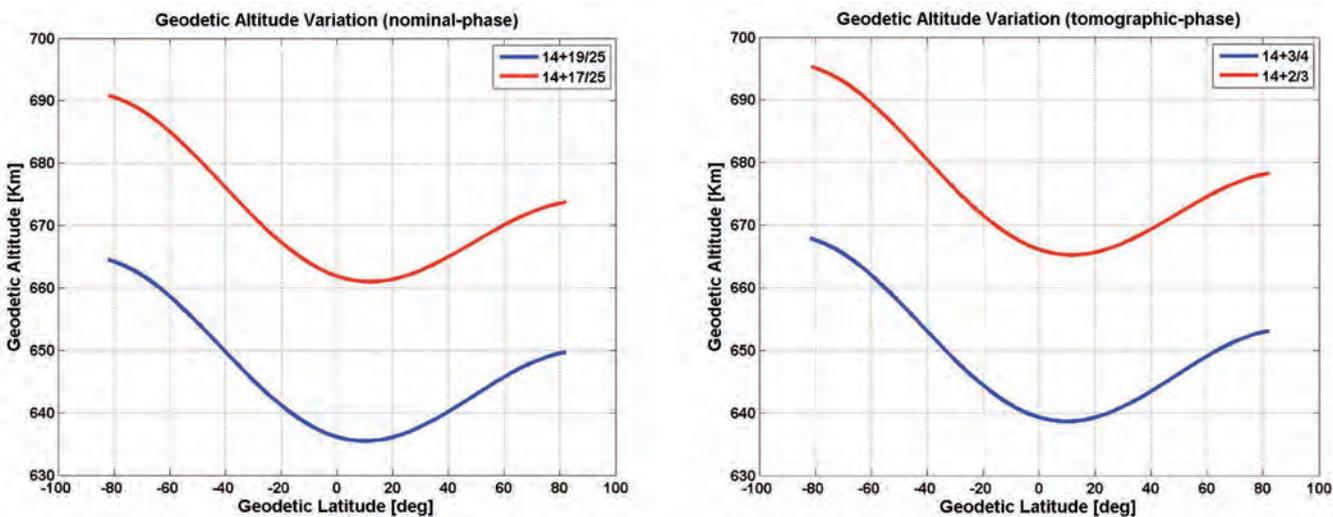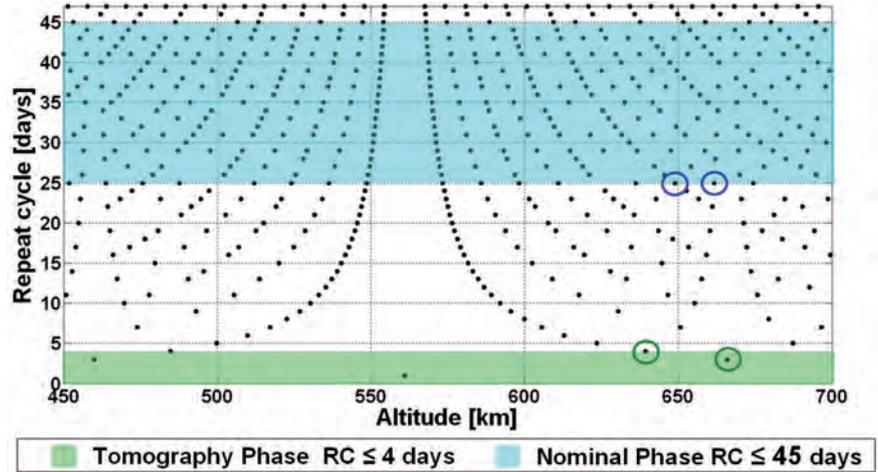
Figure 5.5. Geodetic altitude variation in nominal phase (left) and tomographic phase (right) for orbits selected for Concepts A and B.

The eclipses, for both concepts, are concentrated around the solstices and are a maximum of 19 minutes long. For Concept A they occur around the winter solstice and for Concept B around the summer solstice.

The selection of the RC depends on the SAR swath to achieve the Global Coverage (GC) of forested areas within six months. Figure 5.6 shows the relationship between RC and swath width in three different cases:

(a) GC achieved in one repeat cycle without orbital drift (black dots);

(b) GC achieved in six months with orbital drift (blue triangles);

(c) GC achieved in six months with orbital drift and interleaved mode (green squares).

Figure 5.6 shows how the orbital drift and interleaved sub-swath operations can be exploited to achieve the six-month GC requirement with the smallest swath and with a margin on the payload and/or orbit design. Case (b) allows the swath width to be relaxed with respect to case (a).

Both concepts adopt an interleaved mode of operation (Case (c)), which exploits the fact that two distinct requirements are imposed on RC ($\leq$ 25 days as goal and $\leq$ 45 days as threshold) and GC ($\leq$ six months). In this way, a smaller

swath of only about 50 km is sufficient to achieve a GC within six months with a RC = 25 days. This mode allows for the coverage to be obtained by switching from one sub-swath to the other by means of a spacecraft roll manoeuvre after a certain numbers of cycles.

A representation of the interleaved mode for the two concepts is shown in Fig. 5.7. While for Concept A, the GC requirement is achieved in 4 RC (i.e. 100 days), for concept B it is achieved in 7 RC (i.e. 175 days). Both concepts fulfil the GC requirement with a different swath overlap (i.e. Concept A achieves GC earlier while Concept B provides more interferometric acquisitions).

Figure 5.8 shows an example of the interleaved coverage pattern over the Amazonian forest for a 25-day RC orbit and a 60 km swath for Concept B. The coverage after three consecutive RC is shown in green, leaving gaps between the swaths (left). When the roll manoeuvre is performed the gaps are completely covered after four repeat cycles, as shown in red (right).
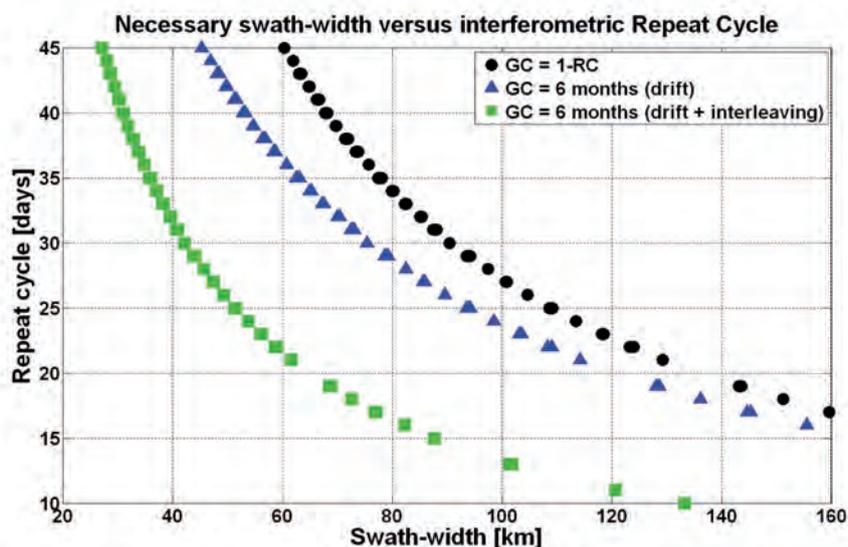
Figure 5.6. Repeat cycle vs. swath width.
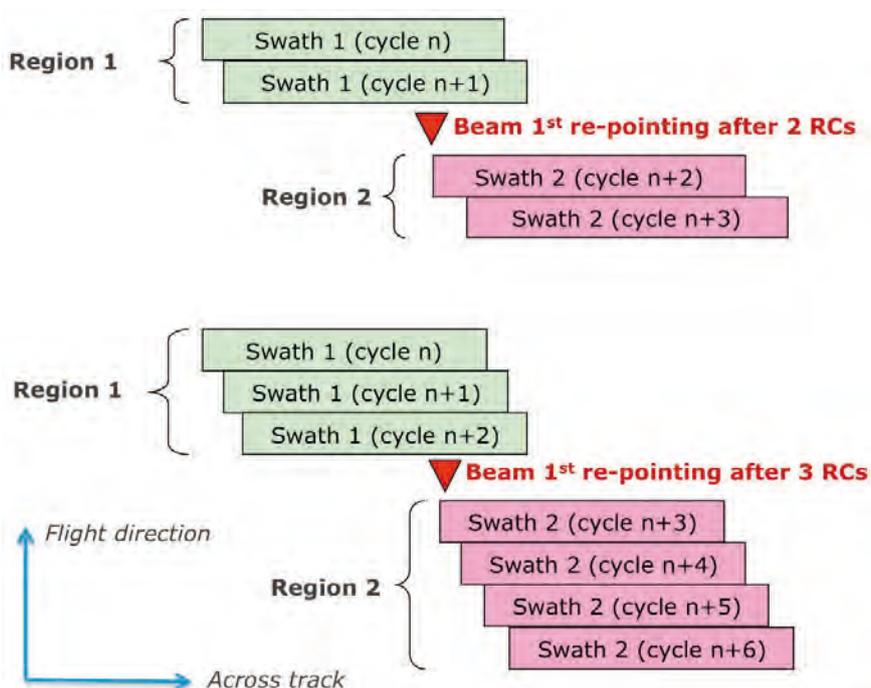
Figure 5.7. Interleaved acquisition approach for Concepts A (above) and B (below).

71
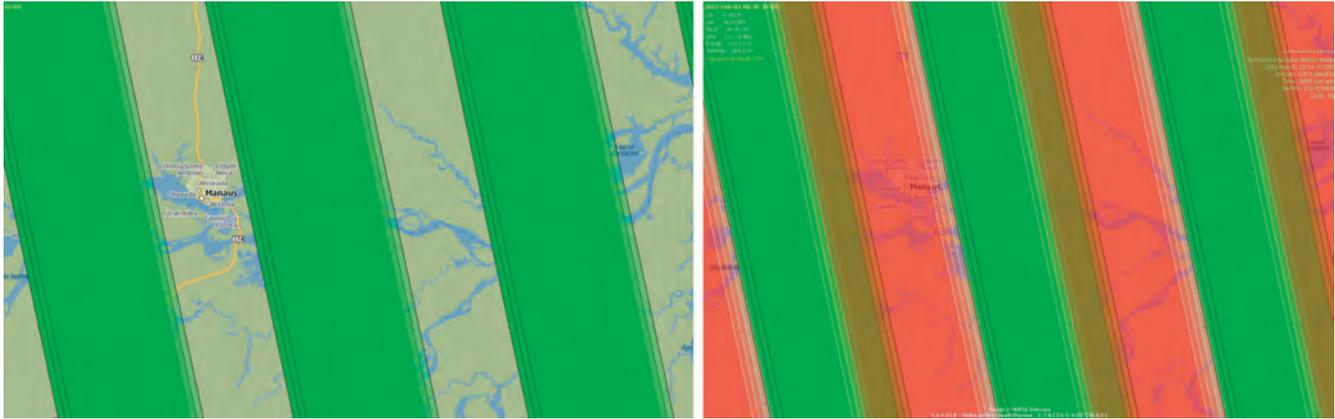
Figure 5.8. Representation of coverage over Amazonian forest with drifting orbit.

Figure 5.9. Repeat cycle vs. altitude. The circles represent selected orbits.
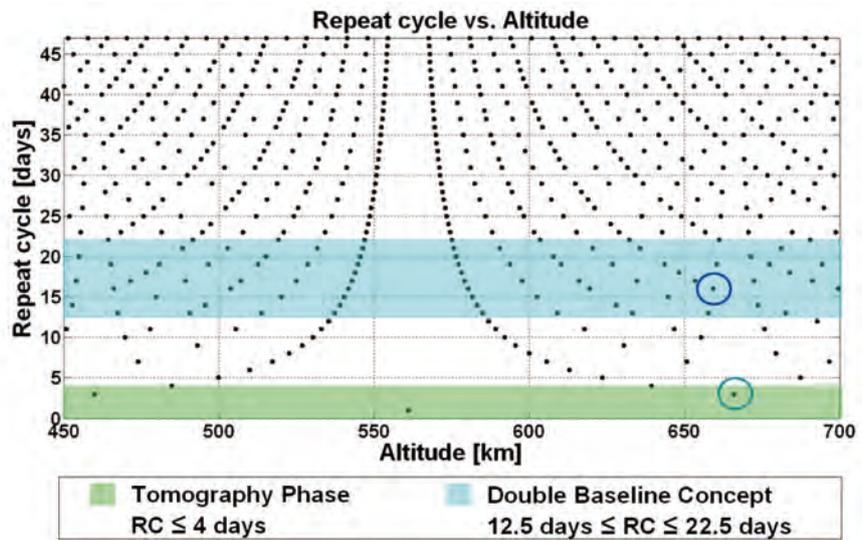
Orbit maintenance requirements in both nominal and tomographic phases stem from the interferometric acquisition requirements. The ground tracks must be maintained in a dead-band of ±10% and ±15% of the critical baseline during the nominal phase and tomographic phase, respectively. This corresponds to a ground track control of about ±350 m for the selected orbits.

The presence of a large antenna causes relatively rapid orbit decay and, as a result, small in-plane manoeuvres must be performed to maintain the nominal orbit. The frequency of manoeuvres is variable over the lifetime of the mission because of the varying solar activity and reaches a maximum of one manoeuvre every three days during periods of high solar activity.

The mission profile foresees a tomographic phase at the beginning of the mission's operational life with a revisit time of up to four days. The repeat cycle of the tomographic phase has been set equal to three days for Concept A and to four days for Concept B. The selected combinations of short repeat cycle and small swath (e.g. 60 km) allows coverage of the selected sites to be achieved.

5.3.2 Double-baseline Interferometry Option

The double-baseline interferometry option has been considered to provide two interferometric acquisitions with temporal decorrelation within the requirements in order to improve the retrieval accuracy during the nominal phase. By introducing a third swath, this option allows the interferometric
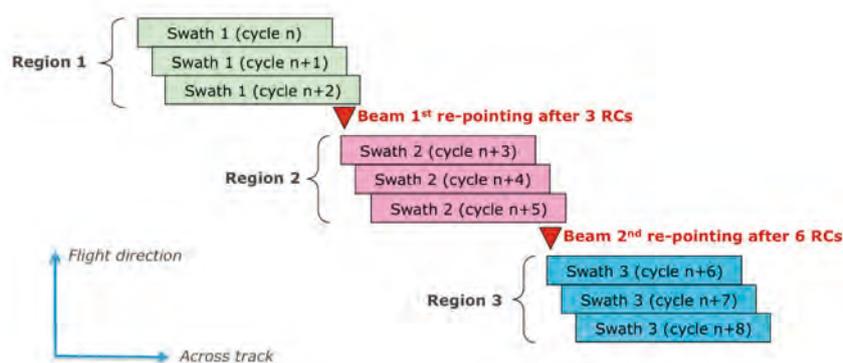
Figure 5.10. Double-baseline interferometry using three interleaved swaths with 16 days orbit repeat cycle.

	Angles
Boresight pointing to Swath 1	23.20°
Boresight pointing to Swath 2	26.37°
Boresight pointing to Swath 3	29.39°
First roll manoeuvre from Swath 1 to Swath 2	+3.17°
Second roll manoeuvre from Swath 2 to Swath 3	+3.02°
Third roll manoeuvre from Swath 3 to Swath 1	−6.19°

Table 5.2. Antenna boresight angles with respect to nadir.

acquisitions to be doubled. The option consists of a set of three acquisitions with a fixed baseline to retrieve the forest height, while the orbit RC is kept to a minimum to ensure good temporal coherence between acquisitions spaced by two repeat cycles.

For double-baseline interferometry, twice the orbit RC for the nominal phase must be less than 45 days (threshold) with a goal of 25 days. The light blue area in Fig. 5.9 indicates where the requirement is met (without exceeding the goal). The figure shows that an orbit with nominal altitude of 660 km and 16-day RC can be found (marked by a dark blue circle). For the tomographic phase, analogous considerations on the RC apply. The figure shows the identified three-day repeat orbit, marked with a dark green circle.

According to the baseline interleaved acquisition approach, three acquisitions are needed to meet the coverage requirement, as shown in Fig. 5.10. Each of the three swaths is imaged over three RCs before the satellite is rolled to observe the next one. The complete coverage is therefore achieved after nine RCs, i.e. in about five months. Table 5.2 summarises the antenna boresight pointing angles towards the three respective swaths and the required roll angles.

The orbit maintenance requirements for the double-baseline interferometric operation are similar to those of single-baseline interferometric operation.

5.4 Space Segment

5.4.1 Overview

The Biomass space segment consists of a single satellite carrying the P-band (435 MHz, i.e. ~69 cm wavelength) SAR. The satellite configuration is strongly constrained by the accommodation of the very large reflector antenna inside the Vega launcher. This large antenna must be folded for launch and deployed in orbit to form a stable aperture throughout the mission's life. The industrial teams investigated different antenna types and folding concepts and both consortia selected a reflector-based concept, which is described below.

Following the satellite platform description in Subsection 5.4.2, the payload concept is described in Subsection 5.4.3, and complemented with the description of the overall satellite subsystems and budgets in Subsections 5.4.4 and 5.4.5.

5.4.2 Satellite Configuration

Concepts A and B are based on a Large Deployable mesh Reflector (LDR) antenna system consisting of a deployable arm and an unfurlable reflector with a projected aperture of approximately 12 m. These large reflectors are produced for mobile telecom satellites in the USA, where the main manufacturers are Northrop Grumman (NG) and Harris Corp. (HC), see Fig. 5.11.

HC base their design on the flight-proven ACeS reflector that uses a proprietary folding rib design. NG provide the AstroMesh LDR, which has, or will have, flight heritage from many satellite projects including Inmarsat-4 and Alphasat. For Biomass, the NG design is also based on a flight-proven concept. Concept A configuration is compatible with both LDR antennas, while Concept B is compatible only with the NG antenna. Each deployment boom is specifically designed for the Biomass concepts.

The Reflector Deployment Hardware (RDH) includes all hardware associated with the hold-down, release and deployment of the LDR, including the deployment boom. Commands in the form of motor drive levels and release
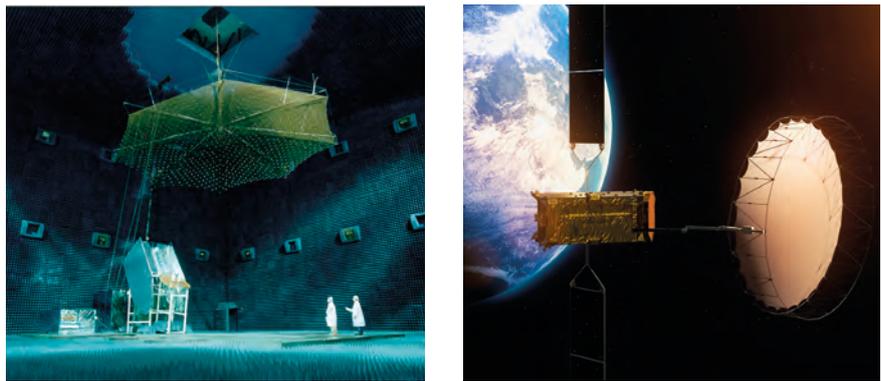
Figure 5.11. LDR deployed configurations. Left: ACeS 12 m reflector, Harris Corp; Right: Alphasat 9 m reflector, Northrop Grumman. (ESA)

Figure 5.12. LDR in stowed configuration Left: Harris Corp.; Right: Northrop Grumman.

signals will be provided directly from the platform to the RDH for release and staged deployment. Examples of stowed configurations for both LDRs are illustrated in Fig. 5.12.

The overall configuration of Concept A is shown in Figs. 5.13 and 5.14 for the HC and NG LDRs, respectively. The LDR is illuminated by a 3×2 array of cavity-backed circular microstrip radiators, which is mounted onto to the –Y wall of the satellite at the lower end (not visible in the figures).

The overall configuration of Concept B, based only on NG LDR, is shown in Fig. 5.15. Here, the LDR is illuminated by a deployable 2×2 array of microstrip patch radiators, which is mounted on the spacecraft top face by means of a supporting structure.

For both concepts, the boresight direction of the LDR is orientated such that the SAR acquires images at the right of the satellite ground track, with its pointing controlled by the roll angle of the spacecraft for imaging Swath 1 or
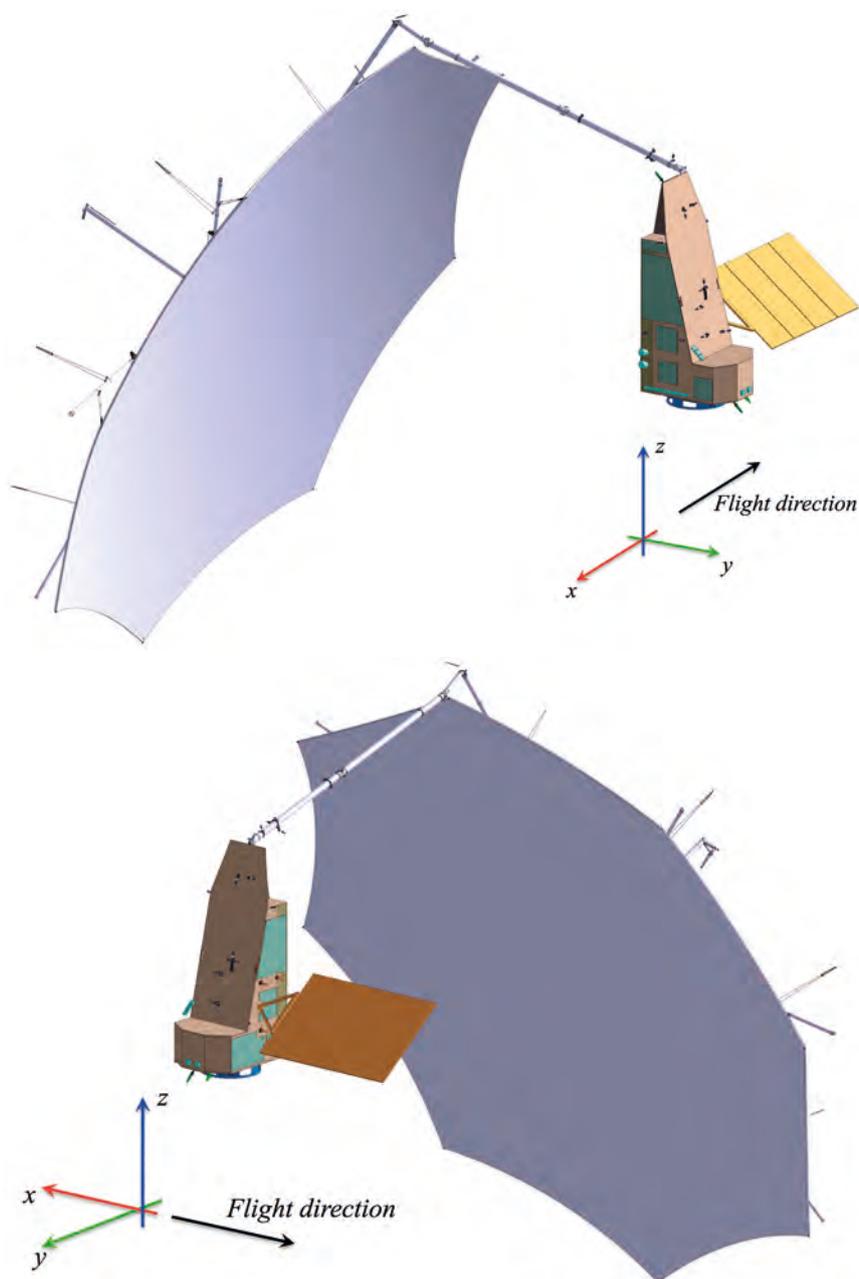
Figure 5.13. Concept A: deployed configuration views with the Harris Corp. LDR.

Figure 5.14. Concept A: deployed configuration views with the NG LDR.
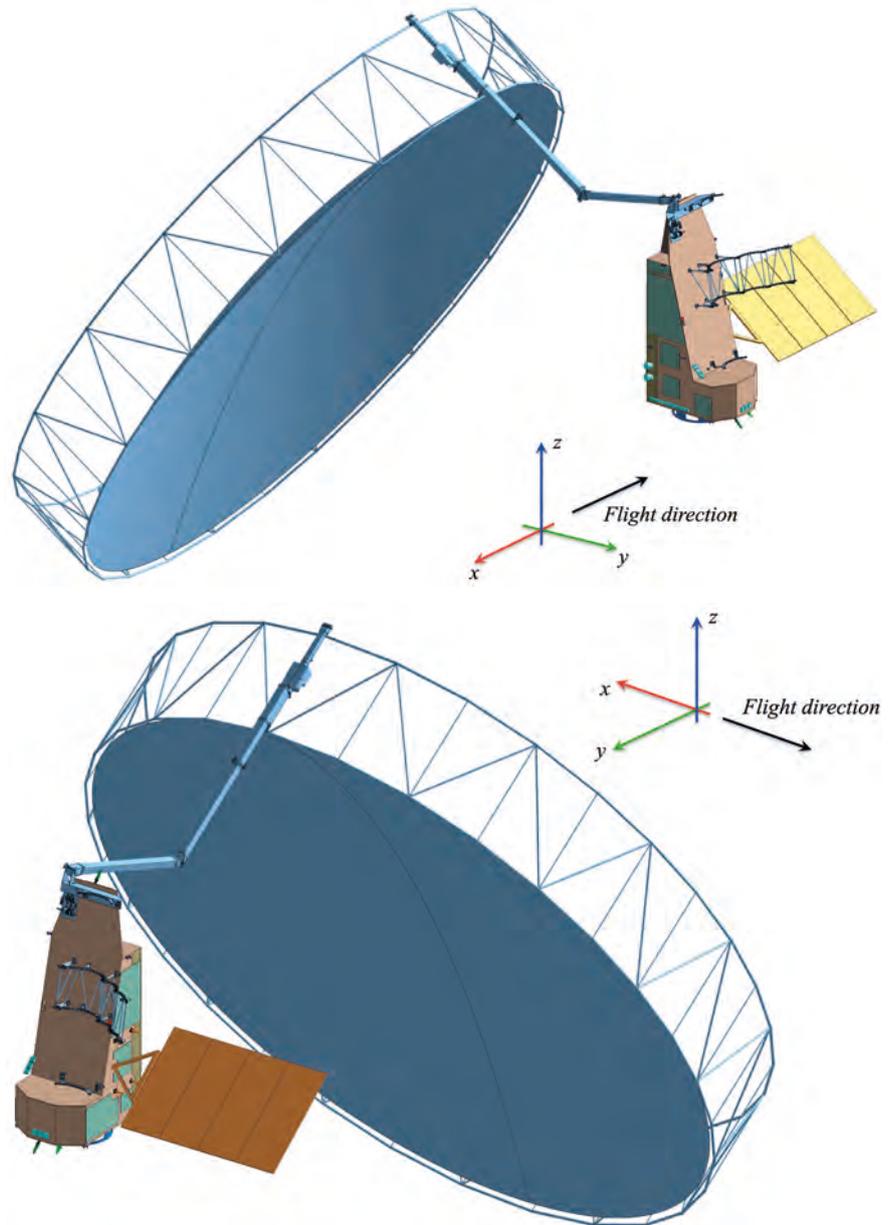
Swath 2 (Fig. 5.7). The stowed configurations are shown in Figs. 5.36, 5.37 and 5.38 of Section 5.5, respectively.

5.4.3 Payload

5.4.3.1 Overview

The Biomass payload is a P-band SAR with full polarimetric and multipass interferometric capabilities. Following the trade-offs performed during the Phase-A with different payload concepts the reflector-based single-beam concept was selected by both industrial consortia for its performance, simplicity and compatibility with the Vega launcher. Other concepts considered included:

— single-beam SAR with a passive, planar (deployable) antenna (single stripmap swath).

— SAR with dual phase-centre (planar) antenna capability in receive (single stripmap swath).

— a switchable dual-beam SAR with a deployable reflector antenna (interleaved stripmap operation).

Commercial Off-The-Shelf (COTS) deployable mesh reflector products from NG and HC have been selected as candidates due to their technological maturity. Consequently, Concepts A and B are rather similar, with differences only in the subsystems.

5.4.3.2 Observation Principles

The SAR will operate in a stripmap mode with a swath illuminated by a single antenna beam, i.e. an imaging configuration similar to that of the ERS-1/2 SAR. Global coverage is obtained by the interleaved stripmap operations among two or three complementary swaths as described in Subsections 5.3.1 and 5.3.2, respectively. The beam re-pointing is performed through a roll manoeuvre of the spacecraft, as there is ample time over the poles for such operations. At most, a roll manoeuvre is required every two RCs (i.e. 50 days). This solution using the spacecraft rolling was preferred over the possibility of electronic
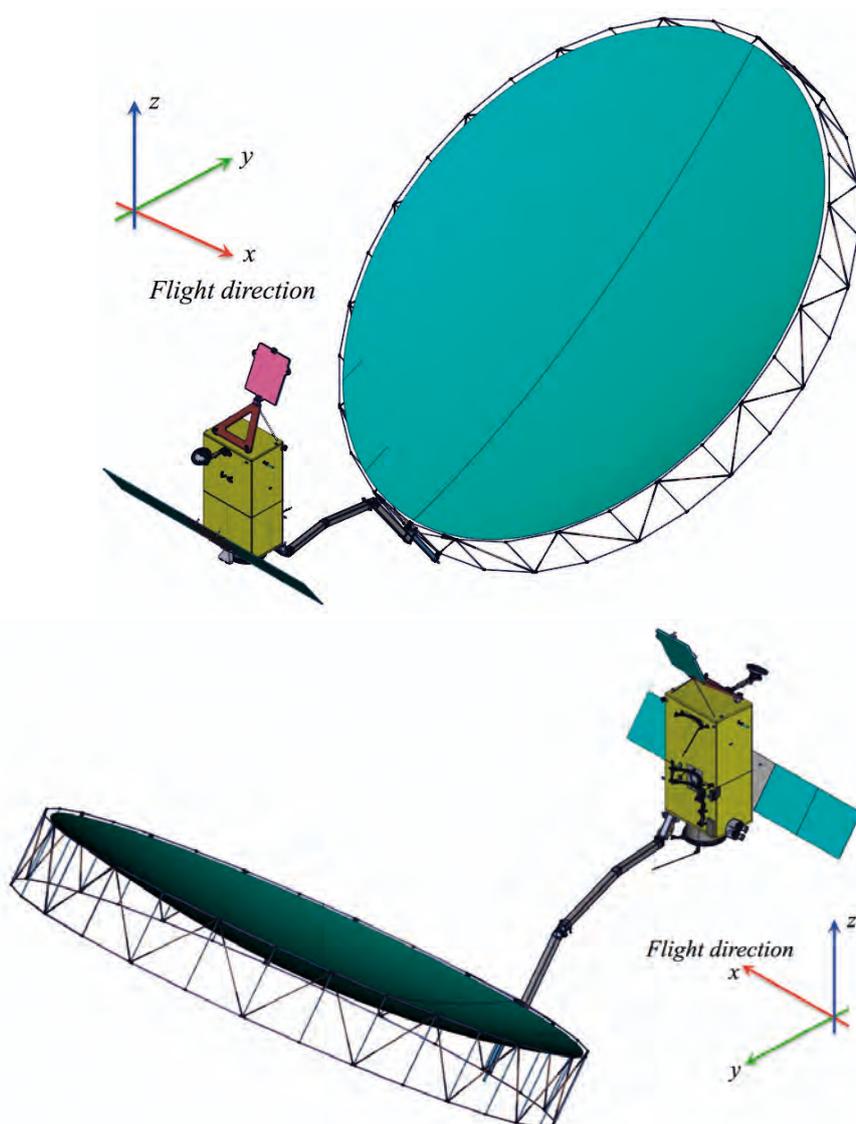
Figure 5.15. Concept B: deployed configuration views with the Northrop Grumman LDR.

Table 5.3 Biomass SAR technical requirements.

Parameter	Requirement
Instrument type	P-band synthetic aperture radar (SAR)
Centre frequency	435 MHz (P-band)
Bandwidth	≤6 MHz (ITU allocation)
Incidence angle (near)	Threshold: 23°; Target: 25°
Polarisation	Fully polarimetric
Cross-polarisation ratio	≤−25 dB (threshold); ≤30 dB (goal)
Spatial resolution	≤60 m (across-track) × 50 m (along-track) (≥4 looks)
Swath	≥50–60 km
Noise equivalent σ^0	Threshold: ≤−27 dB; Target: ≤−30 dB
Total ambiguity ratio	≥20 dB
Radiometric stability	0.5 dB RMS
Absolute radiometric bias	1.0 dB
Dynamic range	30 dB

Table 5.4. ITU Power Flux Density constraints for a spaceborne P-band SAR.

	Value [W/(m^2 Hz)]
Maximum peak PFD on Earth surface from antenna main-lobe	−140 dB
Maximum mean PFD on Earth surface from antenna main-lobe	−150 dB
Maximum mean PFD on Earth surface from first antenna side-lobe	−170 dB

Figure 5.16. Timing sequences for full-polarimetric mode (Tx=Transmit; Rx=Receive).
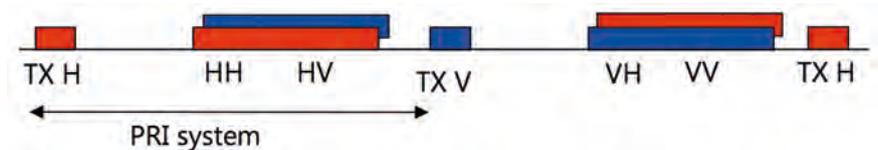
beam switching due to its simplicity. Both concepts are able to accommodate the single-baseline or double-baseline interferometry operation, as shown later in Section 7.2. Table 5.3 summarises the Biomass SAR technical requirements.

A secondary spectrum allocation for active sensing from space exists between 432 to 438 MHz. The ITU constraints (defined in ITU-R RS.1260-1, 2003) on a spaceborne P-band SAR can be divided into technical and operational constraints. The technical constraint for a spaceborne P-band SAR is put on the emitted signal Power Flux Density (PFD) on the Earth surface, as listed in Table 5.4. The 6 MHz bandwidth limits the range resolution at the 25° incidence angle to ~60 m, whereas the PFD limits the maximum peak and average emitted power by the radar. Both constraints have to be met by the system design and therefore limit the trade-off space for optimising the performance. The operational constraints for Biomass are elaborated in Section 5.7.

The Biomass SAR will operate in full-polarimetric mode. This requires that the polarisation is alternated between H and V at each transmitted pulse (Tx-H and Tx-V), which is a linearly Frequency-Modulated (FM) 'chirp'. The echo signals in both polarisations are received simultaneously during the inter-pulse period (Rx-H and Rx-V), as shown by the timing sequence in Fig. 5.16.

5.4.3.2.1 Instrument Concept A

Figure 5.17 shows the instrument block diagram. All the electronics units are fully redundant with the exception of the circulator unit and the feed array (redundant units are not shown in the diagram). The instrument comprises:

— Antenna subsystem, composed of an LDR together with the feed-array
— Circulator unit
— Transmit unit
— Receive unit
— Central Electronics Unit (CEU)
— Instrument Control Unit (ICU)
— Instrument power unit.

A single-sideband transmit pulse (linearly FM) is generated, up-converted, amplified and sent to the polarisation switch in the CEU. The polarisation switch, operating at low power level, toggles between the V and H transmit channels at each Pulse Repetition Interval (PRI), as illustrated in Fig. 5.16. The modulated transmit pulse is then amplified in the corresponding polarisation channel in the transmit unit, routed to the circulator unit and radiated through the feed array. The High Power Amplifier (HPA) is made of three Solid-State Power Amplifiers (SSPAs) in parallel, each delivering a peak RF power of 120 W with 10% duty cycle and Pulse Repetition Frequency (PRF) of 3000 Hz on average. Because of the concentration of high peak power after the power combiner, multipaction must be avoided by an appropriate circuit design of the radar front-end part between the HPA output and the power divider in the feed array.

In reception, the echo signals (V and H) are routed through the circulator unit to the receive unit, where they are filtered and amplified. They are then routed to the CEU for further processing including analogue-to-digital/down-conversion, data compression and packetisation. The Low Noise Amplifiers (LNA) are protected by a limiter at their inputs against possible strong

Figure 5.17. Instrument block diagram of Concept A.
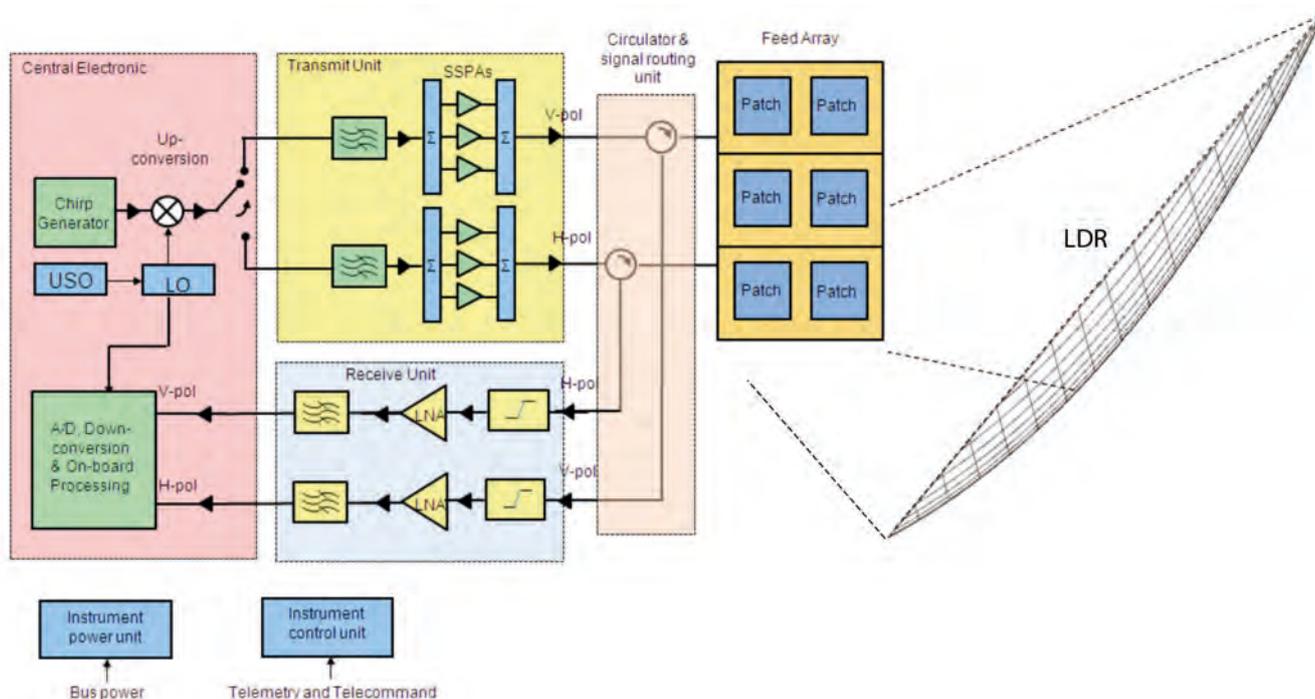
interference signals emitted by the ground-based Space Objects Tracking Radars (SOTR) and wind profilers.

The ICU receives commands and information from the onboard computer. It sets up the instrument operation parameters, controls image acquisitions, relays telemetry information and manages fault/limit checking and takes action where appropriate. It also maintains the instrument time reference, synchronised to an onboard Global Positioning System (GPS) receiver. The instrument power unit converts the 28 V DC unregulated power supply from the platform to appropriately conditioned DC power for all the electronics units as well as provides the heater power for the instrument thermal control. The instrument mass (including margin) is 202 kg with the NG reflector, and 275 kg with the HC reflector. The maximum required power is 463 W for both reflector options and the maximum data rate is 115 Mbit/s.

5.4.3.2.2 Instrument Concept B

Figure 5.18 shows the instrument block diagram. All the electronics units are fully redundant with the exception of the Beam Forming Network (BFN) and the feed array (redundant units not shown in the block diagram). The instrument comprises:

— Antenna subsystem, composed of an LDR together with the feed array
— Transmit/Receive Units (TRU)
— Transmit/Receive BFN
— Central Electronics Unit
— Instrument Control Unit
— Instrument Power Unit

In this concept, the linearly FM transmit pulse is split in the BFN and routed to two parallel transmit chains and amplified. A polarisation switch is placed after the HPA in order to select the transmit polarisation in each of the TRUs, which delivers a peak RF power of 120 W with 12% duty cycle and a PRF of 3050 Hz on average. The two pairs of radiators (upper and lower) are fed separately by the respective TRUs and illuminate the reflector. Splitting the

Figure 5.18. Instrument diagram of Concept B.
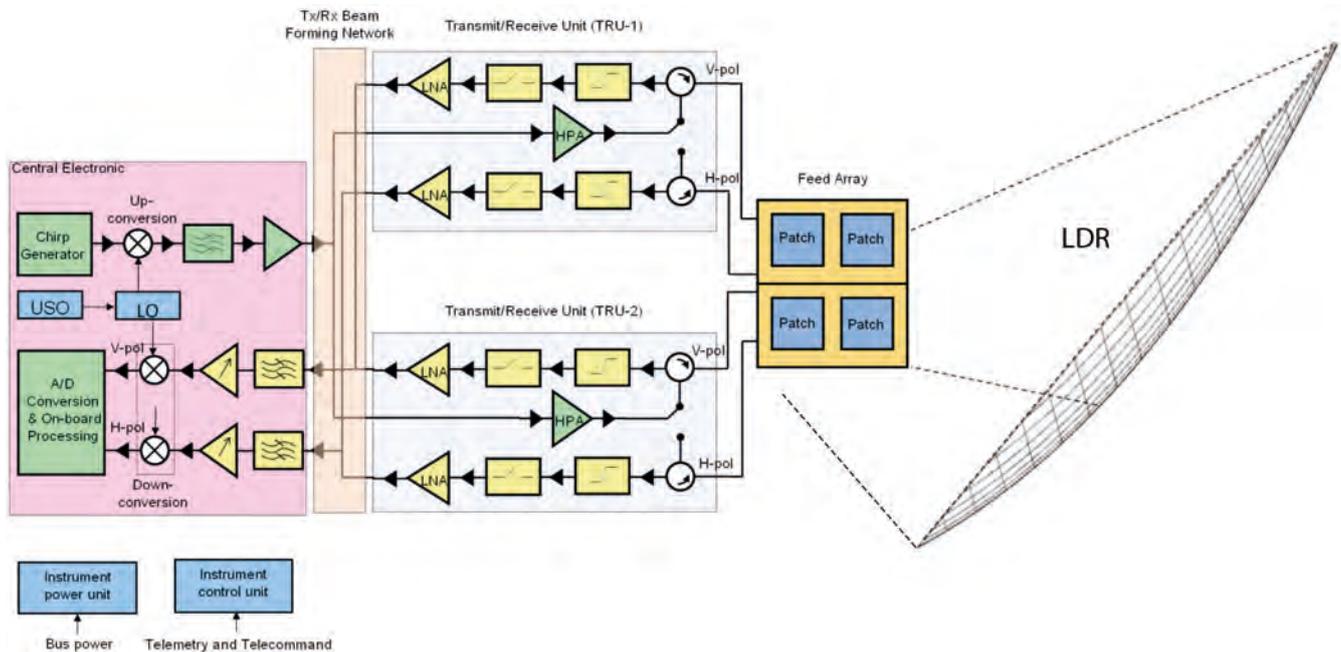
power into two parallel transmit channels helps avoid potential multipaction problems.

In reception, the echo signals from the two radiator pairs are filtered and amplified in four parallel receive chains (TRU-1: V and H and TRU-2: V and H). Those are recombined in the BFN to form the V and H signals and routed to the CEU. They are finally down-converted and digitised, followed by data compression and packetizing. As any amplitude or phase imbalances between the channels would affect the beam pattern, the channel stability is ensured by appropriate design of the TRUs, i.e. of the HPAs and of the LNAs. An additional phase equalisation can be foreseen for compensating relative phase drifts due to aging (included in the CEU). A limiter and an isolation switch at the LNA input protect it against possible strong interference signals. The instrument mass (including margin) is 206 kg. The maximum required DC power is 221 W and the maximum data rate is 117 Mbit/s.

5.4.3.3 Instrument subsystems

5.4.3.3.1 Antenna subsystem

As introduced in Subsection 5.4.2, both concepts use a single-offset reflector antenna system consisting of a feed array and a large deployable mesh reflector with a circular projected aperture diameter of ~11.5 m or ~12 m. The reflector geometry for the two concepts is summarised in Fig. 5.19 and Table 5.5.

The selected single offset reflector geometry is characterised by a relatively short focal length, which was dictated by the need to minimise the distance between the spacecraft and the reflector, thereby reducing the moment of
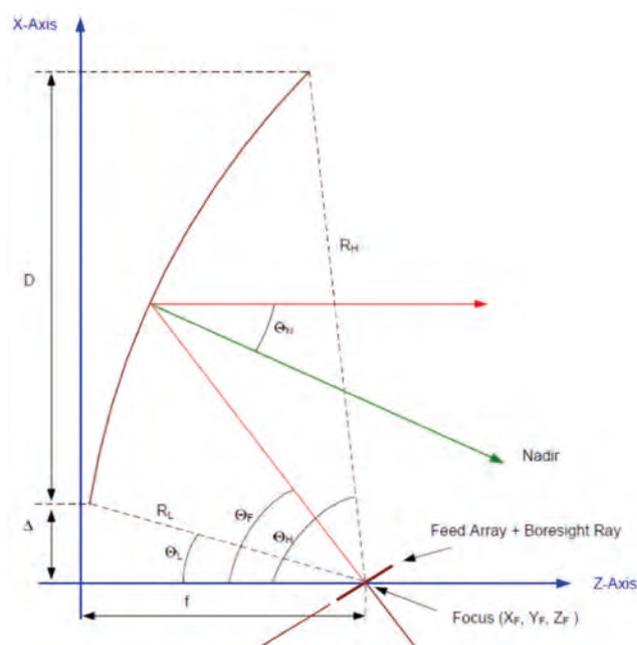
Figure 5.19. Reflector geometry.

	Concept A		Concept B
Reflector supplier	NG	HC	NG
Projected aperture diameter [m]	12.0	12.0	11.5
Clearance $\varDelta$ [m]	3.0	2.1	4.9
Focal length D [m]	6.3	7.8	7.5
Feed offset angle ϑ_F [°]	68.0	52.3	65.7

Table 5.5. Geometrical parameters for the NG and HC reflectors of Concepts A and B.

inertia of the satellite. Because of this short focal length, the reflector, when illuminated by a linearly polarised spherical wave from the feed, would produce a significant cross-polar radiation (12–15 dB below the co-polar peak gain) in its main beam, which has the form of a difference pattern (narrow null along the principal elevation plane). To comply with the cross-polarisation ratio requirement (see Table 5.3), a pre-compensation technique must then be implemented at the level of the feed.

The design of the feed subsystem is driven by the following requirements:

— provide optimum reflector illumination for achieving the required main beam gain and shapes;

— control the secondary antenna pattern side lobe levels in order to achieve the required SAR ambiguity performance;

— provide cross-polarisation pre-compensation, as noted above;

— ensure multipaction-free operation.

The feed array makes use of stacked circular patches for Concept A and stacked square patches for Concept B, as shown in Fig. 5.20. Stacking of the patches is necessary to achieve a sufficient bandwidth at the level of the feed subsystem (>10 MHz). The feed assembly is made of multilayer sandwich structure, consisting of metallised carbon or Kevlar-fibre-reinforced plastic sheets and Kevlar honeycomb or Rohacell foam core, thus lightweight. Concept A uses three pairs of radiators with tapered excitation in elevation, whereas only two pairs of radiators with equal excitation are used for Concept B. The secondary radiation pattern is similar for both concepts.

The cross-polarisation pre-compensation is implemented pair-wise on radiators in the azimuth direction. This is achieved by adding a controlled level of cross-polarisation radiation in antiphase with the feed (Valle 2011, Valle 2012). Figure 5.21 (left) shows an example of the pre-compensation circuit

Figure 5.20. Feed array consisting of 3×2 stacked circular patches and body-mounted on the satellite for Concept A (left); Deployable feed array consisting of 2×2 stacked square patches on a support structure for Concept B (right).
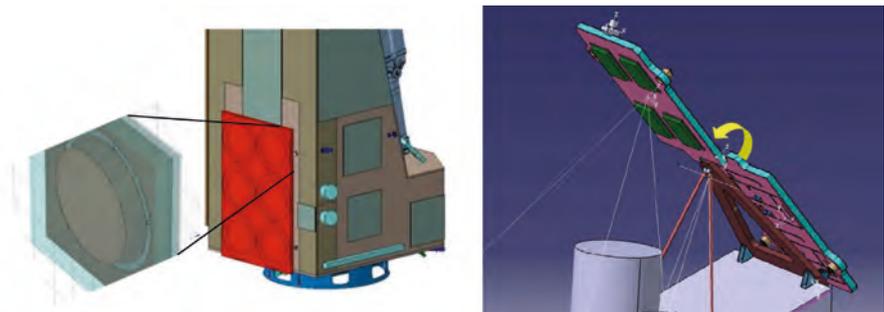
Figure 5.21. A breadboard of the cross-polarisation pre-compensation circuit for a radiator pair (left); 2×2 feed-array breadboard of Concept B under pattern measurements (right).
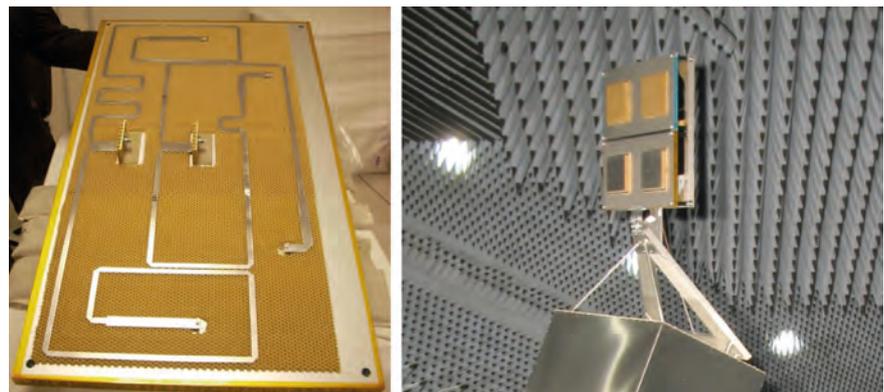
integrated in the backside of a radiator pair, which allows achieving the goal cross-polarisation level of −30 dB (see Section 7.2).

Figure 5.21 (right) depicts a 2×2 feed array breadboard of Concept B under pattern measurements (approximately 1×1 m). A mock-up of the feed support structure and of the satellite was added to characterise their effects on the primary radiation pattern, e.g. multipath effects.

5.4.3.3.2 Radio frequency and digital electronics

The radio frequency (RF) and digital electronics of the Biomass SAR instrument use well-established technologies thanks to the low radar frequency (UHF band) and narrow system bandwidth (6 MHz). Nevertheless, the combination of the low frequency and high peak RF power increases the risk of multipaction. Therefore, a number of specific risk-retirement activities were undertaken and special measures were implemented in the radar front-end design for mitigating possible risks. The following equipment and components are subject to risk of multipaction:

— Transmit unit, in particular the HPA
— High power circulators/isolators
— High power RF switches
— Power dividers and combiners
— Coaxial cables
— RF transitions and connectors.

Multipaction tests as well as electromagnetic simulations were performed on representative sub-assemblies and their limits were determined, which led to improved designs. Figure 5.22 depicts some examples of those sub-assemblies and components that were subjected to the investigation.

The transmit unit consists of a single SSPA or of paralleled SSPA, each with a peak output power of 120 W with duty cycle of 10–12%. Good technological heritage for the low frequency HPA exists from, for example, the Italian SHARAD radar instrument of the Mars Reconnaissance Orbiter mission. A dedicated technology assessment study showed that existing silicon transistor technology, in particular the Laterally Diffused Metal Oxide Semiconductor (LDMOS) transistors, meet the requirements (see Fig. 5.22 left). Radiation tests, in particular using heavy ion bombardments, demonstrated that the transistors can survive the specified mission life. A more attractive alternative is offered by the newly developed gallium nitride (GaN) transistor technology (see Fig. 5.22 centre), which is able to operate at higher power level and is more radiation tolerant. Such high-power GaN transistors are becoming available in Europe from United Monolithic Semiconductor and are considered in the on-going SSPA pre-developments together with some alternative Japanese GaN devices.

The CEU comprises the direct digital pulse synthesis and up-conversion to the radar frequency in transmit, and the down-conversion, analogue-

Figure 5.22. Examples of sub-assemblies and components subjected to multipaction tests: (Left) LDMOS (silicon) power stage with 120 W output; (Centre) Gallium nitride power stage with 120 W output; (Right) High power isolator.
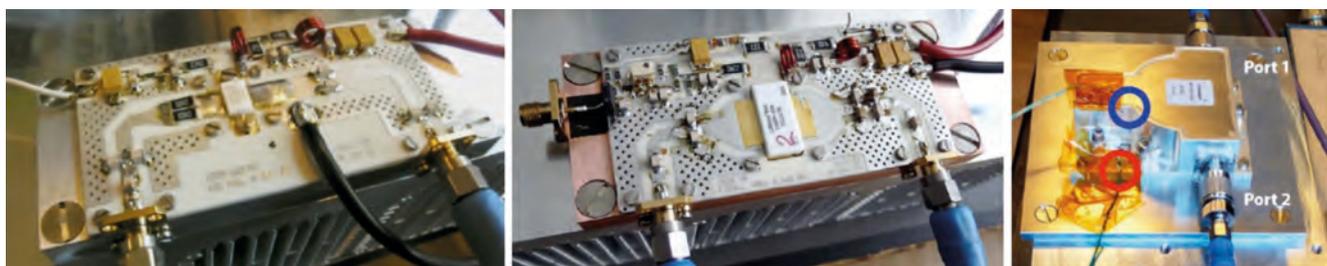
to-digital conversion and data compression/conditioning in reception. In transmission, the single-sideband linearly FM pulse with 6 MHz bandwidth is synthesised directly at an intermediate frequency e.g. 60 MHz, followed by an up-conversion using a local oscillator signal at 375 MHz. This frequency plan enables a good suppression of the undesired sideband product by the sideband filter after the up-conversion. In reception, the same local oscillator signal is used to down-convert the echo signals to 60 MHz. They are then digitised and further down-converted digitally to the baseband. Alternatively, the P-band echo signals can directly be digitised down to the baseband using the sub-sampling technique. This would enable to skip the analogue down-conversion, thus simplifying the CEU design. Thanks to extensive heritage from various past and in-orbit SAR missions, as well as to the low frequency and bandwidth, no criticality has been identified for the CEU development. The industrial teams have selected conservative designs to avoid development risks.

All the radar electronics equipment is accommodated on the inner faces of the payload module panels. In particular, the SSPAs are placed behind the panel that faces the cold space through the reflector mesh, and thus acts as a radiator, in close proximity to the feed array. The remaining equipment is distributed so as to facilitate integration and to balance the mass distribution.

5.4.3.4. Instrument characterisation and calibration

Achievement of the radiometric performance requirements is ensured by:

— On ground: accurate characterisation of the complete Biomass payload over the complete temperature range as predicted in orbit.

— In orbit: internal calibration, external calibration and accurate pointing knowledge (Subsection 5.4.5).
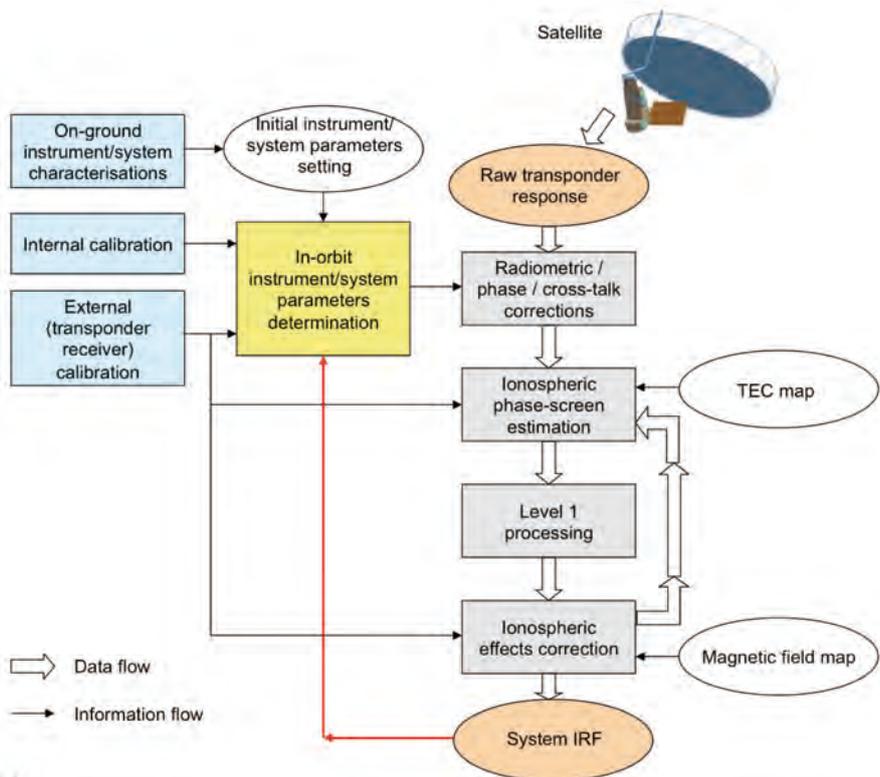
Figure 5.23. Biomass calibration approach involving transponders.

The Biomass mission calls for an ensemble of instrument/system characterisation methods to overcome the uncertainties associated with the characteristics of the propagation medium, namely the presence of the ionosphere. Several calibration approaches are available for polarimetric systems, based on the properties of distributed targets and calibration devices (Yueh et al., 1990; Freeman, 1992; Quegan, 1994). However, those approaches cannot be applied directly in the presence of the ionosphere, and need to be addressed carefully at P-band (Freeman, 2004; Xu et al., 2004).

Assuming that the Biomass system is sufficiently stable, which is generally the case for spaceborne SARs, scene-by-scene updates of the system errors are unlikely to be required. Instead, it should be sufficient to measure the system errors (i.e. channel imbalance and cross-talks) at a limited number of instrumented calibration sites (e.g. transponders and corner reflectors) and then apply these estimated errors to multiple scenes. This is the proposed approach for the system calibration. The same sites will also be used for absolute calibration to yield accurate values of the backscattering coefficient (radiometric performance).

Figure 5.23 illustrates such a calibration approach involving transponders, which comprises the following functions:

— Left:

 – On-ground instrument/system characterisations.
 – Internal calibration.
 – External calibration (transponder receiver calibration).

— Centre:

 – In-orbit instrument/system parameters determination.

— Right:

 – Radiometric/phase/cross-talk correction of raw data.
 – Ionospheric phase-screen estimation using global ionospheric TEC map (see Subsection 6.3.5).
 – Level-1 processing.
 – Ionospheric effects correction using magnetic field map (see Subsections 6.2.1 and 6.2.2).

All of the functions on the right-hand side together form the data processing chain of the Biomass system before the Level-2 product generation. During the external calibration, transponder echoes are processed to generate the system Impulse Response Function (IRF).

5.4.3.4.1 On-ground instrument/system characterisations

The complete transmission and receive chains are characterised prior to launch over the temperature range as predicted in orbit. These measurements also include characterisation of the complete internal calibration subsystem, which will monitor any transfer function variations in the radar electronics in orbit. An exception is made for the antenna subsystem, for which a combination of feed array measurements and theoretical prediction of the secondary radiation pattern is used. This approach has been adopted after a careful analysis of different antenna verification methods in the frame of a dedicated study conducted by ESA's Coordinated Antenna Measurement Facility at the Technical University of Denmark.

A direct measurement of the complete antenna subsystem, including both the reflector, feed array and deployment boom, would require that a

new dedicated facility capable of accommodating the very large Biomass reflector system is developed. Technical complexities associated with such an approach and limited accuracy, which is predicted, led to the rejection of the direct characterisation method. The adopted approach makes use of stepwise characterisations of:

— Feed array primary pattern including the effects of the satellite body and any supporting structure if applicable (see the example picture in Fig. 5.21 right).

— Deployed reflector geometry (including the deployment boom) and its shape, and its uncertainty through repeated deployments and measurements.

Those two sets of measurements are then combined to predict the secondary radiation pattern of the reflector system. This approach has been successfully demonstrated by the numerous mobile telecom satellite missions in orbit that are operating at L- and S-band with the LDRs, thus in the more demanding cases of considerably shorter wavelengths than for Biomass. The in-orbit verification of the antenna pattern will be performed using transponder measurements (external calibration).

The instrument/system parameters as determined on ground are stored and used as initial setting for error corrections and data processing (Initial instrument/system parameters setting in Fig. 5.23).

5.4.3.4.2 Internal calibration

The internal calibration subsystem permanently monitors the transfer function variations of the complete radar electronics with high temporal resolution through the measurements of:

— The SSPA/HPA output RF power level through an attenuator.

— The transmit pulse waveform through a calibration loop.

— The receiver chain transfer function using dedicated calibration pulses through a calibration loop.

— The system noise in the absence of transmit pulse.

It, however, excludes the antenna subsystem, which is covered by the external calibration. Power and gain variations of the radar electronics due to temperature excursions along the orbit and changing solar illumination over the seasons, and due to aging are determined (yellow box in Fig. 5.23). The system noise measurement is used for the noise subtraction (part of the ground processing) in order to remove any biases in the σ^0 estimates. Considerable heritage exists in Europe for achieving high calibration accuracy for spaceborne SARs. This heritage is applied for the design of the instrument internal calibration subsystem.

5.4.3.4.3 External calibration

The external calibration complements the system calibration through an end-to-end characterisation of the complete radar measurement chain using external targets. Its purposes are to:

— Verify/characterise the two-dimensional antenna gain for both V and H polarisations.

— Verify/characterise the beam pointing of the Biomass satellite.

— Verify/characterise the channel imbalance.

— Verify/characterise the cross-polar radiation level, i.e. the system cross-talk.

— Verify/characterise the system IRF.

— Verify/characterise the ambiguity performance.

— Provide direct measurements of FR and propagation/phase-delays due to the ionospheric layer.

— Verify the assumptions made on of ionospheric effects.

— Verify the algorithms used to correct/compensate ionospheric effects.

Being the first spaceborne mission to operate in P-band, Biomass presents a number of novel aspects. Firstly, the long wavelength poses new challenges for the design of calibration devices to be deployed on the ground because of the large antenna size that would be required. Secondly, the ionospheric layers introduce calibration uncertainties owing to the spatially and temporally varying propagation medium between the radar and the target scenes.

The three major impacts on the SAR observations are: (1) propagation delays; (2) signal scintillation at high latitudes; and (3) FR. The linear component of the propagation delays in azimuth and the last two effects need to be corrected in the process of the external calibration for the biomass retrieval, which will be performed on the ground as part of the overall radiometric and phase calibrations of the complex image products, using ionospheric phase-screen estimation and exploiting the full set of polarimetric measurements. Two types of targets are used for the external calibration:

— Point targets with known radar cross-section such as active transponders and corner reflectors.

— Distributed natural targets with well-characterised radar cross-section such as stable ice sheets and well-developed forests.

The primary point targets for the Biomass external calibration are the active transponders. The following specific functionalities are foreseen for the transponders:

— A time delay to avoid coupling between the receive and transmit chains.

— Dual-polarisation channels with high isolation to calibrate the polarimetric system.

— Receivers with high sensitivity to measure polarisation (Faraday) rotation and propagation/phase-delays due to the ionosphere (lowest box on the left-hand side in Fig. 5.23).

— Satellite tracking in azimuth to maintain high polarisation isolation and sensitivity.

— Transmission chains with polarisation flexibilities such as V-only and H-only.

— A collocated GNSS receiver to measure TEC in the vicinity of the radar wave propagation path.

The transponder antenna aperture will be as large as possible to reduce the multipath effects. A diameter from a minimum of 2 m up to 6 m is needed, depending on the performance requirements. A dedicated transponder design was part of Phase-A. A set of transponders will be placed over an equatorial region, more precisely at the magnetic equator (see green line in Fig. 5.24), where, for the Biomass orbit, both scintillation and FR are negligible, thus enabling an accurate external calibration.

A further set of transponders will be placed at a higher latitude to validate the correction algorithms for the ionospheric effects. An important aim of the external calibration using transponders is the verification of the antenna gain pattern, which cannot be characterised adequately on the ground. Taking advantage of the slowly drifting orbit, the complete two-dimensional pattern characterisation is possible with measurements performed over several orbit repeat cycles. If corner reflectors such as trihedrals are used, they should have a sufficiently high radar cross-section to achieve sufficient signal-to-noise ratio. At P-band, this translates to targets with a minimum dimension of 6–8 m.

Inclusion of a receiver function in the transponder (bottom box on the left side of Fig. 5.23) enables direct measurements of the FR and propagation delays (i.e. phase-shifts) on a pulse-by-pulse basis, thus providing an estimate of those ionospheric effects. This information is used in the Biomass processing chain for ionospheric corrections (ionospheric phase-screen estimation and ionospheric effects correction functions in Fig. 5.23).

As indicated above, a set of transponders will be located in a region of low FR (e.g. see Fig. 5.24), ideally at the magnetic equator, which would greatly simplify removal of the ionospheric effects. These provide reference measurements for the most accurate external calibration of the Biomass system. Those subsystems not covered by the internal calibration (e.g. antenna subsystem) are then characterised and added to the system parameter settings after removal of any ionospheric effects (centre box in Fig.5.23). In particular, the channel imbalance and polarisation cross-talks are critical performance parameters for the Biomass system, needed to correct ionospheric effects everywhere, not just where there are transponders. Finally, an end-to-end

Figure 5.24. Main magnetic field inclination – magnetic equator in green. (US/UK World Magnetic Model, *http://ngdc.noaa.gov/geomag/WMM*)
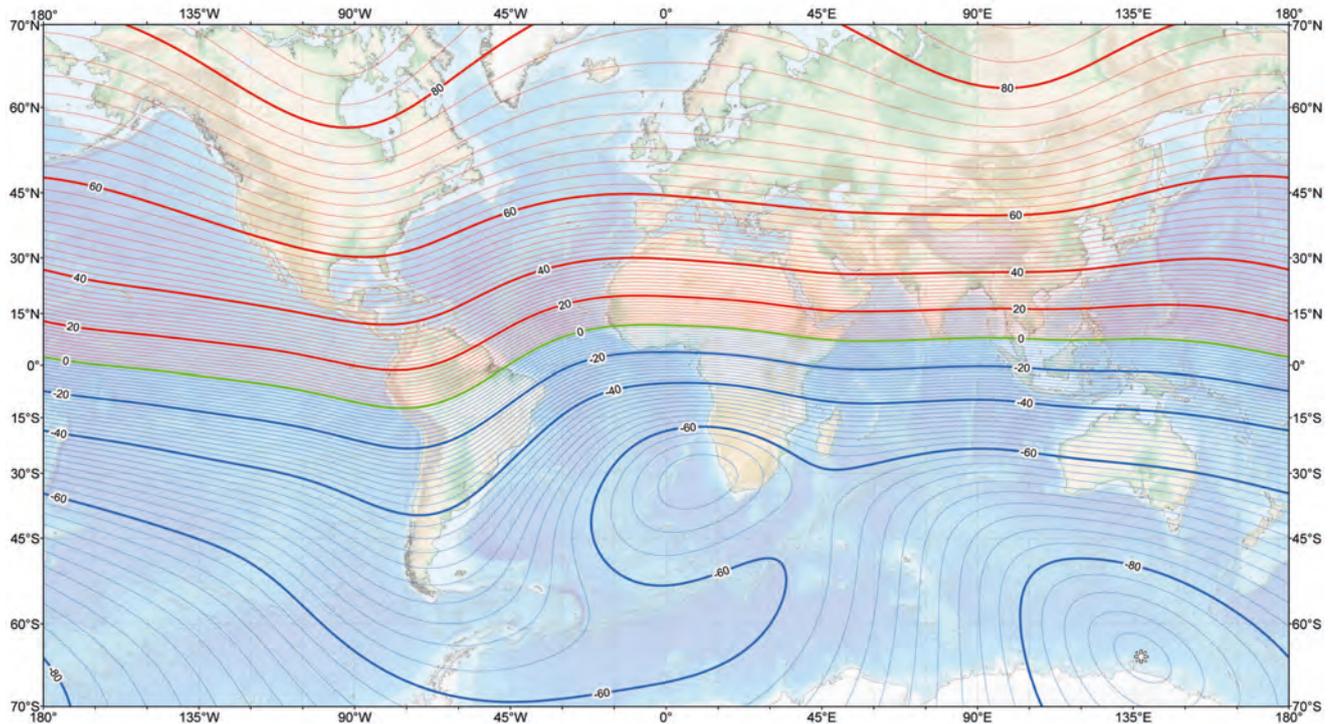
measurement of the system IRF provides the validation of the Biomass performance (right side of Fig. 5.23). Any residual errors observed in the system IRF are used to further improve the knowledge of the system parameters (red arrow in Fig. 5.23).

Another set of transponders at high-latitudes will be used to assess any variation of cross-talk and channel imbalance with latitude. The same calibration procedure as the one described above will be applied in order to characterise any orbit position dependent gain variation of the antenna subsystem. A number of iterations between the system IRF processing and instrument/system parameters determination may be required (loop represented by the red arrow) to achieve accurate calibration.

5.4.4 Platform

5.4.4.1 Overview

The two proposed concepts are very similar in many aspects as they rely on the same reflector class. This drives the satellite configuration, calling for special attention to the areas of attitude control, structural design and launcher accommodation. The platform subsystems are now outlined, placing emphasis on these areas.

5.4.4.2 Structure

The need to accommodate the LDR within the limited volume available under the Vega launcher fairing drives the Biomass mechanical design. The platform structure has been configured to maximise the internal volume available for platform equipment and to accommodate the LDR, the SAR feed array and the solar array. In addition, the external panels must accommodate the deployment mechanism of the reflector.

For Concept A the structure is H-shaped and is made of lightweight aluminium composite panels for all shear walls, floors and external walls, with a 1194-mm aluminium Launch Vehicle Adapter (LVA). The H-shaped core section consists of a central Y wall and four XY shear walls. These five walls are attached to the LVA through the lower floor at six equispaced points via aluminium interface brackets. The central Y wall and four XY shear walls support the large inclined Payload Interface Panel (PIP), which is the main mounting interface for the LDR. The XY shear walls in particular support the PIP along its full length, and the +XY shear wall is extended to support an extension of the PIP that supports the boom assembly when stowed. The use of a single panel for mounting the LDR offers the possibility of dismounting and of providing the panel to the LDR supplier (or the instrument prime contractor) for pre-integration before being reintegrated as a major assembly to the structure, thereby offering the flexibility of full modularity (also for Concept B). The propellant tanks are mounted inside the H structure.

The torsional rigidity of the structure is ensured by four XZ intermediate floors. These are spaced to provide support to the solar array Hold Down and Release Mechanisms (HDRM) on the –X side of the spacecraft. The central shear wall, ±XY shear walls, lower floor, XZ intermediate floors and LVA are shown in Fig. 5.25.

The external structure consists of the PIP, –Y external walls, two X external walls, the +Y external walls, the +YZ floor and the upper floors. The nominal orientation of the spacecraft when in its operational orbit is such that the –Y and X external walls are suitable radiator areas. Therefore, the majority of the dissipating units that require dedicated radiator areas for thermal control will be positioned on these walls. Fig. 5.26 shows the external structural panels.

For Concept B, the structure is based on the classic concept of primary and secondary structures complemented by the tertiary structure for mounting/

Figure 5.25. Concept A structure primary core (−Y view).
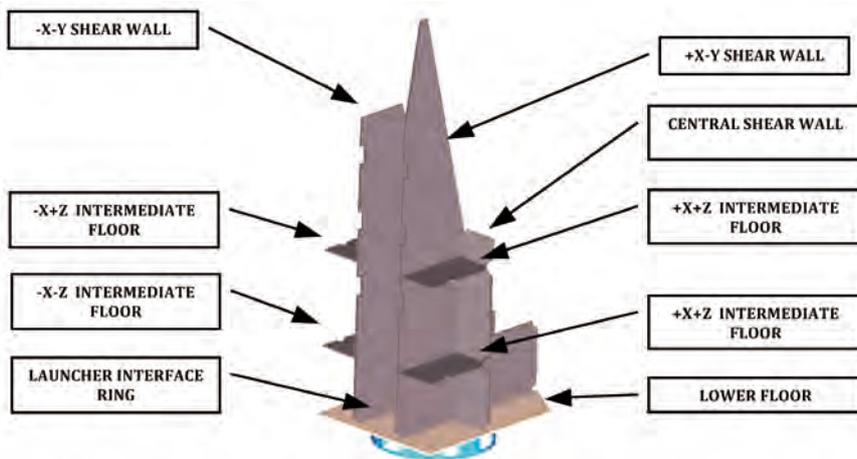
Figure 5.26. Concept A structure external panels (+Y view).
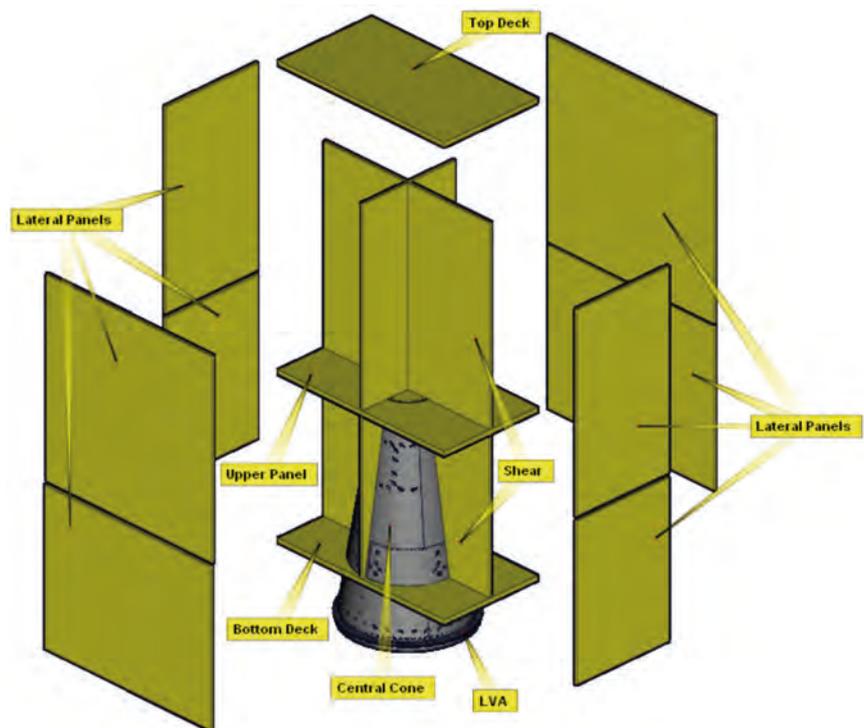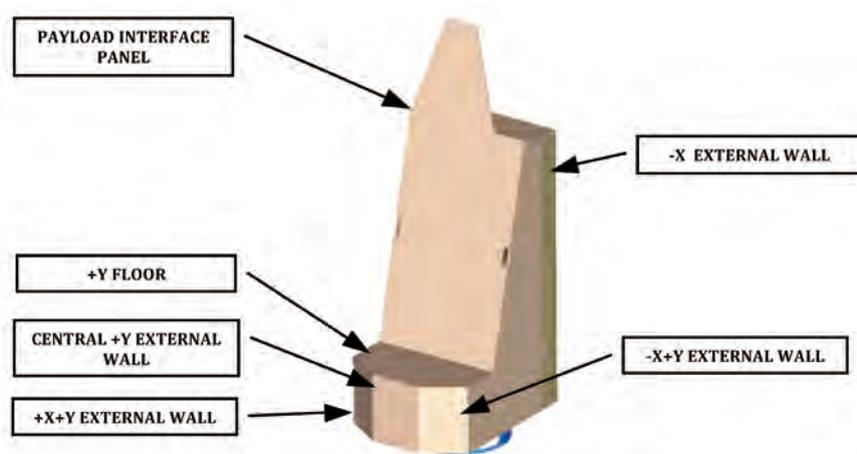
Figure 5.27. Concept B structure overview.

interfacing some particular items at bus level (see Fig. 5.27). The primary structure represents the backbone of the satellite and is the major contributor to the lateral and axial overall stiffness. Within this functional scheme the assembly composed of the LVA ring, the central cone and the four shear webs plays a crucial role:

— The central cone has the main function to carry the structural loads generated during launch and to accommodate the propulsion tank.

— On the lower side of the cone, the LVA conical section interfaces with the launch vehicle and the clamp-band system.

— The shear panels connect the lateral panels to the central cone and provide the necessary support.

— The upper panel provides the necessary stiffness as well as the local load carrying capability.

The lateral panels of the platform are the main elements of the secondary structure. These parts sustain the structural loads generated by the equipment masses, by the forces/moments at the appendages' interfaces and by the acoustic pressure during the liftoff and the transonic part of the launch. They directly transfer the loads to the primary structure and cooperate with the primary structure to achieve the overall dynamic behaviour (lateral and torsional stiffness). The tertiary structure is composed of items specifically designed to hold equipment or assembly interfaces and by generic support/fixation items for the equipment, harnesses and piping.

For both concepts, the satellite structure technology is standard, since only aluminium or Carbon Fibre Reinforced Plastic (CFRP) sandwich panels and standard attachments are used.

Dynamics analyses of the structure flexible modes, including the FEM models of the LDR, have been carried out for the stowed and deployed configurations of both concepts. This data provides an insight into the criticality of each normal mode regarding the loads resulting from dynamic excitation of the spacecraft. The results reported refer to the NG case of Concept A, but similar results apply to Concept B.

The stiffness of the stowed system has been assessed over a frequency range of 0–120 Hz and the normal modes, effective mass and inertia have been identified. These analyses confirm significant modes occurring around 19 Hz and 26 Hz. The axial mode is compliant with the basic frequency requirements for both launchers and with the requirement of 15% margin.

For the deployed configuration the open loop frequency response shows, as expected, a critical first flexible mode occurring between 0.3 Hz and 0.4 Hz. This impacts the tranquilisation time after slew manoeuvres and in general requires proper design and analysis of the attitude controller, as shown later.

5.4.4.3 Mechanisms

The most complex mechanisms are those included in the deployable reflector and providing for the hold-down functionality in the stowed configuration, the release of the stowed reflector assembly and its actual deployment. For both candidate solutions (NG and HC LDRs) the RDH includes minor modification of the flight proven design, driven by the compatibility of the specific satellite configuration with the launcher fairing. The modifications affect the number and/or length of the deployment boom sections and are part of the normal adaptation of the LDR product to meet the specific mission constraints. Since this will not alter the structural/thermal/electrical design of the RDH, no delta qualification campaign is foreseen.

Both concepts make use of a solar array HDRM to keep the solar array in the stowed position during launch and release it for deployment. After deployment a specific mechanism rotates the array to achieve the final fixed cant angle. For all these mechanisms reuse of existing flight-proven design 'as is' or with minor modifications have been considered.

Because of the specific configuration issues, Concept B requires additional mechanisms for the deployment of the X-band isoflux antenna and of the antenna feed array panel. Also in these cases flight-proven solutions can be reused and no criticalities have been identified.

5.4.4.4 Thermal control

The main function of the thermal control subsystem is to guarantee operating and non-operating temperature ranges for all satellite components according to each specific requirement for all the mission phases. The Biomass thermal control is based on a passive design supported by heater lines for specific equipment requiring heating power to remain above their minimum temperature limits during all operating modes. Inside the platform enclosure, a classical thermal control concept is suitable for the majority of the equipment. This is based on:

— High emissivity coatings for structural parts and equipment housings to enhance radiative heat exchanges.

— Thermal doublers to spread heat from the high power density equipment and/or to improve the conductive coupling between some of the units.

— Depending on the concept, heat pipes to connect high dissipative units (SAR transmit/receive unit and central electronics, modulators) to their respective radiators.

— Whenever possible, radiators placed under the most dissipative equipment.

— Heater lines controlled by thermistors for the colder phases.

In addition, the battery and the propulsion module require a specific thermal control based on low emissivity coatings or blankets to provide radiative isolation from the enclosure. The propulsion module is conductively decoupled from the structure. Heater lines controlled by thermistors are provided for cold conditions. Each of the externally mounted equipment has its own dedicated thermal control. Thermal decoupling of these elements from the platform is achieved with the use of isolating washers or low conductive mounts and multilayer insulation blankets. Passive means (coatings and blankets) are used for most of these appendages.

Specific attention is required for the thermal control of the antenna feed assembly in order to minimise thermal gradients and associated thermo-mechanical distortion that would affect the alignment between the feed and the LDR. In Concept A the feed panel is body mounted on the –Y panel, which, during nominal operation, is always in shadow. To achieve acceptable operating temperatures of the feed, high dissipative units are mounted on the rear side of the panel. In Concept B the deployable feed assembly is thermally decoupled from the platform and its thermal control is achieved via passive means using multilayer insulation) and heaters to maintain the temperature within acceptable limits during non-operating conditions.

For both concepts, the radiators required for platform and payload equipment cover an area of about 4.4 m^2.

5.4.4.5 Electrical architecture

The overall system electrical architecture is similar to most Low Earth Orbit (LEO) spacecraft and is composed of the following subsystems and equipment:

— Command and Data Handling Subsystem (CDHS), including the OBC, for primary spacecraft command and control, and dedicated platform and payload command-and-control MIL-1553B data buses and Remote Interface Unit (RIU), catering for payload-specific interfaces and non-MIL-1553B platform equipment interfaces.

— Power Subsystem, including the Power Conditioning and Distribution Unit (PCDU), solar array, battery and heaters.

— Tracking, Telemetry and Command (TT&C) subsystem, including the S-band transponders, for real-time command, telemetry and ranging and the S-band antennas.

— Attitude and Orbit Control System (AOCS).

— Payload Data Handling and Transmission (PDHT) subsystem, including the Solid-State Mass Memory (SSMM) for storage of payload data, auxiliary data and platform telemetry and the X-band data downlink for high data rate downlink system.

— SAR payload Instrument Control Unit (ICU), to control payload and interfaces to OBC and SSMM.

The system electrical architecture is illustrated in Fig. 5.28. The primary power, generated by the solar array and stored in and retrieved from the battery, is distributed to the main bus users by the PCDU via individually switchable latching current elements.

 The OBC acts as the command and control centre of the entire satellite and is therefore the master controller of all communications on board. The main communication is performed via two separate and redundant MIL-1553B buses,
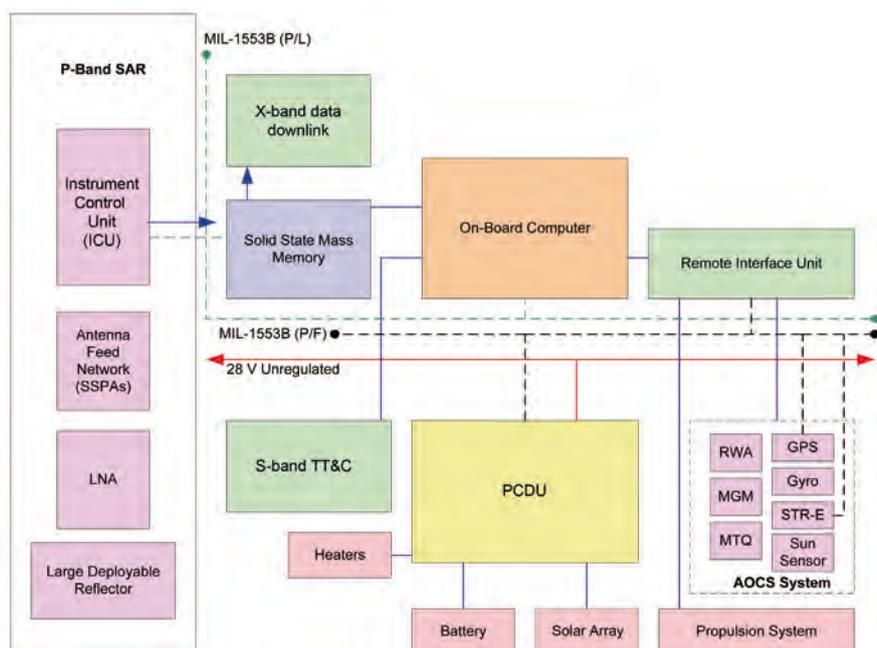
Figure 5.28. Generic system electrical architecture for Biomass.

one for the platform and one for the payload. The OBC acts as the bus controller for both; all other units are remote terminals. While the OBC is communicating via either the nominal or redundant MIL bus, the remote terminals are listening (in hot redundancy) to both the nominal and redundant buses. The OBC also communicates with the RIU via the platform MIL-1553B bus; there is no point-to-point link. Discrete single channel command, control, measurement and status telemetry signals that cannot be addressed through the MIL-1553B bus, as well as a small number of serial I/O interfaces, are operated through the RIU.

The science data communication link from the payload to the mass memory unit is accomplished by a fully cross-strapped cold-redundant Channel-Link interface for high data rate transmission. The OBC communicates with the payload via a redundant MIL-1553B bus dedicated to payload data handling and control.

5.4.4.6 Data handling and transmission

The Command and Data Handling Subsystem (CDHS) provides the following functionality:

— Overall satellite command and control including AOCS algorithms.

— Running the onboard autonomy and Failure Detection Isolation and Recovery (FDIR).

— Provision and distribution of ground- and software-issued commands to the satellite.

— Collection and storage of satellite housekeeping telemetry.

— Onboard time generation, synchronisation, maintenance and distribution

In general the CDHS consists of two units, the OBC and the Remote Interface Unit (RIU). The modular approach of separating the OBC from the mission specific interfaces has the advantage of allowing the reuse of existing hardware with minimal modifications and of enabling early testing. Two MIL-1553B data buses are used, one to connect to platform units and one dedicated to command and control of the payload units.

The OBC is the core part of the command and data handling subsystem, providing the following functionality:

— Processing functions by means of the On-Board Software (OBSW)
— Data memory and safeguard memory management
— Onboard time generation, synchronisation, distribution and servicing
— Bus controllers for the MIL-1553B buses
— TT&C interface functions
— Reconfiguration functions

The processing requirements of the OBC are within the typical range of a standard Earth observation LEO mission. The Biomass mission does not require any specific onboard processing, compression of the SAR data being carried out by the central electronics of the payload. Real-time housekeeping telemetry is acquired by the OBC and transmitted to ground using the S-band

Figure 5.29. Payload data downlink chain.

downlink. A dedicated interface between the OBC and the SSMM enables stored housekeeping telemetry to be downlinked via the X-band system, though during emergency conditions the downlink can be carried out via the S-band system. The onboard time is maintained by the OBC and is synchronised to the UTC GPS time reference provided by the GNSS receiver. The RIU is a mission-specific unit that includes all discrete interfaces from the OBC to the platform and payload equipment for the units that do not use the MIL-1553B data bus. In general, the RIU will contain interfaces to the following equipment:

— Reaction wheels
— Magnetorquers
— Magnetometers
— Propulsion subsystem units
— Thermistors
— X-band modulators and amplifiers
— Solar array deployment mechanism
— Reflector deployment control unit.

The payload data handling architecture has no unusual design drivers and an architecture based on the use of COTS equipment is possible.

The data downlink system architecture consists of all system elements involved in getting the data generated by the payload to the ground processing system (Fig. 5.29). In the space segment this chain starts with the Instrument Control Unit, which passes the data to the onboard mass memory unit. The SSMM stores the data until a scheduled ground station pass occurs, when it passes the data to the X-band system for transmission to ground. Finally, the ground station receives the data and passes it to the ground processing system.

The onboard Payload Data Handling and Transmission (PDHT) subsystem consists of three main elements:

— SSMM
— X-band payload data downlink system
— Interfaces between the payload and SSMM.

The SSMM unit is used to store the payload data, the auxiliary data required for payload data processing (e.g. position, velocity, attitude data) and as a secondary store for payload and platform telemetry. The unit formats the data for transmission to the ground in standard CCSDS transfer frames. The SSMM is based on flash memory and therefore benefits from greatly reduced volume, mass and power consumption. Concept A reuses the Sentinel-2 SSMM as this amply meets the needs of the Biomass mission with an EOL data storage capacity of 2400 Gb. An off-the-shelf 310 Mbit/s X-band data downlink system has been selected for downlink of data.

For Concept B, Fig. 5.30 shows the data volume trend over the entire repeat cycle of 25 days (369 orbits), without compression. The analysis shows that the selected scenario constituted by Kiruna as single ground station and by the Sentinel-1 PDHT, which performs the X-band downlink at a rate of 520 Mbit/s via two channels at 260 Mbit/s, are sufficient to fulfil the operational profile required by the mission. The different data volume between the two concepts is related to optimisation of the acquisition cycle in Concept A with respect to Concept B.

For Concept B, the selected baseline for the SSMM is based on six modules of 192 Gb each, plus an additional module in cold redundancy, providing a memory capacity of 1152 Gb at the end of life.

Figure 5.30. Data volume trend for
Concept B.
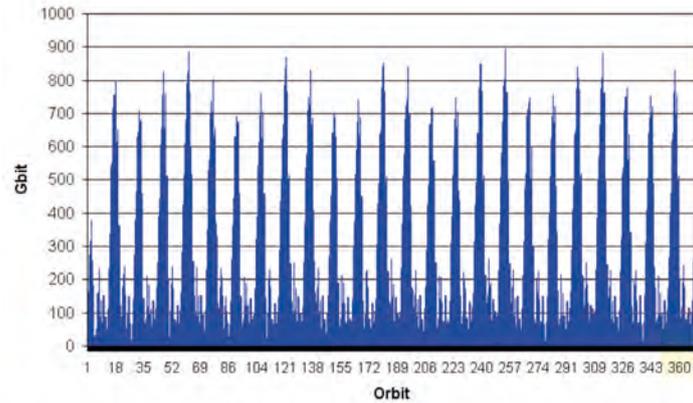
5.4.4.7 Electrical power and energy storage

The Electrical Power Subsystem (EPS) architecture provides the following functionality:

— Generation of electrical power using a solar array with triple-junction GaAs cells.

— Energy storage using a lithium-ion battery.

— Power regulation and distribution to all equipment.

— Heater lines.

— Deployment devices (solar array and reflector hold-down and release mechanisms).

The Power Conditioning and Distribution Unit (PCDU) distributes the power from the solar array and battery to the platform and payload equipment, providing power control and battery charge control. The distribution is achieved via single power lines that are protected by current limiters, which are either Folding Current Limiters (FCLs) or Latching Current Limiters (LCLs). Critical equipment that should not be switched off, namely the OBC and the S-band transponder, is connected to FCLs. All other equipment is connected by LCLs, which can be turned on/off as required.

A trade-off has been performed between the two possible architectures for the PCDU: Direct Energy Transfer (DET) and Maximum Power Point Tracking (MPPT). Analysis has shown that, with Biomass in a stable dawn/dusk orbit with eclipses only around the solstice, the MPPT architecture produces a peak of power on eclipse exit compared to the DET case. This allows the size of the solar array to be decreased at the expense of additional complexity of the PCDU. In conclusion, both consortia preferred the DET architecture because of its lower complexity and cost.

Typically the HPAs used in a SAR instrument are connected to a dedicated power bus to minimise noise effects. However, for Biomass the peak power of the SSPAs is sufficiently low that this is not necessary and a single 28-V DC unregulated power bus has been selected for both concepts. The EPS critical design case corresponds to the summer solstice (in the northern hemisphere) as the longest eclipses, lasting almost 20 minutes, occur around this time. The fixed angle between the solar array and the satellite body is selected to optimise the performance during the eclipse season, lasting about two months. For both concepts, power is generated using a deployable solar array

using triple-junction GaAs cells with an area of ~6.8 m^2 and maximum power generated at EOL of ~1500 W.

The deployed solar array of Concept A is based on the direct reuse of the deployment system used on ADM-Aeolus, as shown in Fig. 5.13 and Fig. 5.14. It consists of a driving mechanism capable of orienting the array to a fixed cant angle, a yoke, the panels and the HDRM. The deployed solar array of Concept B is shown in Fig. 5.15 and consists of four panels covered with solar cells and one middle 'blind' panel that acts like a yoke. The blind panel/yoke (connected to all four solar panels) will move the whole wing from the stowed position attached to the spacecraft body to its fixed tilt position.

The battery selected consists of lithium-ion stackable decks. The stackable deck approach is used by the Sentinel-2 mission. For Concept A, four stackable decks will be used to achieve a battery capacity of 144 Ah. At each orbit the battery is used to provide the peak power required by the SAR in transmission, which has an impact on number of charge/discharge cycles and on the battery sizing.

5.4.4.8 Telemetry, Tracking and Command

The TT&C subsystem provides S-band communication capabilities between the satellite and the ground station. Two active omni-directional antennas ensure a communication link in all nominal and non-nominal conditions (satellite attitudes). The subsystem provides the following functions:

— Command function, for reception and demodulation of commands sent from ground.

— Telemetry function, for transmission of real-time housekeeping data to ground.

— Ranging and range rate functionality, for satellite orbit determination (as backup of the GNSS during emergency operations).

Both concepts rely on downlink/uplink rates of 128 kbit/s and 4 kbit/s using standard S-band off-the-shelf transponders. The S-band subsystem consists of two transponders operated with the receivers in hot redundancy and the transmitters in cold redundancy. Both concepts rely on two quadrifilar helix antennas, mounted on the main satellite body, which can be used prior to deployment of the LDR. In order to meet the requirement for 4π steradian coverage in the fully deployed configuration, it is necessary to add a third antenna as the LDR is not transparent at S-band frequencies and would then block the field-of-view of the zenith S-band antenna. A patch antenna is, therefore, mounted at the top of the boom providing a clear FOV above the reflector. This antenna is not available until the boom is fully deployed. An approach where all S-band antennas are of the patch type, e.g. with heritage from TerraSAR-X, is also possible. A switching network is provided to ensure that the boom (zenith) antenna is available, even if one switch fails. The nadir antenna will nominally be used during the mission.

The S-band subsystem will also have capabilities to downlink recorded housekeeping telemetry in emergency situations.

5.4.4.9 Attitude Orbit Control System

The Biomass Attitude Orbit Control System (AOCS) is based upon five distinct modes of operations. Figure 5.31 summarises the transitions between the various AOCS modes for Concept A; a similar diagram applies for Concept B. All modes are implemented in software, with each mode using a specific set of sensors and actuators. A more detailed description of the main modes follows.

Figure 5.31. AOCS mode transitions.
A – Automatic Transmission.
C – Commanded Transition via TC.
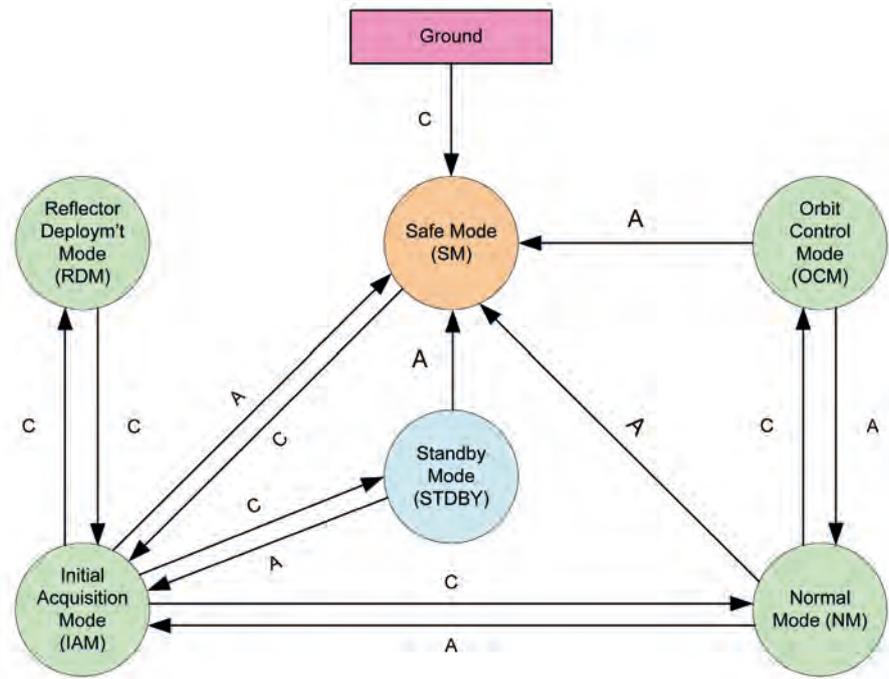
5.4.4.9.1 Initial Acquisition Mode and Safe Mode

Initial Acquisition Mode (IAM) and Safe Mode (SM) are functionally identical, however IAM uses 'prime' units and SM uses 'redundant' units. In these modes the satellite is maintained in an attitude that ensures the solar array is illuminated optimally by adopting a Sun-pointing attitude. Attitude sensing is performed using triple-majority voting Sun sensors. Two sets of sensors are required, one for use prior to deploying the LDR and one after, because of the field-of-view constraints caused by the deploying reflector. Coarse gyroscopes are used to provide rate information in this mode. Since the inertias are an order of magnitude larger after reflector deployment, different actuation strategies can be adopted in SM. Concept A is based on a hybrid scheme of thrusters and magnetorquers: to reduce rates quickly, thrusters are used for initial rate damping, then when the angular rates are sufficiently low, the magnetorquers augmented by a minimal use of thrusters are used in order to reduce propellant utilisation. In Concept B the torque for attitude control is generated by the reaction wheels augmented by magnetotorquers. In case of failure of one reaction wheel, the remaining three wheels can carry on all mission objectives.

5.4.4.9.2 Reflector Deployment Mode

A dedicated mode for reflector deployment is required due to the dynamic constraints imparted on the system by the deploying reflector and to the need for maintaining sufficient power levels. The Reflector Deployment Mode (RDM) uses the Sun sensors to provide attitude measurements supplemented by the coarse gyroscopes to provide rate information. During this short-duration mode the attitude is maintained Sun-pointing and inertially fixed by generating a momentum bias using the reaction wheels.

5.4.4.9.3 Normal Mode

The Normal Mode (NM) is the primary attitude mode used throughout the mission. SAR imaging operations are carried out in this mode. In addition, slew

manoeuvres to switch between the various swaths and slews to support delta-V manoeuvres are also carried out in this mode. The derivation of the AOCS pointing requirements is described in the Pointing and Geo-location budget (Subsection 5.4.5.5). A gyroless NM has been selected as the baseline, as there is no requirement on relative pointing accuracy that would require an accurate angular rate sensor. A single, active head startracker with APS technology will be used and is sufficient to meet the pointing requirements of the mission. In case of startracker failure the FDIR triggers the transition of the AOCS into Safe Mode where the cold redundant (low accuracy) gyroscope is used. A single-frequency GNSS receiver is used to provide orbit position data to the AOCS and to the ground segment for orbit determination and mission planning (e.g. definition of orbit control manoeuvres). In addition, the data is used for geo-location of the SAR data product. A cluster of four reaction wheels provides attitude control authority, which remains sufficient also in the case of failure of one wheel. The wheels will be constantly offloaded using magnetorquers, similarly to most LEO missions. The spacecraft roll manoeuvres will be performed over the poles in order to not interfere with the SAR acquisitions and to avoid loss of scientific data. They will take about four minutes plus three to four minutes for satellite attitude stabilisation (tranquillisation).

5.4.4.9.4 Orbit Control Mode

Orbit maintenance, the correction of launch vehicle injection errors and the transition between the nominal phase and the tomographic phase orbits are carried out in Orbit Control Mode (OCM). This mode is similar to NM, using a startracker as the primary attitude sensor. The reaction wheels are used to perform the attitude slew manoeuvres required to point the thrusters to the desired direction. For both concepts a dedicated single thruster is used to impart the required delta-V, whereas the satellite attitude during the thrust phase is either controlled by the remaining thrusters (Concept A) or by reaction wheels (Concept B).

5.4.4.9.5 Standby Mode

Standby Mode is used when no attitude actuation is required. The AOCS is in this mode prior to separation from the launcher and during solar array deployment.

A summary of the AOCS equipment for Concept A is given in Table 5.6. Similar units have been selected for Concept B. Thrusters are used in Concept A in cold redundancy for the IAM, SM and OCM modes, while for Concept B they are used only in OCM.

The actuators have been sized in order to handle the disturbance forces and torques generated by the semi-transparent mesh of the reflector. When the large reflector is deployed, the gravity gradient torque is the largest static disturbance torque contribution. Aerodynamic and solar radiation disturbance forces and torques have been estimated (Fig. 5.32) using numerical tools based on standard Test Particle Monte Carlo method for aerodynamics and radiation pressure (Brunello, 1993).

The attitude control performance is an important concern in view of the large deployable reflector. For both concepts, the industrial studies have demonstrated that a classical three-axis Proportional Integral Derivative (PID) controller is sufficient to achieve the required pointing performance, with conservative margins with respect to the requirements. The classical controller design uses an established approach of gain rejecting the flexible modes via a phase-lead and an elliptical filter with a phase lag added at low frequencies to improve disturbance rejection. This results in a seventh-order controller. The performance of the classical AOCS design is validated through methodologies from the robust control theory and advanced worst-case analysis techniques.
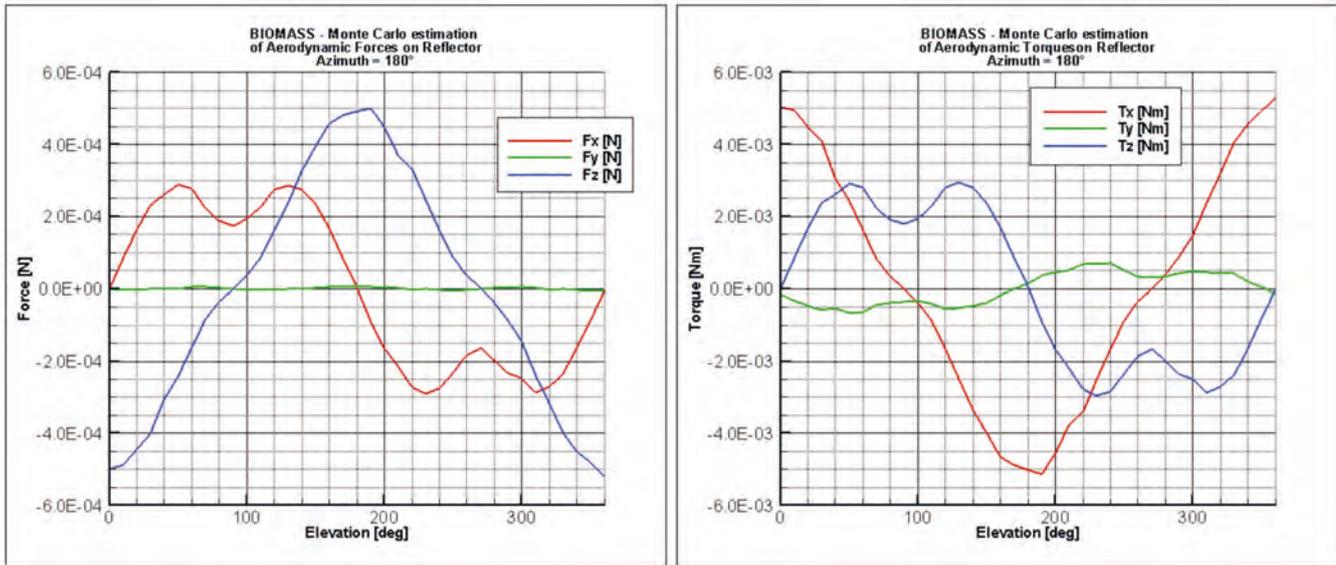
Figure 5.32. Aerodynamic forces (left) and torques (right) on the reflector mesh for Concept A. (NG)

Table 5.6. AOCS equipment characteristics for Concept A.

Sensor	Number	Characteristics	Redundancy
Sun Sensors	2 sets of 3	±1° boresight accuracy ±50° FOV	Triplex Hot Redundant
Gyroscopes	2 x 3 axis	ARW 0.1-0.2°/ hr Scale Factor <2000 ppm	Hot Redundant (IAM only) Cold Redundant (FDIR only)
Magnetometer	2	3-axis	Cold Redundant
Startracker	2	APS Detector Bias <15" NEA <75"	Cold Redundant
GPS	2	Position <10 m 3D in real-time	Cold Redundant
Reaction Wheels	4	Momentum 40 Nms Torque 235 mNm	3 out of 4 4 hot (RDM only)
Magnetorquers	3 x 2	400 Am^2	Cold Redundant

Firstly, the PID controller tuning is performed analytically, allowing the system to be below the ideal envelopes. Successively, robustness analysis is performed in the classical sense, by acquiring a set of randomly-generated models of the system to be controlled within the associated uncertainty boundaries and validating the controller against each of them. Finally, μ-analysis is performed to provide the proof of the classical controller design robustness, showing that the flexible modes are well rejected below −6 dB.

In addition, a robust controller was designed based either on a H-infinity synthesis of a modified three-block criterion of sensitivity, co-sensitivity and control sensitivity functions, or on μ-synthesis techniques. Both the classical and the robust controllers meet the AOCS requirements. Although the robust design generally exhibits better performance and robustness characteristics compared to the classical design, the robust design is only retained as a means of risk mitigation against potential future evolution of the requirements or spacecraft design.

5.4.4.10 Propulsion

The propulsion system is required for orbit maintenance throughout the mission. For Concept A, it is also required for attitude control in Initial Acquisition Mode and Safe Mode. Orbit control manoeuvres are required throughout the mission in order to acquire and maintain the orbit, in particular to meet the needs of the SAR interferometry. The manoeuvre frequency varies between a manoeuvre every 16–20 days to a worst case of a manoeuvre every 3–4 days at the end of the mission, corresponding to the solar maximum. In addition, at the beginning of the mission the spacecraft will be required to manoeuvre to (or from) the tomographic orbit.

The Centre of Mass (CoM) Y-coordinate changes significantly between the 'stowed' and 'reflector deployed' states. To simplify operations, orbit corrections will be carried out only after the reflector has reached the fully deployed state. This allows the thruster configuration to be optimised for the reflector deployed state for both in-plane and out-of-plane manoeuvres. For Concept A, the thrusters also provide the required torque authority in the stowed state for attitude control, an additional constraint leading to the definition of two different thruster modes. The thruster configuration must satisfy the following key constraints:

— Avoid plume impingement on the structure (assuming 45° half cone angle).
— Provide a torque authority greater than 100 mNm.

For Concept A, a six thruster pair configuration has been selected to provide the required orbit and attitude control capability. For reference, the Concept A thrusters configuration is shown in Fig. 5.33 for the NG case. Attitude control is primarily provided by four thrusters (#1–4) orientated along the +Y direction and canted to give torque capability. In addition, these are supplemented by two additional thrusters (#5 and 6) located on the +X side of the spacecraft for the stowed configuration. One thruster (#6) cannot be used once the reflector is fully deployed, as the plumes impinge on it. Orbit maintenance is provided by thruster #5, with the thruster being aligned with the CoM in the deployed configuration. An analysis of the tranquilisation of the reflector after a slew manoeuvre has been performed, showing that the reflector and boom motion is damped after ~200 s.

For Concept B, the number of thrusters is limited to one pair, as it is only needed for orbit maintenance. It should be noted that in this case it is not possible to align the thruster with the CoM of the satellite, resulting in an angle
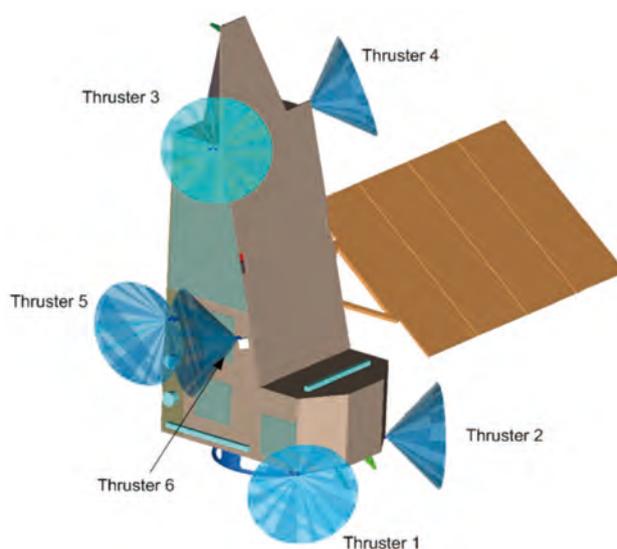
Figure 5.33. Concept A thrusters configuration for the NG LDR.

101

between the thruster and the required thrust direction. As a consequence, it will be necessary to slew the satellite to properly align the thruster in the anti-flight direction.

An adequate thrust level is required to provide sufficient torque authority, particularly at the end of life. Sufficient torque capability can be provided by a 1 N thruster, therefore 1 N thrusters with a specific impulse of 220 s are selected as the baseline. The propellant mass requirements are presented in Table 5.7.

For both concepts, the propulsion subsystem is a conventional pressurised blow-down monopropellant system. The propellant tank selected for Concept A has a total volume of 58 litres providing a propellant capacity of 39 litres pressurised to ~24 bar at BOL, decreasing to ~6 bar at EOL. Two propellant tanks thus provide a total propellant load of 78 litres for the mission. Concept B relies on a single tank with a fuel capacity of 68 litres.

5.4.5 Budgets

5.4.5.1 Mass budgets

Table 5.7 reports the mass budgets for the various cases studied and includes the following margins:

— Harness: 30%.
— Completely new developments: 20%.
— New developments derived from existing hardware: 15%.
— Existing units requiring minor/medium modification: 10%.
— Existing units: 5%.

An additional 15% margin at system level has been applied against unpredictable mass evolutions and/or balancing needs.

	Concept A with NG reflector	Concept A with HC reflector	Concept B with NG reflector
Data Handling	52	52	18
Electrical Power S/S	110	110	73
Harness	69	69	79
X-band comm S/S	12	12	63
S-band comm S/S	11	11	9
AOCS	80	80	85
Structure	269	269	358
Thermal S/S	51	51	35
Propulsion	26	26	14
Platform Total	680	680	734
Payload Total	202	275	206
Dry Mass Total	882	955	940
System mass margin	132	143	145
Balance Mass	55	69	30
Dry Mass with margin	1069	1167	1115
Propellant	59	67	32
Wet Mass	1128	1234	1147
Launcher performance	1352	1352	1360
Launcher adapter	88	88	76
Launch margin	136	30	137

Table 5.7 Mass budgets for Concepts A and B [kg].

	Concept A	Concept B
Orbit injection correction	18.5	18.5
Orbit change between phases	8.2	3.4
Orbit maintenance	34.7	23.7
Collision avoidance	5.4	2.7
Deorbit manoeuvre	0.0	0.0
Total	66.8	48.3

Table 5.8. Delta-V budgets for Concepts A and B [m/s].

The launch margin gives good confidence on the robustness of the concept with respect to the mass aspect, though this is less so with the HC reflector (studied by one industrial consortium only).

5.4.5.2 Delta-V budget

The delta-V increments required for the two concepts are in Table 5.8. The higher allocations of Concept A respect to Concept B are due to the fact that Concept A performs the commissioning in the nominal orbit, while Concept B in the tomographic orbit. In addition, Concept A performs the orbit maintenance using thrusters instead of reaction wheels and for collision avoidance it is based on more conservative assumptions.

5.4.5.3 Power budgets

The instrument will alternate between the Ready and On modes according to the operation plan. For the rest of the orbit, the instrument will remain in Standby mode. The summary of power budgets (including margins) for both concepts is presented in Table 5.9. The sizing case corresponds to the satellite in nominal mode with the payload switched on. The higher power needed by the heaters in Concept A is the reason for the difference in the budgets of the two concepts.

5.4.5.4 Data rate and volume budgets

The data rate and volume budgets are presented in Table 5.10. Both concepts rely on the re-use of COTS memory modules, respectively from Sentinel-2 and Sentinel-1 missions, resulting in memory sizes higher than the required one. The different data volumes are due to the different acquisition strategy adopted by the two concepts.

5.4.5.5 Pointing and geo-location

The relative motion of Earth within the field-of-view of the antenna causes a variation of the radar Doppler centroid, which is the centre frequency of the azimuth spectrum recorded by the SAR.

Operating Mode	Concept A	Concept B
Initial Acquisition	1038	654
Safe Mode	1023	583
Orbit Correction Mode	1087	764
Nominal, with payload Ready	881	649
Nominal, with payload On	1298	786
Nominal, with payload in Standby	668	596

Table 5.9. Power budgets for Concepts A and B [average values in W].

Table 5.10. Mass memory sizing for Concepts A and B.

	Concept A	Concept B
Instrument Data rate [Mbit/s]	115	117
Downlink rate [Mbit/s]	310	520
Average Instrument Duty Cycle [%]	20	22
Mass memory requirement [Gb]	946	896
Mass memory size EOL [Gb]	2400	1152

Uncompensated variations of the Doppler centroid may cause significant errors during azimuth compression, range-cell migration correction and geo-localisation, with non-negligible impacts on the instrument overall calibration and interferometric performance. A yaw steering of the satellite is required to compensate for this effect. The yaw steering law works very well in circular orbits, but a significant residual variation of the Doppler centroid (about 100 Hz) is expected because of the elliptical shape of the orbit and the deviations of the geoid from the spherical Earth model. This residual variation can be suppressed by exploiting an additional pitch steering law as shown in Fig. 5.34.

As the geodetic altitude varies around each orbit (see Fig. 5.5) the SAR PRF must be varied to ensure that the return echo is correctly received between transmit pulses and that the range ambiguity level that results is still acceptable. Adjustments of the PRF along the orbit can be complemented by slow roll manoeuvres in order to improve sensitivity and ambiguity performance. A possible roll steering law can be generated by keeping a constant antenna look angle for a particular incidence angle on the ground, resulting in a variation of the roll angle of 0.11° within the geodetic altitude range.

The Absolute Knowledge Error (AKE) requirement for the SAR line of sight is derived from the radiometric stability requirement as shown in Chapter 7. Table 5.11 shows the AKE requirements.

The Absolute Pointing Error (APE) requirement for the SAR line of sight is derived from the Noise Equivalent σ^0 and Total Ambiguity Ratio requirements as shown in Chapter 7. Table 5.12 shows the APE requirements.

Table 5.13 provides a qualitative summary of the main APE and AKE error contributions applicable to both concepts. Bias, drift, harmonic and noise errors contribute to the APE, whereas only harmonic, drift and noise errors

Table 5.11. AKE requirements for Concepts A and B (3 RMS values).

	Concept A	Concept B
Elevation [°]	0.05	0.03
Azimuth [°]	0.05	0.15

Figure 5.34. Yaw steering law (left) and pitch steering law (right).

System Concept
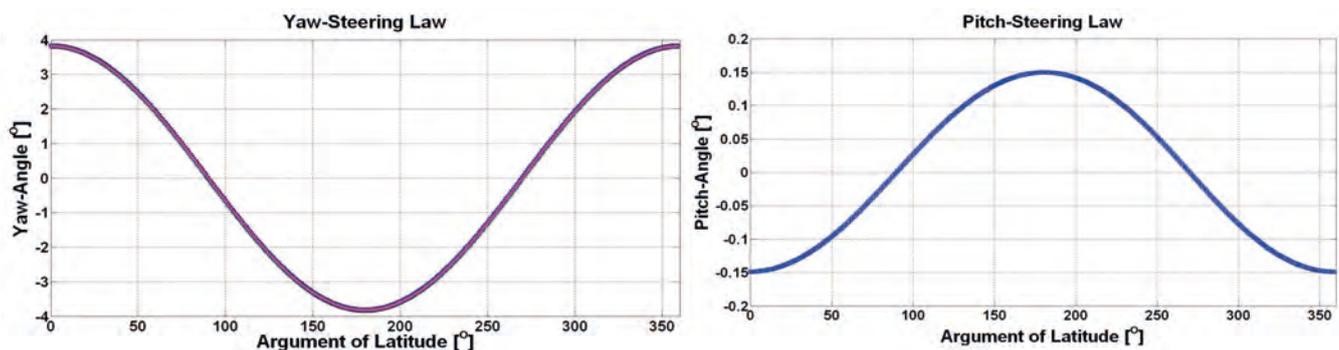
	Concept A	Concept B
Elevation [°]	0.07	0.096
Azimuth [°]	0.07	0.225

Table 5.12. APE requirements for Concepts A and B (3 RMS values).

Error contributions	Sources of error	Class
Platform pointing errors	AOCS error	Noise and bias
	Controller error	Noise and bias
	Residual mechanical misalignment of the startracker with respect to the feed assembly	Bias
	Thermo-elastic distortion of the structure between the startrackers and the feed assembly	Harmonic and bias
Antenna pointing errors	Translation/Rotation of the Reflector Support Assembly relative to the feed assembly	Harmonic and bias
	Translation/Rotation of the LDR assembly relative to the Reflector Support Assembly/Platform interface	Harmonic and bias
	Thermo-elastic distortions of the LDR	Harmonic and bias
	Feed array electrical pointing errors	Harmonic, drift and bias
	Feed array mechanical pointing errors	Harmonic, drift and bias

Table 5.13. Error contributions to the APE and AKE.

contribute to the AKE. The pointing errors of the SAR include platform and antenna pointing error contributions.

A requirement on the Relative Pointing Error over a specified time interval is required if a pointing variation over a defined time interval will affect the performance of the system. If the pointing of the SAR beam drifts over the SAR integration time then the two-way gain for any particular point in the swath will vary, which manifests as an uncertainty in the radiometric performance. An analysis was performed to assess the effects on along-track resolution, integration losses, peak-to-side lobe ratio and integrated side lobe ratio of a 0.2° magnitude pointing error with different error frequencies (0.1–2 Hz). Thanks to the long wavelength (0.689 m) of the transmitted pulses and the Hamming windows applied by the on-ground processor, the sensitivity of the instrument response function to relative pointing errors is negligible.

The geo-location accuracy requirement of 25 m RMS in the along and across track directions must be fulfilled over flat terrain and excluding ionospheric effects. The platform AKE performance driven by the SAR observation requirements allows the geo-location performance to be achieved with margins. Both concepts achieve a geo-location accuracy around 15 m RMS in both along track and across track directions.

5.5 Launcher

The primary launch vehicle is Vega, launched from Kourou, French Guiana. Biomass will be the sole passenger because of its relatively large size and volume. Concept A uses the 1194 mm LVA, developed for Sentinel-2, as the interface between the launcher and Biomass (Fig. 5.35). Concept B uses the standard 937 mm LVA, although this results in lower volume available under the fairing because of the height of the LVA.

105

Table 5.14. Launch vehicle performance (including LVA) and margins (kg).

Launcher	Performance	Wet mass	Margin
Concept A			
VEGA	1264	1234 (HC)	30
		1128 (NG)	136
Taurus II	2200	1234 (HC)	966
		1128 (NG)	1072
Concept B			
VEGA	1284	1147 (NG)	137
PSLV	1360	1147 (NG)	213
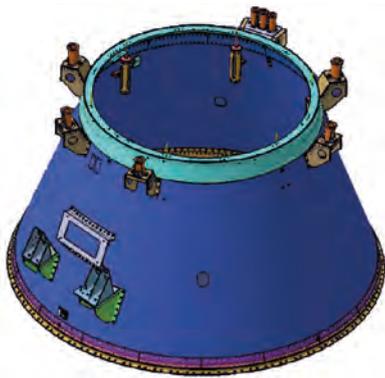
Figure 5.35. Vega 1194 mm LVA interface.

The backup launch vehicle for Concept A is Taurus II, Antares being its new commercial name, a new launcher by Orbital Sciences Corporation (USA) in the final stages of developement. The basic, two-stage Taurus II vehicle would be used, launched either from Vandenberg, California, or Kodiak, Alaska. There is substantial volume margin within the Taurus II fairing.

The capacity of the two launchers is listed in Table 5.14. Vega's performance has been reduced by 100 kg from the figure quoted in the Vega User Manual (Arianespace, 2006) as an additional margin taking into account the current uncertainty in the injection performance. The Taurus II performance shows substantial margin on the injection performance. The stowed configurations inside the Vega fairings are shown in Figs. 5.36, 5.37 and 5.38.

5.6 Ground Segment and Data Processing

5.6.1 Overview

Following the approach of developing a multimission ground segment, the current generation of Earth Explorer ground segments has been designed, built and integrated using generic components configured or adapted to each satellite. This approach has been used for the current six Earth Explorers. In line with this, the Biomass ground segment consists of two main components, the Flight Operation Segment (FOS) and the Payload Data Ground Segment (PDGS), as presented in Fig. 5.39.

5.6.2. Ground Segment Elements

The FOS includes the TT&C Ground Station and the Flight Operations Control Centre (FOCC). The TT&C ground station provides the following main functions:

— Housekeeping telemetry acquisition
— Telecommand uplink
— Satellite tracking
— Data communications to the FOCC
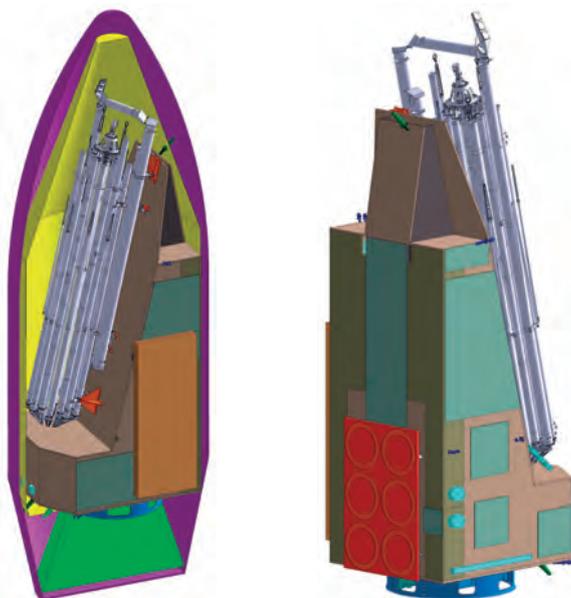
Figure 5.36. Concept A stowed configurations inside the Vega fairing (left) with the Harris Corp LDR.
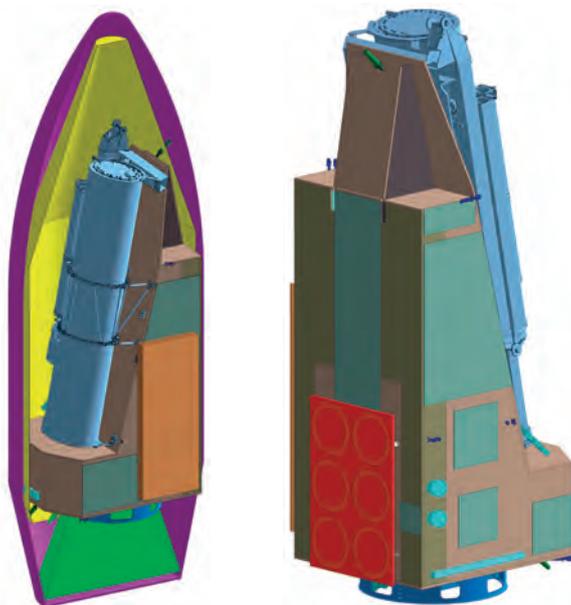
Figure 5.37. Concept A stowed configuration in the Vega fairing (left) with NG LDR.
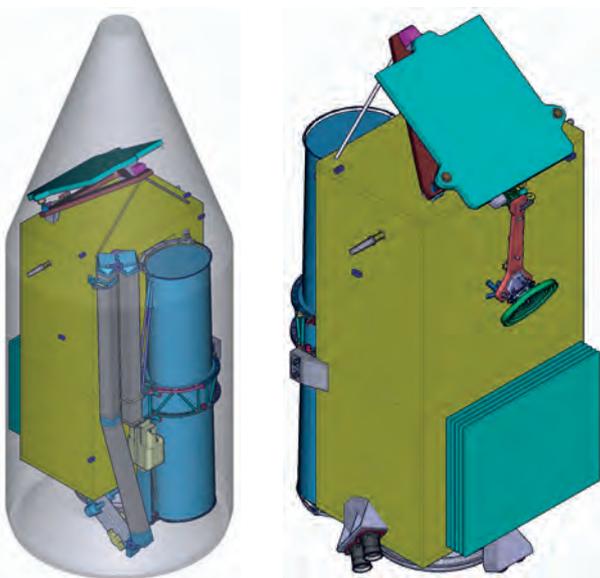
Figure 5.38. Concept B stowed configuration inside the Vega fairing (left).

During Launch and Early Orbit Phase (LEOP), a dedicated ground station network supports the operations. This network uses the Estrack core and enhanced stations where possible. The FOCC will be based at ESA's European Space Operations Centre (ESOC) and will provide the following main functions:

— Satellite monitoring and control
— Flight dynamics and manoeuvre planning
— TT&C ground station network control
— Overall satellite operations planning
— Onboard software maintenance
— Mission simulation
— FOS supervision
— Spacecraft system data distribution
— Interface with the launch site for LEOP

The PDGS is primarily responsible for receiving the science data from the satellite, applying the appropriate processing algorithms and delivering the data products to the users. It comprises the following functions:

— Payload data acquisition and ingestion function for downlink of science data telemetry
— Processing function
— Archiving function
— Dissemination function
— Mission planning function
— Quality control and calibration/validation (cal/val) functions
— Monitoring and control function
— User segment/services.

Figure 5.39. Ground segment architecture.
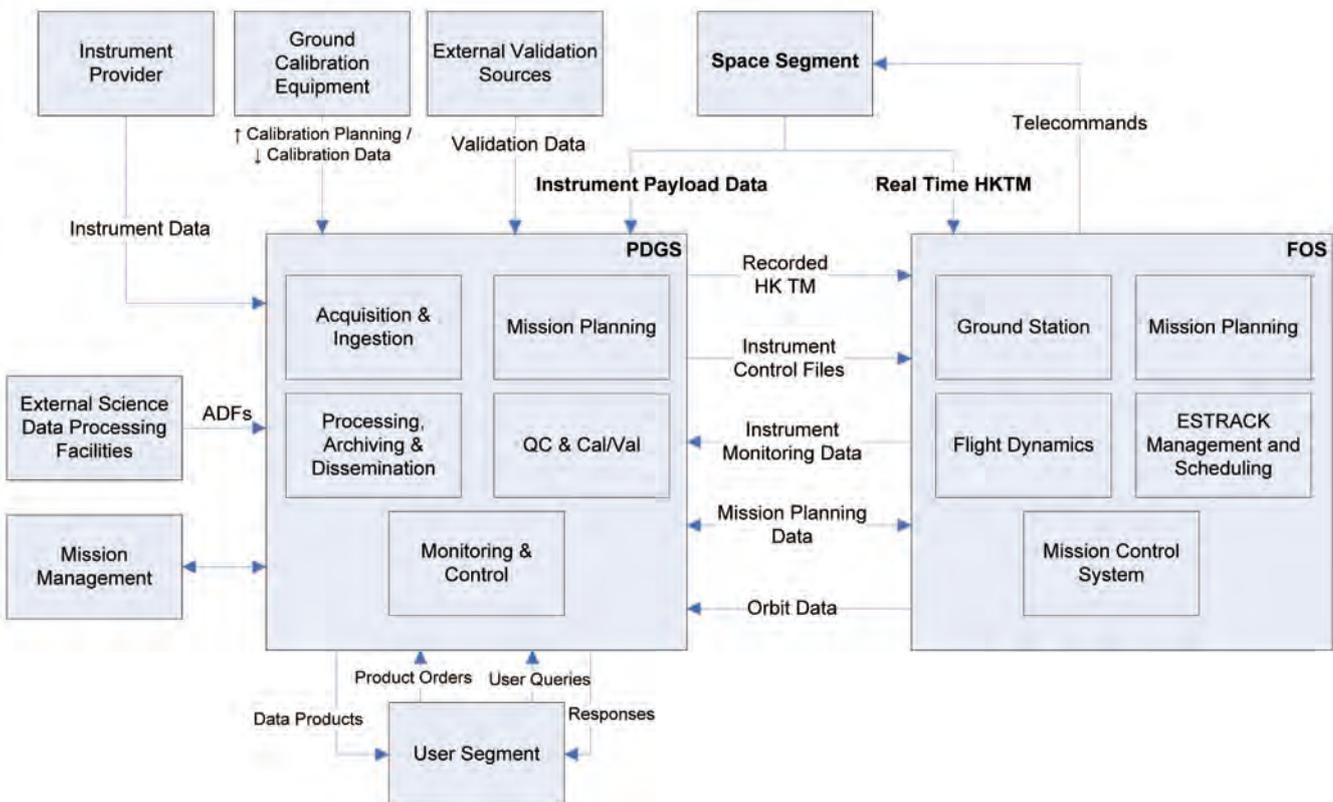
5.6.3 Flight Operation Segment

The FOS is strongly based on existing ESA hardware and software infrastructure, adapted where necessary for Biomass.

5.6.3.1 FOS operational approach

The mission operations are automated, as far as possible, to minimise risk and to contain the size of the operations team. Operations support is restricted to normal working hours, i.e. five days per week. Out of hours, on-call engineers can be alerted automatically should a serious anomaly be detected. A serious anomaly is one that threatens system availability, such as significant data loss or a danger to the health of the satellite. The latter should, in principle, be excluded thanks to the spacecraft autonomy. Other anomalies are investigated only during working hours.

Contacts with the FOS ground station via the TT&C are limited to those necessary for the uplink of the mission plan for nominal operations, this is foreseen twice a week (Monday and Friday), taking full advantage of the spacecraft autonomy. During commissioning, one pass per day is expected. In view of the low frequency of TT&C passes, regular spacecraft health monitoring is assured via recorded HKTM, downlinked in X-band and forwarded to the FOS from the PDGS. Frequency and latency are not critical, but nominally the TM would be acquired at each pass and forwarded as a single file after reception. No near real-time planning is required.

5.6.3.2 FOS-PDGS interface

The FOS and PDGS are kept as independent as possible. In particular, no payload data is processed by or transmitted through the FOS. Data exchanged between FOS and PDGS includes mission planning requests and results, orbit data, recorded HKTM from PDGS to FOS, and processed HKTM from FOS to PDGS. Existing interface formats and specifications supported by the ESA infrastructure software are used wherever applicable.

5.6.3.3 Telemetry, tracking and command

The baseline TT&C ground station is in Kiruna, Sweden. Both telemetry and telecommand functions are transmitted in S-band. No modification to the Kiruna station equipment is required to support Biomass. The primary data source for orbit determination in the routine operations phase is the onboard GNSS receiver. There is, therefore, no need for frequent ground station tracking data in the routine phase.

The principal task for TT&C passes in routine operations is telecommand uplink. Real-time HK telemetry will be acquired during these passes, even if it is not a driver for taking passes. The TT&C ground station is not dedicated to Biomass, but shared between missions. Station allocation planning – both TT&C and PDGS – is performed by Estrack Management and Scheduling system (EMS) in cooperation with Mission Planning System (MPS). EMS also generates the detailed operation schedules executed by Estrack ground station monitoring and control systems.

5.6.3.4 Mission control system

The Mission Control System (MCS) is based on the Earth Explorer MCS (EEMCS), which is an extension of SCOS-2000. The EEMCS is continuously upgraded with functionality needed for specific missions and expected to be more widely useful. A configuration for the Biomass mission will be necessary. A certain degree of customisation of the system (including same functional

modifications) is likely to be necessary, according to satellite design, ground interface specifications, the final operations concept, and the existing capabilities of the EEMCS at the start of implementation for Biomass. No specific functional adaptation has been identified as necessary.

5.6.3.5 Flight dynamics

No mission-specific modifications to ESA flight dynamics infrastructure will be needed. Flight dynamics is a service provided to missions that delivers orbit information and event files to the various planning entities as well as the orbital predictions used by the Estrack ground stations. It also generates command sequences that are transferred to the MCS directly or via the MPS. Flight dynamics receives radiometric measurements from ground stations as well as spacecraft data, including GNSS tracking data, from the MCS.

5.6.3.6 Mission planning system

The FOS MPS is based on the Earth Explorer MCS mission planning kernel. It generates schedules for execution by the MAS as well as command sequences for uplink to the spacecraft. The MPS will require configuration of mission-specific rules and constraints. As for the MCS, some functional modification may be needed but no specific functional adaptation has been identified as necessary at this stage.

The Estrack Management and Scheduling is responsible for planning ground station allocation to missions supported by Estrack, and generation of detailed ground station schedules.

5.6.3.7 Simulator

The spacecraft simulator is built using the SIMSAT infrastructure and the existing ground models and the generic dynamics and space environment models. Spacecraft subsystem models will in general need to be developed specifically for Biomass, though reuse will be possible for heritage subsystems already modelled in predecessor simulators. The flight onboard software is executed on an emulator.

5.6.3.8 FOS implementation

A single S-band TT&C ground station (Kiruna) with one contact per day is assumed. The TT&C ground station is collocated with the science data downlink station. During the LEOP (see Section 5.7), the operations are supported by a dedicated ground station network.

In general, the ground segment architecture is fixed and heavily based on the existing ESA hardware and software. However, there is a desire to limit operations costs by reducing TT&C access to the spacecraft whilst increasing the level of onboard autonomy.

Regardless of the operations model selected for the Nominal Phase, the FOS development will still have to prepare for all reasonable eventualities. However, moving towards office-hours-only support and automated monitoring and alarming during nights and weekends is a natural evolution of the operations concept. Apart from this, the design of the FOS is familiar in terms of the functional blocks to be used: the MCS will be based on the MCS Earth Explorer Kernel, the Mission Automation System will execute control procedures and schedules, in general, the ESA Ground Operations System infrastructure will be employed.

5.6.4 Payload Data Ground Segment

This section details the main functions and features of the PDGS of the Biomass mission.

5.6.4.1 Acquisition and ingestion

Science data, along with recorded HKTM, will be transmitted via X-band to the ground station, nominally placed in Kiruna. Considering that Biomass has no near-realtime requirement and that the data latency for Level-1b products is set to one month, the selection of X-band station is mainly driven by the need to avoid filling the onboard memory. Assuming some optimisation of the instrument duty cycle, a single station located at the latitude of Kiruna or higher is sufficient to support the mission.

5.6.4.2 Processing

The scientific data downlinked at the ground station are systematically processed up to Level-1b, generating the DGM product in all the polarisations (HH, HV, VV and VH), along with intermediate Level-0 and Level-1a products. The user segment will generate higher-level products. Further details on the algorithms can be found in Subsection 5.6.5.

5.6.4.3 Archiving

The Level-0, Level-1a and Level-1b DGM products will be systematically generated and archived by the PDGS archiving function. Level-1c and Level-1d products are not systematically processed and therefore do not require archiving. Over the duration of the mission, the total amount of data resulting from the Level-0, Level-1a and Level-1b products generated will be 4272 TB, which includes capacity to store products from two previous reprocessing campaigns. The archiving function also interfaces with the user services to provide access to products and auxiliary data to users.

5.6.4.4 Reprocessing

Besides the reprocessing of limited reference datasets usually handled by the main processing facility, systematic bulk reprocessing following e.g. upgrades of the processors on ground is supported by a separate infrastructure. In view of the important computing resources required over a limited time by bulk reprocessing campaigns, the current trend is to procure re-processing as a service relying on shared resources.

5.6.4.5 Mission planning

This function is in charge of defining the plan of activities for the SAR instrument. This function is also in charge of planning X-band downlink activities over acquisition stations. For the generation of the payload plan the mission planning will implement a set of Biomass-specific rules and constraints, covering instrument swath model and operations constraints, definition of areas to be observed, ground station visibilities, ground station and payload availability, recording and downlink rates, calibration requests, priorities associated to the areas of interest and to possible calibration requests, etc. A map defining the areas of interest is the main input to the planning sequence (see coverage map in Chapter 2). Such map identifies the geographical distribution of the target biomass areas within the latitude range between 56° S and 76° N and results in average instrument duty cycle of typically about 20% if dawn/dusk ascending and descending acquisitions.

5.6.4.6 Calibration/Validation

The main functions of the calibration/validation facility are:

— Processing of in-flight calibrations measurements and update of onboard instrument settings or calibration parameters used by the ground processors, as required.

— Identification and characterisation of deviation based on the processing of in-flight calibrations or vicarious measurements that may trigger payload planning requests (e.g. additional in-flight calibrations) or possibly processors evolutions.

— Support to calibration/validation users (provision of special calibration products).

— Configuration control of the instruments calibration databases.

Further details about instrument calibration can be found in Subsection 5.4.3.4.

5.6.4.7 Instrument performance and monitoring

The quality control function is responsible for the continuous assessment of the quality of the Biomass products as well as to ensure that the products meet a minimum level of quality prior to distribution. The function is generally split into several sub-functions:

— A service in charge of systematic control of all generated products prior to their distribution to users.

— Offline tools allowing specific analyses on products, triggered by feedback from users.

— The quality control function is supported by the long-loop sensor performance function, which allows monitoring key parameters of the payload.

5.6.4.8 Monitoring and control

The main objective of the Monitoring and Control function is to ensure that the PDGS fulfils its objectives in particular in terms of performance and availability so that the mission requirements can be met.

5.6.4.9 User services

ESA pursues a policy of developing a multimission infrastructure for the distribution of data products to end-users. It is assumed that such multi-mission user services will be upgraded to handle Biomass data products and end users. The user services will support data product browsing, access and visualisation as well as provide general information on the mission status and help desk.

5.6.5 Mission Data Processing

A mission-specific SAR ground processor is required to provide the end-users with Level-1b data for higher level processing up to Level-2 and above. External calibration of the Biomass payload requires interactions with the ground segment to transfer information on the status of the on-ground calibration devices. Processing of the data from Level-0 to Level-1b necessitates access to
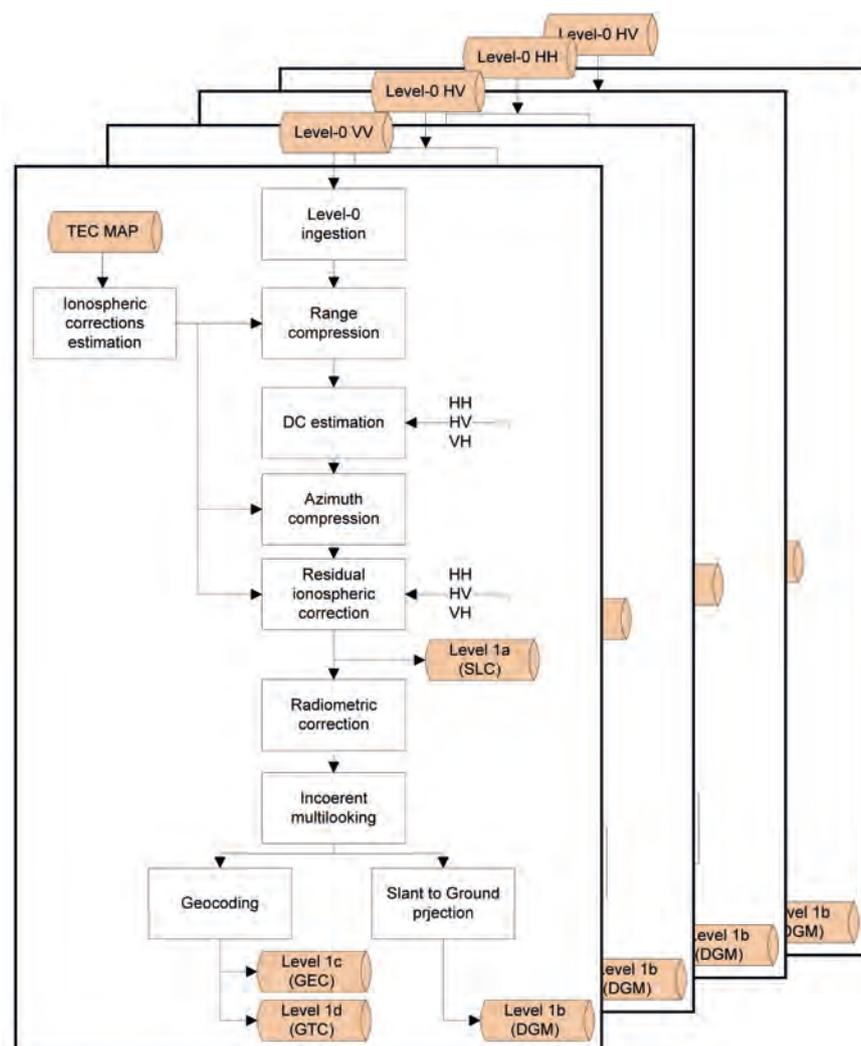
Figure 5.40. Processing chain for Biomass Level-1 products.

information on the state of Earth's ionosphere and magnetic field, which affect the radar signal propagation. A first-order bulk ionospheric correction will be applied as part of the routine processing. There is no requirement for near-real-time data service provision, so the data-latency requirements do not place problematic demands on the ground segment processing time.

To summarise, the ground segment for the Biomass mission does not present any new technology or infrastructure requirements. The SAR ground processor and the P-band devices for instrument external calibration represent the principal mission-specific development activities. In this section the baseline for the processing chain for Biomass SAR data is proposed, as shown in Fig. 5.40.

Since Biomass is a fully polarimetric mission, four Level-0 products, one for each polarisation, are input to four parallel processing chains that perform the same operations. Only three blocks are in common among the four processing chains: the Doppler Centroid (DC) estimation; block, that takes raw data from the four polarisations as input to estimate the DC for the current acquisition and the refined satellite attitude, the ionospheric estimation block, in charge of the estimates of ionospheric effects from the fully polarimetric information, and the residual ionospheric correction block, that needs as inputs the full polarimetric SLC data from all the processing chains to correct the FR. The processing scheme foresees the following basic processing steps:

— **ISP decoding and raw data pre-conditioning**: This block of the IPF will ingest Level-0 products. The main operations performed are ISP decompression, data preconditioning and channel orthogonalisation, if necessary.

— **Range compression**: The range compression step is a convolution along the range direction between the raw data and the chirp replica. The convolution is efficiently performed in the Fourier domain. Then, exploiting the instrument characterisation, the RGC products are co-registered in range.

— **Doppler Centroid estimation**: This block performs the DC estimation exploiting jointly the four polarisation RGC datasets. A three-step approach is foreseen: the ambiguous DC frequency is evaluated from the RGC data, then the absolute DC frequency is computed starting from geometric information and finally the Doppler ambiguity is retrieved combining both the DC information previously computed.

— **Azimuth compression and autofocusing**: The azimuth compression step is a space-varying two-dimensional convolution between target Doppler history and range-compressed data. This operation can be efficiently performed in frequency domain by the definition of a range-dependent operator that takes into account the non-linear mapping in the dual space and correctly takes into account the frequency domain support.

— **Residual Ionospheric corrections and Radiometric corrections**: This step is aimed at correcting as first the FR by processing jointly the four polarisation data. Then, the compensation of the range dependent radiometric factors introduced in the received signal by acquisition geometry (spread loss and incidence angle dependency) and by instrument receiving gain (elevation antenna pattern) is performed.

— **Multilooking**: To comply with the required radiometric resolution on Level-1b data, this block performs a multilooking operation in the frequency domain along azimuth direction.

— **Geocoding and Slant-to-Ground Projection**: The intermediate multilooked, slant range product is converted to the geodetic reference system in order to provide GTC, GEC and DGM products. The conversion is performed exploiting the orbital and attitude information as well as the available topographic model (the TanDEM-X DEM).

A preliminary analysis has been conducted to estimate the expected data volume for a Biomass acquisition of 100 km in azimuth and 60 km in range, resulting in the following file sizes: Level-0 full polarimetric 230 MB, Level-1a 255 MB and Level-1b 73 MB. The expected computation time from Level-0 to Level-1b is of about 10 s (on current computing hardware). It is worth remarking that both the expected data volume and the expected processing time are nearly the same for the two different swaths, due to the interleaved acquisition strategy.

The final selection of the PDGS Facilities and hosting centres is generally performed through open competition at the beginning of Phase-C/D. As a consequence, a list of PDGS centres and their locations cannot be provided.

5.7 Operation and Utilisation Concept

Biomass observations require repetitive coverage of a specified set of regions, which are defined by an imaging mask. The data are acquired on ascending

Operational Phase	Duration
LEOP	‹7 days
Commissioning Phase – Platform – Payload and Ground Segment	 ‹26 days (incl. margin) 126 days
Tomographic Phase (‹3% of nominal lifetime)	55 days
Nominal Operations Phase (>97% of nominal lifetime)	1770 days (4.85 years)
End-of-Life Phase (EOL)	‹9 days
Total Mission Lifetime	1931 days (5.3 years)

Table 5.15. Mission phases and durations, similar values for both concepts.

and descending passes. This process lends itself to an autonomous approach for data acquisition and processing up to Level-1b. The precise orbit control required to deliver the interferometric baselines is achieved via orbit maintenance operations at a frequency that will nominally vary throughout the mission, with the worst case requiring two manoeuvres per week towards the end of the mission. Transitions between the nominal and tomographic phases require dedicated, but small, orbit altitude change manoeuvres. There is no need for a deorbit burn because atmospheric drag alone leads to re-entry of the satellite within 25 years.

5.7.1 Overview

The Biomass mission is divided into a number of different phases, as listed in Table 5.15. Each of the mission phases will be described from the standpoint of operations below.

5.7.2 LEOP and Commissioning

The LEOP covers the period from switch-over to internal power on the launch pad until the satellite is in its deployed configuration in orbit, and the AOCS is operating in Normal Mode. The duration of the Biomass LEOP is estimated to be seven days. The first part of the LEOP sequence is performed autonomously and only requires ground intervention if deployment fails. Upon completion of the sequence, S-band communications will be initiated and an initial satellite checkout will be completed to confirm success of the sequence. The second day of LEOP activities includes the deployment of the LDR, the final deployment of the solar array and the acquisition of the nominal attitude. It should be noted that the reflector blooming should not occur during eclipse to ensure correct deployment.

Days 3–7 of the LEOP will take the satellite from the Initial Acquisition Mode to the Normal Mode. After completion of a further checkout to confirm the nominal attitude is being maintained, the launcher dispersion corrections will be completed. This will conclude the LEOP activities and trigger the start of the commissioning activities.

The commissioning phase concerns the platform and the payload and will last up to five months. This phase consists of the complete characterisation of the performance of the platform, payload and ground segment to verify that the system is ready for the transition into the routine operational phase and ensure the SAR payload is calibrated.

The first part of the commissioning phase will be used to perform in-orbit functional and performance tests of all platform subsystems, including the payload data handling subsystem, to ensure that they are working. Upon completion of the platform commissioning activities, the spacecraft will be in the operational attitude and orbit with the AOCS in NM. At this point, commissioning of the SAR payload can begin. During the payload

commissioning phase, the instrument functionality will be exercised over its full operational range with respect to mode, antenna beam, polarisation, gain control etc. For each state, HKTM and product annotations will be monitored to verify that the instrument responds correctly to the command. Level-0 products obtained in all the operational states of the instrument (covering all modes, antenna beams, polarisations) will be verified by monitoring a range of parameters and comparing them with expected values.

5.7.3 Routine Operations

In the operational phase, the P-band SAR will take imagery over the target areas of interest in a planned acquisition sequence. Data will be acquired on both the ascending and descending passes to increase the number of datasets available for scientific use. Concept A relies on an optimisation algorithm to reduce the number of overlapping acquisitions, while Concept B systematically acquires all areas within the acquisition mask. Any excess capacity, in terms of data volume and energy budget, may be used to acquire additional data to support the secondary mission objectives. However, it is expected that such use will be minimal and directed by mission planning only.

The routine mission operations around the orbit are illustrated in Fig. 5.41. The payload is in Standby during the passes over the polar regions and is switched into Ready or Measurement Mode between the measurement latitudes. For routine activities, the need for ground-based control and monitoring will be minimised. The direct uplink communication between the satellite control centre and the satellite is primarily for the programming of the nominal timeline and manoeuvre parameters for orbital corrections. Station contacts will also allow regular downlinks for the collection of satellite HKTM.

Routine observations of the calibration sites do not require particular operations. Calibration activities will take place at least once a month throughout the mission life, starting from commissioning phase. Equatorial calibration sites are preferred to minimise the effect of ionosphere disturbances.
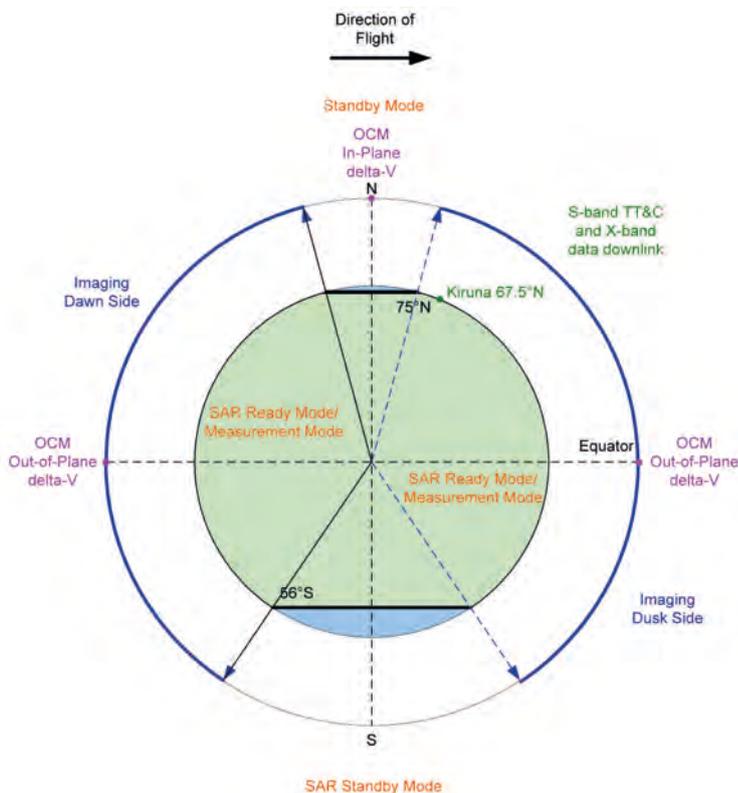
Figure 5.41. Example of sequence of system operations.

Routine orbit maintenance will be carried out over the polar regions to minimise outages. Assuming a launch in 2019 and current predictions of solar activity, at the beginning of the mission the interval between manoeuvres will be 16–20 days. This will reduce to 3–4 days at the end of the mission. Calibration activities will take place at least once every repeat cycle to confirm the correct operation of the instrument.

5.7.3.1 ITU constraints

A frequency allocation in the P-band for Earth observation active sensors was made at the World Radiocommunications Conference 2003 by the ITU, the UN agency for information and communication technologies.

The ITU-R Radio Regulations indicate that the use of the 432–438 MHz frequency band by space sensors in the Earth exploration-satellite service (active) must be in accordance with footnote 5.279A below:

> *"The use of this band by sensors in the Earth exploration-satellite service (active) shall be in accordance with Recommendation ITU-R RS.1260-1. [...]. The provisions of this footnote in no way diminish the obligation of the Earth exploration-satellite service (active) to operate as a secondary service in accordance with Nos. 5.29 and 5.30." (ITU-R RR footnote 5.279A)*

The Recommendation ITU-R RS.1260-1 'Feasibility of sharing between active spaceborne sensors and other services in the range 420–470 MHz' establishes the technical and operational constraints to be taken into consideration by SAR transmissions for the purposes of protecting stations operating in existing services allocated. ITU-R RS.1260-1 recommends the following:

> *"Spaceborne active sensors operating in the range 420–450 MHz not be put into operation within view of the terrestrial space object tracking radars [...], unless detailed analysis, on a case-by-case basis, to include consideration of the effects of the radars' receiver processing upon unwanted SAR signals, and possibly field testing have been performed to confirm compatibility with the mutual agreement of the affected administrations".*

Therefore, the operation of Biomass requires coordination with the US Air Force (USAF), as main responsible for the operation of the terrestrial Space Objects Tracking Radars (SOTR) listed in the ITU-R RS.1260-1. The restriction on the SAR to operate only outside the SOTR radar coverage area would impose a large reduction of the biomass areas of interest for the mission. Therefore an agreement with the USAF on an operational profile for maximising the observed biomass areas is being sought. The following operational scenarios have been proposed, in order of preference, for consideration by USAF:

— No restrictions for SAR operations for certain agreed and coordinated passes.

— SAR operations restricted below the SOTR surveillance fence, however the SAR is allowed to operate at higher elevation angles.

— SAR operations restricted by certain protection criteria set up at each SOTR site.

— SAR operations restricted when the satellite is flying within coverage of the SOTR radar antenna.

For example, in the case of the second option, the Biomass SAR would be capable of operation only when flying above the surveillance fence that is typically set at 10°. The satellite would be recognised during the SOTR surveillance search, but then it would not be tracked by the SOTR radar. Below the surveillance fence, the SAR would not transmit any signal. This scenario implies some restrictions in the observation of limited biomass areas. The SOTR radars with more impact in the coverage would be SOTRs in North Dakota and Greenland, but in particular the SOTR radars with 360° azimuth coverage located in the United Kingdom. For such a case, the coverage would be as marked in red in Fig. 5.42.

A limiter placed before the receiver LNA protects the SAR against unwanted high power signals from the SOTR. Wind profilers transmit out of the SAR operating bandwidth and can be easily filtered out.

5.7.4 Contingency Operations

The Biomass satellite is designed to survive for up to 72 hours in the case of a single failure. A hierarchical FDIR concept is employed, which will fall back to safe mode only for serious failures. The mission will not continue operation in case of a major failure.

The FDIR design follows the common concept tailored in five failure levels, based on the degree of intervention:

— Level-0 failures are those associated to an internal single failure in one equipment unit, which can be automatically recovered by the unit itself without any impact on the rest of the whole system hardware devices or software applications. This level of functionality is fully autonomous and may be transparent to the FDIR system.

— Level-1 failures happen when the unit itself cannot autonomously recover. The surveillance is performed by the OBSW through simple health check on acquired parameters and recovery actions are ordered. The failures might also require ground intervention.

— Level-2 failures are identical to those in Level-1 as they are recovered completely by the OBSW. However, they are not confined to a single subsystem and may require recovery actions reaching across several subsystems. The detection of those failures is based on the monitoring of subsystem health and status information and cross-correlated checks of acquired parameters.
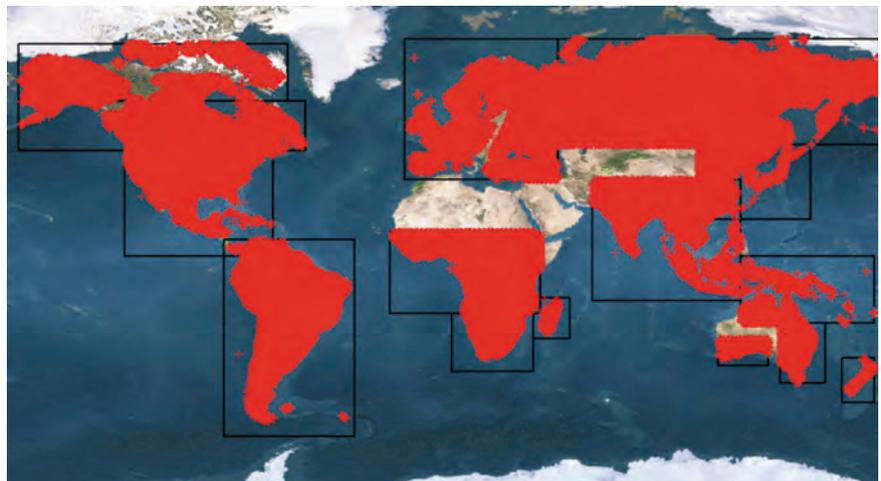
Figure 5.42. Biomass coverage in case of restricted operations below the SOTR surveillance fence.

— Level-3 failures are OBC internal and cannot be neutralised autonomously by the OBSW, and as such are distinctly more severe than Level-0 failures. The recovery is done by hardware via the OBDH reconfiguration module.

— Level-4 failures are those that have not been detected and recovered at lower levels and managed completely by hardware through proper independent system alarms hardwired to the relevant reconfiguration module. These failures are considered as global satellite malfunctions.

A fundamental aspect of an FDIR approach is that survival of the satellite has priority over availability during all phases of the mission lifetime of the satellite. To ensure satellite safety the transponder is completely managed in hot redundancy, i.e. being fail operational without outages.

All FDIR functions implemented in the OBSW are triggered by parameter values stored in the satellite. These functions can be enabled or disabled via TC from ground and may be adapted and set according to the operational needs. A history log stores any FDIR data for investigation on ground. The ground station has the final overall control over all failure recovery activities even if the satellite performs them autonomously.

→ SCIENTIFIC DATA PROCESSING AND VALIDATION CONCEPT

6. Scientific Data Processing and Validation Concept

Biomass proposes a unique approach for estimating forest biomass from P-band polarimetric and interferometric measurements. The processing chain, starting with the PolSAR and PolInSAR covariance matrices, is schematically shown in Fig. 6.1. After calibration for system-induced distortions and ionospheric effects, the radar data, together with the required auxiliary data, are input into the Level-2 product generation algorithm that produces biomass maps. During the Calibration & Validation (Cal-Val) phase of the mission, these maps are validated against ground measurements. A key role in the Cal-Val strategy for Biomass is played by analysis and evaluation of the data collected during the tomographic phase; this will provide crucial insight into how the Level-2 product generation algorithm should be adapted for different forest biomes.

Biomass estimation from P-band PolSAR and PolInSAR data relies on statistical and physical models of the relation between the observables and forest biomass. Initially, two independent estimates of biomass are performed in parallel. One uses the full set of polarimetric data (i.e. HH, HV and VV), suitably corrected for topographic and environmental effects, to give robust algorithms that can be transferred between test sites. The other derives forest height from PolInSAR data, and exploits the physical relation between height and biomass to derive a biomass estimate. Both estimates are then combined using a minimum mean square error (MMSE) approach to yield a final biomass estimate, together with its error, which optimally compensates for the uncertainties in the individual approaches. A schematic of the proposed algorithm is shown in Fig. 6.2.
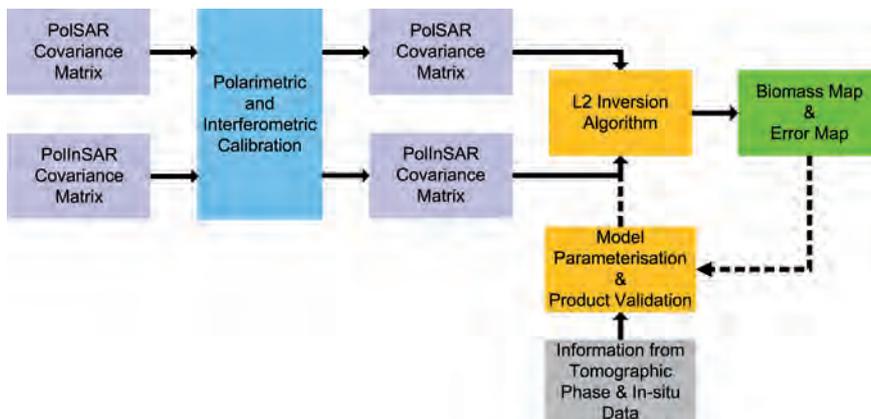
Figure 6.1. The end-to-end processing, retrieval and Level-2 Cal-Val chain. (ESA)
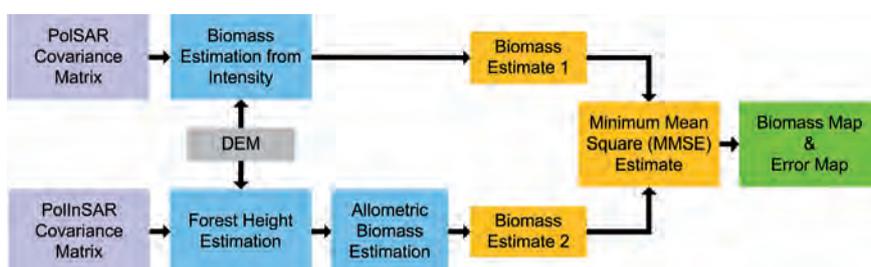
Figure 6.2. Level-2 product generation algorithm. (ESA)

123

6.1 Level-2 Algorithm

The development of the algorithms was strongly influenced by data collected during the three boreal and three tropical campaigns described in Chapter 4 (Table 4.1). From the associated analysis, it became clear that there are strong differences between boreal and tropical ecosystems and that different biomass estimation algorithms are required for each forest type. These are described in the following, first for PolSAR using intensity measurements, then PolInSAR, and finally for the combination of the two biomass estimates using a MMSE approach.

6.1.1 Estimating Biomass from Polarimetric Intensities

The proposed algorithms to estimate forest from PolSAR data combine statistical and physical concepts to develop regressions between biomass and intensity measurements derived from the full HH–HV–VV covariance matrix. Though building on earlier work, the new campaign datasets collected as part of the Biomass studies have allowed new algorithms to be developed. These overcome the limitations of past methods in tropical forests with high levels of biomass, in hilly terrain, and in forests with different structures that are prone to temporal variations of SAR intensity caused by soil moisture variations.

Boreal and tropical forests exhibit different polarisation and temporal behaviours, arising from different physical scattering mechanisms (see Chapter 4). Hence they require specific pre-processing techniques and combinations of polarisations to optimise biomass retrieval.

6.1.1.1 Boreal forests

The algorithm to estimate biomass from polarimetric intensity data for boreal forests has been developed and refined using the experimental data collected during the BioSAR-1 and -2 campaigns. Important observations underpinning the inversion algorithm include:

— Single-date data from the BioSAR-1 campaign in Remningstorp show that the HH and HV intensities exhibit good sensitivity to biomass, with HH giving slightly better retrieval accuracy than HV. In contrast, VV backscatter shows poor sensitivity to biomass (Sandberg et al., 2011).

— Data from BioSAR-1 in Remningstorp and BioSAR-2 in Krycklan show that multiple polarisations are needed to reduce the influence of soil moisture variations and forest structure across test sites and dates (Ulander et al., 2011b; Soja et al., 2012). For example, the stand-level backscatter decreased by up to 2–3 dB, depending on polarisation, when the conditions changed from late winter (wet) to early summer (dry).

— On average, there is a difference of about 2–3 dB between the sites for BioSAR-1 (boreal forest in southern Sweden with little topography) and those for BioSAR-2 (boreal forest in northern Sweden with significant topography). In addition, the spread in backscatter can be up to 6 dB for HV and 8 dB for HH and VV for some biomass levels when all stand-level data are combined. This is not because of fundamental differences in the underlying response of the radar to biomass, but results from soil moisture variations, topography and forest structural differences; the inversion algorithm is specifically designed to counter these effects, as described below.

— Ground topography greatly influences backscatter. The largest effect is observed for HH, since it is sensitive to local topography through the ground-

trunk double-bounce mechanism within the first Fresnel zones (Hallberg et al., 2008). The HV data are less affected, and can be compensated to first order by using the backscattering coefficient γ^0 instead of σ^0, where $\gamma^0 = \sigma^0/\cos\Theta_i$ and Θ_i is the local incidence angle.

A crucial insight from the BioSAR data analysis was that much of the variability can be mitigated by exploiting the polarisation ratio VV/HH, because: (1) forest structure has similar effects on VV and HH, and (2) moisture conditions have less influence on the ratio than on the individual linear polarisations. This led to the following linear model for biomass with four regression coefficients (Soja et al., 2012).

$$\log_{10}(B) = a_0 + a_1 \cdot \gamma^0_{HV} + a_2 \left(\gamma^0_{VV} - \gamma^0_{HH} \right)$$
$$+ a_3 \cdot u \cdot \left(\gamma^0_{VV} - \gamma^0_{HH} \right)$$

(6.1)

where B is biomass in t ha^{-1} and all the γ^0 backscattering coefficients are expressed in dB (so the last two terms effectively involve the VV/HH polarisation ratio). The last term is a topographic correction of the polarisation ratio which compensates for the reduction in double-bounce backscattering when the angle between ground and trunk deviates from 90°. It includes the local slope, u, relative to the vertical, estimated using the SRTM DEM with a 50 m grid. This is always taken to be positive, so the correction has the same sign whether the surface is sloping towards or away from the radar line of sight.

The regression coefficients a_i are determined using training data. One of the most striking and important results of the BioSAR analysis was that, despite the Krycklan and Remningstorp test sites being located ca. 700 km apart and having different types of boreal forests, the linear regression model (Eq. 6.1) developed at Krycklan can be applied unchanged to Remningstorp (Soja et al, 2011). The reverse was not true. This is because the Krycklan site includes a much wider range of biomass, forest structure, moisture conditions and topography than Remningstorp, allowing a more generally applicable regression to be formed. This is strong evidence for the boreal algorithm being stable and robust, as long as the training data cover the range of conditions to be met in the regions where it will be applied. A biomass map for the Remningstorp test site using Eq. 6.1 with parameters derived from the Krycklan site is shown in Fig. 6.8.

6.1.1.2 Tropical forest

Biomass estimation in tropical forest builds on earlier methods (e.g. Hoekman et al., 2000; Saatchi et al., 2007b) that exploited multiple polarisations and topographic correction to derive biomass in tropical forests with biomass less than 300 t ha^{-1} and with moderate topography. The TropiSAR campaign in the Paracou and Nouragues forests, French Guiana, was designed to provide multitemporal datasets that would support the extension of these methods to higher biomass and steeper slopes, as is often encountered in tropical forests. Two key findings from TropiSAR illustrate that different issues need to be addressed in tropical as compared to boreal forests, and provided basic insights underpinning the construction of the retrieval algorithms.

Tropical rain forests are characterised by high biomass density (up to 500 t ha^{-1} or greater), and structured in different layers, in which the main canopy layer contains the largest trees (up to 800 trees of more than 300 species, typically 30–45 m high), and an emergent layer reaching a height of 45–55 m. However, little serious effort has been made in the past to recover values above 250–300 t ha^{-1} because the sensitivity of backscatter to biomass in this range is easily masked, for example, by calibration errors or lack of

adequate *in situ* data for testing. Recovering the biomass signal needs both accurate calibration and careful correction for topographic effects.

Correction for topographic effects has two aspects: (1) correctly accounting for the volume contained in the SAR resolution cell; (2) accounting for the varying contributions of the dominant scattering mechanisms, i.e. volume scattering and double-bounce scattering arising from changes in local incidence angle.

The forest backscatter tends to be stable: the seven flights carried out during the 22 days of the TropiSAR campaign exhibited remarkable stability, with backscatter measured at the sample plots varying by less than 0.3 dB in all polarisations despite several rain events during the campaign period (Dubois-Fernandez et al., 2011). Soil moisture does not tend to change rapidly so is a much less important issue than in boreal forests.

Statistical analysis of the relationship between the backscattering coefficient and biomass, together with information on the scattering mechanisms derived from tomography (Ho Tong et al., 2012) and electromagnetic modelling using the MIPERS model (Villard et al., 2012), showed that double-bounce scattering can be significant. This was particularly the case for higher biomass forests (exceeding 200 t ha^{-1}) in hilly terrain, as is typical of many of the world's tropical forests. Here topography acts to enhance a double-bounce contribution coming mainly from branches in the forest canopy. Such conditions apply to most of the forest plots studied in French Guiana; these have biomass ranging from 250–450 t ha^{-1}, and 70 out of the 90 plots are on slopes exceeding 4°.

Surface slopes not only affect the relative importance of the scattering mechanisms, but also cause polarisation orientation changes, since, for a tilted surface, the horizontally polarised electric field is no longer parallel to the surface. The ensuing polarisation distortion can be corrected (Lee et al., 2001; Lee & Ainsworth, 2011), making it possible to measure and remove the double-bounce, which is not relevant for biomass estimation. This leads to a biomass indicator given by: $0.5|HH+VV|^2+2|HV|^2$ which is proportional to the total backscatter after subtracting the power from double-bounce scattering. Corrections are then needed for changes in effective scattering area induced by slope and, in dense forest where the signal is severely attenuated by the canopy, the shape of the effective scattering volume. Both corrections can be accomplished using a normalisation factor, N^0 (Villard et al., 2012), yielding the final form of the biomass indicator, t^0, in high biomass forests with significant topography as:

$$t^0 = \left\langle \frac{1}{N^0}\left(\frac{1}{2}\,|\,HH + VV\,|^{\,2} + 2\,|\,HV\,|^{\,2} \right) \right\rangle \qquad (6.2)$$

Biomass is derived from t^0 by a simple linear regression:

$$\log_{10}(B) = a_1 t^0 + c_1 \qquad (6.3)$$

where B is biomass in t ha^{-1} and t^0 is in dB; a_1 and c_1 are parameters derived from calibration data.

The above approach is specifically designed to address the important case of high biomass tropical forest in hilly terrain with steep incidence angles. However, for lower biomass tropical forests with moderate topography (typically with slope less than 4°), it is more appropriate to use the normalised backscattering coefficient, γ^0, as in the boreal case. The HV backscatter has the highest dynamic range amongst all the linear polarisations (e.g., the contrast between grasslands and high biomass forests observed in TropiSAR data is 14 dB, 18 dB and 9 dB for HH, HV and VV respectively), and is best suited to biomass inversion (Le Toan et al., 2011). However, all the polarisations are used to correct the coherency matrix as above. Biomass is then derived from the normalised backscattering coefficient γ^0_{HV} by the equation:

$$\log_{10}(B) = a_2 \gamma^0_{HV} + c_2 \qquad (6.4)$$

where B is biomass in t ha^{-1} and γ^0_{HV} is given in dB. The parameters a_2 and c_2 can be derived using ground data. However, the value for a_2 is already available because the sensitivity of backscatter to biomass is stable, as illustrated in Fig. 4.1, though local conditions may lead to some slight modification. The absolute level term, c_2 (which accounts for variations in sensor, processing, site characteristics and temporal variation), can be estimated using a limited amount of ground data.

For scenes with varying characteristics that require the use of both γ^0_{HV} and t^0, biomass estimates from the two measures are combined using linear weighting:

$$B = \alpha B(\gamma^0_{HV}) + (1 - \alpha)B(t^0) \qquad (6.5)$$

where $B(t^0)$ and $B(\gamma^0_{HV})$ are the biomass values derived from Eq. 6.3 and 6.4, and the weight α is defined by:

$$\alpha = 1 - \frac{B(\gamma^0_{HV})}{B_{Max}} \qquad (6.6)$$

where B_{Max} is the maximum value of $B(\gamma^0_{HV})$ occurring in the scene.

Figure 6.3 presents the ensuing biomass map for Paracou. It is very important to note that the regression was trained using four forest plots in Nouragues, which is located about 100 km from Paracou and has more marked topographic conditions, but is still valid at Paracou. This is confirmed by the plot of retrieved vs. *in situ* biomass for 77 plots at Paracou (Fig. 6.3). As for the boreal case, this illustrates that only a limited amount of ground data is likely to be needed to carry out biomass mapping at regional scales.

Note that the French Guiana test site contained only a small number of lower biomass stands and these were untypical (e.g. coconut), hence only the simple general inversion scheme (Eq. 6.4) was used here for the lower biomass regions. More powerful approaches exploiting all the polarisations have been developed to counter soil moisture fluctuations and topographic variation for lower biomass tropical forests. These have been successfully applied (Saatchi et al., 2007b) and would form part of the global inversion scheme.

Figure 6.3. Left: Biomass map at a spatial resolution of 50 m for the Paracou forest, French Guiana, based on training on four plots in the Nouragues forest. Biomass inversion is applied only on the forest, which is shown in green, with biomass from 0 to 600 t ha^{-1} indicated by the colour bar. Water and bare surfaces are shown in dark & light blue respectively. Right: Plot of retrieved vs. *in situ* biomass at the 77 Paracou sample plots. (CESBIO)
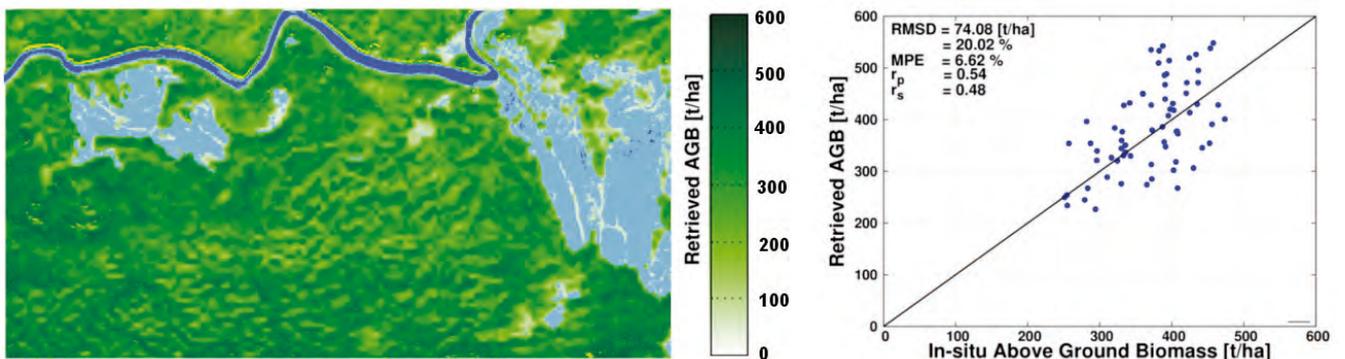
Figure 6.4. Parameterisation of the vertical distribution of scatterers F(z): a) Generalised RVoG model, b) RVoG with exponential vertical distribution of scatterers in the volume layer. (DLR)
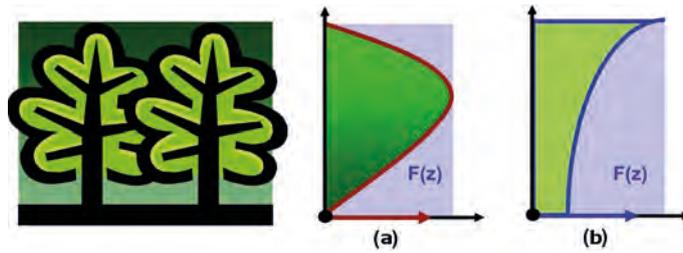
6.1.2 Estimating Biomass from Interferometry

6.1.2.1 Forest height retrieval

As discussed in Chapter 4, the volume contribution $\tilde{\gamma}_{Vol}$ of the interferometric coherence is directly related to the vertical distribution of the scatterers, F(z). Accordingly, the estimation of forest height relies on the reconstruction of F(z) from $\tilde{\gamma}_{Vol}$ measurements performed for different spatial baselines and polarisations (Cloude & Papathanassiou, 1998, Papathanassiou & Cloude, 2001). An effective way to do this is to parameterise F(z) in terms of a limited set of forest parameters by means of a scattering model. A simple but widely and successfully used model is the Random Volume over Ground (RVoG) model. In this, F(z) is modelled as an extended volume layer of height equal to the canopy height, located over a ground layer that scatters like a Dirac function (see middle panel in Fig. 6.4). The propagation through the volume is assumed to be independent of polarisation.

Studies have shown that a particularly useful and effective assumption is that the scatterers in the volume are exponentially distributed (as indicated on the right of Fig. 6.4) and that there is a polarisation channel with a negligible ground component. In this case, the model can be inverted from a single quad-polarised interferometric acquisition without needing *a priori* information (Papathanassiou & Cloude, 2001; Praaks et al., 2006; Lee at al., 2008; 2010; Dubois-Fernandez et al., 2008; Garestier et al., 2008; Kugler et al., 2007; Hajnsek et al., 2008; Garestier & Le Toan, 2010b).

The validity of the model assumptions on F(z) are critical for inversion performance. For tropical and temperate forests the assumption of an exponential reflectivity leads to unbiased and accurate estimates, in less dense forest, such as occurs at the Remningstorp and Krycklan sites, the heights appear systematically underestimated and have a wider spread (see Fig. 6.5). This can be compensated by using a more flexible parameterisation of the vertical reflectivity that includes an increasing scattering contribution at lower heights. This can also account for non-negligible ground scattering in all polarisations. However, in this case, the inversion requires one or more additional interferometric acquisitions, as discussed in Chapter 7.
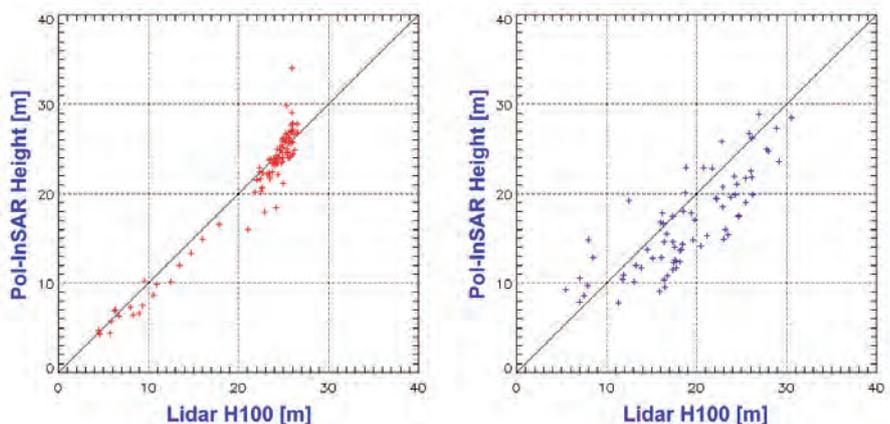
Figure 6.5. Plots of PolInSAR single-baseline forest height vs. lidar top height. Left: Mawas site, Borneo; Right: Remningstorp site, Sweden. For the inversion, an exponential distribution of scatterers in the volume layer and a polarisation channel with a negligible ground component were assumed. (DLR)
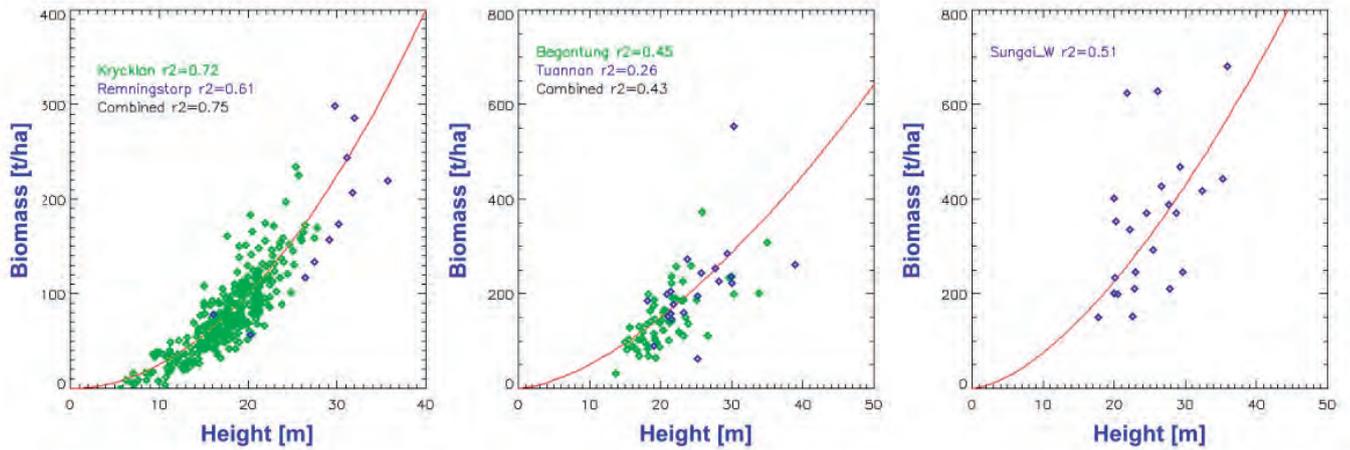
Figure 6.6. Height to biomass allometry for boreal (left) and tropical forest test sites (middle and right). Left: Remningstorp site stands in blue and Krycklan site stands in green. Middle: Tropical peat swamp forest (Mawas site): riverine forest (Tuannan) in blue and a peat dome forest (Begantung) in green. Right: Lowland dipterocarp forest (Sungai Wain site). (DLR)

6.1.2.2 Converting height to biomass using forest allometry

Forest height measurements derived from PolInSAR are converted to biomass using height to biomass allometric relations. A close relationship between height and biomass was first described by Eichhorn in 1902 and has since been refined and extended (Assman, 1961; Pretzsch, 2001). Based on theoretical considerations, Enquist et al. (1998) derived a power law relationship between forest height and biomass, and this has been developed and validated using height derived from remote sensing data (Mette et al., 2007) in the form:

$$B = l_a \cdot 1.66 \cdot H^{1.58} \tag{6.7}$$

Here B is biomass, H is forest height and the allometric level, l_a, acts as a height-related density measure. It accounts for forest types characterised by different growth conditions and natural (or anthropogenic) thinning and distortion (Woodhouse, 2006). For most forest conditions, l_a lies between 0.4 and 1.5.

Figure 6.6 shows the height to biomass relationship derived from ground inventory data and measurements performed in the frame of recent ESA airborne campaigns. On the left, the height to biomass allometry for boreal and semi-boreal forest conditions is shown; this includes the Remningstorp (12 plots in blue) and Krycklan (31 plots in green) stands. Both sites may be represented by a single allometric level, l_a, of 0.8. The other two plots in Fig. 6.6 show the height to biomass allometry in tropical forests: on the left is Mawas (tropical peat swamp forest) and on the right Sungai Wain (lowland dipterocarp forest). For Mawas, the allometric level is 0.6 but Sungai Wain has the value 0.5. In both tropical cases the variance of the allometric relation (Eq. 6.7) is higher than in the boreal case.

The allometric variance of the tropical sites is partly a result of the relatively small plot sizes used (Mawas: 20×20 m and 30×30 m; Sungai Wain: 25×35m). For most forests, the height to biomass relationship becomes more stable with increasing plot sizes. This particularly applies to tropical and heterogeneous forest conditions, as demonstrated in studies in Malaysia, French Guiana, Venezuela/Paraguay, Mexico and Brazil (Chave et al., 2001; Chave et al., 2003; Köhler & Huth, 2010). The large variability in mean biomass and height found in small plots is substantially reduced at a scale of 1 ha, so that a single

Figure 6.7. Reference (left) and combined (right) biomass maps obtained over the Remningstorp test site as well as the biomass maps derived from intensity and PolInSAR forest height. (Chalmers University)

Biomass maps over Remningstorp from BioSAR-1 (2007)

Reference (lidar)   from intensity   from Pol-InSAR   Combined inversion
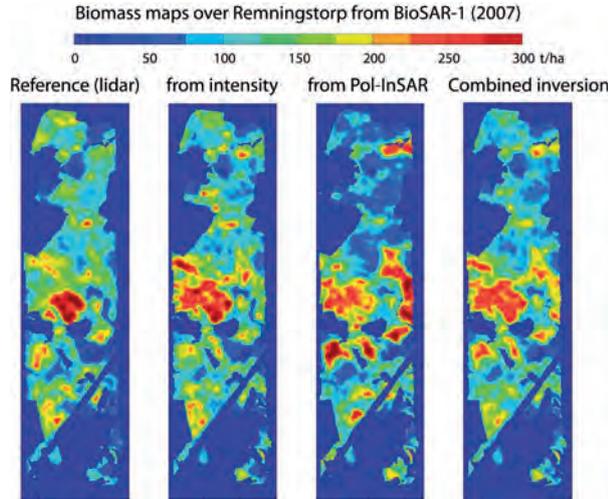
regression equation ($r^2 = 0.9$) could be used for both disturbed and undisturbed tropical forest (Köhler & Huth, 2010):

$$B \approx 0.07 \cdot H^{2.4}$$

(6.8)

6.1.3 Estimating Biomass from Combined Intensity/ Interferometry Data

The two biomass estimates from PolSAR, b_1, and POLinSAR, b_2, are combined using a Bayesian MMSE approach based on unbiased and gaussian distributed biomass estimates, where the standard deviations are derived from the validation data. Figure 6.7 shows boreal results from this approach. The reference map for the Remningstorp test site, shown in the left panel, is based on lidar and *in situ* data and has an accuracy of about 25 t ha^{-1}; the biomass maps derived from PolSAR and PolInSAR height are shown in the centre; and the combined biomass map is on the right. A systematic influence of tree species on PolInSAR biomass is found (pine is overestimated, spruce underestimated), and the combined estimate leads to reduced variance. It is important to note that the intensity model (Eq. 6.1) used to derive the PolSAR map was trained on data from the Krycklan test site, which is located about 700 km away.

Figure 6.8 shows a comparison of the PolSAR (left), height-based (middle) and combined biomass estimates for Paracou. Despite the topographic correction, residual topographic effects are clearly visible in the PolSAR data at 25 m resolution; combination with PolInSAR proves very beneficial in removing them. It also improves the retrieval performance measured at the reference forest plots, as discussed in Chapter 7.

Intensity   PolInSAR   Intensity & PolInSAR
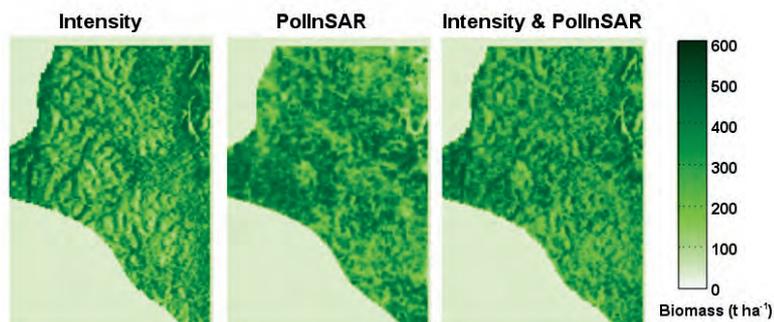
Figure 6.8. Biomass maps derived from PolSAR (left), PolInSAR (middle) and their MMSE combination (right). (CESBIO)

6.2 Mitigating and Correcting Ionospheric Effects

Because the ionosphere could compromise the mission objectives, ionospheric correction is considered as part of the scientific data processing. As shown below, the strategy for dealing with the ionosphere does not rely solely on correction methods, but uses a wise choice of orbit to reduce some potentially disturbing effects to negligible proportions.

Orbital SARs use propagation paths that traverse the ionosphere, giving rise to anisotropic deviations of the refractive index from unity that can have three main effects on spaceborne SAR data:

— Faraday rotation, which is a change in the polarisation state of the propagating wave.

— Scintillation, caused by uncorrected perturbations of the phase front along the synthetic antenna.

— Differential refractive group delays caused by changes in the ionosphere between image acquisitions.

There are associated degradations in backscattering coefficient, polarimetric and interferometric measurements and image geometry. These increase with wavelength, being negligible at C-band, measurable in data from the L-band PALSAR sensor, and potentially serious at P-band. Other propagation effects, such as refraction and dispersion, are negligible at P-band under the 6 MHz bandwidth available under ITU-R regulations (Shteinshleiger et al., 1997).

Both FR and ionospheric group delay are directly proportional to the Total Electron Content (TEC), which is the integrated electron concentration along the propagation paths used by the SAR; geometric distortion is affected by gradients in TEC. TEC has large diurnal and seasonal variations, strong dependence on the 11-year solar cycle, and further stochastic time-variation due to magnetic disturbances. It exhibits marked large-scale spatial structure, with different types of behaviour in the Tropics, mid-latitudes, auroral zones and polar caps. These broadly predictable patterns of behaviour allow us to make representative maps of FR (Fig. 6.9 left), though these are often perturbed by stochastic events, such as magnetic storms. In addition, small-scale variations (irregularities) in electron concentration occur over a wide range of spatial and temporal scales, with the most severely affected regions being the post-sunset equatorial zone, the auroral zones and the polar caps (Fig. 6.9 right).

6.2.1 Correcting Faraday Rotation

Faraday rotation would have very damaging effects on P-band polarimetry if left uncorrected. The largest effects are on the HV backscattering coefficient (Wright et al., 2003), which is a key measurement for retrieving biomass (see Subsection 6.1.1). Faraday rotation as large as is shown in Fig. 6.9 would cause errors of several dBs in the HV channel, and smaller errors in the co-polarised channels. However, measurement and correction of FR is straightforward from the image data, as long as polarimetric data are available. In this case, redundancy in the four polarimetric measurements at each pixel (HH, HV, VH and VV), in particular the fact that the true values of HV and VH should be the same for natural media, yields a system of equations that can be solved to derive FR from the distorted measurements.

Several algorithms have been developed to do this (Bickel & Bates, 1965; Freeman, 2004; Qi & Jin, 2007; Chen & Quegan, 2010). These have different strengths and weaknesses (for example, resistance to system noise or system errors, dependence on properties of the underlying scene, etc.), as investigated
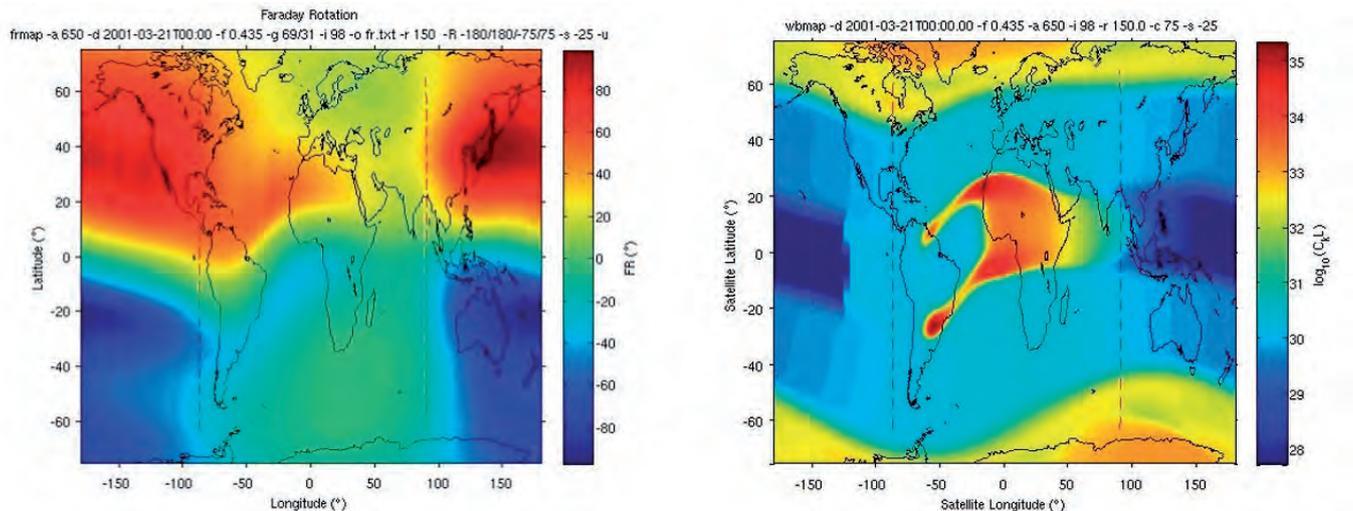
Figure 6.9. Predictions for 00:00 UT on 21 March 2001 (near solar maximum: sunspot number = 150) and geomagnetic index K_p = 3 for a P-band SAR in a 98° inclination, orbit at 650 km and look-angle 25°. Left: Faraday rotation (degrees) derived using the International Reference Ionosphere and International Geomagnetic Reference Field models. Right: The 75th percentile of integrated strength of turbulence (CkL, in electrons^2 m^{-2}, shown on a log$_{10}$ scale) from the Ionospheric Scintillation Model WBMOD model. Scintillations give significant effects for values of CkL > 10^{32}. The vertical red dashed lines indicate the solar terminator; midnight is at image centre. (University of Sheffield)

in Chen & Quegan (2010) and Kim & Papathanassiou (2010). Hence, the specific algorithm or algorithms used for Biomass will depend on the measured properties of the system when it is in orbit.

However, simulations indicate that FR should be measurable to better than 1°, except in regions of very low backscatter where the data may be dominated by noise (Quegan et al., 2012). The distorted image data can then be corrected by multiplying by a simple rotation matrix. Even under the most conservative assumptions, this gives an error in the HV return of less than 0.03 dB, and even smaller errors for the co-polarised channels; this is easily sufficient to meet Biomass science objectives. Note that fully-polarimetric data are essential: dual–polarised data does not contain enough information to separate FR from backscatter.

6.2.2 Ionospheric Irregularities & Scintillations

Variations in TEC within the synthetic antenna can cause loss of resolution, reduction in the measured radar cross-section of point targets, increased sidelobes and reduced contrast; the linear component of the induced phase shifts can also cause geometric distortion. A key reason for proposing a dawn/dusk orbit for Biomass is to avoid the intense scintillations in the post-sunset equatorial region (see Fig. 6.9). In this orbit, scintillation is negligible except at high latitudes, as is clear from simulations of Integrated Sidelobe Ratios (ISLRs) that would be seen for Biomass (Fig. 6.10). Only forest regions in the North American sector are significantly affected because:

— this sector contains the magnetic North Pole, so Alaska and Canada lie at high magnetic latitudes.

— the boreal forest zone extends to higher geographic latitudes in this sector than in Eurasia. Furthermore, the effects are only significant when sunspot activity is above the median and during geomagnetic storms (Quegan et al., 2012).
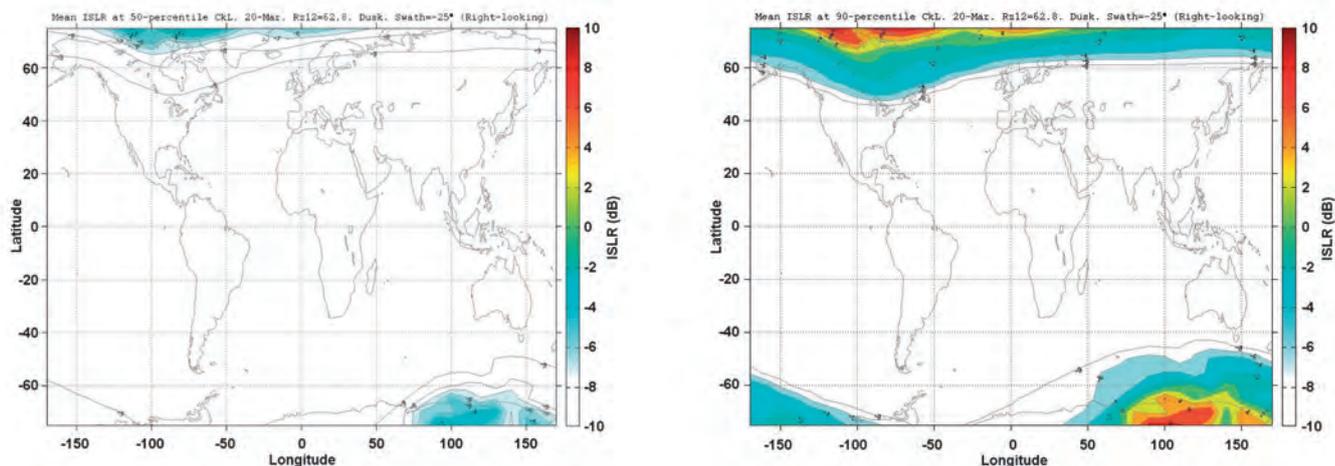
Figure 6.10. Estimated values of the P-band ISLR along the dusk side of the proposed Biomass orbit (local time of descending node = 18:00) at equinox under median sunspot conditions for: (left) median and (right) 90th percentile of strength of turbulence, i.e., performance would be better than this 50% and 90% of the time, respectively. The undisturbed value of ISLR is −9.9 dB. The calculations cover the full range of K_p values. The bottom axis can be interpreted as a 24 hour change in UT as Earth rotates beneath the satellite. Dawn-side results are similar. (University of Sheffield)

Scintillations, therefore, have little impact on Biomass primary objectives, but cannot be ignored for secondary objectives requiring measurements at high latitudes, for example, ice imaging. To counter this, a correction technique for high-latitude scintillation has recently been developed. This derives TEC estimates from measurements of FR and transforms them into an ionospheric phase screen which is used to compensate the scintillations. Preliminary tests based on simulated Biomass data (using airborne P-band data) indicate that (i) under median turbulence, distortions can be corrected for all latitudes, even for K_p values exceeding the 99th percentile, and (ii) for turbulence above the 90th percentile of C_kL, distortions can be corrected for K_p values up to the 75th percentile (Papathanassiou & Kim, 2011). Though further testing is required, this suggests that it may be possible to correct scintillations well enough to meet the needs of high-latitude secondary applications.

6.2.3 PolInSAR, Interferometry and Tomography

Refractive group delays change the absolute phase of the SAR data, and variation in the ionosphere between acquisitions of image pairs distorts their phase difference, with serious consequences for interferometry. However, since PolInSAR is based on relative phase differences between interferograms at different polarisations, and both the absolute and relative phase distortions are the same for all polarisations, PolInSAR is essentially unaffected by ionospheric phase distortions (Quegan et al., 2012). Only polarimetric mismatch due to differential FR and misregistration due to differential TEC gradients need to be corrected; both can be compensated with sufficient accuracy to yield accurate PolInSAR height estimates (Quegan et al., 2012).

For interferometric DEM generation, phase correction methods that exploit stable scatterers and use the full set of acquisitions over the whole Biomass mission are expected to be effective, based on experience with the related problem of atmospheric correction at C-band (Nico et al., 2011). No current approaches seem capable of correcting for phase distortions for individual interferometric pairs.

The impact of ionospheric disturbances on tomography was investigated in a recent ESA study (Iannini et al., 2011). This showed that FR causes negligible loss of performance, as long as it is corrected to within an accuracy of 5°, which is easily accomplished (Subsection 6.2.1). Simulations for fairly disturbed
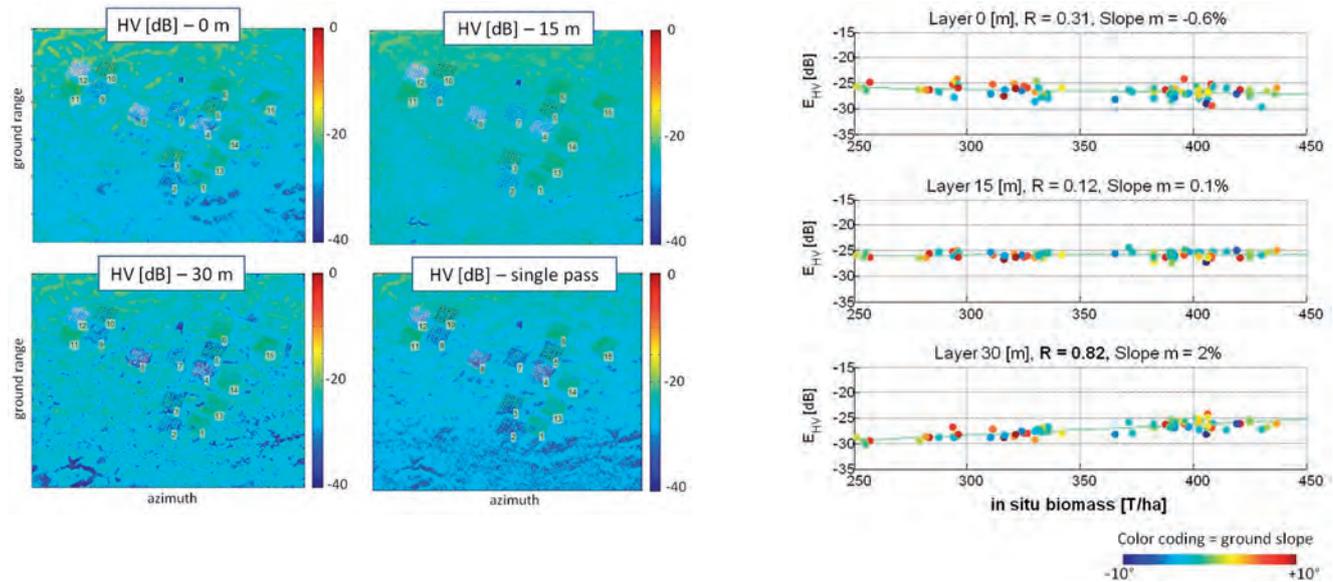
Figure 6.11. Tomographic layering vs. *in situ* biomass measurements using data from the TropiSAR campaign (6 passes). Left: HV intensity for three different tomographic layers (top left: ground level; top right: 15 m above the ground; bottom left: 30 m above the ground) and for non-tomographic data (bottom right). Right: measured correlation between HV intensity for different layers and *in situ* biomass measurements. (POLIMI)

conditions (as may occur at boreal latitudes) also showed that with two or more repeat-pass acquisitions, multisquint interferometry allows scintillations to be estimated and corrected, as long as the scene is temporally coherent and at least one of the acquisitions is scintillation-free.

6.3 Auxiliary Data

6.3.1 Tomography

A key auxiliary dataset will be provided by the Biomass mission itself during its tomographic phase (see Subsection 4.2.3). This is expected to image 10–15% of the world's forests. It will be used to acquire height-resolved measurements of backscattered power at all polarisations from a set of forest biomes representative of all the world's forests. Unlike PolInSAR, these measurements do not rely on any assumptions about the vertical distribution of scatterers in the canopy. The permitted 6 MHz bandwidth means that the height resolution will be about 15 m, allowing 3–4 layers to be separated in mature forest. The tomographic phase will therefore give unprecedented insight into the factors affecting biomass retrieval in different forest biomes. In particular:

— It will identify the dominant scattering mechanisms as a function of height within the canopy, and how these vary with biomes and environmental conditions. This will enable the polarimetric components most closely related to biomass to be identified and exploited in the PolSAR inversion algorithms. It will also help to improve the corrections for ground slopes.

— It will measure the vertical reflectivity profile, thus providing direct insight into how to parameterise the PolInSAR forest height inversion model for different forest biomes.

In addition, the tomographic phase will provide forest height maps, obtained by tracing the upper envelope of the observed tomograms (see Chapter 7),

which can be used to test and optimise PolInSAR inversion, and will yield biomass maps based on *in situ* biomass measurements in the regions covered.

An example of how tomography can help the inversion algorithms is illustrated by Fig. 6.11, which shows the HV intensity for three different tomographic layers and the normal HV image intensity on the bottom right from the Paracou tropical site.

The correlations between *in situ* biomass measurements and the HV intensities for the three layers are shown on the right of the figure. For all terrain slopes, only the 20–30 m layer shows good correlation with biomass (R = 0.82) when biomass exceeds 250 t ha^{-1}. A key implication is that, for high biomass forests, the double-bounce term should be removed before retrieving biomass from PolSAR measurements. This is why this operation forms part of the biomass retrieval method described in Subsection 6.1.1.2.

6.3.2 Global *In Situ* Datasets

Calibration of the Biomass inversion algorithm depends on reliable ground data in a range of environmental conditions, and most critically in tropical rainforests. Estimates of biomass stocks are normally inferred from forest inventories on plots distributed across a landscape. In the context of the Biomass mission, the criteria for site selection include:

— Good coverage in the range 0–500 t ha^{-1} above-ground biomass, spanning the range from bare ground to densely forested landscapes.

— Uniformity on a scale of 4 ha, to accommodate the resolution of the satellite and biomass estimation variability, so highly heterogeneous landscapes are to be avoided.

— Adequate ground measurement of tree height. It would be preferable that the sites have a suitable history of research, so that production and carbon flux data are also available.

Finally, some test sites should be available as chrono-sequences in the same locality, so that they exhibit several stages of recovery from disturbance.

For the temperate zone, an extensive literature-derived database on forest stand structure has been generated by Luyssaert et al. (2007) and includes a total of 297 sites, largely from North America and Western Europe. For the tropical zone, far less primary data are available. In the past, permanent plots have been set up either by forestry institutes (Brown & Lugo, 1992) or by botanists. A concerted effort to organise existing data and to fund new and repeated inventories has led to the Amazon Forest Inventory Network (RAINFOR) project in South America (Malhi et al., 2002), and the African Tropical Rainforest Observation Network (AFRITRON) project in Africa (Lewis et al., 2009). In addition, many tropical forestry institutes have established forestry exploration plots regularly distributed over areas up to 2000 sq. km both in Africa and South America (see Fig. 6.12).

For parameterising the radar inversion algorithms for different biomes, ground plots should be based on large permanent plots with sufficient history on plot establishment and data management. Several of the plots included in the RAINFOR and AFRITRON projects comply with the criteria required for Biomass. In addition, the network of 50 ha plots managed by the Smithsonian's Center for Tropical Forest Science covers all the major tropical forest types (Losos & Leigh, 2004) and will be mobilised for the calibration step, as well as large plot networks established by various national universities or research institutes. The current number of suitable calibration sites exceeds 50 worldwide.
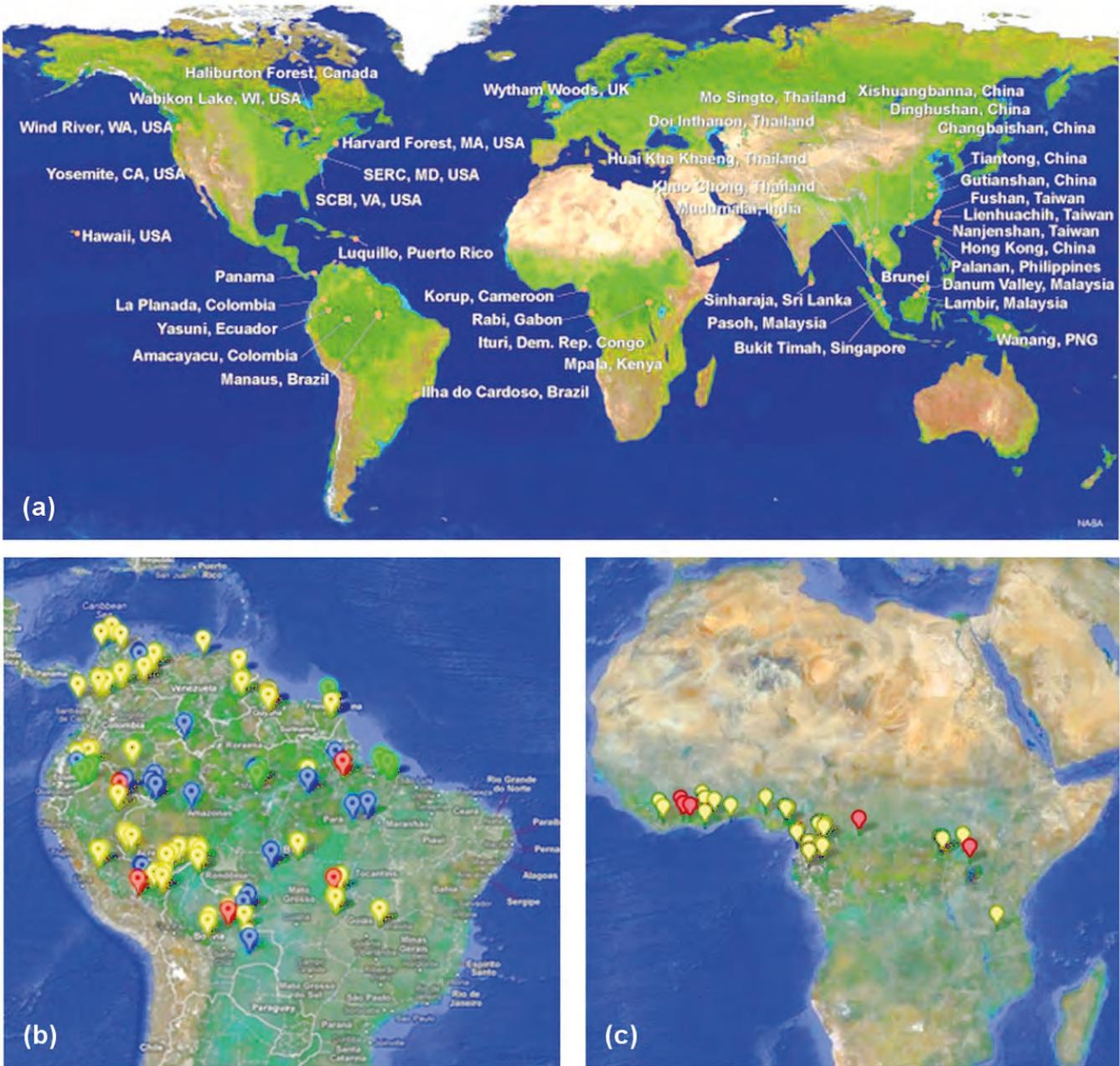
Figure 6.12. Location of forest research plots in three networks: (a) Centre for Tropical Forest Science, (b) RAINFOR and (c) AFRITRON. (Le Toan)

As a complement to *in situ* forestry data, Biomass would benefit from a systematic strategy of small-footprint lidar coverage of the calibration sites. Small-footprint lidar helps in estimating canopy height, constructing digital elevation models, and can even be used to produce small-scale biomass maps (Asner et al., 2010). The Root Mean Square Error (RMSE) of such techniques is relatively low: at 100 m scale, biomass is estimated with an accuracy of 30 t ha^{-1}, or about 10–15% of the mean in a typical tropical forest. Worldwide estimates of tropical forest biomass using the satellite-borne GLAS lidar instrument, though of great value in characterising the large-scale patterns of tropical biomass, are of insufficient accuracy to validate the Biomass instrument (Saatchi et al., 2011).

6.3.3 DEM Data

Biomass requires DEM data: (i) for slope compensation of backscattering coefficients (see Subsection 6.1.1.1); (ii) for calibrating the Biomass DTM to be produced in densely vegetated regions (see Subsection 2.4.2); and (iii) for ice-velocity measurements (see Subsection 2.4.3).

Since the global GTOPO30 DEM was released in 1996, many DEMs with significantly improved quality have become available. Table 6.1 summarises the most important ones, as well as the Biomass DTM. These DEMs are based on a variety of techniques, e.g. single-pass visible near infrared stereo Global Digital Elevation Model (GDEM), radar altimetry (ice sheet DEMs), laser altimetry (GLAxy, ice sheet DEMs), and SAR interferometry (SRTM, TanDEM-X DEM, Biomass DTM). ICESat GLAS data are included in the latest versions of the ice sheet DEMs, while the ICESat GLAS data in the GLAxy products are not real DEMs as they are not raster products. They represent successive laser spots with a diameter of about 70 m and a separation of 172 m along the ground tracks (Schutz et al., 2005), which in turn are spaced by about 80 km at the equator. The GLAxy products are well suited for calibration of the Biomass DTM, as they include information on the return waveform peaks, including a potential ground echo (Harding & Carabajal, 2005). The GLA14 product is also crucial for calibration of the TanDEM-X DEM (González et al., 2010).

During the mission, Biomass will build up a DEM focusing on forested areas. Elsewhere other sensors, such as TanDEM-X provide a superior product, but they cannot provide a bare-earth DEM of forests because the interferometric centre lies somewhere in the forest canopy, which gives a biased height estimate. The Biomass DEM will be available to reprocess the Biomass dataset.

The ice sheet DEMs are based on multiple data sources, including radar altimeter and laser altimeter data. However, these data are not valid at low elevations (near the ice edge of the ice sheets), due to surface slopes. Conversely, stereo techniques are applicable near the ice edge, but cannot be applied at high elevations, where the ice does not have sufficient contrast. Over the ice sheets, application of repeat-pass SAR techniques is complicated by ice motion.

6.3.4 Land-cover Data

Land-cover data will be helpful to the biomass retrieval process for the mission by providing independent information on forest type and, to some extent, structure (for example, distinctions are made between open and closed forest, and evergreen and deciduous foliage). This information will aid in adapting the retrieval algorithms to ground conditions. The extent to which this adaptation is needed cannot be fully established from available datasets, which show that inversion algorithms can be transferred unchanged between widely separated sites (see Subsection 6.1.1).

Table 6.1. Summary of DEM data

	Data source	Release	Coverage	Posting	Height resolution
GTOPO30	Multiple	1996	Global	1 km	30 m
SRTM	SRTM	2003	60°N–54°S	90 m	18 m
GDEM	ASTER	2009	83°N–83°S	30 m	7–14 m
GLAxy	IceSAT GLAS	2003	86°N–86°S	NA	>0.1 m
Ice sheet DEMs	Multiple	1997 and 2001	Ice sheets	5 km	Variable
TanDEM-X	TSX & TDX	2014	Global	12 m	2 m rel., 10 m abs.
Biomass DTM	Biomass	TBD	Forested regions	100 m	20 m

There is a continual process of updating and developing land-cover datasets, so the current situation will not apply by the time of launch. Nonetheless, two representative, well-known and influential global land-cover datasets based on relatively recent satellite data indicate the type of product likely to be available:

— GlobCover, which was created from data acquired with the MERIS sensor onboard the Envisat satellite and has the highest resolution global classification ever produced (Arino et al., 2007). Two global datasets exist, for years 2005 and 2009, with a spatial resolution of 300 m and 23 classes based on the FAO Land Cover Classification System (Di Gregorio et al., 2000).

— Moderate Resolution Imaging Spectroradiometer (MODIS) Collection 5 Land Cover MCD12C1 (MODIS LC) is derived from data from the MODIS Terra & Aqua satellites and is available at 0.05° resolution for years 2001–2007 (Friedl et al., 2010). Pixels are classified into 17 classes defined according to the International Geosphere Biosphere Programme.

Where available, more detailed land-cover maps (e.g. produced by national mapping agencies) could be exploited.

6.3.5 Ionospheric Data

External ionospheric information is needed for removing ambiguities in the corrections for FR described in Subsection 6.2.1. All the algorithms estimate FR directly from the polarimetric data, but for most of them (Bickel & Bates, 1965; Freeman, 2004; Qi & Jin, 2007) the estimate lies in the range $-\pi/4$ to $\pi/4$, while for the Chen & Quegan (2010) algorithm it lies in the range $-\pi/2$ to $-\pi/2$.

However, Chen & Quegan (2010) demonstrate that the global ionospheric TEC maps provided by the Global Navigation Satellite System (GNSS) are of sufficient accuracy to remove these ambiguities for all the algorithms. The International GNSS Service provides bi-hourly global TEC maps with grid-points spaced 5° in longitude and 2.5° in latitude, with overall root mean square error of 3–5 TECU (Mandrake et al., 2005; Sekido et al. 2003).

In Europe, global maps of GPS-measured TEC are available in online databases such as that provided by the Centre for Orbit Determination in Europe (Schaer et al., 2011a; 2011b).The correction also needs a model for the Earth's magnetic field, such as the International Geomagnetic Reference Field, IGRF10 (Olson et al., 2000). This enables FR to be uniquely estimated in the range from $-\pi$ to π.

→ PERFORMANCE ESTIMATION

7.   Performance Estimation

7.1   Introduction

In this chapter, the performance of the proposed mission and system concept is assessed against the mission requirements presented in Chapter 4. In Section 7.2 the performance of Level-1 and Level-2 products as defined in Section 5.4 and Chapter 6 is presented. For Level-1, this is expressed against the radiometric and geometric requirements of the SAR image, whereas for Level-2 (Section 7.3) this is expressed against the geophysical requirements of the scientific data. Finally, the end-to-end ability to produce simulated geophysical results from a synthetic scene is demonstrated to validate the overall data product concept and assess the expected performance of the mission.

7.1.1 End-to-end Simulator

The Biomass end-to-end simulator (BEES) is a tool to simulate and analyse the performance of the mission, i.e. from the observed scene to the retrieved Level-2 geophysical parameters. The simulation starts with maps providing the geophysical description of a forest in terms of biomass distribution. The final outputs of BEES are the estimates of the biomass distribution as observed by the Biomass system. The backscatter characteristics of the input scenes were derived empirically based on campaign data from tropical forests (i.e. TropiSAR, French Guiana) and boreal forests (i.e. BioSAR-1, Sweden). This defines the validity range of the simulations, which is between 300–500 t ha^{-1} for tropical forests and 50–350 t ha^{-1} for boreal forests.

BEES considers the impact of errors from:

— Scene characteristics, including forest structure, geophysical noise and temporal and volume decorrelation.

— The observing system characteristics and errors, including IRF, radiometric bias, stability, NESZ, channel imbalance, cross talk, range and azimuth ambiguities and phase stability.

— Ionospheric effects, including FR, scintillation and TEC gradients.

Temporal decorrelation is simulated for low (0.99), medium (0.95) and high (0.61) decorrelation scenarios. The ionosphere is simulated for mild (Kp=2, CkL=50%) and severe (Kp=3, CkL=90%) states.

Figure 7.1 shows the BEES architecture comprising the following modules:

— The Geometry Module computes the SAR observation geometry (e.g. orbit height, pointing, interferometric baseline).

— The Scene Generation Module generates the test scenes of extended covariance matrices (complex reflectivity including polarimetric and interferometric properties) representing the polarimetric and interferometric backscattering at P-band for the given observation geometry (considering a single-baseline scenario).

— The Observing System Simulator generates the system characteristics affecting the SAR image quality by modelling the instrument IRF and the instrument system errors.

— TzThe Ionosphere Generation Module models the impact of the ionosphere on the SAR observations by simulating FR and scintillation effects.

— The Ionosphere Correction Module models the ionosphere correction residual error affecting the Level-1 product.

— The Level-2 Retrievals Module generates the Level-2 products from the simulated Level-1 data.

— The Performance Evaluation Modules compare the Level-1 and Level-2 outputs with the input scene.

BEES can be used to assess the performance of Level-1 data for boreal and tropical forest scenarios. Assessment of the performance of Level-2 data is currently limited to the boreal scenario owing to delays in the implementation of the tropical inversion method.

7.1.2 Campaign Data

Airborne SAR data were collected over tropical and boreal forests to assess Biomass Level-2 product performance. Reference biomass data were collected to enable realistic RMSE estimates of inversion accuracy. The values of RMSE obtained from full-resolution campaign data, however, are not directly applicable to Biomass since the reduced bandwidth will result in fewer resolution cells being available to average speckle and texture within a given forest area. For example, the number of independent samples (looks) will be about 64 for the Biomass map product at 200 m resolution, whereas many thousands of looks are available within such an area in the airborne SAR data. In order to provide an assessment of the Level-2 inversion performance that is as 'realistic as possible' in terms of scene and instrument characteristics, synthetic P-band fully polarimetric and interferometric datasets were generated from airborne campaign SAR datasets. The simulation of the spaceborne polarimetric and interferometric data is accounted for the Biomass instrument and mission characteristics through successive processing steps (Fig. 7.2):

— Degrade spatial resolution in (slant) range and azimuth (including PSLR and ISLR).

— Degrade NESZ by introducing additive noise.
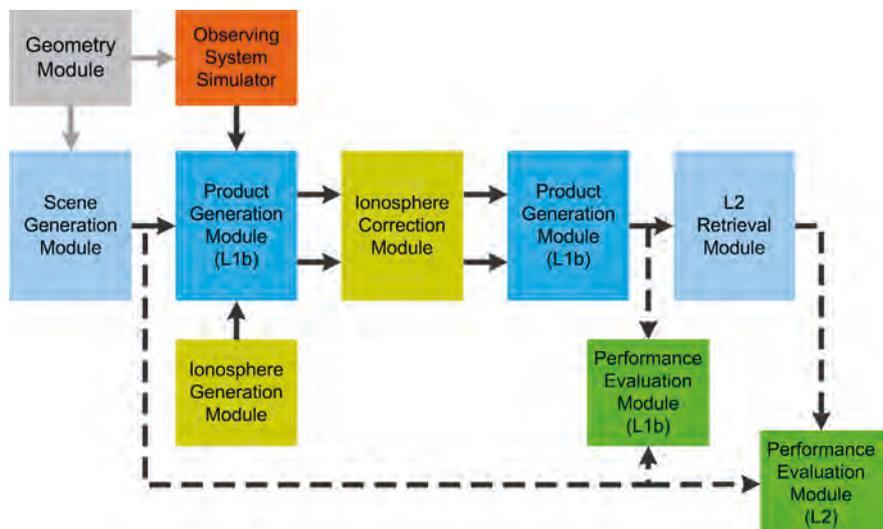
Figure 7.1 High-level block diagram of BEES.
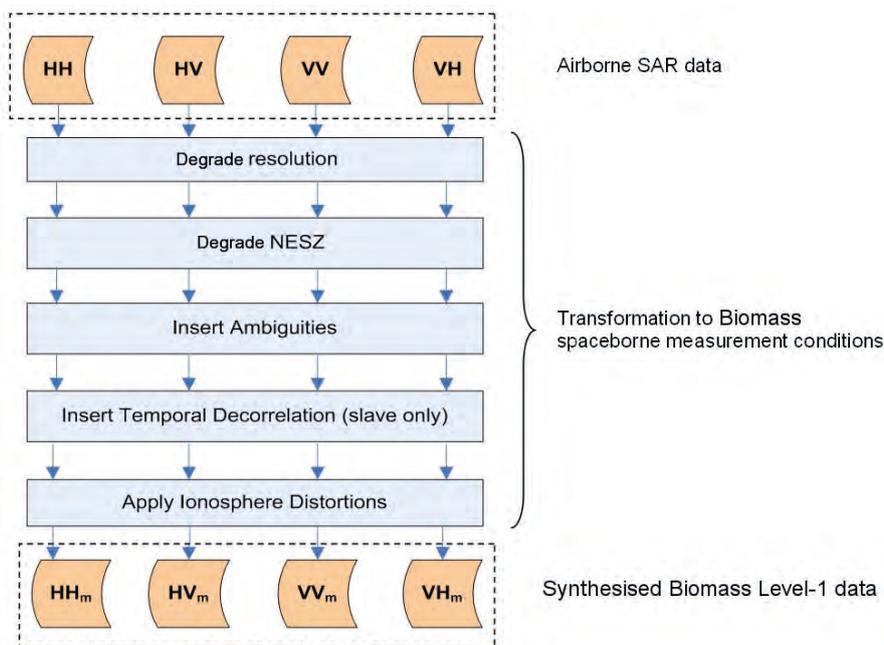
Figure 7.2 Biomass data simulation approach.

— Add range and azimuth ambiguities.

— Simulate temporal decorrelation between images.

— Simulate ionospheric distortions (including scintillation and FR).

7.2   Level-1b Performance

7.2.1 SAR Performance

7.2.1.1   Cross-polarisation ratio

The radiometric performance achieved by the SAR instrument is largely a function of the radiation pattern generated by the antenna subsystem. The azimuth and elevation cuts of the antenna patterns for the H- and V-polarisation are given in Fig. 7.3 for one of the two concepts. The level of cross-polar attenuation achieved within the required main beam regions is better than 29 dB, and it is much better than the goal requirement of 30 dB within the processed Doppler bandwidth of the radar.

7.2.1.2   Noise equivalent and total ambiguity ratio

The variations in the SAR sensitivity and Total Ambiguity Ratio (TAR) as a function of the incidence angle are shown in Fig. 7.4 (the black lines represent the requirements). The HH-polarisation represents the worst-case scenario for the sensitivity analysis, whereas the VH-polarisation is the worst-case scenario for the ambiguity analysis. The dashed and dotted lines show the range of variations owing to the changing satellite altitude over the orbit. The sensitivity requirement is met at the swath edges with margin, and high sensitivity is achieved at the centre of the swaths (<−33 dB).

Figure 7.3. Azimuth and elevation cuts of the antenna pattern in H- (left) and V-polarisation (right) for one of the concepts.
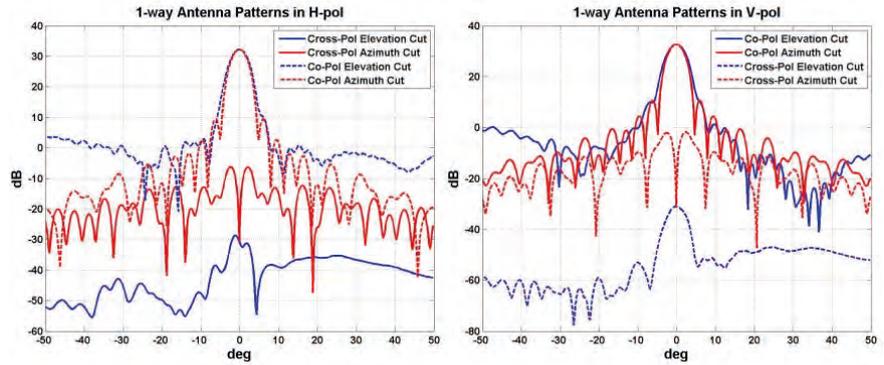
Figure 7.4. Noise equivalent σ^0 (left) and total ambiguity ratio (right) for the double-baseline interferometry option. The solid lines refer to the mean altitude, whereas dashed and dotted lines refer to the maximum and minimum altitude along the orbit. The continuous black line shows the required levels.
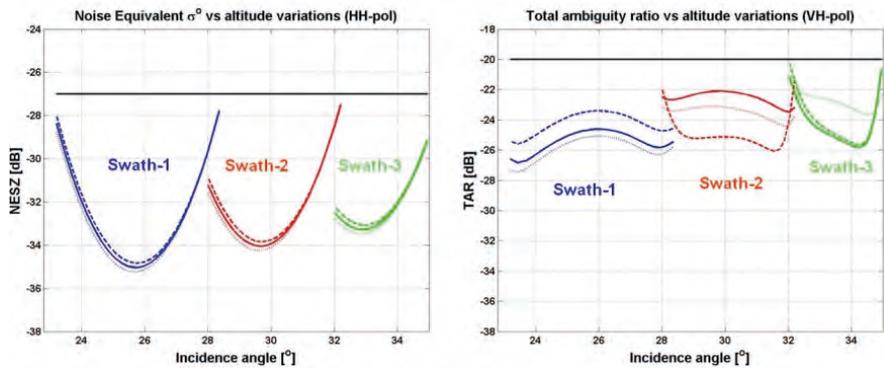
7.2.1.3 Spatial resolution, peak sidelobe ratio and integrated sidelobe ratio

The across- and along-track cuts of the single-look IRF of the SAR system are shown in Fig. 7.5. The IRF, as observed in the output radar imagery, is characterised by a main lobe, where most of the energy is concentrated, and by sidelobes of varying energy content and spatial distribution. The spatial resolution, measured as the half-power width of the IRF, is summarised in Table 7.1.

For both concepts, the IRF analysis has shown that the peak to sidelobe ratio is compliant with the requirement of −16 dB and the 2D integrated sidelobe ratio to the requirement of −9 dB.

7.2.1.4 Radiometric Performance

Two main radiometric parameters are defined for the Biomass mission: the radiometric stability and the absolute radiometric bias. The combination of
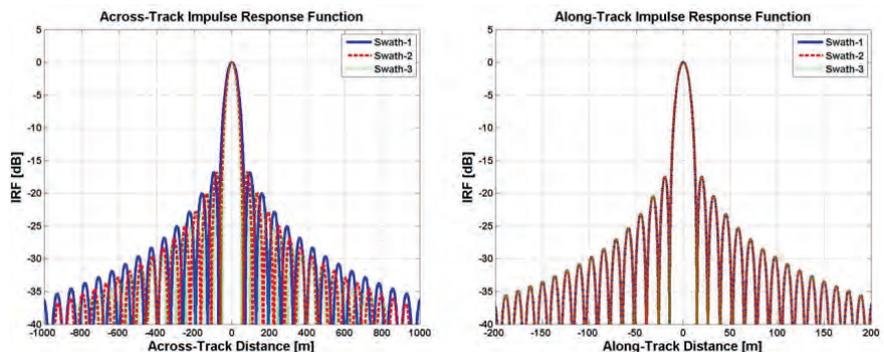
Figure 7. 5. Across- (left) and along-track (right) cuts of the IRF.

	Spatial resolution		
	Swath 1	Swath 2	Swath 3
Across-track resolution [m]	≤60.0	≤51.1	≤44.7
Along-track resolution [m]	≤12.3 single-look ≤49.2 four-looks	≤12.3 single-look ≤49.2 four-looks	≤12.3 single-look ≤49.2 four-looks

Table 7.1. The across- and along-track resolutions are estimated as width at half-power.

these two quantities provides the radiometric accuracy, describing the absolute error in the measurement of σ^0. The radiometric accuracy can be split into these components in different ways, depending on whether a product-oriented approach or an instrument-oriented approach is taken. The basic difference between the two approaches relates to the harmonic errors corresponding to temperature variations along the orbit. In a product-oriented approach, only the measurements corresponding to the same ground-locations can be compared. In this case, the measurements will present a static offset (or bias) that reflects the thermal state at the orbit location where the SAR image is taken, whereas the radiometric stability will only be affected by the thermal variations over the same location. Thanks to the choice of a Sun-synchronous orbit, these variations are expected to be significantly smaller than the total range of temperature variations over the orbit and over the time between external calibrations. In contrast, in an instrument-related approach the complete thermal variation over the orbit and the time between external calibrations contributes to the stability figure, leaving only a systematic error from the external calibration (i.e. an error in the calibration of the transponder itself) in the absolute radiometric bias.

Tables 7.2 and 7.3 show the overall radiometric budgets, where a product-oriented approach has been used. For radiometric stability, harmonic and drift errors are considered, while for absolute radiometric bias, only bias errors are taken into account. The random errors are already included in the evaluation of the instrument IRF and in the computation of the noise equivalent σ^0, so they are not part of the following budgets. The error types are classified according to their time dependence. The bias errors are residual fixed offsets, which are stable over the entire lifetime of the mission. They are assumed to have a uniform distribution within a certain interval around the nominal value. Drift errors are variations due to ageing effects, which appear as slow variations in time from zero to a peak value D. Within the interval D the drift errors are assumed to have a uniform distribution. Harmonic errors have a periodic behaviour along the orbit, with mean value zero (thus, they do not contribute to the bias error) and peak value H. The random errors are all those unpredictable variations quicker than the synthetic aperture time of the instrument. Bias and drift errors are quadratically summed to achieve the total bias error and the total drift error, respectively. The harmonic errors can also be quadratically summed, as long as they have different period or their relative phase is non-zero.

The radiometric stability is defined as the standard deviation of the measurements taken at different times of the radar cross section of an invariant target, of such magnitude that receiver noise is insignificant, with the system operating within its dynamic range. Perturbations owing to the propagation path of the electromagnetic signal are neglected.

As shown in Table 7.2, the pointing AKE is the biggest contributor to the radiometric stability. The AKE is the separation between the actual and measured payload pointing vector, and it causes uncertainty about the exact direction in which the SAR beam is pointed. In order to have a maximum AOCS error contribution of 0.2 dB in the RS budget, the absolute pointing knowledge error must be less than 0.03°. As already discussed at the beginning of this section, thermal variations affect not only the overall pointing stability (because of thermo-elastic deformations of both antenna-reflector and feed

Table 7.2. Radiometric stability budget (requirement is less than 0.5 dB).

Radiometric stability	Sensitivity	Error (1σ)	dB RMS
Knowledge errors			
AOCS error (AKE)	6.25dB/°	0.030°	0.1875
Harmonic errors			
S/C thermo-elastic pointing stability	6.25dB/°	0.002°	0.0125
Antenna thermo-elastic pointing stability	6.25dB/°	0.030°	0.1875
Antenna electrical pointing stability	6.25dB/°	0.017°	0.10
Antenna gain thermal variations	1	0.10 dB	0.10
Internal calibration stability error	1	0.07 dB	0.07
External calibration stability	1	0.10 dB	0.10
$h\mid_{1\sigma} = \sqrt{\sum_i \left(\dfrac{H_i}{\sqrt{2}}\right)^2}$			0.32
Drift Errors			
External calibration (ageing)	1	0.10 dB	0.10
Internal calibration error (ageing)	1	0.10 dB	0.10
$d\mid_{1\sigma} = \sqrt{\sum_i \left(\dfrac{D_i}{\sqrt{3}}\right)^2}$			0.14
Radiometric stability $\sqrt{(d\mid_{1\sigma})^2 + (h\mid_{1\sigma})^2}$			0.35

array), but also the antenna gain (because the antenna frequency changes with the temperature).

The absolute radiometric bias, on the other hand, is defined as the bias in radar cross-section within the scene and over time and includes errors from processing and calibration. Table 7.3 provides the overall bias budget and values for the main contributors; of which, the external calibration error deserves special attention. The external calibration is based on the use of active transponders, which simulate a point target with calibrated cross-section. The transponders produce time-delayed echoes so that the received signal is less affected by ground clutter contamination. Measurements of the antenna pattern are taken at several elevation angles. The combination of these measurements with those performed over uniform distributed targets (such as deserts), allows the 2D antenna pattern to be retrieved. This calibration procedure is subject to the following errors:

— Transponder calibration errors.

— Processing and interpolation errors (including noise-subtraction errors, and all those errors in converting the measured point target response to the distributed target response).

— Bias errors that reflect the thermal state at a specific orbit location.

The budget in Table 7.3 does not include the bias errors that are known, and can be compensated in the ground processor. Among them is the APE, which is the separation between the actual and commanded payload-pointing vector; it generates a bias in the radiometric budget. The APE is constrained to about 0.1° in elevation and 0.39° in azimuth by the instrument requirements in terms of NESZ and TAR, as depicted in Fig. 7.6. The need for sufficient overlap between the Doppler bandwidths of data products so as to be interferometrically correlated imposes an additional constraint on the maximum absolute pointing

Absolute Radiometric Bias	dB RMS
Bias from harmonic stability errors	0.15
Onboard processing errors	0.20
On-ground processing errors	0.15
External calibration error (absolute calibration)	0.35
Radiometric bias $b \mid_{1\sigma} = \sqrt{\sum_i \left(\dfrac{B_i}{\sqrt{3}} \right)^2}$	0.45

Table 7.3. Absolute radiometric bias budget (requirement is less than 1 dB).

error in azimuth. It is therefore wise to also constrain the azimuth absolute pointing error to 0.1°.

7.2.2 Mitigation and Correction of Ionospheric Effects

Section 6.2 identified three principal ionospheric effects that could have serious effects on the Biomass mission if steps were not taken to mitigate or correct them:

— Scintillation, which can corrupt the impulse response function and introduce phase decorrelation.

— Faraday rotation, which affects the balance of the polarisation channels.

— Total Electron Content (TEC) spatial gradients along azimuth, which can induce spatial distortion and associated decorrelation when they differ between interferometric acquisitions.

Scintillation can be reduced to negligible values over all forest areas, with the exception of the higher latitude forests in the North America/Canada sector, by choosing a dawn/dusk orbit. This orbit avoids the post-sunset equatorial scintillation hotspot, as illustrated by Figs. 6.9 and 6.10. This behaviour is clear from Fig. 7.7, which shows the latitude dependence of the mean unweighted azimuthal ISLR under a severe level of disturbance (occurring only 10% of the time) along the 110° W and 90° E meridians (corresponding to the North American and central Siberian sectors) at a local time of 18:00. The ISLR is a

Figure 7.6. Constraints on APE due to NESZ and TAR requirements. The areas bounded by the pink lines identify the range of azimuth and elevation angles within which the NESZ and TAR requirements are met with margins.
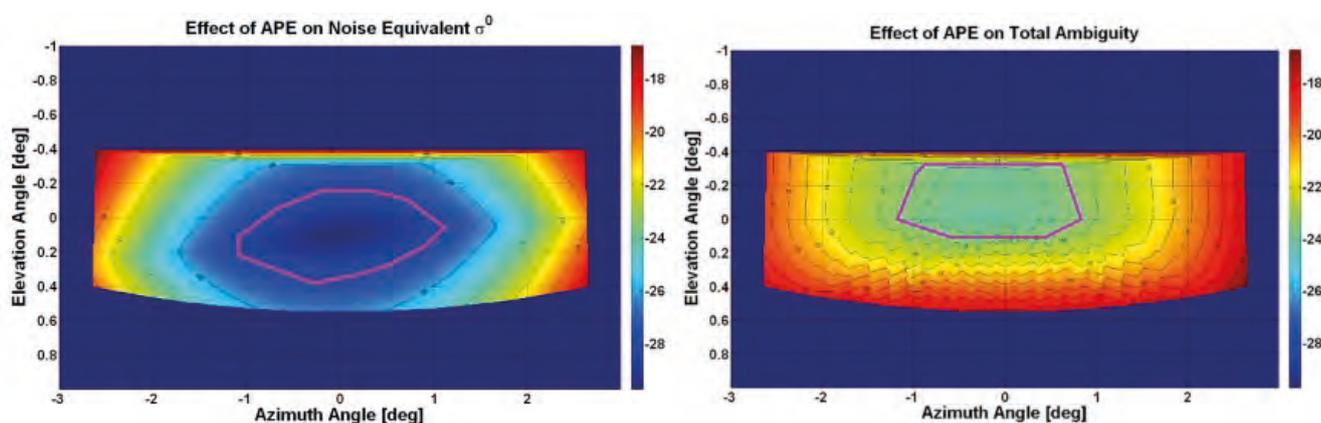
Figure 7.7 Mean ISLR at the 90th percentile of CkL on the dusk side of the orbit for March, plotted against latitude for 25th (blue), 50th (green) and 75th (red) percentile of sunspot number, and for longitudes of 110°W (left) and 90°E (right). The undisturbed value of ISLR is −9.9 dB. Error bars indicate ±1 standard deviation, and points represent the minimum and maximum values.
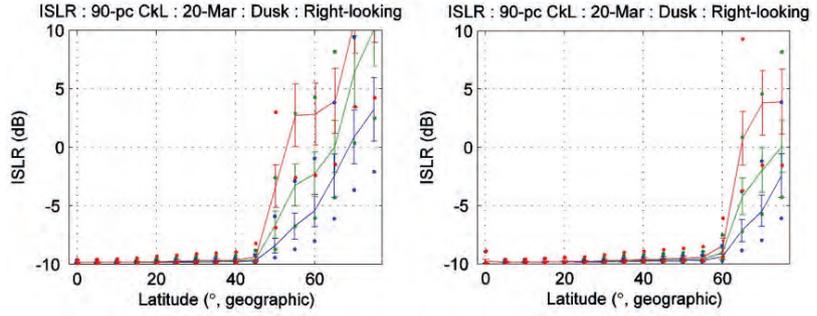
particularly useful performance indicator since PolSAR measurements from a uniform distributed scatterer are unaffected by scintillation (the mean power is unchanged) but the spread of energy at the edges of distributed scatterers reduces the ability to detect deforested patches. It can be seen that scintillations only start to have an effect polewards of 45°N in the North American sector (so affecting the boreal and most northerly temperate forests) and polewards of 60°N in Siberia, which is close to the tree line. This difference occurs because the magnetic pole is in the North American sector, allowing scintillations to penetrate further south. For 90% of the time, the level of disturbance is less and does not extend as far south. The dawn side shows a slightly lower level of disturbance.

As noted in Chapter 6, even the scintillations at high latitudes may be correctable using a new scheme that measures the phase perturbations from the data themselves and uses this to refocus the data. Although the scheme has been successfully tested on simulated Biomass data and real ALOS-PALSAR data, a full performance analysis is not yet available (e.g. in terms of ISLR); nonetheless, current indications are that scintillations can be corrected under median turbulence even for Kp values exceeding the 99th percentile, and under turbulence above the 90th percentile level for Kp values up to the 75th percentile (Papathanassiou & Kim, 2011).

Faraday rotation can be estimated directly from polarimetric data as described in Section 6.2.1, and the measured polarimetric data can then be corrected by a simple linear transformation. The residual FR after this correction must be sufficiently small to have negligible effects on biomass retrieval from PolSAR data. Figure 7.8 shows the ratios (in dB) between the measured HH and HV backscattering coefficients and their correct values, under slightly simplified assumptions about the scattering properties of forests. It can be seen that (i) the HV term, which is the most important for PolSAR retrieval, is also the most sensitive to this residual, and (ii) as long as the residual is less than 1–2°, the error in the HV backscattering coefficient will be a fraction of a dB. In fact, keeping the error in FR to less than 0.5° ensures that, even under worst case assumptions on the HH/HV ratio, the error in the HV backscattering coefficient will be less than 0.007 dB, with corresponding error in the HH backscattering coefficient of less than 6.6×10^{-4} dB. This level
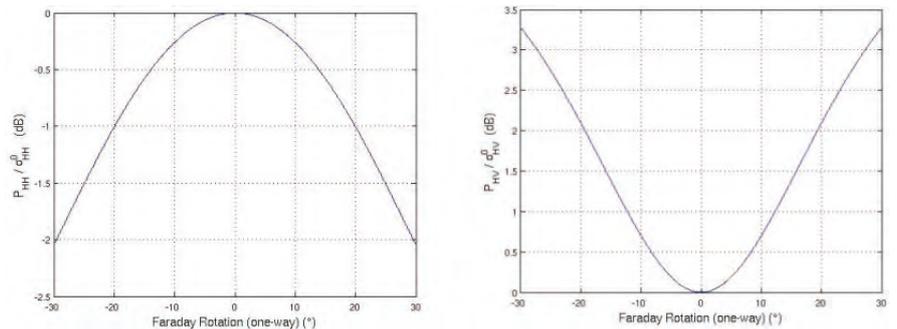
Figure 7.8. (left) Reduction (in dB) in HH (left) and increase in HV backscattering coefficients (right) as a function of residual FR, assuming HH ~ VV, $\sigma^0_{HH}/\sigma^0_{HV}$ =3 and no correlation between HH and VV.
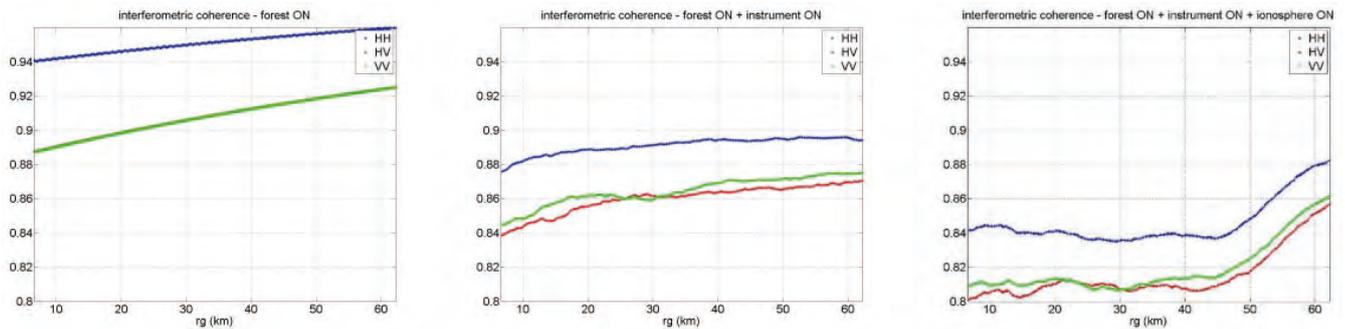
Figure 7.9. Coherence over a simulated scene with a mean biomass level of 15 t ha^{-1} for a boreal forest scenario. Left: input coherence including volume decorrelation and a low level of temporal decorrelation (HH in blue, HV in red and VV in green). Middle: Level-1b coherence including all instrument noise effects. Right: Level-1b coherence including all instrument noise effects and a mild ionosphere. Note: in the left panel the curves for HV and VV polarisation overlap.

of performance is readily achievable using the simplest of the published FR estimators (Bickel & Bates, 1965) because it is unbiased under variation in scene properties, except for very low SNR. Hence, spatial averaging can be used to increase accuracy: the standard deviation of the error in FR is reduced to 0.5° by averaging around 100 independent estimates (equivalent to an area of around 0.5×0.5 km). Since the accuracy of the estimate is proportional to $1/\sqrt{M}$, where M is the number of independent samples averaged, the achievable accuracy is limited mainly by the scale length over which ionospheric variation is small enough to cause little variation in FR. Typically this is several km, except in exceptional circumstances at high latitudes, allowing accuracies of a fraction of a degree to be achieved in most cases.

Variation in TEC along azimuth alters the propagation phase, and its linear component causes the SAR to focus in front of or behind the expected zero-Doppler plane, leading to azimuth shifts and geometric distortion. Both effects will induce decorrelation in interferometric pairs when the ionospheric gradients differ between the two acquisitions. Since correlation is a key quantity used to derive forest height and the associated biomass, both effects will induce errors in biomass estimates. Two correction approaches are available: (i) amplitude correlation can be used to estimate the shifts, and coherence can then be recovered by resampling the 'slave' to the 'master' image; (ii) the ionosphere-induced interferometric phase can be estimated and removed by using the linear relationship between this phase and the difference in FR between the two datasets; this relies on precise estimates of FR, as described above, and leads to better estimates of the coherence. Approaches (i) and (ii) can also be combined to estimate TEC variation, allowing the data to be reprocessed under this model for the ionosphere.

These methods have all been successfully demonstrated on ALOS-PALSAR data, but for P-band it is necessary to turn to end-to-end simulations from BEES, which are based only on approach (i). Figure 7.9 is derived from BEES, and shows the impact on coherence of system errors alone together with the additional impacts from residual ionospheric disturbances after ionospheric correction. The simulations are for a boreal forest of 15 t ha^{-1}, which can be regarded as a worst case. The input coherence as a function of range for a low level of temporal decorrelation is shown in the left figure. Instrument noise results in coherence loss and consequent degradation of height estimation performance is shown in the middle figure. The additional loss of coherence after imperfect correction of the ionospheric effects is shown in the right figure, and has a magnitude of 0.04–0.06, except at far range, where it falls to around 0.01. Although there is no hard threshold for the required level of coherence, values above 0.8 are recommended to allow full inversion of forest heights. Under the given scenario this value is achieved.

7.3   Level-2 Retrieval Performance

The estimation of the performance of Level-2 product retrievals has been performed on the basis of simulated and experimental campaign data. The retrieval tests focussed on primary geophysical parameters; for the Biomass mission, the three primary Level-2 products are above-ground biomass, forest height and a deforestation map. Table 7.4 summarises the accuracy requirements for each. Chapter 6 detailed the algorithms to derive these products and the rationale for treating boreal and tropical ecosystems differently. The following section provides a summary of the performance assessment of these algorithms.

7.3.1 Forest Biomass Product

7.3.1.1 Performance over boreal forests

Simulations with BEES indicate that the accuracy objectives of 20% specified for this product are close to being achieved for the medium decorrelation case over a wide range of biomass levels (Fig. 7.10). Table 7.5 provides the performance statistics for biomass levels of 50 and 250 t ha^{-1}, separated into the component parts of the retrieval and their combination. For the high biomass case, the RMSE, i.e. the sum of the squared bias and standard deviation terms, is 15%, which is fully compliant with requirement of 20%. Table 7.5 also shows that the requirement is almost satisfied (RMSE=20.8%) for the low biomass case by using the intensity (PolSAR algorithm) alone. However, the combined algorithm in this case gives a higher value of 28.6%, indicating that the combined algorithm is being corrupted by the large bias in the PolInSAR estimate, which is itself caused by known inadequacies in the model for PolInSAR retrieval for low biomass sparse forests. After modification of the combined algorithm in the low biomass regime, we expect that the BEES simulations for medium decorrelation will be fully compliant with the accuracy requirements over the full validated range of biomass values (50–350 t ha^{-1}). Further improvements can be expected from a dual baseline PolInSAR inversion which will reduce the biases, but has not yet been implemented in the end-to-end simulator.

Performance analysis of the Biomass Level-2 data product has also been carried out using campaign data from BioSAR-1/2 in Sweden. The assessment was performed by calibrating (training) the algorithm at the northern boreal site, Krycklan, then validating it at the southern site, Remningstorp. The two sites are more than 700 km apart, which ensures that the calibration and validation data are strictly independent; this also provides a stringent test, since the sites have rather different properties. Simulated Biomass performance based on campaign data is given in Fig. 7.11 and shows the RMSE of retrieved biomass as a function of map resolution using the PolSAR retrieval algorithm.

Level-2 Product	Definition	Information Requirements
Forest biomass	Above-ground biomass (dry weight of woody matter – leaves) expressed in t ha^{-1}	200 m resolution accuracy of 20%, or 10 t ha^{-1} for biomass ‹50 t ha^{-1}
Forest height	Upper canopy height defined according to the H100 standard used in forestry	200 m resolution accuracy required is biome-dependent, but shall be 20–30% for trees higher than 10 m
Deforestation detection	Map product showing areas of forest clearing	50 m resolution 90% classification accuracy

Table 7.4. Summary of main Level-2 products.

Reference Scenario	50 t ha⁻¹			250 t ha⁻¹		
	Combined	Intensity	PolInSAR	Combined	Intensity	PolInSAR
Relative Biomass Bias	24.5%	2.5%	54.8%	2.2%	0.6%	5.7%
Relative Biomass Standard Deviation	14.9%	20.7%	24.6%	14.9%	20.5%	17.1%
RMSE	28.6%	20.8%	60.0%	15.0%	20.5%	18.5%

Table 7.5. Performance statistics for a boreal forest scenario with medium temporal decorrelation at 50 t ha⁻¹ and 250 t ha⁻¹ (requirement is 20%).
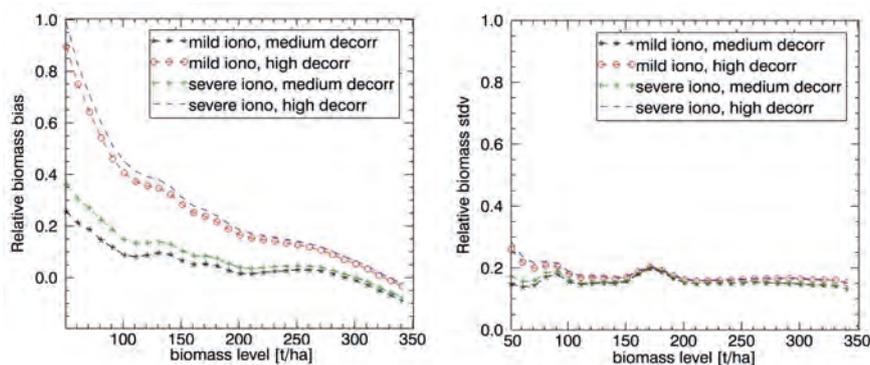
Figure 7.10. Relative bias and relative standard deviation of biomass for a boreal forest scenario. All system errors are considered in the simulation.

As expected, the mean RMSE and variability decrease with map resolution. The RMSE is large below 1 ha owing to speckle fluctuations, since only about 16 looks are available, but the errors decrease rapidly for coarser map resolution due to averaging. The mean RMSE is 45 t ha⁻¹ for the data product resolution of 200 m (4 ha biomass map resolution), corresponding to a relative RMSE of 32% obtained by dividing by the mean biomass of 140 t ha⁻¹.

The combined biomass estimate from PolSAR and PolInSAR has also been evaluated based on simulated Biomass data. Estimates of forest height were obtained from PolInSAR data by performing a two-baseline inversion of simulated data. Figure 7.12 shows a reference biomass map derived from lidar, a best, median and worst-case biomass map derived from PolSAR, and the biomass map derived from PolInSAR. The far-right map is a Bayesian combination of the PolSAR (median case only) and PolInSAR biomass estimates. Although the combined map gives a slightly lower RMSE than the PolSAR case, it is still not compliant with the requirement of 20%. It should be noted, however, that the current results have been obtained by training the algorithm on full-resolution (2 m) airborne SAR data, whereas validation was
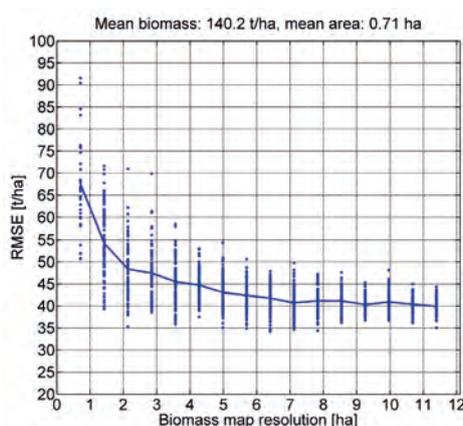
Figure 7.11. Performance of biomass retrieval as a function of map resolution for simulated 6 MHz Biomass images over boreal forest. Each data point represents a biomass estimate from a single simulated image. The black line corresponds to the result for full resolution airborne SAR data.

Figure 7.12. Biomass maps based on, from left to right: reference (small-footprint lidar), PolSAR for best, median and worst case speckle realizations, PolInSAR, and finally a Bayesian combination of the PolSAR (median case) and PolInSAR maps. The map resolution is 200×200 m.
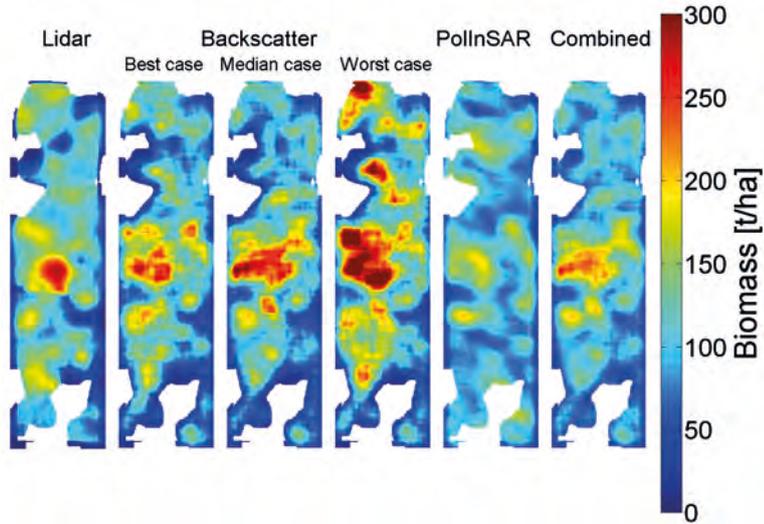
performed on the simulated Biomass data. A lower RMSE is expected if the simulated data are also used for training.

The campaign data analysis supports the findings of the end-to-end simulations, and provides performance evaluation under realistic forest conditions. The observed relative RMSE is about 30% for the Level-2 Biomass data product at 200 m resolution, i.e. larger than from the end-to-end simulation. However, interpretation of the results needs to consider that additional error sources have a substantial impact. For example, the performance is assessed with respect to reference observations which contain uncertainties up to 15–20% of the mean biomass. In addition, a bias is expected, as the algorithms are trained on the high-resolution airborne data, but evaluated on simulated Biomass data. Improved retrieval performance is therefore expected when the algorithm is trained on simulated Biomass data. Finally, it should be noted that further improvement is expected by including multichannel (temporal and polarisation) filtering, which has not been explored in the current analysis.

7.3.1.2 Performance over tropical forests

The biomass inversion performance is evaluated using experimental airborne data over French Guiana. Data are available for the Paracou forest site for seven dates in 2009. To estimate the RMSE between the retrieved and *in situ* biomass, 28 plots of 1 ha with biomass ranging from 320–480 t ha^{-1} are used. Each plot provides 64 looks, corresponding to a Biomass resolution of 200 m. The results are obtained using a bootstrap process with 104 realisations, based on 5 randomly selected forest plots used for training and 23 plots for validation. Figure 7.13 shows the RMSE in percentage of the mean biomass between the retrieved biomass and *in situ* biomass in two cases, Fig. 7.13a for retrieval using intensity alone and Fig.7.13b for combined intensity and PolInSAR. In Fig. 7.13a, the mean RMSE in biomass is 19.7% and the 1 s confidence interval is 14.6–22.8%. The biomass retrieval using 6 MHz data, is compliant with
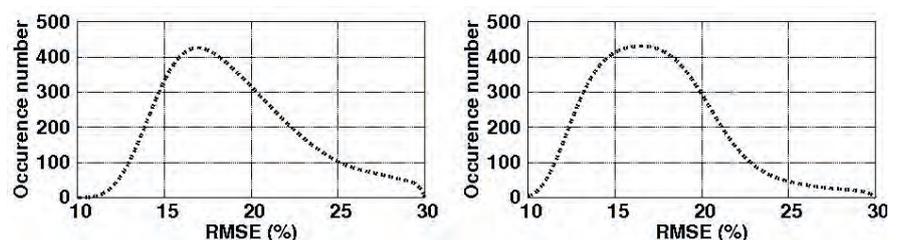
Figure 7.13 Histograms of the RMSE, as a percentage of the mean biomass, between retrieved and *in situ* biomass: a) using intensity retrieval; b) using combined intensity and single-baseline PolInSAR retrieval.
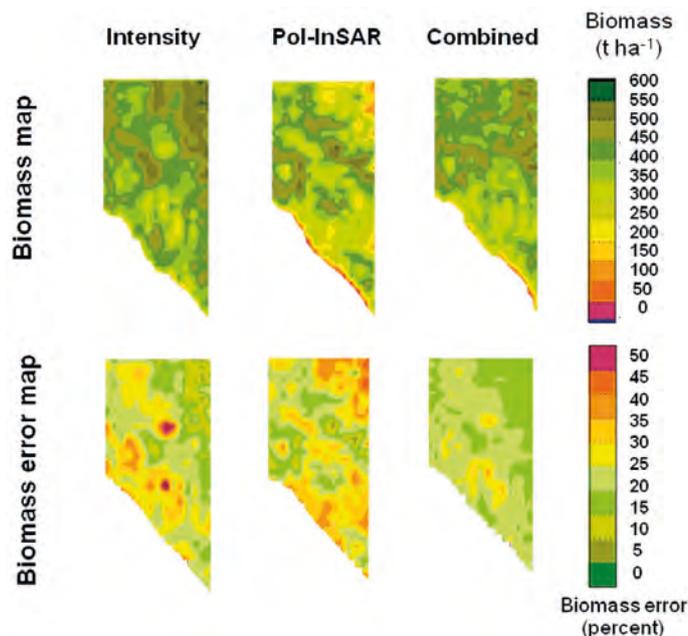
Figure 7.14. Top row: biomass maps from TropiSAR data derived from intensity (left), PolInSAR height (middle) and combined intensity and PolInSAR (right). Bottom row: maps of percentage error in biomass from intensity (left), PolInSAR height (middle), and the combined method (right).

the 20% requirement (RMSE ≤20%) for 65% of the realisations, whereas 35% of the realisations are non-compliant (RMSE >20%). In Fig. 7.13b, the mean RMSE is 17.7%, and the 1 s range is 14–20%. The percentage of non-compliant realisations is 16%. This illustrates the improvement in biomass retrieval from combining intensity and single-baseline PolInSAR.

The values in Figure 7.13 are based on the simulated campaign data, with a radiometric uncertainty corresponding to 64 looks (equivalent to the 200 m resolution Biomass products) and an uncertainty in PolInSAR height of 2.5 m, derived by comparison with lidar data at forest plots. To analyse the impact on the retrieved biomass of higher uncertainties arising from the additional effects of forest structure, environmental change, topography, system errors and larger temporal decorrelation, the uncertainty in intensity was increased to 1 dB and in PolInSAR height to 4 m. Figure 7.14 presents the corresponding maps of biomass and the relative error (as a percentage). For these levels of uncertainty, the biomass accuracy requirement is not met by either the intensity or PolInSAR products alone. However, the combined method clearly improves the retrieval, and yields a biomass error mostly in the range of 20–25%.

In summary, biomass retrieval using intensity, PolInSAR and combined intensity and PolInSAR has been assessed on experimental data degraded to simulate Biomass data. The assessment using *in situ* plots shows that the requirement for biomass retrieval is met in 65% of cases when intensity is used, and in 84% of cases when a combined approach using intensity and PolInSAR is used. The impact of higher levels of uncertainty was also assessed, and indicates that the accuracy requirement is slightly exceeded under these conditions.

7.3.2 Forest Height Product

The baseline PolInSAR scenario for Biomass is the fully polarimetric single-baseline case acquired with a temporal baseline of about 25 (up to 45) days. As discussed in previous chapters, forest height estimation for the single-baseline case is limited by the presence of:

— A ground scattering component contributing to all polarisation channels, as occurs at P-band in less dense forest conditions (e.g. boreal forest).

— Non-volumetric decorrelation contributions, particularly temporal decorrelation, as occurs in the Biomass repeat-pass interferometric mode.

However, both disturbing effects can be adequately compensated when integrated into the inversion approach under a dual-baseline or even a multibaseline mission scenario.

7.3.2.1 Performance over boreal forests

Figure 7.15 shows the forest height relative error and bias for Concept A (Concept B shows similar performance) for a boreal forest scenario derived from a single-baseline scenario simulated by BEES. The input forest height is derived from biomass levels using allometric relations. The simulation takes into account all instrument related error sources, geophysical variability in the forward model and volume decorrelation. The inversion is evaluated for medium- and high-temporal decorrelation scenarios and for a mild and severe state of the ionosphere. The simulations indicate that the accuracy objectives of 20–30% specified for this product can be achieved. For low biomass levels only, the performance is non-compliant, owing to a large bias in the single-baseline PolInSAR retrieval.

The availability of three BioSAR-I fully polarimetric acquisitions separated by intervals of approximately one month allows the assessment of dual-baseline PolInSAR inversion schemes, after using these data to simulate 6 MHz data consistent with the Biomass specification. The temporal decorrelation level was about 0.9 for the March–April pair and 0.8 for the March–May pair. Results obtained for Remningstorp are shown in map form in Fig. 7.16; the corresponding scatterplots based on *in situ* reference plots are shown in Fig. 7.17. A reference lidar height map is on the left in Fig. 7.16, while in the middle is a height map derived using single-baseline data with a temporal decorrelation level of about 0.9 (i.e. using the March–April pair). Severe overestimation is evident, up to 200%, induced by uncompensated temporal decorrelation, making the forest height maps non-compliant with the requirement. In contrast, as shown on the right, the dual-baseline approach successfully compensates for the height bias, and yields an RMSE of about 5 m across a height range of 10–35 m; this characterises the expected boreal inversion performance. The required 20–30% height accuracy is achieved for most of the stands, but the rather small spatial baselines of Biomass make it difficult to reach this performance for stands with lower heights.

7.3.2.2 Performance over tropical forests

Single-baseline inversion for the tropical Mawas site in Indonesia using simulated Biomass data are shown in Fig. 7.18. The RMSE of about 4 m across a height range 10–30 m (corresponding to a RMSE of 20%) characterises the expected tropical inversion performance. The overestimated regions within
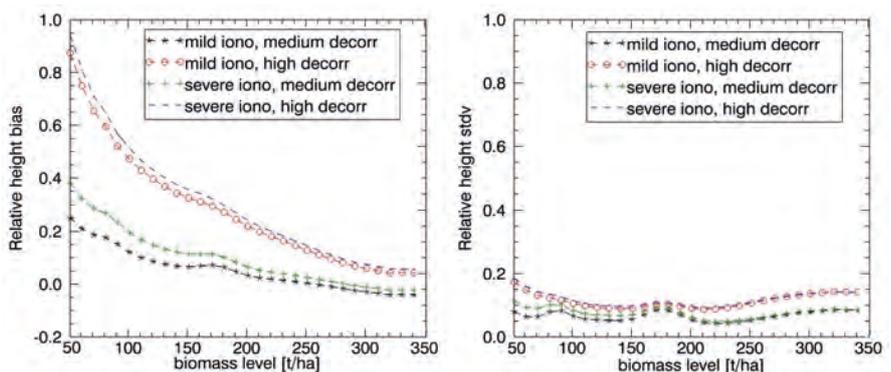
Figure 7.15. Relative bias and relative standard deviation of height for a boreal forest. All system errors are considered in the simulation.
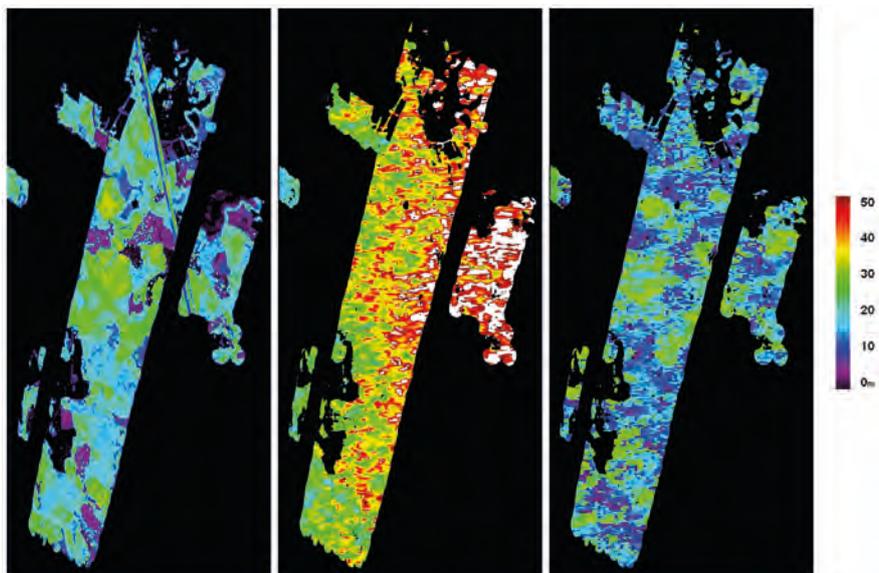
Figure 7.16. Lidar forest height map of the Remningstorp test site (left). Forest height map derived from simulated Biomass P-band PolInSAR measurements using a single-baseline inversion approach on data affected by temporal decorrelation (middle). Forest height map obtained using a dual-baseline inversion (right).
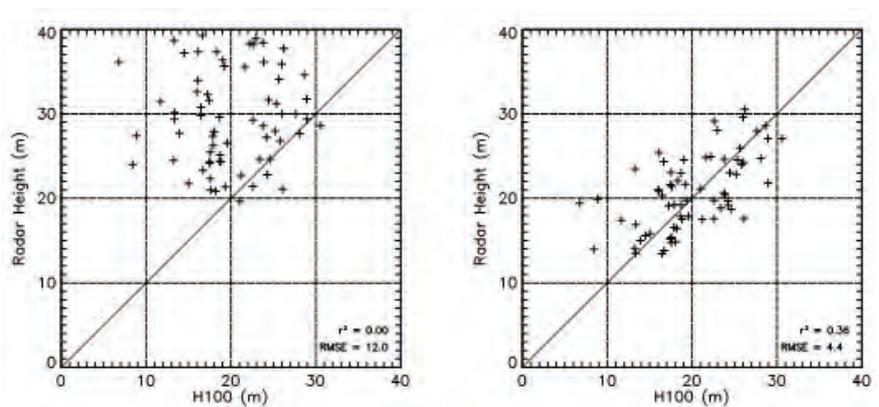
Figure 7.17. Plots of PolInSAR forest height vs. lidar top height for the Remningstorp test site obtained using simulated Biomass data. Single-baseline inversion (left); dual-baseline inversion (right).
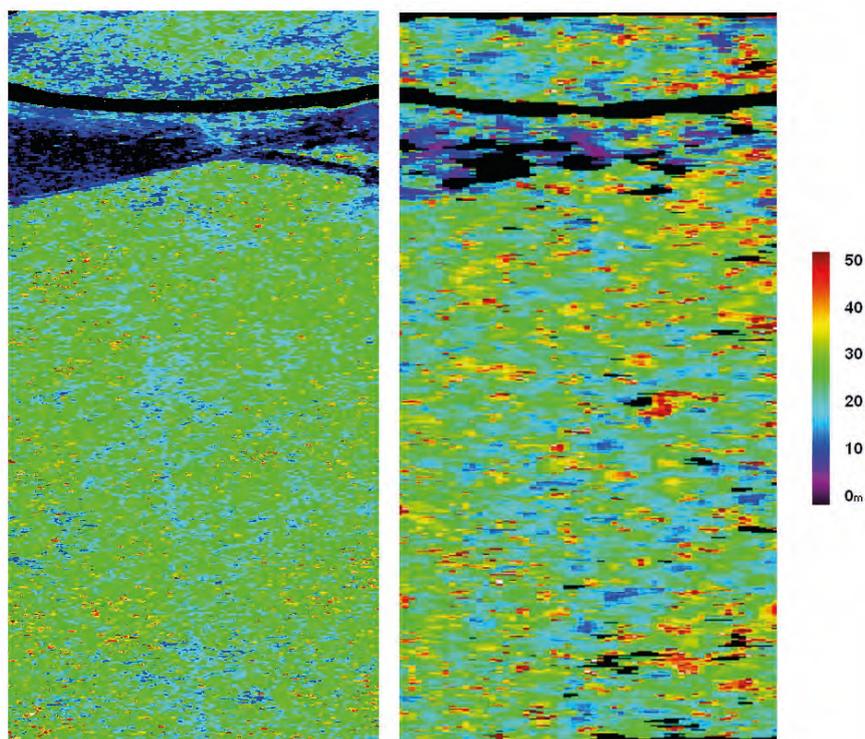
Figure 7.18. Reference lidar forest height map of the tropical Mawas test site (left); Forest height map derived from simulated Biomass P-band PolInSAR measurements using a single-baseline inversion approach (right).

155

the scene are caused by local structure/scattering heterogeneity within the forest and on the borders that bias the coherence estimation at lower spatial resolution. The availability of two or more spatial baselines will allow this to be compensated.

7.3.3 Deforestation Detection

The performance of Biomass with respect to detecting deforestation was assessed from end-to-end simulations. Scenes representative of tropical forest with homogeneous biomass levels of 300 t ha^{-1} and 500 t ha^{-1} were generated and deforestation patches characterised by biomass levels ranging 10–100 t ha^{-1} in steps of 10 t ha^{-1} were introduced. Patches are 1 km² (see Fig. 7.19 for the 300 t ha^{-1} map). All system error sources for a mild ionosphere scenario and geophysical variability were taken into account.

To detect the deforested patches a simple approach using a threshold of intensity difference in HV backscatter was applied. Fig. 7.20 shows the classification accuracy for both scenes (300 t ha^{-1} and 500 t ha^{-1}) together with the 95% confidence interval. Also shown is the theoretical classification accuracy considering only speckle effects, as derived by Davidson et al. (2009), which was used to define the requirements in Chapter 4. The results indicate the required accuracy of 90% is achieved. Only for partly deforested patches does the classification drop below the threshold for lower biomass stands. Further improvements are expected by integrating the HH and VV channels and PolInSAR information in the classification.

7.3.4 Tomography

Tomography is an experimental complementary product from the Biomass mission, providing information about forest structure. In Chapter 6 it

Figure 7.19. Simulated HV backscatter for a tropical forest scenario at a biomass level of 300 t ha^{-1} with deforested patches ranging 10–100 t ha^{-1} in azimuth and a patch size of 1 km^2.
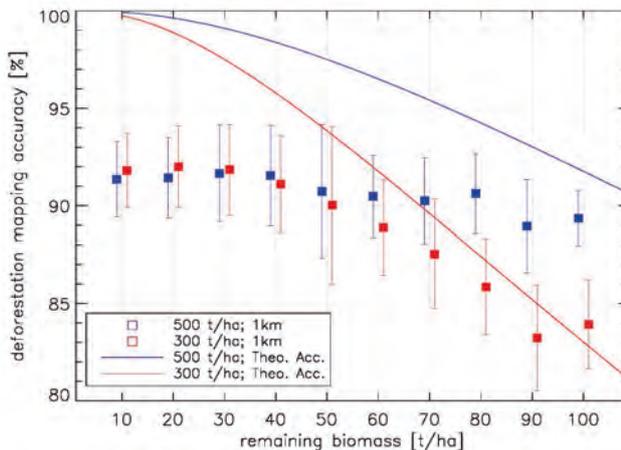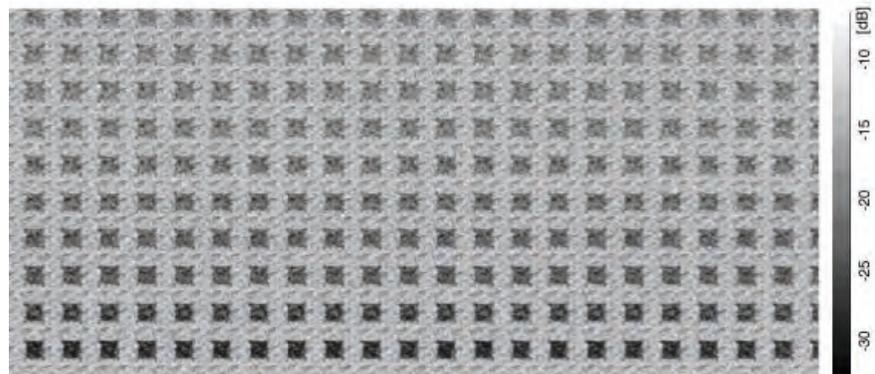
Figure 7.20. Deforestation mapping accuracy with 95% confidence interval.
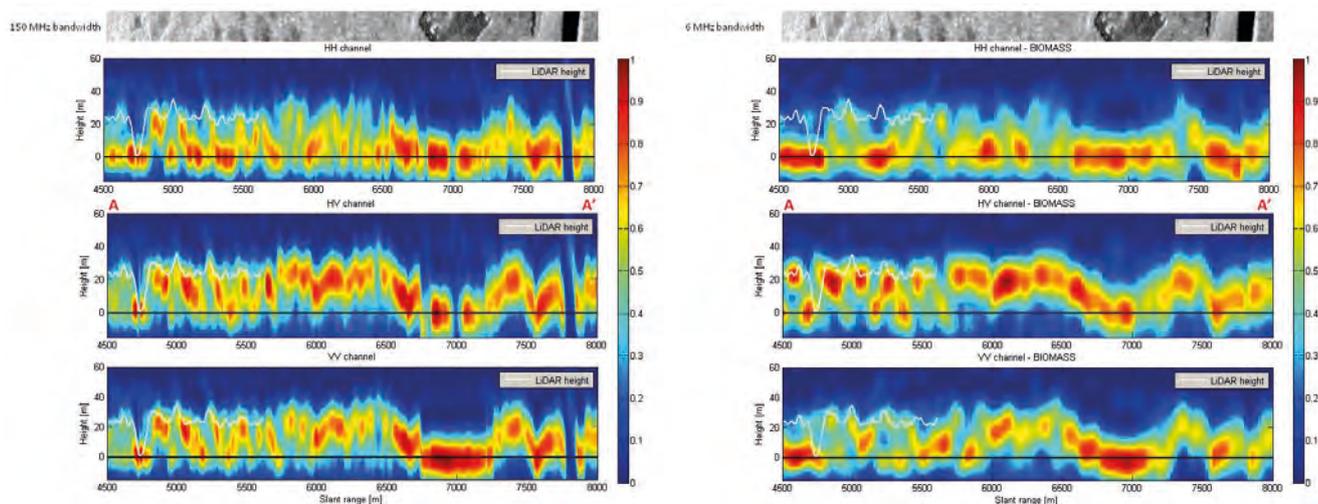
Figure 7.21. Comparison between 150 MHz (left) and 6 MHz (right) tomography of a transect of a tropical forest. The behaviour of the different polarimetric channels is shown.

was highlighted that this product can be used as an important source of information to optimise the retrieval of primary Biomass products. In this section we provide a qualitative assessment of the tomographic product to be delivered by the mission. For this we used the tomographic data collected over a tropical forest site in French Guiana, filtered to a 6 MHz bandwidth. A transect of the survey at about 300 incidence angles was then reconstructed, and a comparison between full bandwidth and Biomass bandwidth results was made. The results from the simulation are shown in Fig. 7.21 after flattening for the local DEM, so that height has to be interpreted as height above the local surface.

The reduction of the bandwidth to 6 MHz from 150 MHz is evident in the loss of horizontal resolution. However, the loss in vertical resolution, even if present and visible, is not damaging, as the campaign was intended to mimic Biomass and not designed to exploit to the maximum the possibility of the wide bandwidth available. In the simulation, neither ionospheric disturbances nor temporal decorrelation has been considered. However, the results from studies carried out and briefly reported in Chapter 4 show that, provided the revisit times for the tomographic campaigns are less than four days (as predicted), neither disturbance should be critical.

7.4 Conclusions

The end-to-end performance estimation of the Biomass mission was carried out using simulated input datasets that were generated either from airborne SAR campaign data or from BEES using values inferred from the campaign data. The Level-1 product was synthesised by transforming the input data using the Biomass system transfer function, including associated system errors. The product generation took both the effects of the ionosphere into account and their corrective measures. The SAR performance described in Section 7.2.1 formed the basis for the simulated system transfer function. The performance figures are compliant and approach the goal values in most cases. In particular, the very good predicted performance of >30 dB cross-polar attenuation ratio would enable precise estimation of FR over those areas covered by mature forests (areas with higher radar backscatter), leading to accurate correction of ionospheric effects. The dawn/dusk orbit selected for Biomass means that scintillations will have negligible effect on biomass inversion performance

except for the northernmost temperate and boreal forests in the North American/Canadian sector. Newly developed algorithms seem able to remove even this limitation, though require further testing. Distortion of polarimetric data caused by FR can be corrected to accuracies that render it negligible as regards biomass inversion. Decorrelation owing to differential spatial gradients in TEC between interferometric pairs can be corrected. Simulations indicate residual associated losses in coherence after correction of at most 0.06. Improvements are likely by combining correction methods based on measuring differential FR and amplitude correlation between the interferometric pairs.

Results of Level-2 product simulations indicate that the biomass map product requirement of 20% accuracy will be met for boreal forests for a wide range of conditions. It is particularly important to note that the requirement is already very close to being met using only the PolSAR algorithm, which is independent of temporal decorrelation, unlike the PolInSAR algorithm. Moreover, the combined algorithm needs to be improved to fully exploit the complementary aspects of the PolSAR and PolInSAR data. Over boreal forest, campaign data analysis indicates a higher RMSE of about 30% which is currently not compliant with the 20% requirement. Nevertheless, the 30% RMSE is a conservative estimate and includes contributions from errors in reference data as well as from the algorithm training methodology. By taking these into account and including multichannel filtering, it is expected that the 20% requirement will be met. In tropical forests, simulations based on degraded TropiSAR data indicate that the relative error mainly lies in the range 20–25%, with larger errors over limited parts of the study area.

The forest height product currently does not meet the 20–30% accuracy requirement. The baseline PolInSAR scenario for Biomass using a single-baseline is limited by the presence of a ground scattering component contributing to all polarisation channels in less dense forest conditions (e.g. boreal forest) and by temporal decorrelation. However, the performance assessment showed that both disturbing effects can be adequately compensated when integrated into the inversion problem under a dual-baseline mission scenario.

Using simple thresholding of HV ratios, the deforestation product meets the required accuracy of 90% except for partly deforested patches in lower biomass stands. Further improvements are expected by integrating the HH and VV channels and PolInSAR information in the classification.

→ MISSION CONTEXT

8. Mission Context

8.1 International Programmes

The current status of the world's forests and information on how they are changing are of major national and international concern. This is because forest resources are crucial for provision of renewable raw materials and energy, mitigating climate change, maintaining biological diversity, protecting land and water resources, providing recreation, improving air quality and helping to alleviate poverty.

Monitoring of forest biomass and its changes is therefore urgent, not just for calculating emissions based on land-use change and carbon sinks from forest growth, but in the wider context of keeping track of the world's forest resources. Hence, Biomass products will be of immediate value to a range of international programmes:

— UNFCCC: Biomass is an ECV (GCOS, 2003; 2004; 2010; Sessa & Dolman, 2008) because of its role as a carbon sink under forest growth, as a carbon source under land-use change and from forest fires, and from its increasing use for bio-energy. All Annex 1 signatory nations to the Framework Convention are required to report annually on emissions due to land-use change, using methods accepted under IPCC guidelines. Basic quantities needed for land-use change calculations are the biomass lost under deforestation and forest degradation, and biomass gain from afforestation. Biomass is uniquely capable of mapping not only the areas of forest change, but also the associated changes in biomass.

— FAO: The importance of knowing about forests and the ecosystem services they provide has motivated production of the GFRAs by FAO every 5–10 years since 1946. They are the main sources of information on worldwide forest biomass stocks and provide, *inter alia*, forest area and average values of biomass at country level (but not gridded data or maps). Country statistics are based on data from national forest inventories, which are normally based on sample plots and direct measurement of tree characteristics, such as growing stock at ground level. The sampling in the developed world can be dense and of high quality, but many developing countries use only a very few sample plots on which to base their national reporting. As a result, the quantities reported in the GFRAs are of inconsistent quality, contain unknown biases and have poorly known accuracies. Biomass data can contribute enormously to the GFRA providing high-resolution biomass maps at country scale to be used in developing national statistics on forest and their changes.

— REDD+: The UN Committee of the Parties in its Bali Action Plan encouraged parties to reduce global greenhouse gas emissions from deforestation and forest degradation in developing countries, and to enhance forest maintenance, sustainable forestry management, and carbon storage by forest lands (Bali Action Plan, Decision 1/CP.13). This was further reinforced at the Durban Committee of the Parties (UNFCCC/SBSTA/2011/L.25/Add.1). A fundamental requirement for REDD+ is that it is underpinned by internationally recognised MRV systems. Associated with this is the Group on Earth Observations (GEO) Global Forest Observations Initiative, which will act as an advisory and enabling organisation to countries who wish to construct MRV systems for national reporting. Biomass will provide a unique capability for mapping the carbon changes associated with deforestation, forest degradation and forest growth and thus will greatly support this endeavour.

Figure 8.1. Overview of the global carbon-cycle data assimilation system envisioned by the GEO Carbon Strategy for the production of maps of greenhouse gas sources and sinks. (Ciais et al., 2010)
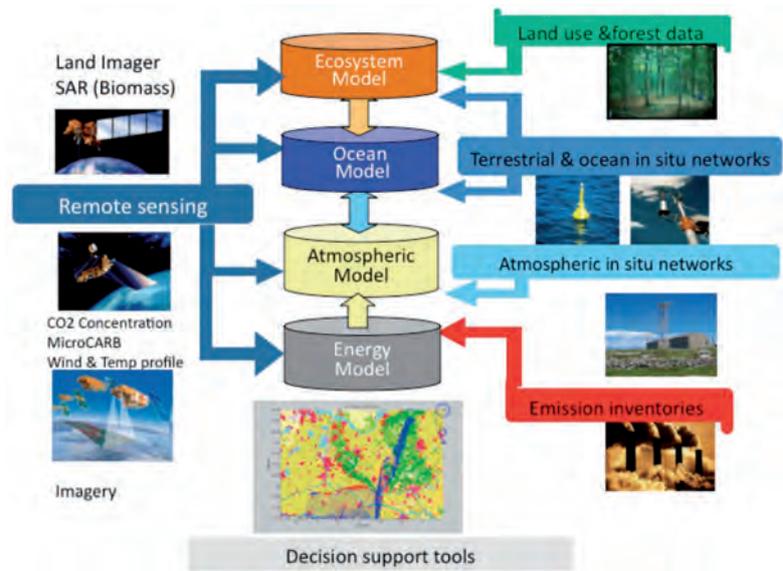
— The GEO Carbon Strategy: Recognising the growing need for improved Earth observations, over 130 governments and leading international organisations are collaborating to establish a Global Earth Observation System of Systems by 2015. GEO has begun work to implement a global carbon observation and analysis system. Observations, reanalysis and product development are planned to contribute to an integrated model that assimilates carbon observations. This is illustrated by Fig. 8.1 (Ciais et al. 2010: GEO Carbon Strategy), which shows SAR estimates of biomass from space as a key element of the remote sensing component of the strategy.

— Project developers for carbon forestry on the voluntary market and afforestation under the Clean Development Mechanism: The estimated total value of transactions for forest carbon projects in 2010 was $178 million. The historical scale of forest carbon markets climbed to 75 million metric tonnes of CO_2 equivalent, with estimated value $432 million, and projects affecting more than 7.9 million hectares in 49 countries from every region of the world (*www.foresttrends.org/documents/files/doc_2963.pdf*). Monitoring of such projects is essential to keep the market secure, and Biomass will have unique power to support this.

— The Global Carbon Project: This science organisation provides annual updates on the state of the carbon cycle, but its estimates of fluxes due to forest change are essentially provided by the FAO GFRAs and are subject to the limitations of those data. Biomass provides a means to make these estimates much more accurate.

8.2 Related Missions and Existing Earth Observation Initiatives

The dataset to be produced by Biomass will be unique and not dependent on other satellite data to be of value. However, many other satellite missions will add greatly to the value of Biomass. Five types of missions of special relevance are:

— Space-based measurements of atmospheric CO2: In January 2009, JAXA launched the Greenhouse gases Observing Satellite (GOSAT) to measure

global CO_2 and CH_4 fluxes, on spatial scales of 100–1000 km. GOSAT is planned to be in orbit for at least five years, and much of its first three years of life has been concerned with improving data quality, correction of biases, etc. NASA is also scheduled to launch the Orbiting Carbon Observatory (OCO-2; OCO-1 was lost at launch in 2009), which is designed to provide global measurements of atmospheric CO_2 to characterise sources and sinks on regional scales at monthly intervals for two years. When embedded in atmospheric inversion schemes, measurements from both missions should improve knowledge of the locations and magnitudes of land sources and sinks. However, they give no direct evidence about the processes that cause carbon fluxes. In addition, they will not have the spatial resolution offered by Biomass, which is needed to resolve whether fluxes are due to disturbances, regrowth, fires, deforestation, etc. It is unclear whether comparable missions will be in orbit to coincide with Biomass.

— Space-based measurements of emissions from fires: Fire is one of the mechanisms by which land-use change gives rise to emissions (but by no means the only one (Houghton, 2005)), and its relative contribution to emissions varies geographically and with circumstances. Information on burnt areas from the MERIS/MODIS class of medium-resolution sensors and higher-resolution Landsat/Sentinel-2 instruments will provide valuable information on the process giving rise to changes in biomass. In addition, the use of Fire Radiated Power (FRP) to estimate biomass consumed by fire (e.g. Wooster et al., 2005) will provide complementary estimates of the biomass lost by fire in land-use change. Global FRP products are likely to be available in the Biomass timeframe from operational meteorological and polar-orbiting satellites.

— Space-based lidar for forest height: The combination of long wavelength radar for biomass mapping with a spaceborne waveform lidar that could sample forest vertical structure would provide an excellent way to map the 3D distribution of vegetation in forests, particularly when combined with the PolInSAR and SAR tomography data from the Biomass mission. Unfortunately the vegetation lidar has been dropped from the proposed NASA Deforestation, Ecosystem Structure and Dynamics of Ice (DESDynI) mission concept. Lidar measurements of vegetation height may become available from NASA's proposed ICESat-2 mission, but these are unlikely to be optimised for vegetation. Airborne lidar is, however, likely to be important as part of the Biomass mission calibration and validation phase.

— L-band radar: The ALOS PALSAR mission, in its five years of operation before failure in April 2011, built up a systematic archive of worldwide L-band forest observations providing valuable information on forest extent and change, and the dynamics of inundated forests. This archive has limited capacity for measuring biomass because of saturation of L-band at a biomass of around 100 t ha^{-1}, except in the boreal forests using winter coherence (Thiel et al., 2009). A successor to PALSAR, planned for launch in 2013, is intended to have a similar systematic acquisition strategy for forest data, but with a stronger focus on disaster monitoring. Current JAXA data policy will involve commercial handling of the data which may affect its usability for science and REDD+. The pair of Argentine Microwaves Observation Satellites (SAOCOM) (the first of which is scheduled to be launched in 2013) will also provide L-band data, though without a systematic forest observation strategy.

— C-band and X-band radar: Continuity in C-band SAR missions is ensured during the timeframe of Biomass through the ESA Sentinel-1 SAR missions and the Canadian Space Agency's Radarsat constellation. These missions are not expected to provide forest biomass information but can provide

complementary information, such as detection of forest disturbances at high resolution and generating up-to-date land-cover maps. X-band data may also be available, e.g. from a TerraSAR-X follow-on, and would play a similar role. The difference between a surface DEM produced at X-band and a bare earth DTM from Biomass may also provide an alternative means to estimate forest height.

The unique role of Biomass and how it complements other satellite missions is best explained using the data assimilation concept illustrated in Fig. 8.2 (adapted from Ciais et al., 2003). This provides a complete framework for integrating ground data, satellite data and models into a global carbon-cycle observation and prediction system and contains a more complete assessment of the role of remote-sensing data than Fig. 8.1. Biomass from space is recognised as a specific satellite contribution within this scheme, along with fires, radiation (e.g. the fraction of Absorbed Photosynthetically Absorbed Active Radiation or fAPAR), land-cover/land-use, vegetation growth cycle and atmospheric CO_2. The realisation of such a scheme would have immediate effects on climate modelling, since the carbon cycle is so deeply embedded in the climate system and the observation requirements for carbon cycle overlap greatly with those needed by climate.

Biomass will also benefit greatly from ground data networks, including the large amount of inventory data and data from the continually developing network of research-oriented sites, particularly those associated with flux tower measurements (for example, the global FluxNet network (*www.fluxnet.ornl.gov/fluxnet/index.cfm*). These data will be used for validation and in better understanding the role of biomass in studies of carbon exchange, for example, in model parameterisation.

8.3 User Community Readiness: Carbon and Forestry

The critical science communities for the Biomass mission are the *in situ* biomass community, the land-use change community, and the carbon-cycle science community. These communities are well connected and have a strong history of data sharing, e.g. through FluxNet. Recent initiatives, in particular the GEO Carbon Strategy (Ciais et al., 2010), provide clear channels for engagement with Biomass. A meeting in Paris, November 2010, funded by
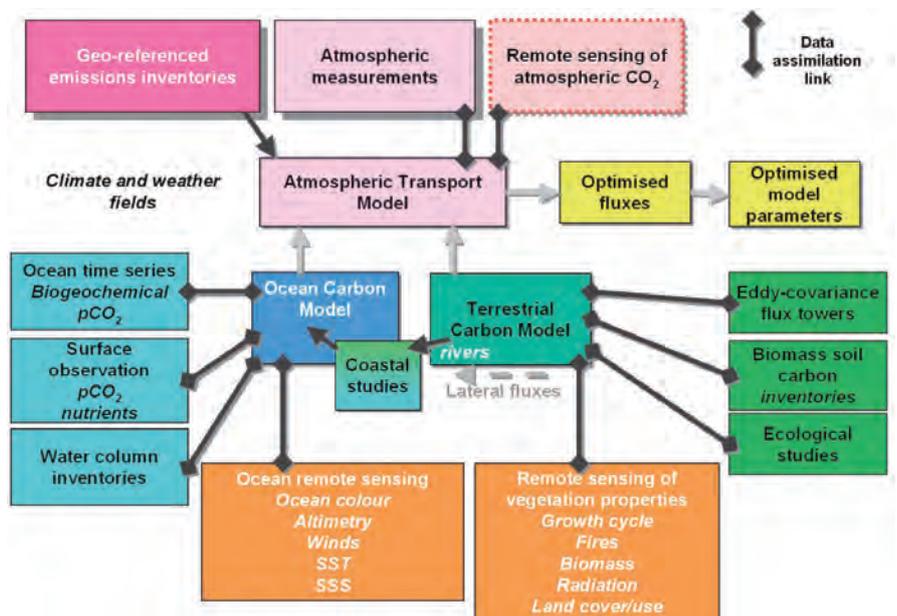
Figure 8.2. The data assimilation concept set out in the Integrated Global Carbon Observing Strategy. (adapted from Ciais et al., 2003).

NERC, ESA and CNES, brought together leading international members from the carbon cycle, measurement (*in situ* and satellite), ecology and modelling communities, together with FAO. User community readiness was clearly indicated, as follows:

— The *in situ* biomass community has developed plot networks of forest data, particularly in the Tropics, over recent decades (see Subsection 6.2.1). Standardised protocols and analyses now link researchers across the globe, and databases have accumulated information with open access agreements (e.g. RAINFOR, AFRITRON). This community is vital for calibration of Biomass products. In return, Biomass provides a means to place these plots in a global context, so there is clear synergy.

— The land-cover change community has developed improved methodologies for land-cover change assessment, and understanding of the challenges in quantifying associated carbon losses over recent decades. This community has been strongly supportive of the development of a satellite mission capable of measuring above-ground woody biomass. There are already strong interactions between the remote-sensing community on land cover and those generating carbon change estimates. These user communities have strong connections to IPCC, to GEO and to activities such as the International Geosphere-Biosphere Programme's Global Land Project, facilitating interactions and readiness.

— The carbon-cycle community has become increasingly interested in disturbance and land-use change effects in their predictions. A key focus in current model developments has been on introducing these factors in their simulations. Data assimilation techniques for linking Earth observation to carbon-cycle models are also now developed, increasing the readiness of these groups for mission products. There are close links among the relevant modelling groups through IPCC, and activities such as the EU Integrated Carbon Observation System (*www.icos-infrastructure.eu*) and the EU Geocarbon project.

Biomass data would be of immediate value to REDD+ and the carbon trading communities, and would be rapidly adopted in MRV systems. It would be readily exploited in the FAO's Global Forest Resource Assessments; FAO have been kept informed about Biomass.

8.4 Mission Context & User Readiness for Secondary Objectives

8.4.1 Subsurface Geology

Potential users of subsurface geological maps include local companies and organisations in charge of water exploitation and management, together with companies involved in geophysical and mineral exploration. Such maps are also of enormous interest for research into palaeo-climates. Groundwater is one of the ECVs defined by the GCOS (IGOS, 2010). In arid regions many aquifers contain fossil groundwater, and can potentially be inferred from palaeo-drainage channels. ESA's Tiger Initiative addresses water-related geo-information in terms of Earth observation technology. Biomass imagery is likely to be of major value to any continuation of this initiative.

In 1999, UN Educational, Scientific and Cultural Organisation and the World Meteorological Organisation established the International Groundwater Resources Assessment Centre (IGRAC) (*www.un-igrac.org/*), which is building a Global

Groundwater Monitoring System (*www.un-igrac.org/publications/104*). In order to assist collection, aggregation, and dissemination of groundwater-related information, IGRAC is developing a web-based application, which is currently handling terrestrial measurements, but a potential inclusion of the NASA Gravity Recovery and Climate Experiment mission data is currently being considered (*www.earthobservations.org/wa_igwco_th_gw.shtml*). Biomass data could potentially be relevant to IGRAC's developing programme.

8.4.2 Terrain Topography Under Dense Vegetation

The use of terrain models is extremely widespread in many communities, and people routinely work with topographic data from various sources. In forested areas the applications include forest management, ecology, water resource management, various types of mineral exploitation, national security and scientific research. A range of global and near-global DEMs have been produced in response to a demand for accurate and consistent DEMs (see Subsection 6.3.3). These DEMs largely represent surface elevations, since they are based on data from sensors with small penetration depths, e.g. SRTM, ASTER, ERS/RA, ICESat/GLAS, and TanDEM-X. The Biomass DEM will improve the quality of these DEMs in forested areas where the terrain topography is of interest, i.e. the bare earth. It is likely to be exploited rapidly in all the applications identified above, and many more besides.

8.4.3 Glacier and Ice Sheet Velocities

The ECVs defined by the GCOS include (i) Ice Sheets and (ii) Glaciers and Ice Caps (IGOS, 2010). A primary ECV parameter is ice velocity for which the Integrated Global Observing Strategy has specified measurement requirements in terms of spatial resolution and temporal resolution (IGOS, 2006; IGOS, 2007). The importance of ice velocity as an ECV parameter is due to its relation to the mass balance of the ice sheets and to sea-level rise resulting from global warming. ESA has launched a Climate Change Initiative related to selected ECVs, including ice sheets. A primary parameter to be addressed is ice velocities, which can be measured with data from existing satellite SAR systems (ASAR, Radarsat-1/-2, and TerraSAR-X /TanDEM-X) and from future systems (Sentinel-1, PALSAR-2).

However, Biomass could be a valuable complement where temporal decorrelation is a limiting factor, e.g. in the melt season. The Greenland Ice Mapping project (GIMP) is one of NASA's Making Earth Science Data Records for Use in Research Environments projects. GIMP provides winter velocity maps for Greenland, based on Radarsat-1 interferometry. So far, ice-velocity data have been provided for the winters 2000–2001, 2005–2006, and 2006–2007. Velocity data for 2007–2008, and 2008–2009 will also be provided.

The National Snow and Ice Data Center at the University of Colorado Boulder manages and distributes more than 500 scientific cryospheric datasets, including data from the GIMP proje1ct. The user group of GIMP data and all other ice-velocity data is an international research community, which is relatively unorganised in terms of a formal programme. The community includes the ice-monitoring community, the ice-modelling community, and the climate-modelling community. A small set of open-source ice sheet models is widely used, and these programmes can ingest ice velocities in order to validate and constrain the models. Ice-sheet models can interface to climate models, e.g. the ice-sheet component of the Community Climate System Model is the Glimmer model, which will be used for the next IPCC climate assessment report. The mass balance of the ice sheets is of most interest to politicians and international organisations such as the IPCC, but ice velocities are needed to estimate and predict mass balance.

→ PROGRAMMATICS

9. Programmatics

9.1 Introduction

This chapter presents the technical maturity, heritage and risks associated with both the mission-level scientific concepts and the system-level technical concepts as developed in the frame of the Phase-A activities and described in Sections 9.2 and 9.3. The corresponding development approach and schedule is presented and discussed in Section 9.4.

9.2 Scientific Maturity, Critical areas and Risks

9.2.1 Previous Earth Science Advisory Committee Recommendations

Scientific Phase-A studies addressed the issues raised by the Earth Science Advisory Committee (ESAC) at the down-selection after the Assessment Phase (Phase-0). ESAC identified the following areas where further work was needed to mitigate risk: (a) improve and validate methods to correct for the ionospheric disturbance of the radar signals; (b) carry out flight campaigns, particularly in high forest-density regions, to verify the robustness of the height and biomass retrieval algorithms; (c) define and demonstrate procedures for end-to-end calibration of the PolInSAR measurement; (d) define a post-launch protocol for global validation considering different biomes; and (e) elaborate additional potential objectives of the first P-band mission in space in relation to the cryosphere (ice and permafrost), arid regions, oceanography (surface currents), soil moisture, tomography (vegetation canopy, subsurface structures) and topographic correction below dense forests.

9.2.2 Maturity

Biomass is a scientifically unique and highly innovative mission concept. It will provide the scientific community with urgently-required spatially-explicit maps of biomass height and disturbance patterns for the most critical and vulnerable forest ecosystems of the world. In addition the mission responds to the pressing need for biomass observations in support of global treaties, including the UNFCCC REDD+ initiative.

During Phase-A, major progress was made in understanding the physics of P-band scattering from forests. This was greatly aided by new campaign data that allowed, inter alia, to achieve a demonstration of the significant potential of SAR tomography to give insight into the physics underlying the sensitivity of PolSAR and PolInSAR to forest properties in different biomes. This contributed to the development of new biomass retrieval methods from combined PolSAR and PolInSAR that can counteract the disturbing effects of topography, variations is soil moisture and structural differences between forests. These have been applied successfully to new airborne campaign data, and, in particular, were demonstrated under hilly heterogeneous dense tropical forest conditions in French Guiana and boreal forests in Sweden. Performance assessment of these algorithms based on synthetic simulations showed that the required accuracy can be achieved.

Assessments based on campaign data over boreal forests indicate slightly larger uncertainties that are non-compliant with the requirement. This can be partly explained by uncertainties in the *in situ* data and should be reduced when use is made of speckle reduction methods that exploit multiple channels (polarisation and time). The forest height product derived from a single-

baseline (the baseline PolInSAR scenario for Biomass) was assessed and found not to meet the 20–30% accuracy requirement. This occurs because of a ground scattering component contributing to all polarisation channels in less dense forest conditions (e.g. boreal forest) and temporal decorrelation. However, the performance assessment showed that both disturbing effects can be adequately compensated when integrated into the inversion problem under a dual-baseline mission scenario, which is feasible for Biomass and which is being analysed at system level during the extension of Phase-A.

Major progress was made in understanding and mitigating the impact of the ionosphere on Biomass measurements. The dawn/dusk orbit selected for Biomass means that scintillations have negligible effect on biomass inversion performance except for the northernmost temperate and boreal forests in the North American/Canadian sector. Distortion of polarimetric data caused by FR can be corrected to accuracies that render it negligible with regard to biomass inversion. The only limitations on the achievable accuracy of the correction are adequate signal-to-noise ratio and the scale lengths over which variability in the ionosphere is small enough to allow spatial averaging (typically several km except under unusual conditions). Decorrelation owing to differential spatial gradients in TEC between interferometric pairs can be corrected, with a residual loss of coherence of at most 0.06.

A validation strategy for Biomass was discussed with over 40 invited key scientists from the international *in situ* measurement and ecological modelling communities at a dedicated workshop in November 2010. Data for mission evaluation will build on existing programmes of the scientific community covering all major biomes of the world, and will benefit from both the growth in the number and spread of *in situ* sites, and the growing exploitation of airborne lidar campaigns to provide local biomass maps. A draft concept for the post-launch protocol for global validation is being developed in the Phase-A extension.

Under constraints imposed by primary mission objectives, subsurface mapping in arid regions, topographic mapping of the forest floor below forests and ice-flow monitoring have been identified as sufficiently mature and capable of being addressed as secondary mission objectives.. The assessment of these applications will benefit from analysis of recent and planned airborne campaign data. For ice applications, the opportunities opened up by the very recent developments in the correction of scintillations must be taken into consideration.

9.2.3 Critical Areas

Important sources of uncertainty in the PolSAR inversion schemes arise from topographic effects and the limited system bandwidth. Efforts to address these issues are continuing and will benefit from further work on the use of ascending and descending measurements, exploiting multiple baselines, and better understanding of the error structure in the height and biomass measurements to optimise combined use of PolSAR and PolInSAR observations in estimating biomass. This work continues during the Phase-A extension and will benefit from further campaign data analysis and from end-to-end mission performance simulations. The accuracy of the PolInSAR inversion critically depends on the availability of a dual-baseline (or multibaseline) scenario. The implementation of such a mission scenario is being investigated during the Phase-A extension.

Newly-developed algorithms seem able to remove some of the limitations imposed on the mission by the ionosphere, especially methods that first reconstruct the ionosphere using measurements of FR, amplitude correlation between interferometric pairs, and/or their combination. Although successfully demonstrated on synthetic simulations and ALOS data, further testing is required. If proven robust, these methods should enable high-latitude

imaging for ice objectives, but are unlikely to be sufficient to permit differential InSAR for ice motion.

A concept for end-to-end calibration of the Pol-InSAR signal has been developed and published. This is being refined during the Phase-A extension to assess its sensitivity to ionospheric conditions and to confirm whether an independent LOS estimate of TEC between the satellite and the ground at a limited number of instrumented calibration sites is needed. During the implementation phase, it will be necessary to establish the number and positioning of these calibration sites, given logistical constraints and expected properties of the instrument.

Finally, further development of the post-launch protocol for global validation of Biomass products during the implementation phase should include steps to consolidate and harmonise these databases in key biomes. Although available campaign data and analysis indicate that algorithms and parameterisations can be transferred between regions, the extent to which forests need to be stratified in order to define the sampling strategy needs further campaign data.

9.2.4 Risks

It is recognised that, due to logistics and variation in natural conditions, no amount of campaign activities can address all potential forest systems and conditions that may be encountered globally by the Biomass mission. A particular data gap at present is for high-quality polarimetric and PolInSAR data from tropical forests of moderate biomass levels (i.e. less than 300 t ha^{-1}), with and without topography. Here, unlike dense tropical forest, environmental change (e.g. soil moisture) is likely to matter and it is presently not known if the methods developed to counteract these effects in boreal forests can be transferred. Hence, further campaigns are highly desirable. Although the transferability of algorithms between widely separated locations was demonstrated during Phase-A, we have limited evidence on which to define the stratification and density of ground sites needed to parameterise the PolSAR inversion methods (this is less of a concern for height inversion). Although it is expected that enhanced retrieval algorithms (e.g. by exploiting multichannel filtering) should significantly improve current results. This needs to be demonstrated, probably using the BEES simulator, since both temporal and polarimetric diversity are needed. Additional BEES experiments are already in progress to test the range of natural variability under synthetic conditions.

9.3 Technical maturity, critical areas and risks

The maturity of the mission concept for the satellite platform is different than for the SAR payload. At platform level, no critical elements have been identified for the Biomass development. At payload level, some development risks are associated with specific elements of the P-band SAR payload, specifically in the feed system, the power amplifier and the instrument calibration aspects. In all cases, dedicated activities are being conducted to mitigate these risks. At mission level, the following risks are particular to the Biomass mission and are being considered:

Operation of Space Objects Tracking Radar (SOTR) systems restricts the imaging opportunities for Biomass because of the potential impact on the SOTR performance from the Biomass SAR signal. The list of the operative SOTR is described in the ITU-R Recommendation RS.1260-1 in accordance with the footnote 5.279A of the ITU Radio-Regulations. These SOTR stations are all under the authority of the USA. Discussions have taken place between ESA and the USA Department of Defense (DoD). DoD has recently requested that ESA do no operate Biomass when in sight of SOTR stations. If a different agreement

Figure 9.1. Reduction in the observed forested areas due to LOS limitation of US SOTR.
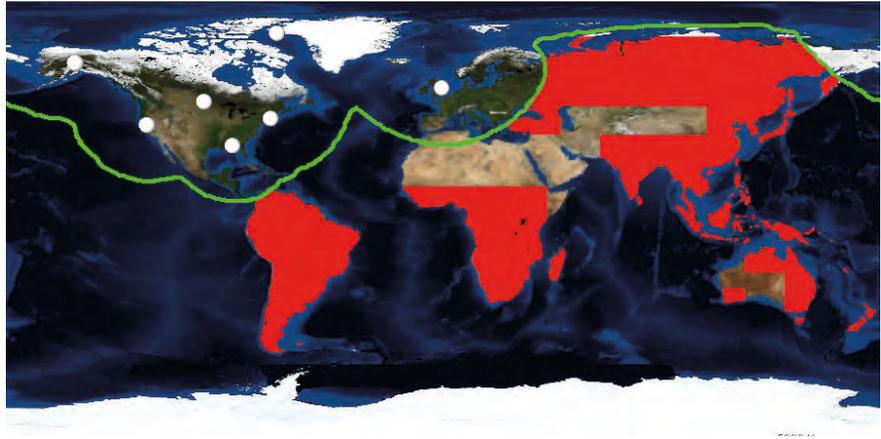
is not reached, the impact at mission level will be a reduction of the observed forested areas. Figure 9.1 shows, in red, the observed forested areas, while the green line shows the boundary contour of the SOTR LOS region where no Biomass operations would be allowed. It is underlined that, according to the mentioned ITU-R Recommendation, the operational limitation is due to the SOTR vulnerability with respect to the Biomass transmission – a very different situation to Radio Frequency Interference (RFI) from ground sources that impairs the operations of, for instance, Earth-observing radiometers.

In terms of impact on the mission objectives, the complete loss of the SOTR LOS region will have limited effect on the primary objectives, since the only part of the critical tropical belt not covered would lie in Central America (e.g. Costa Rica). Hence, estimates of tropical land-use fluxes from deforestation and regrowth would only be slightly affected and biomass data for treaty purposes (e.g. REDD) would be available for almost all developing countries. Sinks of biomass originating from regrowth and afforestation in the temperate forests of the US and Europe would not be measurable, nor would those in the boreal forests of the US, Canada and northern Europe. However, the region with the largest temperate biomass sink is China, which is responsible for half the global temperate biomass sink in the last decade of the 20th century and the first decade of the 21st century (Pan et al., 2011); this region is unaffected, as are the vast boreal forests of Siberia. The fact that the loss of coverage is over the US, Canada and Europe greatly reduces its impact, because of the highly developed forest inventory systems in these countries. It is also likely that reasonable estimates of boreal biomass would be available from L-band winter coherence, assuming proposed missions such as ALOS-2 are successfully launched. Limited information on the biomass of lower biomass temperate forests should also be available from L-band. With respect to the secondary objectives of the mission, the complete loss of the SOTR LOS region will render impossible northern high-latitude ice applications. However, the unaffected region of Antarctica is more important in terms of sea-level rise, as shown in Chapter 2.

Deployment failure of the reflector antenna would effectively result in loss of the mission. A study is in place to further consolidate the attitude control strategy during the critical phase of the reflector deployment phase.

The ionosphere influences the instrument external calibration. A study is in place to further detail the external calibration approach and to consolidate the anticipated performance budgets.

The following sections list the most critical items, assess their technical maturity along with their heritage, and underline the status of related on-going pre-development activities.

9.3.1 Satellite Platform

Analysis of the platform subsystems shows that the majority is at Technology Readiness Level (TRL) 8–9, having all flown on a number of spacecraft missions in the past. To err on the side of caution, these have been categorised as TRL 8 and will therefore be procured as Proto Flight Model (PFM) units – to clearly gain qualification against the specific Biomass environmental requirements. For other platform components the TRL assessment is 6 or greater because of the minor adaptations required to fulfil the specific mission needs.

Deployment of a large appendage attached to a light satellite body under active control is relatively novel and merits deep analysis. Further development and simulation of the reflector deployment AOCS mode will help to reduce the development risk and give greater confidence in the system design, thus improving confidence in the robustness of the concept. A dedicated activity is planned to study the use of active control during the deployment phase and to analyse the FDIR aspects of the deployment (e.g. wheel failure momentum management).

9.3.2 Instrument

9.3.2.1 Large deployable reflector

The Large Deployable Reflector (LDR) is a commercial off-the-shelf US product. Its heritage in space has been demonstrated on several telecom programmes with a number of deployment strategies (see Figs. 5.11 and 5.12). The equipment is already completely developed and will be qualified for the Biomass environment through the PFM programme. It is considered to be a TRL 9 item.

The deployment arm is to be developed from an existing qualified mechanism. The number of joints, the overall reach and geometry will be specific to Biomass. The antenna manufacturer will be responsible for the delta development (e.g. addition of an extra hinge and adjustment of boom lengths). This is considered to be a TRL 7 item.

Procurement of the reflector and deployment arm assembly from the US is under ITAR control. Since the same reflector was also purchased for the AlphaSat ESA mission, no risk is expected in its procurement.

9.3.2.2 Reflector feed-array

The P-band reflector feed-array comprises large radiating elements as shown in Chapter 5. Performance of the feed is critical to ensure the required polarisation purity, sensitivity and ambiguity performance. A first breadboard using space-qualifiable materials was built and successfully tested achieving TRL 4 (see Fig. 5.21). Two parallel developments of a beamforming network and feed array to Engineering Model (EM) standard are on-going to determine the RF performance of the system, including testing for confirmation of multipaction-free operation. The feed array will require a full qualification programme after the on-going EM development, permitting it to reach TRL 5. The development approach will then include an Engineering Qualification Model (EQM) and PFM model sequence.

9.3.2.3 Central electronics unit

The Central Electronics Unit (CEU) has extensive heritage from previous ESA flight programmes and from national agencies. Thanks to the low operating frequency, low bandwidth and single operating mode (stripmap), the Biomass CEU is much simpler than those of SAR instruments currently in orbit. All of the required components, e.g. local oscillators, mixers, amplifiers, Application Specific Integrated Circuits (ASICs) and Field Programmable Gate Array

(FPGAs), have flight heritage and can be reused for developing the CEU. The CEU is assigned TRL 6 and will be developed following the EM, EQM and FM approach.

9.3.2.4 Transmit unit/high power amplifier

A Solid-State Power Amplifier (SSPA) with an RF peak power of up to 120 W forms the main building block of the transmit unit. Some European technological heritage exists for low-frequency SSPA from space programmes, such as the SHARAD Mars radar flown in cooperation with NASA. A technology assessment study was performed by the Technical University of Denmark to evaluate technical risks associated with the development of the SSPA and other necessary high power RF components, such as the power divider, connectors and isolator (see Fig. 5.22-right). A suitable European silicon power transistor, LDMOS (see Fig. 5.22-left), was identified, which would meet the power and radiation environment requirements. More recent gallium nitride (GaN) power transistors from the US were also found suitable (see Fig. 5.22-centre).

Two parallel developments of an elegant SSPA breadboard are on-going. Newly available European GaN devices, as well as Japanese GaN devices, will be tested, in addition to the readily identified LDMOS. The breadboards will undergo functional and performance testing and will be subjected to temperature testing and multipaction testing. The objective of this development is to achieve TRL 4, including multipaction compatibility tests to ensure design confidence. This would allow the main development to proceed securely with an EQM/PFM approach to the model philosophy.

9.3.2.3 Ground calibration

Recognising the complexity that the ionosphere introduces into calibration of low-frequency polarimetric radar on one hand, and the long wavelength at P-band leading to a large calibrator antenna aperture on the other hand, dedicated parallel studies to design a Biomass calibration transponder were initiated. The objectives are to consolidate the in-orbit calibration approach of the Biomass system and to design a calibration transponder. This work is closely coordinated with the on-going ionospheric mitigation study.

9.4 Development Approach and Schedule

9.4.1 Overall Design and Development Approach

Biomass will follow the traditional phased development process (Phases B/C/D/E) with system reviews (System Requirements Review (SRR), Preliminary Design Review (PDR), Critical Design Review (CDR) etc.) to assess the status of system design, development, procurement and integration of the flight models. In order to establish a robust development schedule, instrument and satellite platform development are nearly decoupled, i.e. parallel development activities on instrument, platform and spacecraft level are foreseen, with integration performed during the AIT phase.

For both concepts the model philosophy at system level has been developed to maximise the reuse of models considered essential for the safe development of the Biomass mission. The payload and platform development, integration, testing and verification will be performed as independently as practicable to minimise schedule impacts propagating into other areas. At satellite level, a 'hybrid approach' according to ECSS-E-10-03A has been chosen. It comprises the following models:

PFM for full qualification and acceptance testing in terms of mechanical, thermal, EMC and functional/operational requirements.

Specific qualification and validation tasks in critical areas are performed on dedicated models and test benches:

Structural Model (SM) for qualification of the structure against launch loads, for verification of structural stability, strength and stiffness, for verification of the finite element model and for validation of the interface loads for platform equipment and instruments.

Electrical and Functional Model (EFM) for command, control and electrical interface verification of the platform avionics, for onboard software/hardware interaction verification, for AOCS performance verification by closed loop testing, for development and debugging of checkout software, and for initial validation of onboard flight procedures. This model initially uses EMs of the OBC, RIU and SSMM in conjunction with numerical models of the sensors and actuators. As flight hardware deliveries are available, these are integrated and tested on the EFM prior to their integration to the satellite proto-flight model.

The specific AIT of the LDR consists typically of four distinct phases:

1. Initial installation and first motion test prior to spacecraft vibration.
2. Spacecraft vibration motion test, reflector removal and shipping to US.
3. Post-vibration reflector full deployment, photogrammetry and mesh cleaning.
4. Reflector returns to Europe for final installation for flight.

To simplify the removal of the stowed LDR prior to shipment to the US (step 2) and successive re-integration (step 4), the LDR is mounted on a single, dedicated external panel, which is shipped together with the LDR to the US.

The overall instrument development is not considered risky due to its classical SAR operating mode, low power, small bandwidth and low frequency.

9.4.2 Schedule

Assuming the start of the Phase-B1 is in early 2013, the mission implementation schedule is as shown in Fig. 9.2.

Two parallel and competitive Phase-B1 studies, of five months duration, are devoted to consolidating the technical requirements, captured in the System Requirements Specification, and, upon completion of the detailed technical definition, of further implicit or derived requirements for all subsystems, including the General Design and Interface Requirements specification. Furthermore the programmatic elements will be consolidated. The outcome of the Phase-B1 will be assessed at the Intermediate System Requirements Review. A period of eight months has been identified between the end of Phase-B1 and the start of Phase-B2 for completing the preparation of the Phase-B2/C/D ITT,

Figure 9.2. Biomass outline schedule.
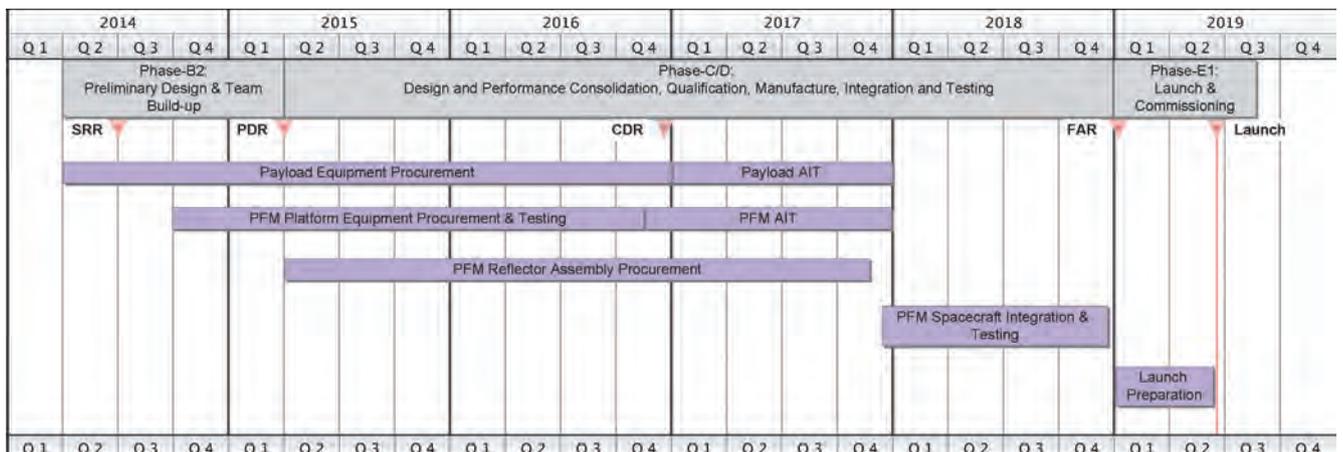
for proposal submission, and for evaluation and contract negotiations. Early in Phase-B2, a Final System Requirements Review will be held to consolidate any final updates arising through the procurement activities and to set the baseline for the full development contract.

9.5 Conclusion

Assuming successful outcome of on-going pre-developments, as expected, the maturity of critical technologies will reach the required level prior to the start of the implementation phases. The worst-case operational restriction that could arise if no agreement can be reached with the US DoD, would not significantly affect the primary objectives of the mission. The development schedule is compatible with a launch in 2019.

→ REFERENCES

References

Achard, F., Eva, H.D., Stibig, H.-J., Mayaux, P., Gallego, J., Richards, T., & Malingreau, J.-P. (2002). Determination of Deforestation Rates of the World's Humid Tropical Forests. *Science* **297**, pp999–1002.

Achard, F., Eva H.D., Mayaux, P., Stibig, H.-J. & Belward, A. (2004). Improved Estimates of Net Carbon Missions from Land Cover Change in the Tropics for the 1990s. *Global Biogeochemical Cycles* **18**, GB2008, doi:10.1029/203GB02142.

Ahlstrøm, A.P., Gravesen, P., Bech Andersen S., van As, D., Citterio, M., Fausto, R.S., Nielsen, S., Jepsen, H.F., Savstrup Kristensen S., Lintz Christensen, E., Stenseng, L., Forsberg, R., Hanson, S. & Petersen, D. (2008). A new Programme for Monitoring the Mass Loss of the Greenland Ice Sheet. *Geological Survey of Denmark and Greenland Bulletin* **15**, pp61–64.

Albinet, C., Borderies, P., Koleck, T., Rocca, F., Tebaldini, S., Le Toan, T. & Villard, L. (2012). TROPISCAT: A Ground Based Polarimetric Scatterometer Experiment in Tropical Forests. *The IEEE Journal of Selected Topics in Applied Earth Observations and Remote Sensing*, in press.

Allison, I., Alley, R.B., Fricker, H.A., Thomas, R.H. & Warner, R.C. (2009). Ice Sheet Mass Balance and Sea Level. *Antarctic Science* **21**(5), pp413–426.

Antonarakis, A.S., Saatchi, S.S., Chazdon, R.L. & Moorcroft, P.R. (2011). Using Lidar and Radar measurements to Constrain Predictions of Forest Ecosystem Structure and Function. *Ecological Applications* **21**(4), pp1120–1137.

Arianespace, 2006 VEGA User Manual Issue 3 Revision 0.

Arino, O., Leroy, M., Ranera, F., Gross, D., Bicheron, P., Nino, F., Brockman, C., Defourny, P., Vancutsem, C., Achard, F., Durieux, L., Bourg, L., Latham, J., Di Gregorio, A., Witt, R., Herold, M., Sambale, J., Plummer, S., Weber, J-L., Goryl, P., Houghton, N. (2007). GlobCover – A Global Land Cover Service With MERIS, *Proceeding of the 2007 IEEE International Geoscience and Remote Sensing Symposium*, Barcelona, Spain.

Asner, G.P., Powell, G.V.N., Mascaro, J., Knapp, D.E., Clark, J.K., Jacobson, J., Kennedy-Bowdoin, T., Balaji, A., Paez-Acosta, G., Victoria, E., Secada, L., Valqui, M. & Hughes, R.F. (2010). High-resolution forest carbon stocks and emissions in the Amazon. *Proceedings of the National Academy of Sciences* **107**, pp16738–16742.

Assmann, E. (1961). Waldertragskunde. Organische Produktion, Struktur, Zuwachs und Ertrag von Waldbeständen. München, Bonn, Wien: BLV Verlagsgesellschaft, p490.

Baccini, A., Laporte, N., Goetz, S.J., Sun, M. & Dong, H. (2008). A First Map of Tropical Africa's Above-Ground Biomass Derived from Satellite Imagery. *Environ. Res. Lett.* **3**, 045011.

Baker DF, Doney SC and Schimel DS (2006) Variational Data Assimilation for Atmospheric CO_2. Tellus, 58B, pp359–365.

Balzter, H., Davidson, M., Le Toan, T., Paillou, P., Papathanassiou, K., Plummer, S., Quegan, S., Rocca, F., Saatchi, S.S., Shugart, H. & Ulander, L. (2008) *Biomass Report for Assessment*, ESA SP 1313/2, European Space Agency.

Bamler, R. & Hartl, P. (1998). Synthetic Aperture Radar Interferometry, *Inverse Problems* **14**(4), R1–R54.

Barlow, J., Gardner, T.A., Araujo, I.S., Bonaldo, A.B., Costa, J.E., Esposito, M.C., Ferreira, L.V., Hawes, J., Hernandez, M.I.M., Leite, R.N., Lo-Man-Hung, N.F., Malcolm, J.R., Martins, M.B., Mestre, L.A.M., Nunes-Gutjahr, A.L., Overal, W.L., Parry, L., Peters, S.L., Ribeiro-Junior, M.A., da Silva Motta, C., da Silva, M.N.F. & Peres, C.A. (2007). Quantifying the Biodiversity Value of Tropical Primary, Secondary and Plantation Forests. *Proceedings of the National Academy of Science of the United States of America* **104**(47), pp18555–18560.

Beaudoin, A., Le Toan, T., Goze, S., Nezry, E., Lopes, A., Mougin, E., Hsu, C.C., Han, H.C., Kong, J.A. & Shin, R.T. (1994). Retrieval of Forest Biomass from SAR Data. *International Journal of Remote Sensing* **15**, pp2777–2796.

Beer, C., Reichstein, M., Tomelleri, E., Ciais, P., Jung, M., Carvalhais, N., Rodenbeck, C., Arain, M.A., Baldocchi, D., Bonan, G.B., Bondeau, A., Cescatti, A., Lasslop, G., Lindroth, A., Lomas, M., Luyssaert, S., Margolis, H., Oleson, K.W., Roupsard, O., Veenendaal, E., Viovy, N., Williams, C., Woodward, F.I. & Papale, D. (2010). Terrestrial Gross Carbon Dioxide Uptake: Global Distribution and Covariation with Climate. *Science* **329**, pp834–838.

Bellassen, V., Le Maire, G., Dhote, J.F., Ciais, P. & Viovy, N. (2010). Modelling Forest Management Within a Global Vegetation Model Part 1: Model Structure and General Behaviour. *Ecological Modelling* **221**(20), pp. 2458–2474.

Bellassen, V., Delbart, N., Le Maire, G., Luyssaert, S., Ciais, P. & Viovy, N. (2011). Potential Knowledge Gain in Large-Scale Simulations of Forest Carbon Fluxes from Remotely Sensed Biomass and Height. *Forest Ecology and Management* **261**, pp. 515–530.

Bickel, S.H. & Bates, R.H.T. (1965). Effects of Magneto-Ionic Propagation on the Polarization Scattering Matrix. *Proceedings of the IEEE* **53**(8), 1089–1091.

Blanc L., Echard, M., Herault, B., Bonal, D., Marcon, E., Chave, J. & Baraloto, C. (2009). Dynamics of Aboveground Carbon Stocks in a Selectively Logged Tropical Forest. *Ecological Applications* **19**(6), pp1397–1404.

Bonan, G.B. (2008). Forests and Climate Change: Forcings, Feedbacks, and the Climate Benefits of Forests. *Science* **320**, pp1444–1449.

Brown, S. & Lugo, A. E. (1992). Above Ground Biomass Estimates for Tropical Moist Forests of the Brazilian Amazon. *Interciencia* **17**, pp8–18.

Brunello P. (1993). Solar Pressure Evaluationon Large Reflectors for Space Applications, *Communications in Numerical Methods in Engineering* **9**, pp.787–795.

Bunker, D.E., De Clerck, F., Bradford, J.C., Colwell, R.K., Perfecto, I., Phillips, O.L., Sankaran, M. & Naeem, S. (2005). Species Loss and Aboveground Carbon Storage in a Tropical Forest. *Science* **310**(5750), pp1029–1031.

Canadell, J.G., Le Quere, C., Raupach, M.R., Field, C.B., Buitenhuis, E.T., Ciais, P., Conway, T.J., Gillett, N.P., Houghton, R.A. & Marland, G. (2007). Contributions to Accelerating Atmospheric CO_2 Growth from Economic Activity, Carbon Intensity, and Efficiency of Natural Sinks. *Proceedings of the National Academy of Sciences* **104**, pp18866–18870.

Cairns, M.A., Brown, S., Helmer, E.H. & Baumgardner, G.A. (1997). Root Biomass Allocation in the World's Upland Forests. *Oecologia* **111**, pp1–11.

Chave, J., Riéra, B. & Dubois, M.A. (2001). Estimation of Biomass in a Neotropical Forest of French Guiana: Spatial and Temporal Variability. *Journal of Tropical Ecolology* **17**, pp79–96.

Chave, J., Condit, R., Lao, S., Caspersen, J.P., Foster, R.B. & Hubbell, S.P. (2003) Spatial and Temporal Variation in Biomass of a Tropical Forest: Results from a Large Census Plot in Panama. *Journal of Ecology* **91**, pp240–252.

Chave, J., Andalo, C., Brown, S., Cairns, M.A., Chambers, J.Q., Eamus, D., Folster, H., Fromard, F., Higuchi, N., Kira, T., Lescure, J.P., Nelson, B.W., Ogawa, H., Puig, H., Riera, B. & Yamakura, T. (2005). Tree Allometry and Improved Estimation of Carbon Stocks and Balance in Tropical Forests. *Oecologia* **145**, pp87–99.

Chen, J., & Quegan, S. (2010). Improved Estimators of Faraday Rotation in Spaceborne Polarimetric SAR Data. *IEEE Geoscience and Remote Sensing Letters* **7**(4), pp846–850.

Ciais, P., Moore, B., Steffen, W., Hood, M., Quegan, S., Cihlar, J., Raupach, M., Rasool, I., Doney, S., Heinze, C., Sabine, C., Hibbard, K., Schulze, D., Heimann, M., Chédin, A., Monfray, P., Watson, A., LeQuéré, C., Tans, P., Dolman, H., Valentini, R., Arino, O., Townshend, J., Seufert, G., Field, C., Chu, I., Goodale, C., Nobre, A., Inoue, G., Crisp, D., Baldocchi, D., Tschirley, J., Denning, S., Cramer, W. & Francey, R. (2003). *Final Report on the IGOS-P Carbon Theme, The Integrated Global Carbon Observing Strategy: A Strategy to Build a Coordinated Operational Observing System of the Carbon Cycle and its Future Trends*, FAO.

Ciais, P., Dolman, A.J., Dargaville, R., Barrie, L., Bombelli, A., Butler, J., Canadell, P. & Moriyama, T. (2010). *GEO Carbon Strategy*, GEO Secretariat Geneva, United Nations Food and Agriculture Organisation, Rome, Italy, 48 pp.

Cloude, S.R. & Papathanassiou, K.P. (1998) Polarimetric SAR Interferometry. IEEE Transactions on Geoscience and Remote Sensing 36(5), pp1551–1565.

Cloude, S.R. (2007). Dual-baseline coherence tomography. *IEEE Geoscience and Remote Sensing Letters* **4**(1), pp127–131.

Conradsen, K., Nielsen, A.A., Schou, J. & Skriver, H. (2003). A Test Statistic in the Complex Wishart Distribution and its Application to Change Detection in Polarimetric SAR Data. *IEEE Transactions on Geoscience and Remote Sensing* **41**(1), pp4–19.

Cox, P.M., Betts, R.A., Jones, C.D., Spall, S.A. & Totterdell, I.J. (2000). Acceleration of Global Warming due to Carbon-Cycle Feedbacks in a Coupled Climate Model. *Nature* **408**, pp184–187.

Davidson, M., Attema, E.P.W., Floury, N., Rommen, B. & Snoeij, P. (2009). A Closed-Form Expression Relating Classification Accuracy to SAR System Calibration Uncertainty. *IEEE Geoscience* and *Rem. Sens. Lett* **6**, no. 3, pp467–470.

De Fries, R.S., Houghton, R.A., Hansen, M.C., Field, C.B., Skole, D. & Townshend, J. (2002). Carbon Emissions from Tropical Deforestation and Regrowth Based on Satellite Observations for the 1980s and 1990s. *Proceedings of the National Academy of Sciences* **99**, pp14256–14261.

Delbart N., Ciais, P., Chave, J., Viovy, N., Mahli, Y. & Le Toan, T. (2010). Above Ground Biomass Simulated by a Dynamic Vegetation Model in Amazonia: Mortality as a Key Pilot of the Spatial Distribution. *Biogeosciences* **7**(10), pp2989–3386.

Di Gregorio, A. & Jansen, L.J.M. (2000). Land Cover Classification System: Classification Concepts and User Manual United Nations Food and Agriculture Organization, Rome, Italy, Rome. ISBN: 92-5-105327-8

Denman, K.L., Brasseur, G., Chidthaisong, A., Ciais, P., Cox, P.M., Dickinson, R.E., Hauglustaine, D., Heinze, C., Holland, E., Jacob, D., Lohmann, U., Ramachandran, S., da Silva Dias, P.L., Wofsy, S.C. & Zhang, X. (2007). Couplings Between Changes in the Climate System and Biogeochemistry. In: Climate Change 2007: The Physical Science Basis. Contribution of Working Group I to the Fourth Assessment Report of the Intergovernmental Panel on Climate Change, Cambridge University Press, Cambridge, United Kingdom and New York, NY, USA.

Dobson, M.C., Ulaby, F.T., Le Toan, T., Beaudoin, A., Kasischke, E. & Christensen, N.L. (1992). Dependence of Radar Backscatter on Coniferous Forest Biomass. *IEEE Transactions Geoscience and Remote Sensing* **30**(2), pp412–415.

Dubois, P., Champion, I. & Paillou, P. (2004). Potential of Low Frequency SAR for Vegetation Characterization and Sub-surface Mapping: A Case Study from RAMSES Data. Final Report, ESA Contract 18501/04/NL/CB.

Dubois-Fernandez P., Le Toan, T., Daniel, S., Oriot, H., Chave, J., Blanc, L., Villard, L., Davidson, M. & Petit, M. (2012) The TropiSAR Airborne Campaign in French Guiana: Objectives, Description and Observed Temporal Behavior of the Backscatter Signal. *IEEE Transactions Geoscience and Remote Sensing*, in press.

EADS Astrium Ltd. (2011), BIO.RP.ASU.SY.00017 ISS01.1 BIOMASS Final Report.

Elachi, C., Roth, L.E. & Schaber, G.G. (1984). Spaceborne Radar Subsurface Imaging in Hyperarid Regions. *IEEE Transactions on Geoscience and Remote Sensing* **22**, pp383–388.

Enquist, B.J.; Brown, J.H.; West, G.B. (1998). Allometric Scaling of Plant Energetics and Population Density. *Nature* **395**, pp163–166.

ESA. (2006). The Changing Earth. ESA SP-1304.

FAO. (1993). Forest Resources Assessment 1990: Tropical Countries. United Nations Food and Agriculture Organization, Rome, Italy.

FAO. (2001). Global Forest Resources Assessment 2000, Main Report. FAO Forestry Paper 140, Nations Food and Agriculture Organization, Rome, Italy.

FAO. (2006). Global Forest Resources Assessment 2005. FAO Forestry Paper 147, United Nations Food and Agriculture Organization, Rome, Italy.

FAO. (2010). Global forest resources assessment, United Nations Food and Agriculture Organization, Rome, Italy. ISBN 978-92-5-106654-6.

FAO/UNEP. (1981). Tropical Forest Resources Assessment Project, United Nations Food and Agriculture Organization, Rome, Italy.

Farr, T.G., Elachi, C., Hartl, P. & Chowdhury, K. (1986). Microwave Penetration and Attenuation in Desert Soil: A Field Experiment with the Shuttle Imaging Radar. *IEEE Transactions on Geoscience and Remote Sensing* **24**(4), pp590–594.

Farr T. (2001). Imaging Radar in the Mojave Desert – Death Valley Region. Workshop on the Martian highlands and Mojave desert analogs, Las Vegas, USA.

Ferrazzoli, P., Paloscia, S., Pampaloni, P., Schiavon, G., Sigismondi, S. & Solimini, D. (1997). The Potential of Mulitfrequency Polarimetric SAR in Assessing Agricultural and Arboreous Biomass. *IEEE Transactions Geoscience Remote Sensing* **35**(1), pp5–17.

Fisher, J.I., Hurtt, G.C., Thomas R.Q. & Chambers J.Q. (1998) Clustered Disturbances Lead to Bias in Large-Scale Estimates Based on Forest Sample Plots. *Ecology Letters* **11**(6), pp554–563.

Fisher, R., McDowell, N., Purves, D., Moorcroft, P., Sitch, S., Cox, P., Huntingford, C., Meir, P. & Woodward, F.I. (2010). Assessing Uncertainties in a Second-Generation Dynamic Vegetation Model Caused By Ecological Scale Limitations. *New Phytologist* **187**, 666–681.

Fox, A., Williams, M., Richardson, A. D., Cameron, D., Gove, J. H., Quaife, T., Ricciuto, D., Reichstein, M., Tomelleri, E., Trudinger, C. M. & van Wijk, M. T. (2009). The REFLEX Project: Comparing Different Algorithms and Implementations for the Inversion of a Terrestrial Ecosystem Model Against Eddy Covariance Data. *Agricultural and Forest Meteorology* **149**, 1597–1615.

Freeman, A. (1992). SAR Calibration: An Overview. *IEEE Transactions on Geoscience and Remote Sensing* **30**(11), pp.1107–1121.

Freeman, A. (2004). Calibration of Linearly Polarized Polarimetric Sar Data Subject to Faraday Rotation. *IEEE Transactions Geoscience Remote Sensing* **42**(8), pp1617–1624.

Friedl, M.A, Sulla-Menashe, D., Tan, B., Schneider, A., Ramankutty, N., Sibley, A. & Huang, X. (2010). MODIS Collection 5 Global Land Cover: Algorithm Refinements and Characterization of New Datasets. *Remote Sensing of Environment* **114**, pp168–182

Friedlingstein, P., Cox, P., Betts, R., Bopp, L., Von Bloh, W., Brovkin, V., Cadule, P., Doney, S., Eby, M., Fung, I., Bala, G., John, J., Jones, C., Joos, F., Kato, T., Kawamiya, M., Knorr, W., Lindsay, K., Matthews, H. D., Raddatz, T., Rayner, P., Reick, C., Roeckner, E., Schnitzler, K.G., Schnur, R., Strassmann, K., Weaver, A.J., Yoshikawa, C. & Zeng, N. (2006). Climate-Carbon Cycle Feedback Analysis: Results from the C4MIP Model Intercomparison. *Journal of Climate* **19**, pp3337–3353.

Friedlingstein, P., Houghton, R.A., Marland, G., Hackler, J., Boden, T.A., Conway, T.J., Canadell, J.G., Raupach, M.R., Ciais, P. & Le Quere, C. (2010). Update on CO_2 Emissions. Nature Geoscience 3, pp811–812.

Fung, A.K. (1994). Microwave Scattering and Emission models and their Applications. Artech House. ISBN 978-0890065235.

Galbraith, D., Levy, P.E., Sitch, S., Huntingford, C., Cox, P., Williams, M. & Meir, P. (2010). Multiple Mechanisms of Amazonian Forest Biomass Losses in Three Dynamic Global Vegetation Models Under Climate Change. *New Phytologist* **187**, pp647–665.

Garestier, F., Dubois-Fernandez, P. & Champion, I. (2008). Forest Height Inversion Using High Resolution P-Band PolInSAR Data. *IEEE Transactions Geoscience Remote Sensing* **46**(10), pp3544–3559.

Garestier, F. & Le Toan, T. (2010a) Forest Modeling for Height Inversion Using Single Baseline InSAR/PolInSAR Data. *IEEE Transactions Geoscience Remote Sensing* **48**(3), pp1528–1539.

Garestier, F. & Le Toan T. (2010b). Estimation of a Forest Backscatter Profile at P-Band Using Single Baseline PolInSAR. *IEEE Transactions Geoscience Remote Sensing* **48**(9), pp3340–3348.

GCOS. (2003). Second Report on the Adequacy of the Global Observing System for Climate in Support of the UNFCCC. GCOS-82, WMO/TD No. 1143, World Meteorological Organization, 74 pp.

GCOS. (2004). Implementation Plan for the Global Observing System for Climate in Support of the UNFCCC. GCOS-92, WMO/TD No. 1219, World Meteorological Organization, 153 pp.

GCOS. (2006). Systematic Observation Requirements for Satellite-Based Products for Climate – Supplemental Details to the Satellite-Based Component of the Implementation Plan for the Global Observing System for Climate in Support of the UNFCCC. GCOS-107, WMO/TD No. 1338, World Meteorological Organization, 102 pp.

GCOS (2010), Implementation Plan for the Global Observing System for Climate in Support of the UNFCCC (2010 Update). GCOS-1338 (ES), World Meteorological Organization, 25 pp.

Gedney, N., Cox, P.M., Betts, R.A., Boucher, O., Huntingford, C. & Stott, P.A. (2006). Detection of a Direct Carbon Dioxide Effect in Continental River Runoff Records. *Nature* **439**, pp835–838, doi:10.10138/nature04504.

Gibbs, H.K., Brown, S., Niles, J.O. & Foley, J.A. (2007). Monitoring and Estimating Tropical Forest Carbon Stocks: Making REDD a Reality. *Environmental Research Letters* **2**, doi/10.1088/1748-9326/1082/1084/045023.

Gibson, L., Lee, T.M., Koh, L.P., Brook, B.W., Gardner, T.A., Barlow, J., Peres, C.A., Bradshaw, C.J.A., Laurance, W.F., Lovejoy, T.E. & Sodhi, N.S. (2011). Primary Forests are Irreplaceable for Sustaining Tropical Biodiversity. *Nature* **478**, pp378–381.

Goetz, S.J., Baccini, A., Laporte, N., Johns, T., Walker, W.S., Kellndorfer, J.M., Houghton, R.A. & Sun, M. (2009). Mapping and Monitoring Carbon Stocks with Satellite Observations: A Comparison of Methods. *Carbon Balance and Management* **4**(2).

Gonzalez, J.H., Bachmann, M., Krieger, G. & Fiedler, H., (2010). Development of the TanDEM-X Calibration Concept: Analysis of Systematic Errors. *IEEE Transactions Geoscience Remote Sensing* **48**(2), pp716–726.

Grace, J., Ryan, C., Williams, M., Powell, P., Goodman, L. & Tipper, R. (2010). A Pilot Project to Store Carbon as Biomass in African Woodlands. *Carbon Management* **1**, pp227–235.

Grainger, A. (2008). Difficulties in Tracking the Long-Term Global Trend in Tropical Forest Area. *Proceedings of the National Academy of Sciences* **105**, pp818–823.

Gray, A.L., Mattar, K.E. & Vachon, P.W. (1998). InSAR Results from the Radarsat Antarctic Mapping Mission Data: Estimation of Data Using a Simple Registration Procedure, *Proceedings of the 1998 IEEE International Geoscience and Remote Sensing Symposium*, Seattle, USA, pp1638–1640.

Grinsted, A., Moore, J.C. & Jevrejeva, S. (2009). Reconstructing Sea Level from Paleo and Projected Temperatures 200 to 2100AD. *Climate Dynamics* **34**(4), doi: 10.1007/s00382-008-0507-2. pp461–472.

Gurney, K.R., Law, R.M., Denning A.S., Rayner, P.J., Baker, D., Bousquet, P., Bruhwiler, L., Chen, Y-H., Ciais, P., Fan, S., Fung, I.Y., Gloor, M., Heimann, M., Higuchi, K., John, J., Maki, T., Maksyutov, S., Masarie, K., Peylin, P., Prather, M., Pak, B.C., Randerson, J., Sarmiento, J., Taguchi, S., Takahashi, T. & Yuen, C-W. (2002). Towards Robust Regional Estimates of CO_2 Sources and Sinks Using Atmospheric Transport Models. *Nature* **415**, pp626–630.

Gurney, K.R. & Eckels, W.J. (2011). Regional Trends in Terrestrial Carbon Exchange and their Seasonal Signatures. *Tellus B* **63**(3), pp328–339.

Haberl, H. & Erb K.-H. (2006). Assessment of Sustainable Land Use in Producing Biomass. In: Dewulf, J. & Langenhove, H.V. (eds.): Renewables-Based Technology: Sustainability Assessment. Chichester: John Wiley & Sons, pp175–192.

Hajnsek I., Scheiber, R., Ulander, L., Gustavsson, A., Sandberg, G., Tebaldini, S., Guarnieri, A.M., Rocca, F., Bombardini, F. & Pardini, M. (2008). BIOSAR 2007: Technical Assistance for the Development of Airborne SAR and Geophysical Measurements during the BioSAR 2007 Experiment, Final Report, ESA contract No.: 20755/07/NL/CB.

Hajnsek, I., Scheiber, R., Keller, M., Horn, R., Lee, S., Ulander, L., Gustavsson, A., Sandberg, G., Le Toan, T., Tebaldini, S., Monte Guarnieri, A. & Rocca, F. (2009). BIOSAR 2008: Final Report. ESTEC contract 22052/08/NL/CT-002, p302.

Hajnsek, I., Kugler, F., Lee, S.K. & Papathanassiou, K.P. (2009). Tropical Forest Parameter Estimation by Means of PolInSAR: The INDREX-II Campaign. *IEEE Transactions Geoscience Remote Sensing* **47**(2), pp481–493.

Hansen, M.C., Shimabukuro, Y.E., Potapov, P. & Pittman, K. (2008) Comparing Annual MODIS and PRODES Forest Cover Change Data for Advancing Monitoring of Brazilian Forest Cover. *Remote Sensing of Environment* **112**(10), pp3784–3793.

Hallberg, B., Smith-Jonforsen, G., Ulander, L.M.H. & Sandberg, G. (2008). A Physical-Optics Model for Double-Bounce Scattering from Stems Standing on an Undulating Ground Surface, *IEEE Transactions Geoscience Remote Sensing* **46**(9), pp2607–2621.

Hall, F., Bergen, K., Blair, J., Dubayah, R., Houghton, R., Hurtt, G., Kellndorfer, J., Lefsky, M., Ranson, J., Saatchi, S., Shugart, H., Wickland, D. (2011). Characterizing 3D Vegetation Structure from Space: Mission Requirements. *Remote Sensing of Environment* **115**(11), pp2753–2775.

Harding, D.J. & Carabajal, C.C. (2005). ICESat Waveform Measurements of Within-Footprint Topographic Relief And Vegetation Vertical Structure. *Geophysical Research Letters* **32**, L21S10.

Hoekman, D.H. & Quinones, M.J. (2000). Land Cover Type And Biomass Classification Using AirSAR Data for Evaluation of Monitoring Scenarios in the Colombian Amazon. *IEEE Transactions Geoscience Remote Sensing* **38**(2), pp685–696.

Ho Tong, M.D., Rocca, F., Le Toan, T., Tebaldini, S., d'Alessandro, M.M. & Villard, L. (2012). Relating P-Band SAR Tomography to Tropical Forest Biomass, *IEEE Transactions on Geoscience and Remote Sensing*, submitted.

Ho Tong, M.D., Le Toan, T., Tebaldini, S., Rocca, F. & D'Alessandro, M.M. (2012). Linear and Circular Polarization P-Band SAR Tomography for Tropical Forest Biomass Study.

Houghton, R.A. & Hackler, J.L. (2000). Changes in Terrestrial Carbon Storage in the United States. 1: The Roles of Agriculture and Forestry. *Global Ecology and Biogeography* **9**, pp125–144.

Houghton, R.A., Lawrence, K.T., Hackler, J.L. & Brown, S. (2001). The spatial distribution of forest biomass in the Brazilian Amazon: A comparison of estimates. *Global Change Biology* **7**, pp731–746.

Houghton, R.A., Lawrence, K.T. & Hackler, J.L. (2003). The Spatial Distribution of Forest Biomass in the Brazilian Amazon: A Comparison of Estimates. *Global Change Biology* **7**, pp731–746.

Houghton, R.A. (2003). Why are estimates of the terrestrial carbon balance so different? *Global Change Biology* **9**(4), pp500–509.

Houghton, R.A. (2005). Aboveground Forest Biomass and the Global Carbon Cycle. *Global Change Biology* **11**, pp945–958.

Houghton, R.A., Hall, F. & Goetz, S. J. (2009). Importance of Biomass in the Global Carbon Cycle. *Journal of Geophysical Research* **114**, G00E03.

Hsu, C.C., Han, C., Shin, R.T., Kong, J.A., Beaudoin, A. & Le Toan, T. (1994). Radiative Transfer Theory for Polarimetric Remote Sensing of Pine Forest At P-Band. *International Journal of Remote Sensing* **15**, pp2943–2954.

Iannini, L., Tebaldini, S. & Rocca, F. (2011). Calibration of the Tomographic Phase. Final Report on ESA/ESTEC Contract No. 22849/09/NL/JA/ef.

IGOS. (2007). IGOS Cryosphere Theme Report for the Monitoring of our Environment from Space and from Earth, WMO/TD-No. 1405, August 2007.

IGOS. (2006). IGOS Cryosphere Theme Report for the Monitoring of our Environment from Space and from Earth, Version 0.9.5.1, November 2006.

IPCC. (2003). Good Practice Guidance for Land Use, Land Use Change and Forestry (eds. Penman, P., Gytarsky, M., Hiraish, T., Krug, T., Kruger, D., Pipatta, R., Buendia, L., Miwa, K., Ngara, T., Tanabe, K. & Wagner, F.).

IPCC. (2007). IPCC Fourth Assessment Report: Climate Change 2007, The Physical Science Basis. Cambridge University Press, Cambridge, UK.

Imhoff, M.L. (1995) Radar Backscatter and Biomass Saturation: Ramification for Global Biomass Inventory. *IEEE Transactions on Geoscience and Remote Sensing* **33**, pp511–518.

ITU. (2004) ITU-2004 Article 5 ("Frequency Allocations") of the Radio Regulations, Edition 2004, International Telecommunication Union.

ITU-R RS.1260-1 Feasibility of Sharing Between Active Spaceborne Sensors and Other services in the Range 420–470 MHz.

ITU-R M.1462 Characteristics of and Protection Criteria for Radars Operating in the Radiolocation Service in the Frequency Range 420–450 MHz.

Jacobson, A.R., Mikaloff Fletcher, S.E., Gruber, N., Sarmiento, J.L. & Gloor, M. (2007). A Joint Atmosphere-Ocean Inversion for Surface Fluxes of Carbon Dioxide: 2. Regional Results. *Global Biogeochemical Cycles* **21**, GB1020, doi:10.1029/2006GB002703.

Kasischke, E.S., Melack, J.M. & Dobson, M.C. (1997) The Use of Imaging Radars for Ecological Applications – A Review. *Remote Sensing of Environment* **59**, pp141–156.

Karam, M.A., Fung A.K., Lang R.H., Chauhan N.S. (1992). A Microwave Scattering Model for Layered Vegetation. *IEEE Transactions Geoscience Remote Sensing* **4**(30), pp767–784.

Kim, J. S. & Papathanassiou, K. P. (2010). Faraday Rotation Estimator Performance Analysis. *Proceedings of EUSAR 2010*, Aachen, Germany.

Keeling, H.C. & Phillips, O.L. (2007). The Global Relationship Between Forest Productivity and Biomass. *Global Ecology and Biogeography* 16, pp618–631.

Keith, H., Mackey, B.G. & Lindenmayer, D.B. (2009). Re-Evaluation of Forest Biomass Carbon Stocks and Lessons from the World's Most Carbon-Dense Forests. *Proceedings of the National Academy of Sciences* **106**, pp11635–11640.

Köhler, P. & Huth, A. (2010). Towards Ground-Truthing of Satellite-Based Estimates of Aboveground Biomass and Leaf Area Index in Tropical Rain Forests. *Biogeosciences* 7, pp2531–2543.

Krieger, G., Moreira, A., Fiedler, H., Hajnsek, I., Werner, M., Younis, M. & Zink, M. (2007). TanDEM-X: A Satellite Formation for High-Resolution SAR Interferometry. *IEEE Transactions Geoscience and Remote Sensing* **45**(11).

Krinner, G., Viovy, N. & Noblet-Ducoubre, N. (2005). A Dynamic Global Vegetation Model for Studies of the Coupled Atmosphere-Biosphere System. *Global Biogeochemical Cycles* **19**, GB1015, doi: 10/1029/2003GB002199.

Kugler, F., Papathanassiou, K.P., Hajnsek, I., Hoekman, D. (2006). Forest Height Estimation in Tropical Rain Forest Using PolInSAR Techniques. *Proceedings of the 2006 IEEE International Geoscience and Remote Sensing Symposium*, Denver, USA.

Kurz, W.A., Dymond, C.C., Stinson, G., Rampley, G.J., Neilson, E.T., Carroll, A.L., Ebata, T. & Safranyik, L. (2008). Mountain Pine Beetle and Forest Carbon Feedback to Climate Change. *Nature* **452**, pp987–990.

Kwok, R. & Fahnestock, M.A.(1996). Ice Sheet Motion and Topography from Radar Interferometry. *IEEE Transactions on Geoscience and Remote Sensing* **34**(1), pp189–200.

Lang, R.H., Chauhan, N.S., Ranson, K.J. & Kilic, O. (1994). Modelling P-Band SAR Returns from a Red Pine Stands. *Remote Sensing of Environment* **47**, pp132–141.

Lefsky, M.A., Harding, D.J., Keller, M., Cohen, W.B., Carabajal, C., Del Bom Espirito-Santo, F., Maria, O. & de Oliveira, R. (2005). Estimates of Forest Canopy Height and Aboveground Biomass Using ICESat. *Geophysical Research Letters* **32**, L22S02, doi:10.1029/2005GL023971.

Le Quéré, C., Raupach, M.R., Canadell, J.G., Marland G., Bopp, L., Ciais, P., Conway, T.J., Doney, S.C., Feely, R.A., Foster, P., Friedlingstein, P., Gurney, K., Houghton, R.A., House, J.I., Huntingford, C., Levy, P.E., Lomas, M.R., Majkut, J., Metzl, N., Ometto, J.P., Peters, G.P., Prentice, I.C., T. Randerson, J.T., Running, S.W., Sarmiento, J.L., Schuster, U., Sitch, S., Takahashi, T., Viovy, N., van der Werf, G.R. & Woodward, F.I. (2009). Trends in the Sources and Sinks of Carbon Dioxide. *Nature Geoscience* **2**, pp831–836.

Le Toan, T., Beaudoin, A., Riom, J. & Guyon, D. (1992). Relating Forest Biomass to SAR Data. *IEEE Transactions on Geoscience and Remote Sensing* **30**, pp403–411.

Le Toan, T., Quegan, S., Davidson, M., Balzter, H., Paillou, P., Papathanassiou, K., Plummer, S., Rocca, F., Saatchi, S., Shugart, H. & Ulander, L. (2011). The BIOMASS Mission: Mapping Global Forest Biomass to Better Understand the Terrestrial Carbon Cycle. *Remote Sensing of Environment* **115**, pp2850–2860.

Lee, J.-S., Schuler, D.L., Ainsworth, T.L., Krogager, E., Kasilingam, D. & Boerner, W.-M., (2002). On the Estimation of Radar Polarization Orientation Shifts Induced By Terrain Slopes. *IEEE Transactions on Geoscience and Remote Sensing* **40**(1), 30–41.

Lee, J.S. & Ainsworth, T.L. (2011). The Effects of Orientation Angle Compensation on Coherency Matrix and Polarimetric Target Decomposition. *IEEE Transactions on Geoscience and Remote Sensing* **49**(1), pp53–64.

Lee, S.K., Kugler, F., Papathanassiou, K.P. & Hajnsek, I. (2008). Quantifying Temporal Decorrelation over Boreal Forest at L- and P-band. *Proceedings of the 7th European Conference on Synthetic Aperture Radar (EUSAR 2008)*, Friedrichshafen, Germany.

Lewis, S.L., Lopez-Gonzalez, G., Sonke, B., Affum-Baffoe, K., Baker, T.R., Ojo, L.O., Phillips, O.L., Reitsma, J.M., White, L., Comiskey, J.A., Djuikouo, M.N., Ewango, C.E.N., Feldpausch, T.R., Hamilton, A.C., Gloor, M., Hart, T., Hladik, A., Lloyd, J., Lovett, J.C., Makana, J.R., Malhi, Y., Mbago, F.M., Ndangalasi, H.J., Peacock, J., Peh, K.S.H., Sheil, D., Sunderland, T., Swaine, M.D., Taplin, J., Taylor, D., Thomas, S.C., Votere, R. & Woll, H. (2009). Increasing Carbon Storage in Intact African Tropical Forests. *Nature* **457**, U1003.

Losos, E. & Leigh, E.G. (2004). Tropical Forest Diversity and Dynamism – Finding from a Large-Scale Plot Network. The University of Chicago Press, Chicago, Illinois, USA. 645 pp.

Luyssaert, S., Gielen, B., Janssens, I., et al. (2007). CO_2 Balance of Boreal, Temperate, and Tropical Forests Derived from a Global Database. *Global Change Biology* **13**(12), pp2509–2537.

Malhi, Y., Phillips, O.L., Lloyd, J., Baker, T., Wright, J., Almeida S., Arroyo, L., Frederiksen, T., Grace, J., Killeen, T., Laurance, W.F., Leano, C., Lewis, S., Meir, P., Monteagudo, A., Neill, D., Vargas, P.N., Panfil, S.N., Patino, S., Pitman, N., Quesada, C.A., Rudas-Li, A., Salomao, R., Saleska, S., Silva, N., Silveira, M., Sombroek, W.G., Valencia, R., Martinez, R.V., Vieira, I.C.G. & Vinceti, B. (2002). An International Network to Monitor the Structure, Composition and Dynamics of Amazonian Forests (RAINFOR). *Journal of Vegetation Science* **13**, pp439–450.

Malhi, Y. & Phillips, O.L. (2004). Tropical Forests and Global Atmospheric Change: A Synthesis. *Philosophical Transactions of the Royal Society* **359**(1443), pp549–555.

Malhi, Y., Wood, D., Baker, T.R., Wright, J., Phillips, O.L., Cochrane, T., Meir, P., Chave, J., Almeida, S., Arroyo, L., Higuchi, N., Killeen, T.J., Laurance, S.G., Laurance, W.F., Lewis, S.L., Monteagudo, A., Neill, D.A., Vargas, P.N., A. Pitman, N.C., Quesada, C.A., Salomao, R., Silva, J.N.M., Lezama, A.T., Terborgh, J., Martinez, R.V. & Vinceti, B. (2006). The Regional Variation of Aboveground Live Biomass in Old-Growth Amazonian Forests. *Global Change Biology* **12**, pp1107–1138.

Mandrake, L., Wilson, B., Wang, C., Hajj, G., Mannucci, A. & X. Pi (2005). A Performance Evaluation of the Operational Jet Propulsion Laboratory/University of Southern California Global Assimilation Ionospheric Model (JPL/USC GAIM). *Journal of Geophysical Research* **110**, A12306, doi:10.1029/2005JA011170.

Massonnet, D., Rossi, M., Carmona, C., Adragna, F., Peltzer, G., Feigl, K. & Rabaute, T. (1993). The Displacement Field of the Landers Earthquake Mapped by Radar Interferometry. *Nature* **364**, pp138–142.

McCauley J.F., Schaber, G.G., Breed, C.S., Grolier, M.J., Haynes, C.V., Issawi, B., Elachi, C. & Blom, R. (1982). Subsurface Valleys and Geoarchaeology of the Eastern Sahara Revealed by Shuttle Radar. *Science* **218**, pp1004–1020.

Mette, T. (2007). Forest Biomass Estimation from Polarimetric SAR Interferometry. PhD Thesis, Technischen Universität München, 2007.

Mesquita, H.N., Dupas, C.A., Silva, M.C. & Valeriano, D.M. (2008). Amazon Deforestation Monitoring System with ALOS SAR Complementary Data. The International Archives of the Photogrammetry, Remote Sensing and Spatial Information Sciences. Vol. XXXVII. Part B8. Beijing 2008, pp1067–1070.

Michel, R. & Rignot, E. (1999). Flow of Glaciar Moreno, Argentina, from Repeat-Pass Shuttle Imaging Radar Images: Comparison of the Phase Correlation Mehod with Radar Interferometry. *Journal of Glaciology* **45**(149), pp93–100.

Milne, G., Gehrels, W., Hughes, C., & Tamisea, M. (2003). Identifying the Causes of Sea-Level Change. *Nature Geoscience*, pp471–478, doi: 10.1038/NGEO544.

Mitchard, E.T.A., Saatchi, S.S., Woodhouse, I.H., Feldpausch, T.R., Lewis, S.L., Sonké, B., Rowland, C. & Meir, P. (2011). Measuring Biomass Changes due to Woody Encroachment and Deforestation/Degradation in a Forest-Savanna Boundary Region of Central Africa Using Multi-Temporal L-Band Radar Backscatter. *Remote Sensing of Environment* **115**, pp2861–2873.

Mitchard, E.T.A., Saatchi, S.S., White, L.J.T., Abernethy, K.A., Jeffery, K.J., Lewis, S.L., Collins, M., Lefsky, M.A., Leal, M.E., Woodhouse, I.H. & Meir, P. (2012) Mapping Tropical Forest Biomass With Radar and Spaceborne LiDAR in Lope National Park, Gabon: Overcoming Problems of High Biomass and Persistent Cloud. *Biogeosciences* **9**, pp179–191.

Mokany, K., Raison, R.J. & Prokushkin, A.S. (2006) Critical analysis of root : shoot ratios in terrestrial biomes. *Global Change Biology* **12**(1), pp84–96.

Moreira, A., Krieger, G., Hajnsek, I., Werner, M., Hounam, D., Riegger, S. & Settelmeyer, E. (2004). TanDEM-X: A TerraSAR-X Add-On Satellite for Single-Pass SAR Interferometry. *Proceedings of the 2004 IEEE International Geoscience and Remote Sensing Symposium*, Anchorage, USA, pp1000–1003.

Nepstad, D.C., Veríssimo, A., Alencar, A., Nobre, C., Lima, E., Lefebvre, P., Schlesinger, P., Potter, C., Moutinho, P., Mendoza, E., Cochrane, M., & Brooks, V. (1999). Large-Scale Impoverishment of Amazonian Forests by Logging and Fire. *Nature* **398**, pp505–508.

Oliver, C.J. & Quegan, S. (1998). Understanding synthetic aperture radar images, Artech House. ISBN 978-1891121319.

Olson, J.S., Watts, J.A. & Allison, L.J. (1983). *Carbon in Live Vegetation of Major World Ecosystems*. Report ORNL-5862. Oak Ridge National Laboratory, Oak Ridge, USA, 164pp.

Paillou, P. & Dreuillet, P. (2002). The PYLA'01 experiment: Flying the New RAMSES P-Band Facility. *AIRSAR Earth Science and Application Workshop*, Pasadena, USA.

Paillou, P., Schuster, M., Farr, T., Tooth, S., Rosenqvist, A., Lopez, S. & Malézieux, J.-M. (2009). Mapping of a Major Paleodrainage System in Eastern Libya Using Orbital Imaging Radar: The Kufrah River. *Earth and Planetary Science Letters* **277**, pp327–333.

Paillou, P., Dall, J., Dubois-Fernandez, P., Hajnsek, I. & Lucas, R. (2011). BIOMASS secondary objectives assessment study. Final Report, ESA contract AO 1-6543/10/NL/CT.

Pan, Y., Birdsey, R.A., Fang, J., Houghton, R., Kauppi, P.E., Kurz, W.A., Phillips, O.L., Shvidenko, A., Lewis, S.L., Canadell, J.G., Ciais, P., Jackson, R.B., Pacala, S.W., McGuire, A.D., Piao, S., Rautiainen, A., Sitch, S. & Hayes, D. (2011). A Large and Persistent Carbon Sink in the World's Forests. *Science* **333**, pp988–993.

Papathanassiou, K.P. & Cloude, S.R. (2001). Single-baseline Polarimetric SAR Interferometry. *IEEE Transactions on Geoscience and Remote Sensing* **39**(11), pp2352–2363.

Penman, J. (2006). Good Practice Guidance for Land Use, Land-Use Change and Forestry, Hayama, Kanagawa, Japan. Published by the Institute for Global Environmental Strategies for the IPCC.

Picard, G., Le Toan, T., Quegan, S., Caraglio, Y. & Castel, T. (2004). Radiative Transfer Modeling of Cross-Polarized Backscatter from a Pine Forest Using the Discrete Ordinate and Eigenvalue Method. *IEEE Transactions Geoscience Remote Sensing* **8**(42), pp1720–1730.

Pimm, S.L. & Raven, P.H. (2000). Biodiversity: Extinctions by Numbers. *Nature* **403**(6772), pp843–845.

Pitman, A.J., de Noblet-Ducoudre N., Cruz, F. T., Davin, E.L., Bonan, G.B., Brovkin, V., Claussen, M., Delire, C., Ganzeveld, L., Gayler, V., van den Hurk, B.J.J.M., Lawrence, P.J ., van der Molen, M.K., Müller, C., Reick, C.H., Seneviratne, S.I., Strengers, B.J. & Voldoire, A. (2009). Uncertainties in Climate Responses to Past Land Cover Change: First Results from the LUCID Intercomparison Study. *Geophysical Research Letters* **36**, L14814,

Potter, C. (1999). Terrestrial Biomass and the Effects of Deforestation on the Global Carbon Cycle. *Bioscience* **49**, pp769–778.

Pretzsch, H. (2001). Modellierung des Waldwachstums. Berlin, Wien, Blackwell, 341 p.

Praaks, J., Kugler, F., Papathanassiou, K.P., Hajnsek, I. & Hallikainen, M. (2007). Treeheight Estimation for Boreal Forest by Means of L- and X-Band POLInSAR and HUTSCAT Scatterometer. *IEEE Transactions on Geoscience and Remote Sensing Letters* **4**(3), pp466–470.

Pritchard, H.D., Arthern, R.J., Vaughan, D.G. & Edwards, L.A. (2009). Extensive Dynamic Thinning on the Margins of the Greenland and Antarctic Ice Sheets. *Nature*, DOI 10.1038/nature08471.

Qi, R.-Y. & Jin, Y.-Q. (2007). Analysis of the Effects Of Faraday Rotation On Spaceborne Polarimetric SAR Observations at P-Band. *IEEE Transactions Geoscience Remote Sensing* **45**(5), pp1115–1122.

Quegan, S. (1994). A Unified Algorithm for Phase and Cross-Talk Calibration of Polarmetric Data – Theory and Observations. *IEEE Transactions on Geoscience and Remote Sensing* **32**(1), pp89–99.

Quegan, S. & Yu, J.J. (2001). Filtering of Multi-Channel SAR Images. *IEEE Transactions Geoscience Remote Sensing* **39**(11), pp2373–2379.

Quegan, S., Rogers, N., Papathanassiou, K., Kim, J.S., Rocca, F. & Tebaldini, S. (2012). Study of Ionospheric Disturbance Mitigation Schemes, Final Report, ESTEC Contract No. 22849/09/NL/JA/ef

Rabus, B., Eineder, M., Roth, A. & Bamler R. (2003). The Shuttle Radar Topography Mission—A New Class of Digital Elevation Models Acquired by Spaceborne Radar. *ISPRS Journal of Photogrammetry and Remote Sensing* **57**(4), pp241–262.

Rahmstorf, S. (2010). A new view on sea level rise. *Nature Reports Climate Change* **4**. doi:10.1038/climate.2010.29

Randerson, J.T., Hoffman, F.M., Thornton, P.E., Mahowald, N.M., Lindsay, K., Lee, Y.-H., Nevison, C.D., Doney, S.C., Bonan, G., Stöckli, R., Covey, C., Running, S.W. & Fung, I.Y. (2009). Systematic Assessment of Terrestrial Biogeochemistry in Coupled Climate–Carbon Models. *Global Change Biology* **15**, pp2462–2484.

Ranson, K.J., Sun, G., Lang, R.H., Chauhan, N.S., Cacciola, R.J. & Kilic, O. (1997). Mapping of Boreal Forest Biomass from Spaceborne Synthetic Aperture Radar. *Journal of Geophysical Research* **102**(D24), pp599–629.

Reigber, A., & Moreira, A. (2000). First Demonstration of Airborne Sar Tomography Using Multi-Baseline L-Band Data. *IEEE Transactions on Geoscience and Remote Sensing* **38**(5), pp2142–2152

Richardson, A.D., Williams, M., Hollinger, D.Y., Moore, D.J.P., Dail, D.B., Davidson, E.A., Scott, N.A., Evans, R.S., Hughes, H., Lee, J.T., Rodrigues, C. & Savage, K. (2010). Estimating Parameters of a Forest Ecosystem C Model with Measurements of Stocks and Fluxes as Joint Constraints. *Oecologia* **164**, pp25–40.

Rignot, E.J. & Van Zyl, J.J. (1993). Change Detection Techniques for ERS-1 SAR Data. *IEEE Transactions on Geoscience and Remote Sensing* **31**(4).

Rignot, E.J., Way, J., Williams, C. & Viereck, L. (1994). Radar Estimates of Aboveground Biomass in Boreal Forests of Interior Alaska. *IEEE Transactions on Geoscience and Remote Sensing* **32**(5), pp1117–1124.

Rignot, E.J., Zimmerman, R. & Van Zyl, J.J. (1995). Spaceborne Applications of P Band Imaging Radar for Measuring Forest Biomass. *IEEE Transactions on Geoscience and Remote Sensing* **33**(5), pp1162–1169.

Rignot, E.J., Ostro, S.J., van Zyl, J.J. & Jezek, K.C. (1993). Unusual Radar Echoes from the Greenland Ice Sheet. *Science* **261**(5129), pp1710–1713.

Rignot, E. & Thomas, R.H. (2002). Mass Balance of Polar Ice Sheets. *Science* **297**, pp1502–1506.

Rignot, E. (2008). Changes in West Antarctic Ice Stream Dynamics Observed with ALOS PALSAR Data. *Geophysical Research Letters* **35**, L12505, doi:10.1029/2008GL033365, pp1–5.

Rödenbeck, C., Houweling, S., Gloor, M. & Heimann, M. (2003). CO_2 Flux History 1982–2001 Inferred from Atmospheric Data Using a Global Inversion of Atmospheric Transport. *Journal of Atmospheric Chemistry and Physics* **3**, pp1919–1964.

Rosen, P.A., Hensley, S., Joughin, I.R., Li, F.K., Madsen, S.N., Rodriguez, E. & Goldstein, R. (2000). Synthetic aperture radar interferometry. *Proceedings of the IEEE* **88**(3), pp333–382.

Rosenqvist, A., Shimada, M. & Watanabe, M. (2007). ALOS-PALSAR: A Pathfinder Mission for Global-Scale Monitoring of the Environment. *IEEE Transactions on Geoscience and Remote Sensing* **45**(11), pp3307–3316.

Ryan, C.M., Hill, T.C., Woollen, E., Ghee, C., Mitchard, E.T.A., Cassells, G., Grace, J., Woodhouse, I.H. & Williams, M. (2012). Quantifying Small-Scale Deforestation and Forest Degradation in African Woodlands Using Radar Imagery. *Global Change Biology*, **18** pp. 243–257.

Saatchi, S., & McDonnald, K. (1997). Coherent Effects in Microwave Backscattering Models for Forest Canopies. *IEEE Transactions on Geoscience and Remote Sensing* **35**, pp585–598.

Saatchi, S.S., Houghton, R.A., Dos Santos Alval, R.C., Soares, J.V. & Yu, Y. (2007a). Distribution of Aboveground Live Biomass in the Amazon Basin. *Global Change Biology* **13**, pp816–837.

Saatchi, S.S., Halligan, K., Despain, D.G. & Crabtree, R.L. (2007b). Estimation of Forest Fuel Load From Radar Remote Sensing. *IEEE Transactions Geoscience Remote Sensing* **45**(6), pp1726–1740.

Saatchi, S.S., Harris, N.L., Brown, S., Lefsky, M., Mitchard, E.T.A., Salas, W., Zutta, B.R., Buermann, W., Lewis, S.L., Hagen, S., Petrova, S., White, L., Silman, M. & Morel, A. (2011). Benchmark map of forest carbon stocks in tropical regions across three continents. *Proceedings of the National Academy of Sciences* **108**(24), pp9899–9904.

Sandberg, G., Ulander, L.M.H., Holmgren, J., Fransson, J.E.S., & Le Toan, T. (2011) L- and P-band backscatter intensity for biomass retrieval in hemiboreal forest. *Remote Sensing of the Environment* **115**, pp2874–2886.

Santoro, M., Beer, C., Cartus, O., Schmullius, C., Shvidenko, A., McCallum, I., Wegmüller, U., Wiesmann, A. (2011). Retrieval of growing stock volume in boreal forest using hyper-temporal series of Envisat ASAR ScanSAR backscatter measurements. *Remote Sensing of Environment* **115**, pp490–507.

Sarmiento J.L. & Gruber, N. (2002) Sinks for anthropogenic carbon. *Physics Today* **55**(8), pp30–36.

Schaer, S., Bock, H., Dach, R., Lutz, S., Meindl, M., Orliac, E. & Thaller, D. (2011a). CODE Contributions to the IGS. Swiss National Report on the Geodetic Activities in the years 2007–2011, Section 1 (Reference Frames), Swiss Geodetic Commission, A. Wiget (Ed), pp1–2, XXV *General Assembly of the IUGG*, Melbourne, Australia.

Schaer, S. & Lutz, S. (2011b) CODE Contribution to Global Ionosphere Monitoring. Swiss National Report on the Geodetic Activities in the years 2007–2011, Section 4 (Positioning and Applications), Swiss Geodetic Commission, P.-Y. Gilliéron (Ed), pp100–101, XXV *General Assembly of the IUGG*, Melbourne, Australia.

Schutz, B.E., Zwally, H.J., Shuman, C.A., Hancock, D. & DiMarzio, J.P. (2005). Overview of the ICESat Mission. *Geophysical Research Letters* **32**(21), L21S01.

Sekido, M., Kondo, T., Kawai, E. & Imae, M. (2003). Evaluation of GPS-based ionospheric TEC map by comparing with VLBI data. *Radio Science* **38**(4).

Sessa, R. & Dolman, H. (2008). Terrestrial Essential Climate Variables for Climate Change Assessment, Mitigation and Adaptation. GTOS-52, United Nations Food and Agriculture Organisation, Rome, Italy, pp. 40.

Shteinshleiger, V.B., Dzenevitch, A.V., Manakov, Y.Y., Meinikov, L.Y. & Misezhnikov, G.S. (1997). Obtaining high resolution in trans-ionospheric space-borne VHF-band SAR for Earth remote sensing. *IEEE Conference Proceedings, Radar Systems* (Radar 97), pp268–272, doi:10.1049/cp:19971676.

Soja, M.J., Sandberg, G. & Ulander, L.M.H. (2012). Biomass Retrieval for Boreal Forests in Sloping Terrain using P-band SAR Backscatter. *IEEE Transactions on Geoscience and Remote Sensing*, submitted.

Stephens, B.B., Gurney, K.R., Tans, P.P., Sweeney, C., Peters, W., Bruhwiler, L., Ciais, P., Ramonet, M., Bousquet, P., Nakazawa, T., Aoki, S., Machida, T., Inoue, G., Vinnichenko, N., Lloyd, J., Jordan, A., Heimann, M., Shibistova, O., Langenfelds, R.L., Steele, L.P., Francey, R.J. & Denning, A.S. (2007). Weak northern and strong tropical land carbon uptake from vertical profiles of atmospheric CO_2. *Science* **316**, pp1732–1735.

Tebaldini, S. (2010). Single and Multipolarimetric SAR Tomography of Forested Areas: A Parametric Approach. *IEEE Transactions on Geoscience and Remote Sensing* **48**(5), pp2375–2387.

Tebaldini, S., D'Alessandro, M.M., Ho Tong, M.D. & Rocca, F. (2011). P-Band Penetration in Tropical and Boreal Forests: Tomographical Results. *Proceedings of the 2011 IEEE International Geoscience and Remote Sensing Symposium*, Vancouver, Canada, pp4241–4244.

Tebaldini, S. & Rocca, F. (2012). Multibaseline Polarimetric SAR Tomography of a Boreal Forest at P- and L-Bands. *IEEE Transactions on Geoscience and Remote Sensing* **50**(1), pp232–246.

Teuling, A.J., Seneviratne, S.I., Stöckli, R., Reichstein, M., Moors, E., Ciais, P., Luyssaert, S., van den Hurk, B., Ammann, C., Bernhofer, C., Dellwik, E., Gianelle, D., Gielen, B., Grünwald, T., Klumpp, K., Montagnani L., Moureaux, C., Sottocornola, M. & Wohlfahrt, G. (2010), Contrasting Response of European Forest and Grassland Energy Exchange to Heatwaves. *Nature Geoscience* **3**, pp722–727.

Thales Alenia Space Italy (2011), TNO-BIOM-0016-TASR – Final Report.

Thiel, C.J., Thiel, C. & Schmullius, C.C. (2009). Operational Large-Area Forest Monitoring in Siberia Using ALOS PALSAR Summer Intensities and Winter Coherence. *IEEE Transactions on Geoscience and Remote Sensing* **47**(12), pp3993–4000.

Ulaby, F.T., Sarabandi, K., McDonald, K., Whitt, M. & Dobson, M.C. (1990). Michigan Microwave Canopy Scattering Model. *International Journal of Remote Sensing* **11**, pp1223–1254.

Ulander, L.M.H., Gustavsson, A., Flood, B., Murdin, D., Dubois-Fernandez, P., Dupuis, X., Sandberg, G., Soja, M.J., Eriksson, L.E.B., Fransson, J.E.S., Holmgren, J. & Wallerman J. (2011a). BioSAR 2010: Technical Assistance for the Development of Airborne SAR and Geophysical Measurements during the BioSAR 2010 Experiment, Final Report, ESA contract no. 4000102285/10/NL/JA/ef.

Ulander, L.M.H., Sandberg, G. & Soja, M.J. (2011b) Biomass Retrieval Algorithm Based on P-Band BioSAR Experiments of Boreal Forest. *Proceeding of the 2011 IEEE International Geoscience and Remote Sensing Symposium*, Vancouver, Canada, pp4245–4248.

UN-REDD Programme. (2008). UN Collaborative Programme On Reducing Emissions From Deforestation And Forest Degradation In Developing Countries (UN-REDD). FAO, UNDP, UNEP.

Valle P., Mizzoni R., Zolesi M., Orlando G., Piccinini G., Heliere F. & Van't Klooster K., A Patch Feed Array for Large Reflector SAR. *Proc. 33rd ESA Antenna Workshop*, ESTEC, Noordwijk, the Netherlands, October 2011.

Valle P., Orlando G., Mizzoni R., Heliere F. & Van 't Klooster K., P-Band Feed Array for BIOMASS. *Proc. EUCAP 2012*.

Villard, L., Le Toan, T., Lasne, Y. & Mermoz, S. (2012). Relating P-Band Backscatter to Tropical Forest Biomass: Angular Normalisation Issue. *IEEE Transactions on Geoscience and Remote Sensing*, submitted.

Werner, M. (2001). Shuttle Radar Topography Mission (SRTM): Mission Overview. *J. Telecommun. (Frequenz)* **55**(3/4), pp75–79.

Wilkie, M. (2010). Country Report: Mozambique. In: Global Forest Resources Assessment 2010. Forestry Department, Food and Agriculture Organization of the United Nations.

Williams, M., Schwarz, P.A., Law, B.E., Irvine, J. & Kurpius, M. (2005). An Improved Analysis of Forest Carbon Dynamics Using Data Assimilation. *Global Change Biology* **11**, pp89–105.

Williams, M., Hill, T., Ryan, C. & Peylin, P. (2011). Final Report BIOMASS Level-2 Product to Flux Study, ESA contract No 4000102042/10/NL/CT, ESTEC, Nordwijk, The Netherlands.

Woodhouse, I.H. (2006). Predicting Backscatter-Biomass and Height-Biomass Trends Using a Macroecology Model. *Transactions on Geoscience and Remote Sensing* **44**(4), pp871–877.

Wooster, M.J., Roberts, G., Perry, G.L.W. & Kaufman Y.J. (2005). Retrieval of Biomass Combustion Rates and Totals from Fire Radiative Power Observations: FRP Derivation and Calibration Relationships Between Biomass Consumption and Fire Radiative Energy Release. *Journal Geophysical Research* **110**.

Wright, P., Quegan, S., Wheadon, N. & Hall, D. (2003). Faraday Rotation Effects on L-Band Spaceborne SAR Data. *IEEE Transactions Geoscience Remote Sensing* **41**(12), pp2735–2744.

Xu, Z.-W., Wu, J. & Wu, Z.-S. (2004). A Survey of Ionospheric Effects on Space-based Radar. *Waves in Random Media* **14**(12), pp. 189–272.

Yueh, S.H., Kong, J.A., Barnes, R.M. & Shin, R.T. (1990). Calibration of Polarimetric Radars Using In-scene Reflectors. *Polarimetric Microwave Remote Sensing* (ed. Kong, J.A.), PIER 3, pp.451–510.

Zebker, H.A. & Villasenor, J. (1992). Decorrelation in Interferometric Radar Echoes. *IEEE Transactions of Geoscience and Remote Sensing* **30**(9), pp950–959.

Zheng, D., Heath, L.S. & Ducey, M.J. (2008). Identifying Grain-Size Dependent Errors on Global Forest Area Estimates and Carbon Studies. *Geophysical Research Letters* **35**, L21403.

→ ACRONYMS

Acronyms

AASR	Azimuth Ambiguity to Signal Ratio
A/D	Analogue-to-Digital
ADM-Aeolus	Atmospheric Dynamics Mission-Aeolus
AFRITRON	African Tropical Rainforest Observation Network
AIRSAR	Airborne Synthetic Aperture Radar System (NASA)
AIT	Assembly, Integration & Testing
AKE	Absolute Knowledge Error
ALOS	Advanced Land Observing Satellite (JAXA)
AOCS	Attitude and Orbit Control System
APE	Absolute Pointing Error
ASAR	Advanced Synthetic Aperture Radar (Envisat)
ASIC	Application Specific Integrated Circuit
ASTER	Advanced Spaceborne Thermal Emission and Reflection Radiometer (NASA)
BEES	Biomass End to End Simulator
BFN	Beam Forming Network
BOL	Beginning Of Life
CCSDS	Consultative Committee for Space Data Systems
CDHS	Command and Data Handling Subsystem
CDR	Critical Design Review
CEU	Central Electronics Unit
CFRP	Carbon Fibre Reinforced Plastic
CoM	Centre of Mass
CoReH$_2$O	Cold Regions Hydrology high-resolution Observatory
COTS	Commercial Off-The-Shelf
DALEC	Data Assimilation Land Ecosystem Carbon model
DESDynI	Deforestation, Ecosystem Structure and Dynamics of Ice
DC	Doppler Centroid
DC	Direct Current
DEM	Digital Elevation Model
DET	Direct Energy Transfer
DGM	Detected Ground Multilook
DInSAR	Differential Interferometric Synthetic Aperture Radar
DLR	Deutsches Zentrum für Luft- und Raumfahrt (German Aerospace Center)
DoD	Department of Defense (US)
DTM	Digital Terrain Model
EarthCARE	Earth Clouds Aerosols and Radiation Explorer
ECV	Essential Climate Variable
EEMCS	Earth Explorer Mission Control System
EFM	Electrical and Functional Model
EGOS	ESA Ground Operations System
EM	Engineering Model
EMC	Electromagnetic Compatibility
EMS	Estrack Management and Scheduling system
ENL	Equivalent Number of Looks
Envisat	ESA Earth observation satellite
EOL	End Of Life
EPS	Electrical Power Subsystem
EQM	Engineering Qualification Model
ERS	European Remote Sensing satellite (ESA)
ESA	European Space Agency
ESAC	Earth Science Advisory Committee
ESAR	The Experimental airborne SAR System of DLR
ESM	Earth System Models
ESOC	ESA's European Space Operations Centre
ESTEC	ESA's European Space Research and Technology Centre
Estrack	ESA tracking stations' network
FAO	Food and Agriculture Organisation (United Nations)
FCL	Folding Current Limiters
FDIR	Fault Detection Isolation and Recovery
FEM	Finite Element Models
FM	Flight Model
FM	Frequency Modulated
FOCC	Flight Operations Control Centre
FOS	Flight Operations Segment
FOV	Field Of View
FPGA	Field Programmatic Gate Array
FR	Faraday Rotation
FRP	Fire Radiative Power
GaN	Gallium Nitride
GFRA	Global Forest Resource Assessments
GC	Global Coverage
GCOS	Global Climate Observing System
GDEM	Global Digital Elevation Model (ASTER)
GEC	Geo-coded Ellipsoid Corrected
GEO	Group on Earth Observations
GIMP	Greenland Ice Mapping Project
GLAS	Geoscience Laser Altimeter System
GLC2000	Global Land Cover 2000 Project
GNSS	Global Navigation Satellite System
GOCE	Gravity field and steady-state Ocean Circulation Explorer
GOSAT	Greenhouse gases Observing Satellite
GPP	Gross Primary Production
GPS	Global Positioning System
GtC	Giga tonne Carbon
GTC	Geo-coded Terrain Corrected
H	Horizontal Polarisation
HC	Harris Corporation
HDRM	Hold Down and Release Mechanisms
HKTM	House Keeping and Telemetry

HH	Horizontal Polarisation transmitted–Horizontal Polarisation received		**NPP**	Net Primary Production
HV	Horizontal Polarisation transmitted–Vertical Polarisation received		**OBC**	On-Board Computer
			OBDH	On-Board Data Handling
HPA	High Power Amplifier		**OBSW**	On-Board Software
HW	Hardware		**OCM**	Orbit Control Mode
IAM	Initial Acquisition Mode		**OCO**	Orbiting Carbon Observatory
ICESat	Ice, Cloud and Land Elevation satellite (NASA)		**ORCHIDEE**	Organizing Carbon and Hydrology In Dynamic Ecosystems model
ICU	Instrument Control Unit		**ORCHIDEE-FM**	Organizing Carbon and Hydrology In Dynamic Ecosystems model – Forest Management
IGRAC	International Groundwater Resources Assessment Centre			
IPCC	Intergovernmental Panel on Climate Change		**PALSAR**	Phase Array L-band Synthetic Aperture Radar (ALOS)
IPF	Instrument Processing Facility		**PCDU**	Power Conditioning and Distribution Unit
IRF	Impulse Response Function			
ISLR	Integrated Sidelobe Ratios		**PDR**	Preliminary Design Review
ISP	Instrument Source Packets		**PFM**	Proto Flight Model
ITAR	International Traffic in Arms Regulations		**PID**	Proportional Integral Derivative
ITU	International Telecommunications Union		**PIP**	Payload Interface Panel
JAXA	Japan Aerospace Exploration Agency		**PFD**	Power Flux Density
JERS	Japanese Earth Resource Satellite		**PDHT**	Payload Data Handling and Transmission
JRC	Joint Research Centre		**P/L**	Payload
LAI	Leaf Area Index		**PLM**	Payload Module
LC	Land Cover		**PSLR**	Peak Side Lobe Ratio
LCC	Land Cover Change		**PolInSAR**	SAR polarimetric interferometry
LCL	Latching Current Limiters		**PolSAR**	Polarimetric SAR
LDR	Large Deployable Reflector		**PREMIER**	Process Exploration through Measurements of Infrared and millimetre-wave Emitted Radiation
LDMOS	Laterally Diffused Metal Oxide Semi-conductor			
LDR	Large Deployable Reflector		**PRF**	Pulse Repetition Frequency
LEO	Low Earth Orbit		**PRI**	Pulse Repetition Interval
LEOP	Launch & Early Orbit Phase		**RAINFOR**	Amazon Forest Inventory Network
LNA	Low Noise Amplifier		**RASR**	Range Ambiguity Signal Ratio
LO	Local Oscillator		**RC**	Repeat Cycle
LOS	Line Of Sight		**RDH**	Reflector Deployment Hardware
LSCE	Laboratoire des Sciences du Climat et de l'Environment		**RDM**	Reflector Deployment Mode
			REDD	Reduction of Emissions due to Deforestation and Forest Degradation
LUC	Land Use Change			
LVA	Launch Vehicle Adapter		**RF**	Radio Frequency
MAG	Mission Advisory Group		**RFI**	Radio Frequency Interference
MCS	Mission Control System		**RGC**	RanGe Compressed
MERIS	Medium Resolution Imaging Spectrometer (Envisat)		**RIU**	Remote Interface Unit
			RMS	Root Mean Square
MMSE	Minimum Mean Square Error		**RMSE**	Root Mean Square Error
MODIS	Moderate Resolution Imaging Spectroradiometer		**RPE**	Relative Pointing Error
			RVoG	Random-Volume-over-Ground
MPPT	Maximum Power Point Tracking		**SAR**	Synthetic Aperture Radar
MPS	Mission Planning System		**S/C**	Spacecraft
MRV	Monitoring, Reporting and Validation		**SCS**	Single-look Complex Slant
NASA	National Aeronautics and Space Adminstration		**SETHI**	Système Expérimental de Télédétection Hyperfréquence Imageur
			SIR-C	Shuttle Imaging Radar-C
NEP	Net Ecosystem Production		**SLC**	Single Look Complex
NESN	Noise Equivalent Sigma Nought		**SM**	Safe Mode
NESZ	Noise Equivalent Sigma Zero		**SMOS**	Soil Moisture and Ocean Salinity mission
NG	Northrop Grumman		**SNR**	Signal to Noise Ratio
NM	Normal Mode		**SOTR**	Space Objects Tracking Radars

SRD	System Requirements Document
SRR	System Requirements Review
SRTM	Shuttle Radar Topography Mission
S/S	Sub System
SSMM	Solid State Mass Memory
SSPA	Solid-State Power Amplifiers
SVM	Service Module
SW	Software
TAR	Total Ambiguity Ratio
TanDEM-X	TerraSAR-X add-on for Digital Elevation Measurements
TC	Telecommand
TEC	Total Electron Content
TECU	Total Electron Content Unit
TM	Telemetry
TRANSCOM	Atmospheric Tracer Transport Model Intercomparison Project
TRL	Technology Readiness Level
TRU	Transmit/Receive Units
TT&C	Telemetry, Tracking & Command
UHF	Ultra High frequency
UMS	United Monolithic Semiconductor
UNEP	United Nations Environment Programme
UNFCC	United Nations Framework Convention on Climate Change
USAF	United States Air Force
USO	Ultra Stable Oscillator
UTC	Coordinated Universal Time
V	Vertical Polarisation
VV	Vertical Polarisation transmitted–Vertical Polarisation received
VH	Polarisation transmitted–Horizontal Polarisation received
WMO	World Meteorological Organization

ESA Member States

Austria
Belgium
Czech Republic
Denmark
Finland
France
Germany
Greece
Ireland
Italy
Luxembourg
Netherlands
Norway
Portugal
Romania
Spain
Sweden
Switzerland
United Kingdom